MODELLING METHODS FOR LOW-TEMPERATURE PLASMAS

document de synthèse
présenté en vue de l'obtention de
l'Habilitation à Diriger des Recherches

par

Gerardus Johannes Maria (Gerjan) HAGELAAR

Laboratoire Plasma et Conversion d'Energie (LAPLACE)
Université Paul Sabatier, Bâtiment 3R2
118 route de Narbonne, 31062 Toulouse Cedex 9, France
gerjan.hagelaar@laplace.univ-tlse.fr
05 61 55 86 49

Exposé le 5 décembre 2008 devant le jury composé de

Rapporteurs	Willem Jan GOEDHEER	Professeur	FOM Rijnhuizen, Pays-Bas
	Miles TURNER	Professeur	Dublin City University, Irlande
	Tiberiu MINEA	Professeur	LPGP, Université Paris-Sud, Orsay
Examinateurs	Pascal CHABERT	CR CNRS	LPTP, Ecole Polytechnique, Palaiseau
	Olivier SIMONIN	Professeur	IMFT, Toulouse
	Richard FOURNIER	Professeur	LAPLACE, UPS, Toulouse
	Jean-Pierre BOEUF	DR CNRS	LAPLACE, Toulouse

Avant propos

La majeure partie de mes travaux de recherche concerne le développement de modèles physiques de plasmas hors équilibre thermodynamique et des codes numériques associés, dans le cadre d'applications technologiques diverses.

Au cours des années j'ai rédigé de nombreuses notes relatives à ces modèles, détaillant par exemple des adaptations des équations physiques, des méthodes numériques, etc. J'ai souvent distribué ces notes auprès de mes collègues et des doctorants que j'ai encadrés ; je pense qu'elles sont susceptibles d'intéresser plus généralement tous les chercheurs développant des modèles physiques et numériques de plasmas hors équilibre.

Il m'a donc semblé utile de synthétiser dans ce document, en vue de l'obtention de l'habilitation à diriger des recherches, non seulement mes travaux de recherche publiés mais aussi les notes mentionnées ci-dessus. J'ai choisi de rédiger le texte principal du manuscrit en anglais afin de le rendre accessible aux collègues et étudiants étrangers. La chronologie de mes activités de recherche et d'encadrement est décrite à la fin du premier chapitre, mon projet de recherche dans le dernier chapitre. Des informations complémentaires d'ordre administratif sont données en français dans la partie annexe.

Gerjan Hagelaar
Toulouse, 1 septembre 2008

P.S. 9 janvier 2009
Depuis ma soutenance le 5 décembre, avant de distribuer ce document, j'y ai fait de nombreuses corrections et quelques ajouts (notamment dans les chapitres 5 et 7). De plus, je tiens à remercier vivement mes rapporteurs et membres de jury d'avoir examiné ces travaux.

CONTENTS

Chapter 1

INTRODUCTION

Plasma physics

Plasma is (partially) ionised gas which behaves so differently from normal gas that it is sometimes considered the fourth state of matter. Among the remarkable properties of plasma are : electrical conductivity, light emission, self-organisation, extraordinary chemical activity. Although plasma makes up over 99% of the visible matter in the universe, it does almost not exist naturally on earth but is created by man for technological purposes, in a process called gas discharge. Plasma physics studies the origin of the plasma behaviour and develops ways to create, sustain, and control plasma. This chapter outlines the physical principles of (man-created) discharge plasmas, then focuses on so-called low-temperature plasmas and how these are studied by modelling, and eventually outlines the scope of my own work.

In order to understand the behaviour of plasma, the first thing to recognise is that it consists of particles of different species with different elementary properties : electrons, ions, and neutrals. Electrons have a negative electric charge $-e$ and a mass $2000 - 10^6$ times smaller than ions and neutrals. Ions can have different charges $+e$, $-e$, $+2e$, $+3e$, etc. ; most common are singly charged positive ions. Neutrals and ions have an internal structure which can be excited to different atomic or molecular quantum states ; spontaneous decay of excited states leads to emission of photons. Depending on these properties, the plasma particles have different interactions with each other and with surrounding materials.

Short-range interactions can be represented as collisions : discrete interaction events between two particles at the time. Elastic collisions cause scattering of the particle velocities and kinetic energy transfer depending on the particle mass ratio ; elastic energy transfer between electrons and other species is very small due to the small electron mass. Inelastic collisions involve changes in the particle nature or internal state in which a certain (quantum) amount of kinetic energy is absorbed or released ; they can lead to creation or loss of particles and are essential to sustain the plasma : ionisation of neutrals is due to inelastic collisions (mainly with electrons) at high impact energy (of the order of 10 eV). Short-range interactions with the walls bounding the plasma generally cause loss of plasma particles : electrons and ions recombine at the walls and excited neutrals are often de-excited.

In addition to these short-range interactions, the electrons and ions interact over long distances through electromagnetic fields, which gives rise to the collective behaviour that is most characteristic of plasma. Assume (for simplicity) that all ions have a charge $+e$; then any difference in the electron and ion number densities implies a space charge density which induces a so-called ambipolar field[1] driving the electrons and ions together. As a result, the electron and ion densities become and remain nearly equal : the plasma is quasineutral. Since the electrons move and diffuse much faster than the ions (due to their small mass) the ambipolar field is systematically directed against the gradient of the electron density to limit the electron diffusion and accelerate the ions. The field is particularly strong in front of the walls bounding the plasma, where wall-recombination leads to the formation of a (non-

[1] The term 'ambipolar field' is used throughout this text to indicate the electrostatic field arising from the plasma charges without distinction of sheath, presheath, plasma bulk field etc.

quasineutral) boundary layer containing almost no electrons, called sheath. The total electrostatic potential drop of the ambipolar field is proportional to the electron temperature and usually occurs for 80-90 per cent across the sheath. The thickness of the sheath, characterised by the Debye length, decreases as the plasma density increases ; quasi-neutrality can only be maintained if the plasma density so high that : Debye length << plasma size ; this condition is part of the definition of plasma.[2] The ambipolar field also reacts to externally applied electric fields : the sheath thickness and potentials tend to adjust such as to screen the plasma from the applied field and prevent separation of electrons and ions.

Electrons and ions are continuously lost by (wall) recombination and need to be re-created by ionisation, which costs energy. This energy is provided to the plasma by long-range electromagnetic interaction with electrically powered conductors in the surroundings : electrodes or antennas generate an applied field, which drives a current through the plasma, which heats the plasma particles ; this process is called gas discharge and is the main means of artificial plasma creation. Many different discharge configurations are possible, driving direct, pulsed, or alternating currents, at higher or lower frequency, by electrostatic fields or electromagnetic waves, etc. Due to their small mass and fast motion, the electrons are heated more efficiently than the ions (especially by alternating fields) whereas they also collide more often, hence the plasma is generated and sustained mainly by electron-impact ionisation. Neutral gas breaks down into plasma if each electron is sufficiently heated and has enough collisions to create at least one new electron on average during its life time. As the plasma density increases, the plasma gradually screens its interior from the applied field by space charges (sheaths) or currents (skin effect). Initially this screening effect can be favourable for electron heating and ionisation because the field becomes stronger near the plasma edge ; the plasma can then be sustained at weaker applied field than necessary for breakdown. Eventually, however, the screening reduces the heating efficiency and this limits the plasma density ; the ionisation degree, i.e. the ratio of electron density to total particle density, often remains close to zero.

Plasma breakdown and sustainment are most easily achieved at some intermediate neutral gas pressure (density), such that the electrons have many collisions but not so many as to lose significant energy in (elastic) collisions before attaining the ionisation threshold energy. The electron temperature is then of the order of the ionisation energy whereas the other species stay close to room temperature ; this is characteristic of low-temperature plasmas. At higher pressure, (elastic) energy transfer leads to the simultaneous heating of all species together and breakdown requires a stronger applied field. At lower pressure, the electrons tend to be lost at the walls before ionising ; however, plasma can be sustained if the applied field does not drive the electrons to the wall so that the ambipolar field forms a stationary potential trap (e.g. inductively coupled plasmas). Low-pressure plasmas are often generated with the use of steady magnetic fields that trap the electrons in cyclotron orbits to reduce the electron wall loss and increase the ionisation probability ; this also modifies the ambipolar field and the interaction with the applied electric field, e.g. magnetized wave modes can provide special kinds of plasma heating.

[2] Plasma can be theoretically defined by two criteria. First, there are enough charged particles for the electric interaction to strongly perturb the thermal motion of the electrons : the Debye length $\lambda_D = (\varepsilon_0 T_e/en_e)^{1/2}$, characterising the distance over which the plasma fields can produce an electron velocity change of order of the electron thermal speed, is small with respect to the plasma size. Second, the electrons have enough thermal motion to interact with some average charged particle population, rather than with specific individual particles : the number of particles in the Debye sphere $N_D = (4/3)\pi\lambda_D^3 n_e >> 1$. From this second condition, it is appropriate to consider electrons and ions as separate continuous media interacting through macroscopic fields.

The electrons do not only sustain the plasma by ionisation, but also excite the neutrals to various kinds of excited quantum states, which activates chemical processes, causes the emission of electromagnetic radiation, and interferes with the electron heating and ionisation. Excitation kinetics and chemistry depend strongly on the parent gas. Noble gases are used to limit chemical activity, but molecular ions can be formed and metastable atomic species can play an important role in stepwise ionisation. In molecular gases, the electrons lose much energy by vibrational and rotational excitation, leading to gas heating and molecular dissociation. In gases with high electron-affinity (oxygen), a significant part of the electrons can get attached to neutrals and form negative ions, which reduces the ionisation efficiency and modifies the ambipolar field in complex ways. Also the wall surfaces can be involved in the plasma chemistry : wall material can be sputtered or etched, solid layers can be deposited, etc. Surface treatment is an important technological application of plasma.

According to their physical principles, plasmas are historically divided into several categories which are studied by rather distinct research communities : thermal, fusion, and low-temperature plasmas. Thermal plasmas are highly collisional plasmas where all species are near thermal equilibrium with deviations due mainly to radiation transport, created in high pressure (atmospheric) arc discharges or appearing in natural phenomena such as lightning. Fusion plasmas are fully ionised, magnetically confined, deuterium plasmas that are heated to extremely high temperatures (10 keV) for the purpose of achieving (in the future) controlled nuclear fusion exploitable as an energy source. The present text, however, focuses on low-temperature plasmas : weakly ionised discharge plasmas with high electron temperature (1 – 50 eV) and low gas temperature (300 – 2000 K), created at low to intermediate gas pressure or at small size in a large variety of discharge configurations for a large variety of applications.

Plasma modelling

Most of the fundamental physics involved in plasmas is well established [Rax05] [Rai91] and low-temperature plasma research is nowadays mainly concerned with the development and optimisation of specific plasma configurations for technological applications [Lie05]. This is done by a combination of experimental study, involving various electrical and optical measurements, and modelling. A plasma model is a system of general fundamental physical equations that are adapted, combined, and solved to describe (simulate) a specific plasma configuration. The solution of the model equations is intended to reproduce observed and measured plasma behaviour, thus explaining it in terms of fundamental physics, and if possible to predict it, thus guiding experimental development. Some basic principles of low-temperature plasma models are as follows :

- Different particle species are described separately. By order of importance : electrons (sustain the plasma and interact intensively with applied fields), ions (influence the electron motion through ambipolar coupling), excited neutrals (lead to stepwise ionisation and plasma chemistry), ground-state neutrals (feed stock for all other species). Often the neutral gas particles are so numerous that they are hardly affected by the plasma and require no description other than constant density.
- The behaviour of a single particle species is described by the Boltzmann equation, solved either by particle (Monte-Carlo) methods or through approximation by a set of fluid equations. Fluid models are more usual at high gas density, when collision effects are dominant, particle models at low gas density. Sometimes fluid equations and particle methods are combined into so-called hybrid models.

- The long-range electromagnetic interaction of charged particle species is described by electromagnetic fields from the Maxwell equations. The Poisson equation is used for the ambipolar field and electrostatic applied field, the Maxwell-Ampere equation for electrodynamic fields. Self-consistent description of the fields couples the Maxwell equations directly with all charged particle equations.
- The frequency and effects of collisions are described by cross sections, transport coefficients, and rate coefficients from the literature, deduced from measurements and (quantum-mechanical) calculations. Well-established collision data exist only for the most common (noble) gases ; much is lacking and of limited accuracy.
- The equations are solved by computer implementation of numerical methods, often standard methods from fluid mechanics and electrodynamics. The main difficulty is not so much to solve a specific equation with high accuracy, but rather to deal with the couplings between the different particle equations and the Maxwell equations.

These principles should not be taken too literally : a wide variety of more or less elaborate plasma models has been developed (and continues to be developed) all over the world for a wide variety of purposes ; some models represent all major aspects of the plasma behaviour self-consistently ; others focus on certain aspects to address specific questions. In fact, the complexity of plasma physics is such that ad hoc assumptions and approximations are required for each specific plasma configuration. The challenge of plasma modelling is to represent all the physics that is relevant to a given configuration and a given purpose at the same level of approximation, given the limited capabilities to solve the coupled plasma equations, given the limited availability and accuracy of collision data. Since quantitative predictions from plasma models are often not very good, the purpose of plasma modelling is more to predict qualitative trends in the plasma behaviour and to help understand observed or measured trends ; relatively simple models can be more effective for this purpose than comprehensive models.

Scope of my own work

I have been an active researcher and publishing author in low-temperature plasma modelling for more than 10 years, since my Ph. D. in the Netherlands, then as a post-doctoral researcher in France, and as from 2005 as an Ingénieur de Recherche at the CNRS-LAPLACE in Toulouse. During these years I have developed a number of plasma models for different technological applications and in the context of different research projects :

- During my Ph. D. research at the university of Eindhoven and in collaboration with experimental researchers at the Philips laboratories, I developed a comprehensive self-consistent 2D fluid model of microdischarges for plasma-addressed-liquid-crystal (PALC) and plasma-display-panel (PDP) televisions, as well as a series of Monte-Carlo models for electrons, ions, and resonance photons in these microdischarges. The aim was to help interpret various experimental results and optimise the discharge configurations. Publications (in refereed international journals) : [1] [2] [3] [4] [5] [6] [7] [8] [9] [15].
- During a two-year post-doc in the group of J. P. Boeuf at the CPAT[3] in Toulouse, I developed a 2D hybrid model of Hall effect thrusters for space propulsion ; later I adapted this model for double-stage thrusters. The model has been extensively used in the context of the GDR[4] Propulsion Plasma and different industrial contracts by

[3] Centre de Physique des Plasmas et de leurs Applications de Toulouse, now part of LAPLACE

[4] Groupement de Recherche = French national research program regrouping many laboratories and industrial partners, supported by the CNRS for periods of 4 years renewable.

several colleagues at the CPAT / LAPLACE[5] : researcher L. Garrigues and Ph.D. students J. Bareilles, C. Boniface, J. Perez-Luna. Purposes : thruster optimisation, interpretation of experimental data from the GDR test facility in Orléans, basic understanding of the operation of new thruster concepts. Publications [10] [12] [13] [14] [16] [18] [21] [24] [27] [30] [36] [39] [40] [41] [42] [44].

- During a one-year contract at the LIMHP[6] in Paris, I rewrote, extended, and used a self-consistent fluid model (originally developed by K. Hassouni) of a microwave plasma reactor for diamant production ; I later adapted this model to study surface wave plasma sources used at the CPAT. Publications [17] [20] [23].
- In collaboration with L. Pitchford at the CPAT / LAPLACE, I developed BOLSIG+, a user-friendly solver for the homogeneous Boltzmann equation to obtain transport coefficient and rate coefficients for fluid models from cross section data ; this code is freely available to the international plasma physics community and widely used. Publication [22] and web-site http://www.bolsig.univ-tlse.fr
- During a two-month stay at the Australian National University and also later at the LAPLACE, I was involved in the Ph.D. research project of A. Meige (co-tutelle) on modelling of electric double layers appearing in helicon and electronegative plasmas ; I also helped N. Balcon (Ph.D. co-tutelle) to develop a fluid model of an atmospheric pressure glow discharge. Publications [19] [28] [35].
- I participated in the development of a 2D model of post-arc plasma decay in a vacuum circuit breaker, in the context of a contract with Schneider Electric and the Ph.D. research of P. Sarrailh. Publications [29] [32] [38].
- In the context of an ANR[7]-project involving collaboration between the LAPLACE and several French experimental groups, I developed a 2D fluid model of micro-hollow-cathode-sustained discharges, a novel concept to sustain low-temperature plasmas at atmospheric pressure ; this model was used by two post-doctoral researchers : E. Muñoz-Serrano and K. Makasheva. Main purpose : interpretation of experimental data. Publications [25] [31] [37].
- During the past one-and-a-half years, in the context of a collaboration between the LAPLACE and the CEA[8] Cadarache, I developed a comprehensive 2D model of a inductive negative ion source for neutral beam injection for ITER ; I initially focussed on the inductive discharge in the ionisation stage of the source and am currently extending the model to describe the magnetised plasma in the source body. This research project is rapidly gaining importance and recently two new colleagues joined me on it : researcher G. Fubiani and post-doc S. Kolev ; two new Ph.D. students will start in October : N. Kohen and N. Oudini. The eventual purpose is to guide future development and optimisation of the source. Publications so far : [33] [34].
- In the context of an ANR project with the group of J. Pelletier in Grenoble, I have recently developed a 2D self-consistent model of a microwave plasma source based on electron-cyclotron resonance ; further development and exploitation of the model will be done together with post-doc K. Makasheva.

[5] Laboratoire Plasma et Conversion d'Energie = research laboratory in Toulouse were I currently work, created in 2007 by merging of three laboratories, one of which the CPAT

[6] Laboratoire d'Ingénierie des Matériaux et des Hautes Pressions, Université Paris 13, Villetaneuse

[7] Agence National de la Recherche = French government agency providing financial support for research on the basis of 3-year projects involving a small number of laboratories

[8] Commissariat à l'Energie Atomique = French atomic energy agency, hosting the ITER fusion experiment

Note that I have actively participated in the supervision of several Ph.D. students, in particular J. Bareilles, C. Boniface, A. Meige, N. Balcon, and J. Pérez-Luna with whom I share numerous (19) refereed journal papers ; I was also part of the Ph.D. jury of the first four of them (as a supervisor).

Organisation of the present document

Although my research activities cover a rather wide range of plasma configurations, conditions, and technological applications, they show clear coherence from a more technical point of view : I have taken on each new modelling project on the basis of my previous experiences, starting from and extending the concepts, equations, and numerical methods that I was familiar with and that worked well before. Over the years this has yielded a series of well-developed methods and concepts that I consider the heart of my expertise. Therefore, rather than presenting my work in chronological order or by research project, I have decided to present (in the next 10 chapters) a more technical synthesis of my work by an overview of these modelling methods ; this will be useful as a reference for my colleagues, my students, myself, and anyone else working with the models I developed. The methods cover much of the standard methods in low-temperature plasma modelling but include many original contributions not published anywhere else ; these contributions are each time identified by footnotes and illustrative examples from my publications are shown throughout the presentation. Reflecting the practical reality of low-temperature plasma modelling, physical and numerical questions are often discussed together.

Chapters 2-3 treat particle description on a microscopic level, chapter 4 some methods to obtain the electron distribution function in velocity space from the Boltzmann equation, chapters 5-7 direct macroscopic description of a plasma particle species by fluid equations, chapter 8 ambipolar coupling between electrons and ions, and chapters 9-10 plasma interaction with electrodynamic fields. Chapter 11 concludes on the state of the art of my work and presents my future research projects.

Chapter 2

PARTICLE MODELS

Particle models describe the trajectories of individual plasma particles (electrons, ions, neutrals) interacting with other plasma particles and surrounding materials. These individual particles are randomly sampled from the total physical particle population, which is too large (by many orders of magnitude) to be described completely, and are called test particles, super-particles, or macro-particles. Macroscopic quantities and distribution functions, representative of the total population of a certain species, are obtained by averaging over a large number of macro-particles and contain statistical errors (fluctuations) which decrease slowly as the number of macro-particles is increased.

The interaction between particles is usually not described directly but indirectly : each macro-particle sees the other particles through macroscopic electromagnetic fields and macroscopic collision probabilities. The macro-particle trajectory in phase space is calculated by integration of Newton's equations

$$\frac{d\mathbf{v}}{dt} = \frac{q}{m}\left(\mathbf{E} + \mathbf{v}\times\mathbf{B}\right) \tag{2.1}$$

$$\frac{d\mathbf{x}}{dt} = \mathbf{v}, \tag{2.2}$$

where **x** is the particle position, **v** is the particle velocity, q is the particle charge, m is the particle mass, **E** is the electric field, and **B** is the magnetic field (induction). The fields can be assumed (applied fields) or calculated self-consistently from Maxwell's equations. In the latter case, a large number of particles must be followed simultaneously, so that statistically relevant space charge densities and currents can be calculated during the time advancement of the trajectories. This technique is called particle-in-cell (PIC) [Bir94] [Ver05].

For a given macro-particle, the occurrence and effect of collisions are randomly sampled from probability distributions, based on a continuous (macroscopic) representation of the target particles. [Nan00] This random sampling is known as the Monte-Carlo-collision (MCC) method. The collision probability per unit time, called the collision frequency, is given by

$$\nu = n\sigma(v_r)v_r, \tag{2.3}$$

where n is the number density of the target particles, σ is the cross section, and v_r is the magnitude of the relative velocity of the macro-particle with respect to the target particle. The density and velocity distribution of the target particles can be assumed or calculated self-consistently. For electron and ion collisions with neutrals, the target velocity can often be neglected so that $v_r = v$ is directly the macro-particle velocity. Cross sections for the different collision types are given in the literature, usually as a function of the relative energy $Mv_r^2/2$, where M is the reduced mass of the collision partners, or the laboratory energy $mv^2/2$, where m is the electron or ion mass. Cross sections for (electron-impact) excitation or ionisation have a threshold as a function of energy[9] ; the impacting particle (electron) loses exactly the threshold energy U so its velocity after the collision is $v' = (v^2 - 2eU/m)^{1/2}$. In case of electron-impact ionisation, the remaining kinetic energy is distributed over the original electron and the new electron, which is then followed as a new macro-particle.

[9] kinetic energy in the frame of the particle being excited or ionised ≈ (electron) laboratory energy

The probability distribution of the collisional velocity scattering angle θ is in principle determined by the differential cross section $I(v,\cos\theta)$, but this is generally not available for direct use in particle models. Usually a simplified scattering angle distribution is assumed, e.g. isotropic scattering in the center-of-mass frame. For elastic collisions, the definition of the collision event and the cross section σ depend directly on the assumed scattering angle distribution. Assuming isotropic scattering, σ is defined as the momentum transfer cross section

$$\sigma_m(v) \equiv 2\pi \int (1-\cos\theta)\, I(v,\cos\theta)\, d\cos\theta\,, \tag{2.4}$$

such that macroscopic momentum transfer to the target particles is consistently obtained. Elastic momentum-transfer cross sections, deduced from measured differential cross sections and macroscopic transport coefficients, are directly available from the literature. [Hay81] Elastic ion-neutral interaction is described by two collision types : isotropic-scattering collisions and backward-scattering collisions, for which effective cross sections are available. [Phe94]

For electrons and ions, Coulomb (electric) interaction can contribute to elastic scattering. Since the electric field in equation (2.1) accounts only for the macroscopic charge density, averaged over individual particles, the effect of (three-dimensional) microscopic field fluctuations due to individual particle charges must be represented by so-called Coulomb collisions. The effective momentum-transfer cross section for Coulomb collisions is

$$\sigma_m(v) = \frac{e^4 \ln\Lambda}{4\pi\varepsilon_0{}^2 m_r{}^2 v^4} \qquad \Lambda = \frac{12\pi\varepsilon_0 T_e}{e}\sqrt{\frac{\varepsilon_0 T_e}{e n_e}} = 9N_{\mathrm{D}}\,, \tag{2.5}$$

where m_r is the reduced particle mass and the Coulomb logarithm $\ln\Lambda \approx 10$ is related to ambipolar screening, which suppresses the microscopic field at distances beyond the Debye length ; N_{D} is the number of electrons in a Debye sphere. In most low-temperature plasmas the electron and ion kinetics are dominated by collisions with neutrals so Coulomb collisions have little influence, but at higher ionisation degree $>10^{-5}$ the energy transfer associated with electron-electron collisions leads to Maxwellisation of the electron energy distribution. To capture this effect in detail, particle-in-cell models use rather sophisticated methods, involving sampling of pairs of nearby macro-electrons [Nan97].

It is important to realise that the particle models described here do not provide a real microscopic description of the plasma kinetics, because the particles are not represented directly but only statistically as macro-particles. At best, if the macro-particles are properly sampled, the macro-particle average distribution function can be generalised to the real particle population (with some statistical error), but the microscopic nature of the real kinetics is not captured. Even PIC models, generally considered the most accurate method to describe the plasma kinetics, involve important approximations in this respect : whereas the real electromagnetic interaction between electrons and ions is essentially a three-dimensional n-body problem, PIC models approximate it by superposition of macroscopic fields and binary Coulomb-collisions. [Tur06] In fact, a particle model of a certain species is exactly equivalent to a Monte-Carlo solution of the Boltzmann equation (see chapter 4).

Particle models are used for a wide variety of purposes, ranging from educational use to get insight in individual particle trajectories (e.g. in a complex magnetic field) to complete self-consistent PIC simulation of the plasma. They are also often combined with fluid equations into hybrid models to obtain detailed description of a specific aspect of the plasma but avoid the large computational effort required by complete PIC simulation ; figure 2.1 shows an example of such a hybrid simulation.

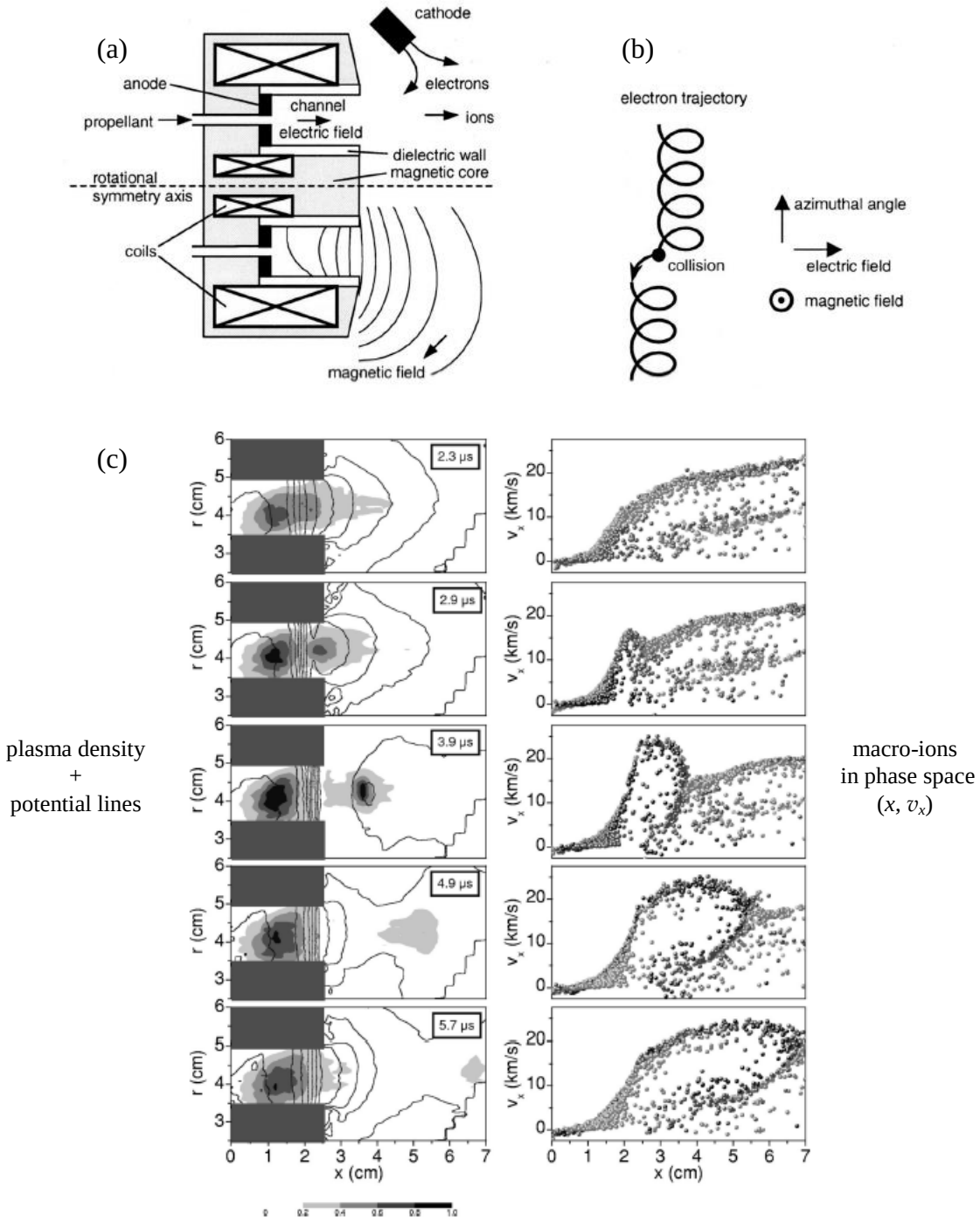

Figure 2.1. Simulation of a discharge in a Hall effect thruster for satellite propulsion by a self-consistent hybrid model combining particle description of ions and neutrals with electron fluid equations [10]. The discharge takes place in an annular channel (figure a), across a steady radial magnetic field of about 0.02 T near the thruster exit, between an anode at the bottom of the channel and an external hollow cathode with an applied voltage of 300 V. The cathode emits electrons that drift towards and multiply as they ionise the xenon gas injected at the anode. The magnetic field reduces the axial electron transport by inducing cyclotron orbits and an azimuthal Hall current as shown in figure b and discussed in chapter 5 ; hence the applied electric field penetrates inside the plasma and concentrates around the thruster exit to ensure current conservation. Due to their large mass the ions are insensitive to the magnetic field and are electrically accelerated through the thruster exit without collisions. The discharge exhibits different kinds of self-induced oscillations (instabilities). Figure c shows time evolution of the plasma density, potential, and the ion distribution in phase space during so-called transit-time oscillations at a frequency of about 100 kHz ; these oscillations strongly affect the properties of the ion beam : some ion energies exceed the applied voltage. From [16].

Chapter 3

NUMERICAL METHODS FOR PARTICLE MODELS

Leapfrog method

Newton's equations (2.1-2) are usually integrated numerically by the leapfrog method. The position **x** and the velocity **v** are calculated at different discrete moments in time, shifted by half time steps, such as to obtain central-difference approximations for the time derivatives:

$$\mathbf{v}^{k+1/2} = \mathbf{v}^{k-1/2} + \frac{q\Delta t}{m}\mathbf{E}(\mathbf{x}^k) + \frac{q\Delta t}{2m}\left(\mathbf{v}^{k+1/2} + \mathbf{v}^{k-1/2}\right)\times\mathbf{B}(\mathbf{x}^k) \tag{3.1}$$

$$\mathbf{x}^{k+1} = \mathbf{x}^k + \Delta t\mathbf{v}^{k+1/2}, \tag{3.2}$$

where Δt is the numerical time step, upper indexes refer to moments in time as $t^{k+1} = t^k + \Delta t$, and **E** and **B** are functions of space. In case there is magnetic field, equation (3.1) does not yield $\mathbf{v}^{k+1/2}$ directly and needs to be rewritten as

$$\mathbf{v}^{k+1/2} = \frac{2}{1+b^2}\left(\mathbf{v}_1 + \mathbf{v}_1\times\mathbf{b} + (\mathbf{v}_1\cdot\mathbf{b})\mathbf{b}\right) - \mathbf{v}^{k-1/2}, \tag{3.3}$$

where

$$\mathbf{v}_1 = \mathbf{v}^{k-1/2} + \frac{q\Delta t}{2m}\mathbf{E} \tag{3.4}$$

$$\mathbf{b} = \frac{q\Delta t}{2m}\mathbf{B} \tag{3.5}$$

and the time step must be small enough to resolve the cyclotron motion : $\Delta t < 0.2m/qB$. For optimal accuracy, the time shift $\Delta t/2$ between the velocity and the position should be observed when introducing new particles in the model, e.g. by off-setting the initial velocity from equation (3.1) with a negative half time step (replace Δt by $-\Delta t/2$) ; this is of special interest for momentum conservation in particle-in-cell models.

Use of random numbers

To sample particles from the total physical population and to simulate collisions, random events are sampled from probability distributions using a numerical random number generator. Such generator yields uniformly distributed random numbers R between 0 and 1 which can be used as follows. The occurrence of an event with probability p can be sampled by a Bernouilli test $R < p$, i.e. the event occurs if $R < p$. A random event i can be sampled from a set of possible events j with probabilities p_j by

$$\sum_{j=1}^{i-1} p_j < R < \sum_{j=1}^{i} p_j . \tag{3.6}$$

A random value u_R can be sampled from a probability distribution $p(u)$ between $u = a$ and $u = b$ by

$$\int_a^{u_R} p(u)du = R\int_a^b p(u)du ; \tag{3.7}$$

the right hand side reduces to R if $p(u)$ is normalized.

Rejection method

Often the random value u_R cannot be solved analytically from equation (3.7) ; then a rejection method can be used. First a tentative random value u_R is chosen, not from the distribution $p(u)$, but from a more convenient distribution $p'(u) = p(u)/g(u)$ where $g(u)$ is an arbitrary

function of u. Subsequently a second random number R is used to decide whether this tentative u_R is accepted or rejected : u_R is rejected and the procedure must be repeated if $R > g(u_R)/g_{\max}$ where $g_{\max}$ is the maximum of $g(u)$ over the entire range $[a, b]$. It can be shown that the accepted u_R values are distributed exactly according to $p(u)$. A convenient choice for g is $g(u) = p(u)$ such that the tentative u_R can be straightforwardly sampled from a uniform distribution $p'(u) = 1$ as $u_R = a + R(b-a)$, but this is not always the most efficient : to minimize the number of rejections, $g(u)$ should vary as little as possible, i.e. $p'(u)$ should be as close as possible to $p(u)$.

Random position

Initial particle positions are sampled from the spatial profile of the macroscopic particle number density n or source term S. This can be done by (numerical) spatial integration of n according to equation (3.7) but often the rejection method is more convenient. First a uniform random position $\mathbf{x}_R$ is sampled, then it is tested by another random number R and rejected if $R > n(\mathbf{x}_R)/n_{\max}$. In axisymmetric coordinates, the uniform position probability is proportional to the radius r, so equation (3.7) gives for a radial position between a and b :

$$r_R = \sqrt{a^2 + R(b^2 - a^2)} \,. \tag{3.8}$$

Random Maxwellian velocity

Initial particle velocities are often sampled from a Maxwellian velocity distribution, corresponding to thermal equilibrium. Each Cartesian velocity component then has a Gaussian probability distribution function between $-\infty$ and $+\infty$:

$$p(v_x) = \frac{1}{\sqrt{\pi} v_T} \exp(-v_x^{\,2} / v_T^{\,2}) \,, \tag{3.9}$$

and similar for v_y and v_z, where $v_T = (2eT/m)^{1/2}$ is the nominal thermal speed and T is the temperature in eV. From substitution in equation (3.7) it is clear that there is no analytical expression to sample directly a random Maxwellian velocity component. However, if we consider the magnitude of two Cartesian velocity components together $v_\perp = (v_x^{\,2} + v_y^{\,2})^{1/2}$ then the probability distribution between 0 and ∞ is

$$p(v_\perp) = \frac{2}{v_T^{\,2}} v_\perp \exp(-v_\perp^{\,2} / v_T^{\,2}) \,. \tag{3.10}$$

Due to the additional factor $v_\perp$, equation (3.7) yields

$$v_{\perp R} = v_T \sqrt{-\ln R} \,. \tag{3.11}$$

From this random value it is possible to generate two separate random Cartesian components v_x and v_y by sampling a random angle with respect to the v_x-axis :

$$\begin{aligned} v_{xR} &= v_T \sqrt{-\ln R_1} \cos(2\pi R_2) \\ v_{yR} &= v_T \sqrt{-\ln R_1} \sin(2\pi R_2) \,. \end{aligned} \tag{3.12}$$

So random Maxwellian velocity components can be generated in pairs. Since the components are completely independent, they can be interchanged and used arbitrarily to form random Maxwellian velocity vectors, e.g. two random velocity vectors can be generated as three pairs of Cartesian components.[10]

[10] This method to generate random Maxwellian velocity components is more elegant and efficient than the methods proposed in the standard text books [Bir91] [Bir94].

Random half-Maxwellian velocity

In case Maxwellian particles are introduced at a boundary surface, they are sampled from a flux rather than a density, and the probability distribution of the velocity component perpendicular to the surface contains an additional factor velocity with respect to equation (3.9). In fact, the perpendicular velocity component has exactly the probability distribution (3.10) and can be directly sampled by equation (3.11). The parallel velocity components are generated by equation (3.12) as before. This way of introducing particles results in a Maxwellian particle distribution in front of the surface, but only in the half of velocity space directed away from the surface, the other half being filled by particles coming from the volume.

Random shifted Maxwellian velocity

If particles are introduced at an open domain boundary, not corresponding to a physical wall, and if there is net particle influx, then half-Maxwellian velocity sampling leads to an unnatural discontinuity in the particle velocity distribution and the formation of an artificial boundary layer. These effects can be prevented (or at least reduced) by sampling the particles from a more natural shifted-Maxwellian distribution, i.e. the perpendicular velocity component $v_\perp$ has a probability

$$p(v_\perp) = \frac{2}{{v_T}^2} v_\perp \exp\left(-(v_\perp - w_\perp)^2 / {v_T}^2\right), \tag{3.13}$$

where $w_\perp$ is the mean velocity into the domain. Due to the velocity shift, direct sampling of $v_\perp$ is impossible, but the following rejection method is quite efficient.[11] Approximate (3.13) by

$$p'(v_\perp) = \frac{2(v_T - \beta w_\perp)}{{v_T}^3} v_\perp \exp\left(-{v_\perp}^2 (1 - \beta w_\perp / v_T) / {v_T}^2\right), \tag{3.14}$$

which corresponds to a centred Maxwellian distribution at slightly higher temperature, where β is a parameter of order unity. Now sample a tentative random velocity from p' as

$$v_{\perp R} = v_T \sqrt{\frac{-\ln R_1}{1 - \beta w_\perp / v_T}} \tag{3.15}$$

and accept this if

$$\exp\left(-\beta w_\perp (v_{\perp R} - v_T / \beta)^2 / {v_T}^3\right) > R_2, \tag{3.16}$$

otherwise reject it and repeat the procedure. The rejection probability is minimized by setting

$$\beta = \sqrt{1 + {w_\perp}^2 / 4{v_T}^2} - w_\perp / 2v_T \approx 1, \tag{3.17}$$

and is only a few per cent for $w_\perp < v_T$. To prevent boundary layer effects, the mean velocity $w_\perp$ must be consistent with the macroscopic mean velocity in the volume and if necessary iteratively adjusted. This can be done by equating the ratio of the numbers of macro-particles leaving and entering the domain, to the corresponding expectation value from the probability distribution (3.13). Approximating for $w_\perp << v_T$, this yields

$$w_\perp \approx \frac{v_T}{2\sqrt{\pi}} \left(1 - N_{\text{out}} / N_{\text{in}}\right). \tag{3.18}$$

Occurrence of collisions

As a particle advances in time, collisions of different types j occur at random moments with a total probability per unit time (mean frequency)

[11] To the best of my knowledge this method is original and more efficient than the method proposed in the standard text book [Bir94].

$$\nu(\mathbf{x},v)=\sum_j \nu_j(\mathbf{x},v)=\sum_j n_j(\mathbf{x})\sigma_j(v)v\,, \tag{3.19}$$

which in general depends on the magnitude of its velocity and possibly also on its position. For simplicity we neglect the velocity of the target particles ; this is reasonable for electrons and ions colliding with neutrals. The particle trajectory is integrated (by the leapfrog method) by small time steps Δt during which it has a small probability $\nu\Delta t << 1$ to collide. Collision events can be sampled by testing this probability each time step against a new random number as $R < \nu\Delta t$ but this is very inefficient. A better way to sample collisions is as follows. The probability that the particle has no collisions until a future time t_c is

$$P(t_c)=\exp\left(-\int_t^{t_c}\nu(t')dt'\right), \tag{3.20}$$

where ν is a function of time through $v(t)$ and $\mathbf{x}(t)$. Hence the probability distribution for the time at which the next collision occurs is

$$p(t_c)=-\frac{dP}{dt_c}=\nu(t_c)\exp\left(-\int_t^{t_c}\nu(t')dt'\right). \tag{3.21}$$

Sampling a random collision time from this distribution by equation (3.7) is impossible because the function $\nu(t)$ is not known a priori. This problem can be solved by a variant of the rejection method known as the null collision method [Sku68]. The null collision method introduces an additional collision type (the null collision) without effect on the particle but with a frequency $\nu_0(\mathbf{x},v) = \nu_{\max} - \nu(\mathbf{x},v)$, where $\nu_{\max}$ is the maximum of ν over the entire parameter range, so that the total collision frequency becomes a constant $\nu_{\max}$. Equations (3.21) and (3.7) then give directly a random collision time

$$t_{cR}=t-\frac{1}{\nu_{\max}}\ln R_1\,. \tag{3.22}$$

The particle trajectory is integrated until t_{cR} without further collision sampling. Once arrived at $t = t_{cR}$ the frequencies of the different collision types j (including the null collision) are evaluated and a collision type i is sampled by a second random number R_2 as

$$\sum_{j=0}^{i-1}\nu_j < R_2\nu_{\max} < \sum_{j=0}^{i}\nu_j\,. \tag{3.23}$$

If this yields the null collision ($R_2\,\nu_{\max} < \nu_0$) then no collision is simulated, i.e. the collision event is rejected.

Null collision method in particle-in-cell models

In particle-in-cell simulations, where a large number of particles is followed simultaneously, the null collision method is often used differently. [Vah95, Ver05] Rather than sampling and storing a random collision time t_c for each macro-particle, a certain number of colliding macro-particles is randomly sampled each time step. If there are N macro-particles, then the expectation value for the number of macro-particle collisions (including null collisions) during one time step is

$$N_c=\mathrm{int}\left(N\nu_{\max}\Delta t\right)+1\,, \tag{3.24}$$

where we have rounded off to the next higher integer. To compensate for the rounding off, $\nu_{\max}$ must be corrected as

$$\nu_{\max}{}'=\frac{N}{N_c\Delta t}\,, \tag{3.25}$$

i.e. the null collision frequency is slightly increased. Now each time step, perform N_c collision tests: choose a random macro-particle, evaluate the different frequencies ν_j for that macro-particle, and sample a collision type by equation (3.23) using the corrected $\nu_{\max}'$. Some authors [Vah95] take special care to prevent that a same macro-particle is chosen twice during the same time step, but this does not seem pertinent : if N_c is the number of macro-particle collisions (rather than the number of colliding macro-particles) then each particle should be allowed to collide more than once.

Target particle velocity

Sometimes the velocity of the target particles cannot be neglected and affects not only the change in the macro-particle velocity, but also the collision probability, which essentially depends on the relative velocity of the macro-particle with respect to the target particles, see equation (2.3). Since the target particles are not considered individually but macroscopically, it seems complicated to take this into account, but it is not. Using the null collision method, the collision frequency $\nu_{\max}$ is constant and a collision time t_c can be sampled by equation (3.22) as before. Now, before sampling the collision type by equation (3.23), sample a random target particle velocity e.g. from a Maxwellian distribution by equation (3.12), then calculate the relative velocity and use it to find the different frequencies ν_j. If necessary, different target velocities can be sampled for different target species.

Isotropic elastic collisions

Isotropic elastic collisions are most easily described by transformation to the center-of-mass (CM) frame. Consider a macro-particle with mass m_1 and velocity $\mathbf{v}_1$ colliding with a target particle with mass m_2 and velocity $\mathbf{v}_2$ (e.g. sampled from a Maxwellian distribution). The CM velocity is

$$\mathbf{v}_{CM} = \frac{m_1\mathbf{v}_1 + m_2\mathbf{v}_2}{m_1 + m_2}. \tag{3.26}$$

To find the macro-particle velocity $\mathbf{v}_1'$ after the collision, transform $\mathbf{v}_1$ to the CM frame, turn it to a random direction, and transform back to the laboratory frame :

$$\mathbf{v}_1' = |\,\mathbf{v}_1 - \mathbf{v}_{CM}\,|\,\mathbf{e}_R + \mathbf{v}_{CM} = \mathbf{v}_1 + \frac{m_2}{m_1 + m_2}\big(|\,\mathbf{v}_1 - \mathbf{v}_2\,|\,\mathbf{e}_R - (\mathbf{v}_1 - \mathbf{v}_2)\big), \tag{3.27}$$

where $\mathbf{e}_R$ is unit vector with random isotropic direction, which can be generated from two random numbers R_1 and R_2 as follows. Consider an isotropic distribution in spherical coordinates: the azimuthal angle ϕ is distributed uniformly between 0 and 2π and the cosine of the zenith angle θ uniformly between −1 and 1. Equation (3.7) then yields $\cos\theta_R = 1 - 2R_1$ and $\phi_R = 2\pi R_2$. Now use these random angles to define an isotropic unit vector with respect to the Cartesian coordinate axis :

$$\mathbf{e}_R = \begin{pmatrix} \cos\theta_R \\ \sin\theta_R \sin\varphi_R \\ \sin\theta_R \cos\varphi_R \end{pmatrix} = \begin{pmatrix} 1 - 2R_1 \\ 2\sqrt{R_1(1-R_1)}\sin(2\pi R_2) \\ 2\sqrt{R_1(1-R_1)}\cos(2\pi R_2) \end{pmatrix}. \tag{3.28}$$

The components can be interchanged. The above method is exact for arbitrary particle masses and (non-relativistic) velocities and is much simpler than the method used by many authors [Vah95] where a scattering angle is sampled with respect to the incident velocity $\mathbf{v}_1$. Equation (3.27) implicitly describes the elastic energy transfer between the particles. Averaging $\mathbf{e}_R$ and assuming Maxwellian target particles with temperature T, the expected energy change of the macro-particle is

$$\frac{1}{2}m_1({v_1}'^2 - v_1^2) = -\frac{2m_1m_2}{(m_1+m_2)^2}\left(\frac{1}{2}m_1v_1^2 - \frac{3}{2}eT\right). \qquad (3.29)$$

This is more important as the masses are closer together.

Constant macroscopic quantities

If the model system is constant and infinite in space and time or if it describes local equilibrium, then macroscopic quantities can be calculated from a single macro-particle trajectory by averaging over time (ergodic theorem) :

$$\langle u\rangle = \langle u\rangle_t = \int u dt \Big/ \int dt \approx \sum u \Big/ \sum 1, \qquad (3.30)$$

where u is an arbitrary quantity dependent on the particle velocity. The macro-particle is to be followed and the average to be taken over a time much longer than the characteristic time of the collisional energy transfer to the target particles. In principle the time average can be calculated by integrating u numerically over time, i.e. summing u over successive time steps, but is this not efficient because the particle velocities at successive time steps are strongly correlated. A more efficient way to calculate the time average is to sum only over certain observation times, randomly sampled by equation (3.22), with a mean frequency of the order of the total collision frequency, e.g. by defining an 'observation collision'. Macroscopic collision frequencies or collision rate coefficients can be obtained in two ways : either count the collision events of the macro-particle and divide by time, or average the collision probability $\nu(v)$ over time by equation (3.30) ; the latter is more efficient for collisions with a relatively small probability. To calculate the energy distribution function f_ε, define a series of energy intervals $\Delta\varepsilon$, count for each interval the number of observations when the particle energy is contained in the interval, and divide by the total number of observations :

$$f_\varepsilon = \frac{1}{\Delta\varepsilon}\int\limits_{\varepsilon\in\Delta\varepsilon} dt \Big/ \int dt \approx \frac{1}{\Delta\varepsilon}\sum_{\varepsilon\in\Delta\varepsilon} 1 \Big/ \sum 1\ . \qquad (3.31)$$

Macroscopic quantities as a function of space

If the system is space-dependent and bounded but constant in time, then macroscopic quantities can be obtained by following different macro-particles successively, one at the time. A macro-particle is sampled from a volume source S or from a boundary flux Γ, followed until it is lost or leaves the system, a next particle is sampled, and so on. To calculate the particle density n at a certain observation point in space, define a volume element ΔV around the observation point, then integrate the total time of particle presence inside ΔV, and continue this integral over successive macro-particles:

$$n = \frac{\int S dV + \int \Gamma dA}{N\Delta V}\int\limits_{\mathbf{x}\in\Delta V} dt \approx \frac{\int S dV + \int \Gamma dA}{N\Delta V}\Delta t \sum_{\mathbf{x}^k\in\Delta V} 1, \qquad (3.32)$$

where N is the number of macro-particles and the numerator is the number of physical particles entering the system per unit time (from which the macro-particles are sampled). The time integral is conveniently approximated by counting the total number of time steps when the particle position $\mathbf{x}^k$ is contained in ΔV. The macroscopic average of a quantity u is

$$\langle u\rangle = \int\limits_{\mathbf{x}\in\Delta V} u dt \Big/ \int\limits_{\mathbf{x}\in\Delta V} dt \approx \sum_{\mathbf{x}^k\in\Delta V} u^k \Big/ \sum_{\mathbf{x}^k\in\Delta V} 1, \qquad (3.33)$$

where u^k should be interpolated from $\mathbf{v}^{k-1/2}$ and $\mathbf{v}^{k+1/2}$ to account for the time-shift of the leapfrog method. Summing over the time steps when $\mathbf{x}^k$ is inside ΔV is efficient only if ΔV is large enough that the macro-particles do not cross it within one time step. To obtain high spatial resolution (in one direction) another averaging method can be used. Define a surface

element ΔA around the observation point and consider a volume element $\Delta V = \delta \Delta A$ with infinitesimal thickness δ. If a particle crosses ΔA, the time spent inside ΔV is $\delta/|v_\perp|$ where $v_\perp$ is the particle velocity component perpendicular to ΔA. Therefore, each time a particle crosses ΔA, cumulate its absolute inverse perpendicular velocity:

$$n = \frac{\int S dV + \int \Gamma dA}{N \Delta A} \sum_{\Delta \mathbf{x} \to \Delta A} \frac{1}{|v_\perp|} \tag{3.34}$$

$$\langle u \rangle = \sum_{\Delta \mathbf{x} \to \Delta A} \frac{u}{|v_\perp|} \Big/ \sum_{\Delta \mathbf{x} \to \Delta A} \frac{1}{|v_\perp|} . \tag{3.35}$$

For optimal accuracy, $v_\perp$ and u must be interpolated to correspond to the exact crossing of ΔA. Realise however that depending on the quantity u to be averaged, the surface element method (3.35) is not necessarily more efficient than the volume method (3.33), due to statistical errors of particles with a near-zero perpendicular velocity.

Macroscopic quantities as a function of time and space
can be obtained by following a large number of macro-particles simultaneously. This is of particular interest for particle-in-cell (PIC) models where the electric field is calculated self-consistently at every time step from the complete spatial profiles of the electron and ion densities. The spatial domain is then divided into small volume elements centred around a grid of observation points, as shown in figure 3.1 for a two-dimensional domain. The spaces between the grid points are called cells. The number of simultaneous macro-particles has to be sufficiently large for each volume element to contain at least a hundred or so macro-particles, such that statically relevant averages can be calculated. It is customary to assign to each macro-particle a weight, defined as the number of physical particles it statistically represents.

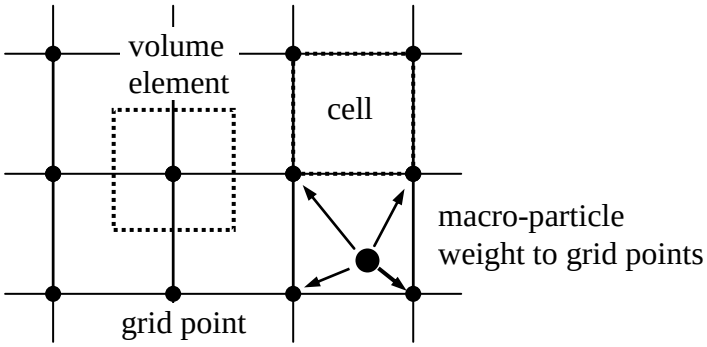

Figure 3.1. Two-dimensional grid for particle-in-cell models.

The particle density at each grid point can be straightforwardly calculated by summing the weights of the macro-particles inside the volume element and dividing by the volume (nearest grid point method), but this method is not very appropriate for PIC models. Smoother density profiles are obtained by distributing the macro-particle weight over the surrounding grid points with fractions according to proximity. Commonly used in PIC models is the linear distribution method : a macro-particle with one-dimensional position x is distributed over the surrounding grid points at x_1 and x_2 with respective fractions $(x_2-x)/(x_2-x_1)$ and $(x-x_1)/(x_2-x_1)$; for a macro-particle with two-dimensional position (x, y) inside a cell $(x_1\text{-}x_2, y_1\text{-}y_2)$, the fraction distributed to the grid point (x_1, y_1) is then $(x_2-x)/(x_2-x_1)\times(y_2-y)/(y_2-y_1)$ etc. Using this linear weight distribution method, the volume elements around the grid points must be defined consistently (such that dividing the cumulative weight by the volume yields the

proper particle density) by linear distribution of the cell volumes over the grid points. In Cartesian space, consistent volume elements are defined from the central positions between the grid points. In axisymmetric cylindrical space however, the radial edges of the volume elements do not correspond to the central positions between the grid points. Consider a cell between radial positions r_1 and r_2 with a volume $\pi(r_2^2-r_1^2)$, which is to be distributed over the grid points at r_1 and r_2. The part of the volume distributed to r_1 is

$$\int_{r_1}^{r_2} \frac{r-r_2}{r_2-r_1} 2\pi r dr = \frac{\pi}{3}\left(r_2^{\,2} + r_2 r_1 - 2r_1^{\,2}\right) \equiv \pi(r_{1+1/2}^{\,2} - r_1^{\,2}) \,. \tag{3.36}$$

The last member of this equation defines the effective edge of the volume element:

$$r_{1+1/2} = \frac{1}{\sqrt{3}} \sqrt{r_1^{\,2} + r_1 r_2 + r_2^{\,2}} \,. \tag{3.37}$$

Alternatively in cylindrical space, the particle weights can be distributed according to the quadratic radial positions, i.e. with fractions $(r_2^2-r^2)/(r_2^2-r_1^2)$ and $(r^2-r_1^2)/(r_2^2-r_1^2)$; the effective volume element edge is then given by the average quadratic radius $r_{1+1/2}^{\,2} = (r_2^2 + r_1^2)/2$. It can also be useful to define uniform quadratic radial grid positions rather than a uniform grid, such as to obtain constant volume elements and avoid bad particle statistics near the axis.

In PIC models, the particle weight distribution method must be consistent with the interpolation of the electric field to the macro-particle positions, otherwise artificial particle acceleration can occur, known as self-forces. Linear particle weight distribution is usually combined with linear interpolation of the electric field, calculated at the grid points by finite difference approximation of $\mathbf{E} = -\nabla\Phi$, where Φ is the electrostatic potential from finite-difference solution of Poisson's equation (see chapter 8).

Chapter 4

BOLTZMANN EQUATION

A plasma usually contains so many particles that statistical fluctuations of the number of particles contained in an arbitrary phase space interval (resolving the space and velocity scales of interest) can be neglected.[12] Hence it is appropriate to represent the particles of a certain species as a continuum by the distribution function f defined as the particle number density in phase space, i.e. $f(\mathbf{x},\mathbf{v},t)d^3\mathbf{x}d^3\mathbf{v}$ is the number of particles present at time t in an infinitesimal volume $d^3\mathbf{x}$ around position $\mathbf{x}$ with a velocity within an infinitesimal interval $d^3\mathbf{v}$ around $\mathbf{v}$. The evolution of the distribution function under the influence of electromagnetic fields and binary collisions is described by the Boltzmann equation

$$\frac{\partial f}{\partial t} + \mathbf{v}\cdot\nabla f + \frac{q}{m}(\mathbf{E}+\mathbf{v}\times\mathbf{B})\cdot\nabla_{\mathbf{v}} f = C[f], \tag{4.1}$$

where $\nabla_{\mathbf{v}}$ is the gradient operator in velocity space and C is the collision operator, representing the rate at which particles are transferred from one velocity (interval) to another in collisions ; without the collision term equation (4.1) is known as the Vlasov equation. The Boltzmann equation is one of the main tools to study the kinetics of plasma particles, but its solution (other than by Monte-Carlo particle methods) requires extensive approximations. Various approaches are used, focussing either on the solution of f as a function of velocity $\mathbf{v}$ while assuming simple space and time dependence, or rather on the description of f in space and time while approximating for the velocity ; the fluid approach presented in the next chapter falls into the second category.

Two-term approximation

For electrons, which are nearly isotropic due to elastic scattering by collisions and trapping by the ambipolar field, the distribution function is commonly approximated by spherical harmonics expansion in velocity space and truncation after the first order :

$$f(\mathbf{x},\mathbf{v},t) \cong f_0(\mathbf{x},v,t) + (\mathbf{v}/v)\cdot\mathbf{f}_1(\mathbf{x},v,t), \tag{4.2}$$

where f_0 is the isotropic part of the distribution function and $\mathbf{f}_1$ is an anisotropic perturbation in a certain direction ; the last term represents f_1 times the cosine of the velocity angle with respect to this direction. This is known as the two-term approximation. Substituting the two-term distribution function and averaging over angle space, the Boltzmann equation can be decomposed into

$$\frac{\partial f_0}{\partial t} + \frac{v}{3}\nabla\cdot\mathbf{f}_1 - \frac{e}{3m_e v^2}\frac{\partial}{\partial v}(v^2\mathbf{E}\cdot\mathbf{f}_1) = C_0[f_0] = \sum_j C_{0j} \tag{4.4}$$

$$\frac{\partial \mathbf{f}_1}{\partial t} + v\nabla f_0 - \frac{e}{m_e}\mathbf{E}\frac{\partial f_0}{\partial v} = -\sum_j n_j \sigma_{m,j} v \mathbf{f}_1, \tag{4.5}$$

where $\sigma_{m,j}$ is the momentum transfer cross-section (2.4) for collisions with other species j and the magnetic force has been omitted (for simplicity). The collision term C_0 is related to energy transfer and consists of various contributions for which appropriate expressions are derived in the literature. For elastic collisions with neutrals or ions :

$$C_{0j} = \frac{m_e n_j}{m_j v^2}\frac{\partial}{\partial v}\left(\sigma_j v^4\left(f_0 + \frac{eT_j}{m_e v}\frac{\partial f_0}{\partial v}\right)\right), \tag{4.6}$$

[12] This assumption is not as well justified as one might think : in some low-temperature plasmas the number of charged particles in a Debye sphere $N_D = 5.5\times10^{13}(T_e^3/n_e)^{1/2}$ is only a few thousand ; the high-energy tail of the distribution function can then be expected to be 'statistically noisy'.

where m_j and T_j are the target particle mass and temperature. For electron-electron collisions this expression (assuming Maxwellian target particles of mass >> m_e) is not appropriate and a more complex non-linear expression is necessary :

$$C_{0j} = \frac{4\pi e^4 \ln\Lambda}{\varepsilon_0{}^2 m_e{}^2 v^2} \frac{\partial}{\partial v}\left(\left[\int_0^v f_0 v'^2\, dv' \right] f_0 + \left[\frac{1}{3v} \int_0^v f_0 v'^4\, dv' + \frac{v^2}{3} \int_v^\infty f_0 v'^4\, dv' \right] \frac{\partial f_0}{\partial v} \right). \qquad (4.7)$$

This vanishes for a Maxwellian electron distribution function $f_0 \sim \exp(-v^2/v_T{}^2)$ at arbitrary temperature : electron-electron collisions Maxwellise the distribution function but do not control the electron temperature. For inelastic excitation and ionisation collisions C_{0j} is non-local in velocity space, removing particles at velocity v and injecting them elsewhere at a velocity v', respectively :

$$C_{0j} = -n_j v \sigma_j(v) f_0(v) + n_j (v'/v) v' \sigma_j(v') f_0(v') \qquad v'^2 = v^2 - 2eU_j/m_e \qquad (4.8)$$

$$C_{0j} = -n_j v \sigma_j(v) f_0(v) + 4 n_j (v'/v) v' \sigma_j(v') f_0(v') \qquad v'^2 = v^2/2 - eU_j/m_e \qquad (4.9)$$

where U is the threshold energy and the factor 4 accounts for electron creation[13], assuming that the remaining energy is distributed equally over the old and new electrons.

Homogeneous approach

Given these two-term collision integrals, equations (4.4-5) can be combined and solved numerically for simple configurations. The simplest configuration is that of a homogeneous, unbounded plasma in a constant electric field : all gradients vanish and $\mathbf{f}_1$ is defined along the electric field direction.[14] To account for the creation of new electrons it is assumed that the distribution function grows exponentially in time as $\partial f / \partial t = \bar{\nu}_i f$.[15] Then :

$$-\frac{e^2 E^2}{3 m_e{}^2} \frac{\partial}{\partial v}\left(\frac{v^2}{\nu_m} \frac{\partial f_0}{\partial v} \right) = C_0[f_0] - \bar{\nu}_i f_0 \qquad (4.10)$$

$$\nu_m = \sum_j n_j \sigma_{m,j} v + \bar{\nu}_i \qquad \bar{\nu}_i = 4\pi \sum_i n_i \int_0^\infty \sigma_i v^3 f_0 dv\,, \qquad (4.11)$$

where ν_m is the effective frequency for momentum transfer to neutrals and ions, summed over all collisions, and $\bar{\nu}_i$ is the net macroscopic ionisation frequency, summed over all ionisation collisions, which introduces non-linearity in equation (4.10) and is usually evaluated iteratively. Equation (4.10) is frequently used as an approximation for collisional electrons, assuming that the characteristic length for energy transfer (energy relaxation length) is short with respect to all macroscopic length scales of the plasma ; this is called the local-field approximation.

Homogeneous plasmas in a high-frequency electric field are described by assuming (in addition to exponential growth) harmonic time variation $\exp(i\omega t)$ for $\mathbf{f}_1$ while neglecting the time variation of f_0 ; this is reasonable if the characteristic frequency for energy transfer is much lower than the field frequency :

$$-\frac{e^2 E^2}{6 m_e{}^2} \frac{\partial}{\partial v}\left(\frac{v^2 \nu_m}{\nu_m{}^2 + \omega^2} \frac{\partial f_0}{\partial v} \right) = C_0[f_0] - \bar{\nu}_i f_0 \qquad (4.12)$$

[13] My paper [22] contains an error on this point: instead of a factor 4, equation (29) shows a factor 2.

[14] This approach is the basis of BOLSIG+, the freeware Boltzmann solver that I developed together with Leanne Pitchford, documented in [22] and available at www.bolsig.univ-tlse.fr

[15] This exponential growth model was originally used to describe pulsed Townsend experiments. Alternatively, electron creation can be included in the homogeneous Boltzmann equation by a spatial growth model, corresponding to steady state Townsend experiments. Some authors altogether neglect growth effects and treat ionisation as excitation.

where E is the field amplitude.

Originally developed to check consistency between cross sections and measured macroscopic swarm parameters [Roc73], the homogeneous Boltzmann equations (4.10) and (4.12) are nowadays often used to obtain transport coefficients and rate coefficients for fluid models as described in chapter 5 [22]. Some examples of results are shown in figure 4.1. Neglecting electron-electron collisions, the shape of the distribution function $f_0(v)$ below the excitation threshold energy is directly controlled by the velocity-dependence of $\nu_m(v)$ and is Maxwellian only if ν_m is constant. Beyond the excitation threshold energy, f_0 is generally depleted by the inelastic collision terms, which has a strong effect on the macroscopic ionisation rate coefficient.

Nonlocal approach

Another approach for the solution of the two-term Boltzmann equation is the so-called non-local approach[16] [Kor96], describing configurations where the electrons have only few collisions but are trapped by an ambipolar field $-\nabla\Phi$ perpendicular to the applied field, as is (sometimes) the case in positive columns or inductive discharges. It is then assumed that f_0 and $\mathbf{f}_1$ are functions of the total energy $\varepsilon = m_e v^2/2e - \Phi(\mathbf{x})$ including the ambipolar potential energy. After a coordinate transformation $(\mathbf{x},v) \rightarrow (\mathbf{x},\varepsilon)$ the equations (4.4-5) are integrated over the total plasma volume accessible to electrons of energy ε and combined into one differential equation for $f_0(\varepsilon)$ that is similar to equation (4.10). The distribution function $f_0(\mathbf{x},v)$ is found from $f_0(\varepsilon)$ by simple back-substitution. In fact, when electron-electron collisions are dominant, the trapped electrons have a Maxwell-Boltzmann distribution

$$f_0(\mathbf{x},v) = \frac{n_0}{\pi^{3/2} v_T{}^3} \exp\left(-(v^2 - 2e\Phi(\mathbf{x})/m_e)/v_T{}^2\right), \qquad (4.13)$$

where n_0 is the electron density in the centre of the plasma (where $\Phi = 0$). The non-local two-term Boltzmann solutions show the deviations from this distribution due to the applied field, collisions with neutrals, and wall recombination, e.g. depletion of the tail beyond $v^2 > 2e(\Phi(\mathbf{x})-\Phi_w)/m_e$ where Φ_w is the wall potential.

[16] I have considered this approach for the model of the inductive ion source for ITER and did some preliminary calculations ; the problem is that the heating mechanism is still assumed local and that the description of nonlocal inductive heating is precluded by the standard two-term expansion ; I found however that it is possible to account for harmonic spatial variation of the heating field by a slightly different expansion.

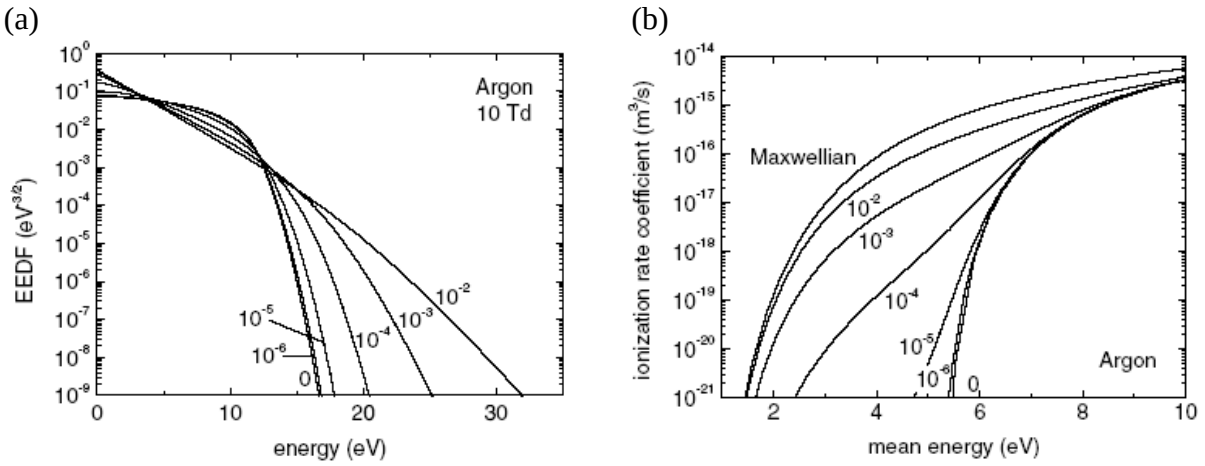

Figure 4.1. Results from the two-term homogeneous Boltzmann equation for electrons in an argon plasma accounting for both electron-neutral collisions and electron-electron collisions, solved by my freeware solver BOLSIG+. Figure a shows the electron energy distribution function (EEDF) = $(4\pi e/m_e n_e)vf_0$ as a function of energy $m_e v^2/2e$ in a reduced electric field E/n = 10 Td = 10^{22} Vm^2 for different ionisation degrees n_e/n. At low ionisation degree, the shape of the EEDF is determined by electron-neutral collisions and is depleted beyond the excitation threshold ≈ 12 eV. As the ionisation degree increases, the EEDF becomes increasingly Maxwellian due to electron-electron collisions. The consequences for the ionisation rate coefficient $(4\pi/n_e)\int \sigma v^3 f_0 dv$ are shown in figure b as a function of the mean electron energy $(2\pi e/m_e n_e)\int v^4 f_0 dv$: at lower mean energy and low ionisation degree, the ionisation rate is much lower than for Maxwellian electrons. From [22].

Chapter 5

FLUID MODELS

Fluid models describe the behaviour of particle species in terms of macroscopic quantities such as the particle density n, mean velocity $\mathbf{w}$, and mean energy ε. The evolution of these quantities is described by fluid equations such as the continuity, momentum, and energy equations, which are partial differential equations in time and space. The macroscopic quantities correspond to velocity moments of the distribution function, i.e. integrals of some power of velocity times the distribution function over velocity-space:

$$n(\mathbf{x},t) = \iiint f(\mathbf{x},\mathbf{v},t)d^3\mathbf{v} \tag{5.1}$$

$$\mathbf{w} = \langle \mathbf{v} \rangle = \frac{1}{n}\iiint \mathbf{v} f d^3\mathbf{v} \tag{5.2}$$

$$\varepsilon = \frac{m}{2e}\langle v^2 \rangle = \frac{m}{2en}\iiint v^2 f d^3\mathbf{v} \tag{5.3}$$

where the triangular brackets indicate the macroscopic average

$$\langle u \rangle(\mathbf{x},t) = \frac{1}{n(\mathbf{x},t)}\iiint u(\mathbf{v}) f(\mathbf{x},\mathbf{v},t)d^3\mathbf{v}\,. \tag{5.4}$$

The fluid equations correspond to velocity moments of the Boltzmann equation, which form an infinite series, based on higher and higher powers of velocity, where each moment equation is linked to the next because it contains the gradient of the next-order moment of the distribution function (from the second term of the Boltzmann equation). The series is truncated at a certain order (usually first or second) by assumptions or approximations on the next-order moment, called closure approximations. In addition, various approximations are used to simplify the fluid equations and facilitate their solution coupled with that of the fluid equations for other species and the Maxwell equations. All these approximations are made from kinetic considerations, either by neglecting the microscopic time and length scales (inverse collision frequency $1/\nu$, mean free path $1/n\sigma$, Larmor radius mv_T/eB etc) with respect to the macroscopic scales, or by explicit assumptions on the distribution function.

Collisions are represented in the fluid equations by various transport coefficients and rate coefficients, corresponding to averages of cross-section related quantities depending on the relative velocity of the collision partners. Assuming independent shifted Maxwellian distributions for two colliding species 1 and 2, the average relative velocity $v_r = |\mathbf{v}_1 - \mathbf{v}_2|$ can be characterized by a relative temperature

$$eT_r \equiv \frac{m_1 m_2}{3(m_1+m_2)}\langle v_r^{\,2} \rangle_{1,2} = \frac{m_2 eT_1 + m_1 eT_2}{m_1+m_2} + \frac{m_1 m_2}{3(m_1+m_2)}|\mathbf{w}_1 - \mathbf{w}_2|^2\,. \tag{5.5}$$

For particle species in thermal equilibrium this reduces to $T_r = T_1 = T_2$; for electron collisions $T_r = T_e$ due to the small electron mass ; for ion-neutral collisions the directed ion energy is important. Hence, experimentally measured transport and rate coefficients are often given in the literature as a function of gas temperature, electron temperature, or effective ion temperature.

One of the main problems of fluid plasma models is the description of ionisation, which is due mainly to fast electrons that tend to be badly characterized by a Maxwellian temperature. To account for the non-Maxwellian character of the electron distribution, the ionisation rate coefficients and other electron fluid coefficients are often obtained from solutions f_0 of the homogeneous Boltzmann equation (4.10/12). In collisional conditions these

homogeneous Boltzmann results can be generalized to fluid models by the local field approximation, assuming local equilibrium between electric acceleration and collisional momentum and energy losses, so that the transport and rate coefficients are direct functions of the local electric field *E*, or rather, the reduced electric field *E/n* since the collision frequency is proportional to the gas density *n*. The local field approximation is also used for collisional ions, for which experimental transport coefficients as a function of reduced field are available from the literature. [Ell76]

Continuity equation

The continuity equation, describing conservation of particles, is the integral of the Boltzmann equation (4.1) over velocity space:

$$\frac{\partial n}{\partial t} + \nabla \cdot (n\mathbf{w}) = S \,. \tag{5.6}$$

The source term *S* is the net number of particles created per unit time per unit volume, and consists in general of different contributions from collisions or chemical reactions :

$$S = \sum_i N_i n_{1i} n_{2i} k_i \tag{5.7}$$

where *N* is the number of particles created in one collision (negative in case of destruction), n_1 and n_2 are the densities of the colliding particles, and $k = <\sigma v_r>$ is the rate coefficient in units m^3/s. Sometimes there are three particles involved so a third factor density n_3 is included and the rate coefficient *k* has units m^6/s. Rate coefficients for electron-impact reactions can be calculated from the two-term Boltzmann solution as

$$k = \frac{4\pi}{n} \int_0^\infty \sigma v^3 f_0 dv \,. \tag{5.8}$$

The electron and ion source term due to electron-impact ionisation is sometimes evaluated from the electron flux as $S = n_e w_e \alpha$ where α is the Townsend coefficient, for which semi-empirical expressions are available as a function of the reduced electric field [Bro66] [Rai91].[17]

Momentum equation

The momentum equation is the first-order velocity moment of the Boltzmann equation : multiply (4.1) by **v** and integrate over velocity space :

$$\frac{\partial n\mathbf{w}}{\partial t} + \nabla \cdot (n\mathbf{w} \otimes \mathbf{w}) + \frac{1}{m} \nabla \cdot \mathbf{P} - \frac{qn}{m} (\mathbf{E} + \mathbf{w} \times \mathbf{B}) = -n \sum_j \frac{m_j}{m + m_j} n_j k_{m,j} (\mathbf{w} - \mathbf{w}_j) \,, \tag{5.9}$$

where

$$\mathbf{P} = m \int (\mathbf{v} - \mathbf{w}) \otimes (\mathbf{v} - \mathbf{w}) f d^3\mathbf{v} \tag{5.10}$$

is the pressure tensor and $k_m = <\sigma_m v_r>$ is an effective rate coefficient for momentum transfer to particles of other species *j* based on the momentum transfer cross section as defined in equation (2.4). The momentum equation (5.9) is generally solved for the mean velocity **w**, but this requires different approximations to simplify it. A first standard approximation for plasma particles is to assume that the pressure tensor is diagonal and isotropic :

$$\mathbf{P} = enT\mathbf{I} \tag{5.11}$$

where

$$enT = \frac{1}{3} m \int |\, \mathbf{v} - \mathbf{w} \,|^2 \; f d^3\mathbf{v} \tag{5.12}$$

[17] My freeware solver BOLSIG+ calculates both rate coefficients *k* and Townsend coefficients α as a function of reduced field *E/n* or electron mean energy ε_e.

is the scalar pressure, T is the (generalized) temperature, and $\mathbf{I}$ is the identity matrix. Next, since most collisions are with neutral gas particles, the mean target velocity $\mathbf{w}_j$ is neglected in the last term of equation (5.9). After substitution of equations (5.6) and (5.11) the momentum equation becomes

$$\frac{\partial \mathbf{w}}{\partial t} + (\mathbf{w}\cdot\nabla)\mathbf{w} + \bar{\nu}_m \mathbf{w} + \frac{q}{m}\mathbf{B}\times\mathbf{w} = \frac{q}{m}\mathbf{E} - \frac{e}{mn}\nabla(nT) \tag{5.13}$$

where

$$\bar{\nu}_m = \sum_j \frac{m_j}{m+m_j} n_j k_{m,j} + \frac{S}{n} \tag{5.14}$$

is the macroscopic momentum transfer frequency.[18] Without the collision term, equation (5.13) is known as the Euler equation.

Drift-diffusion equation

For collisional charged particles, the momentum equation (5.13) can be further simplified by neglecting the inertia terms and the magnetic term on the left-hand side with respect to the collision term, assuming that collisions take place on much shorter time and length scales than macroscopic field and pressure variations and cyclotron motion :

$$n\mathbf{w} = \frac{q}{m\bar{\nu}_m} n\mathbf{E} - \frac{e}{m\bar{\nu}_m}\nabla(nT) \equiv \frac{q}{|q|}\mu n\mathbf{E} - \nabla(Dn)\,. \tag{5.15}$$

This is the drift-diffusion equation, containing two transport coefficients : the mobility μ and the diffusion coefficient D, each inversely proportional to the gas density. For Maxwellian particles, the ratio D/μ (called characteristic energy) equals the temperature according to the Einstein relation, which is often used to estimate the diffusion coefficient from the mobility as $D = \mu T$. The drift-diffusion equation is consistent with the local-field approximation and the two-term Boltzmann equation. Substitution of equation (4.5) into $n\mathbf{w} = \iiint \mathbf{v}(\mathbf{v}/v)\cdot\mathbf{f}_1 d^3\mathbf{v}$ and identification with (5.15) yields

$$\mu_e = -\frac{e}{m_e}\frac{4\pi}{3n_e}\int_0^\infty \frac{v^3}{\nu_m}\frac{\partial f_0}{\partial v}dv \qquad\qquad D_e = \frac{4\pi}{3n_e}\int_0^\infty \frac{v^4}{\nu_m} f_0 dv\,, \tag{5.16}$$

which are commonly used expressions for electrons, where f_0 is either solved from equation (4.10) or assumed Maxwellian.[19] For positive ions the diffusion term is usually negligible. A compilation of measured ion mobilities μ_{0j} in various pure gases j at standard gas density n_0 is given in [Ell76] as a function of the effective temperature (5.5) and the reduced field $E/n = E_0/n_0$. From equation (5.14), the mobility in a gas mixture is then given by the Blanc law [Bla08]

$$\mu = \frac{n_0}{\sum_j n_j / \mu_{0j}}\,; \tag{5.17}$$

more accurate mobility mixture-rules are discussed in [Pis03]. Equation (5.15) is also used with zero mobility for (excited) neutral species diffusing in much denser gas species.

[18] The inclusion of the creation (ionisation) frequency S/n in the momentum-transfer frequency is not standard but done here for simplicity and consistency with the microscopic momentum-transfer frequency (4.11) for the exponential growth model. Note that in (5.9) and (5.13) it is assumed that all particle creation takes place in the laboratory frame and hence appears as an effective momentum loss for the fluid ; this assumption is often reasonable especially for electrons and ions. More rigorously, the frequency S/n in equation (5.14) should only include the positive contributions (creation) to the particle source term (5.7).

[19] These coefficients are provided by my freeware solver BOLSIG+ as a function of reduced field E/n or electron mean energy ε_e.

Boltzmann relation

Even further simplification of the momentum equation is obtained for non-collisional electrons and negative ions trapped in the ambipolar field, by neglecting all terms on the left-hand side of (5.13) with respect to the field and pressure gradient :

$$q\mathbf{E} = \frac{e}{n}\nabla(nT)\,. \tag{5.18}$$

This is the Boltzmann relation, which is consistent with the Maxwell-Boltzmann distribution (4.13) and the assumption of constant temperature T. Contrary to the other approximated momentum equations, the Boltzmann relation does not describe the mean velocity, but rather the spatial profile of the particle density

$$n = n_0 \exp(-q\Phi / eT)\,, \tag{5.19}$$

where n_0 is a reference density corresponding to $\Phi = 0$. When using this relation explicitly, the absolute density and temperature can only be obtained from global balance equations corresponding to the space integrals of the continuity equation (5.6) and the energy equation (5.31). However, in self-consistent models the Boltzmann relation is automatically recovered from the drift-diffusion equation if μ and D are sufficiently large : the ambipolar field then adjusts to satisfy equation (5.18).

Magnetised drift-diffusion equation

The drift-diffusion equation can be extended to describe magnetized particles, i.e. charged particles in a steady magnetic field so strong that the Larmor radius cannot be neglected with respect to the collision length. Neglecting only the inertia terms in equation (5.13) and keeping the magnetic force :

$$n\mathbf{w} + \boldsymbol{\Omega}\times(n\mathbf{w}) = \frac{q}{|q|}\mu n\mathbf{E} - \nabla(Dn) \equiv \mathbf{G} \tag{5.20}$$

where **G** is the non-magnetized drift-diffusion flux as given by equation (5.15) and

$$\boldsymbol{\Omega} = \frac{q\mathbf{B}}{m\bar{\nu}_m} = \frac{q}{|q|}\mu\mathbf{B} \tag{5.21}$$

is the magnetisation vector whose magnitude Ω is called Hall parameter and is a measure for the influence of the magnetic field ; this is generally much larger for electrons than for ions due to the small electron mass. Then

$$n\mathbf{w} = \frac{1}{1+\Omega^2}\left(\mathbf{G} - \boldsymbol{\Omega}\times\mathbf{G} + (\boldsymbol{\Omega}\cdot\mathbf{G})\boldsymbol{\Omega}\right) \equiv \frac{q}{|q|}n\boldsymbol{\mu}\cdot\mathbf{E} - \nabla(\mathbf{D}n)\,, \tag{5.22}$$

which defines the magnetized mobility and diffusion tensors. These tensors have anisotropic diagonal components : $\mu_{//}/\mu = D_{//}/D = 1$ parallel to **B** and much smaller values $\mu_\perp/\mu = D_\perp/D = 1/(1+\Omega^2)$ perpendicular to **B** ; in addition they have non-diagonal components $\mu_\times/\mu = D_\times/D = \pm\Omega/(1+\Omega^2)$ causing a flux in the direction of **G**×**B** (Hall effect). So an electric field driving the particles across the magnetic field mainly results in particle drift in the **E**×**B** direction rather than the **E** direction. Magnetized plasmas often have a cylindrical configuration with the fields in the axial-radial plane so that the **E**×**B** drift is closed along the azimuthal direction.

Equation (5.22) is sometimes used also for non-collisional electrons (mean free path > macroscopic lengths), e.g. in figure 5.1. In the direction perpendicular to the magnetic field this is justified by the fact that the perpendicular distance travelled between successive collisions is limited to the Larmor radius. Parallel to the magnetic field, equation (5.22) leads to the establishment of the Boltzmann relation (5.19) due to the large mobility and diffusion coefficient, but the parallel flux may be not correctly described. Equation (5.22) also fails to describe the effects of curvature and gradients of the magnetic field, due mainly to the

assumption of a diagonal isotropic pressure tensor (5.11). Another, more general problem with the description of magnetized electrons is that the transport across the magnetic field can be increased by microscopic (turbulent) field fluctuations so that the effective transport coefficients $\mu_\perp/\mu = D_\perp/D > 1/(1+\Omega^2)$ are anomalously high and hard to evaluate.[20] [39]

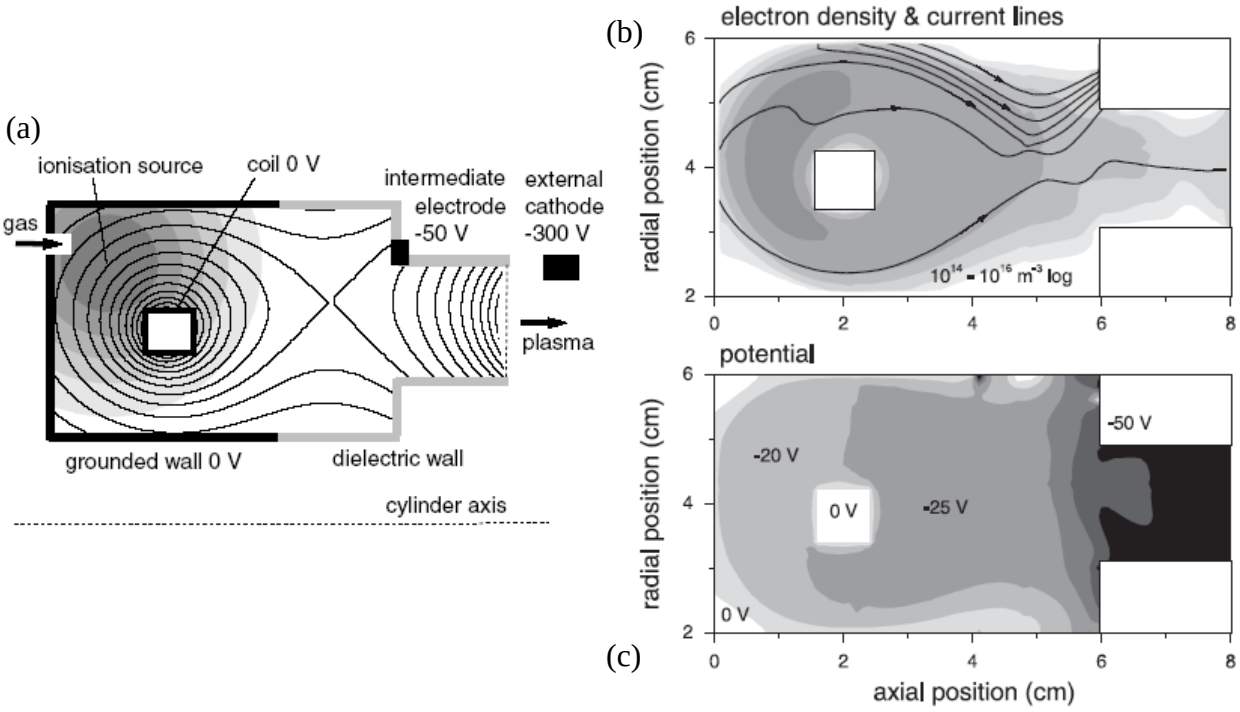

Figure 5.1. Plasma density, current and potential in the ionisation stage of a double-stage plasma thruster, obtained from a self-consistent model based on the continuity equation (5.6) and the magnetized drift-diffusion equation (5.22) for electrons coupled with Poisson's equation and an ion particle simulation. The discharge configuration consists of an annular chamber with a complex steady magnetic field approximately parallel to the walls and steady voltages applied to several electrodes as shown in figure a. Electrons are emitted by the intermediate electrode (filament) and driven to the chamber wall across the magnetic field, meanwhile ionising the gas injected in the back of the chamber. Due to the large anisotropy of the electron transport, the discharge current (≈ the electron current emitted by intermediate electrode) tends to follow the magnetic field lines (figure b) and the Boltzmann relation (5.19) is established along the lines : $\Phi = T_e \ln(n_e/n_0)$ such that the potential of the intermediate electrode propagates along the entire magnetic field line intercepting it (separatrix) ; this creates a potential well guiding the (non-magnetised) ions to the chamber exit into the acceleration stage of the thruster (figure c). From [27].

<u>High-frequency momentum equation</u>

For charged particles in high-frequency fields, another approximation of the momentum equation (5.13) is appropriate : assume that the distance travelled over one field period is small with respect to the length scale of field and pressure variations, so neglect all gradients :

$$\frac{\partial \mathbf{w}}{\partial t} + \bar{\nu}_m \mathbf{w} + \frac{q}{m}\mathbf{B}\times\mathbf{w} = \frac{q}{m}\mathbf{E}\,. \qquad (5.23)$$

This is often used for electrons in microwave plasmas and describes oscillations of the mean velocity with a phase shift with respect to the field between 0 and $\pi/2$ depending on the momentum-transfer frequency. The (non-linear) force due to the magnetic component of the high-frequency field is usually negligible, but the force of steady magnetic fields can be

[20] This is a major concern in modelling of Hall-effect thrusters. In our thruster simulations based on equation (5.22) anomalous electron transport is accounted for by an effective frequency, fitted to obtain agreement with current and performance measurements as discussed in [12]. Recent progress on this issue is reported in [39].

important, e.g. in electron-cyclotron-resonance discharges. Equation (5.23) is not fully consistent with the high-frequency two-term Boltzmann equation : assuming forms exp($i\omega t$) for $\mathbf{f}_1$ and E, equation (4.5) yields the mean velocity

$$w_e = -\frac{eE}{m_e}\frac{4\pi}{3n_e}\int_0^\infty \frac{\nu_m - i\omega}{\nu_m{}^2 + \omega^2} v^3 \frac{\partial f_0}{\partial v} dv \equiv -(\mu_r + i\mu_i)E \qquad (5.24)$$

which can be rewritten as

$$\frac{\partial w_e}{\partial t} + \left[-\omega\mu_r/\mu_i\right] w_e = -\left[m_e\omega(\mu_r{}^2 + \mu_r{}^2)/e\mu_i\right]\frac{e}{m_e}E. \qquad (5.25)$$

Compared with (5.23) this has an additional factor on the right hand side[21]. The factor vanishes (equals unity) for constant momentum frequency $\nu_m(v)$.

Navier-Stokes equation

For dominant gas particles that are colliding mainly among themselves, the non-diagonal components of the pressure tensor cannot be neglected, but if the mean free path is sufficiently short they can be related to velocity gradients as viscosity. A common approximation of the momentum equation (5.9) for gas particles is the Navier-Stokes equation

$$\frac{\partial \mathbf{w}}{\partial t} + (\mathbf{w}\cdot\nabla)\mathbf{w} + \bar{\nu}_m\mathbf{w} - \eta\left(\nabla^2\mathbf{w} + \frac{1}{3}\nabla(\nabla\cdot\mathbf{w})\right) = \mathbf{g} + \sum_j \frac{m_j}{m+m_j} n_j k_{m,j}\mathbf{w}_j - \frac{e}{mn}\nabla(nT), \qquad (5.26)$$

where η is the kinematic viscosity coefficient, given in the literature for pure gases and approximately related to the momentum coefficients as[22]

$$\eta \approx 0.7\frac{eT}{m}\left(\sum_i \frac{m_i}{m+m_i} n_i k_{m,i}\right)^{-1}, \qquad (5.27)$$

where the sum includes all species so also the species of interest. Momentum transfer with other particle species occurs as a mutual process and can cause acceleration of the gas particles by the drag force term on the right-hand side, e.g. by positive ion impact in the (cathode) sheath. The gravitational acceleration **g** (neglected in all other equations) can play a role e.g. in thermal convection. The Navier-Stokes equation (5.26) is only marginally used in low-temperature plasma models ; often the gas is quasi-stationary and so little affected by the plasma that it is sufficient to assume constant gas pressure. Excited neutral species are described by the diffusion equation (5.15) (with zero mobility).

Energy equation

The energy equation is the second-order, scalar-product velocity moment of the Boltzmann equation : multiply (4.1) by $mv^2/2$ and integrate over velocity space :

$$\frac{\partial en\varepsilon}{\partial t} + \nabla\cdot\left(en\mathbf{w}\varepsilon + \mathbf{P}\cdot\mathbf{w} + \mathbf{Q}\right) - qn\mathbf{w}\cdot\mathbf{E} = \Pi \qquad (5.28)$$

where Π is the net power density gained in collisions and chemical reactions (negative in case of power loss) and **Q** is the heat flux vector defined as

$$\mathbf{Q} = \frac{1}{2}m\int |\mathbf{v}-\mathbf{w}|^2 (\mathbf{v}-\mathbf{w}) f d^3\mathbf{v}. \qquad (5.29)$$

[21] My freeware solver BOLSIG+ provides both coefficients appearing in square brackets in equation (5.25).

[22] This expression is not standard but derived by myself from the collision term of the second (tensor-product) velocity-moment of the Boltzmann equation. For simplicity it is assumed that the shear pressure per particle **P**/n is the same for all species. The factor 0.7 corresponds to the experimental ratio of the kinematic viscosity to the self-diffusion coefficient for most gases ; it is 1 for constant k_m and 5/6 for constant σ_m. To be verified.

Note that from the definition (5.12) the mean energy can be decomposed into thermal energy and directed energy : $\varepsilon = (3/2)T + mw^2/2e$.

Electron energy equation

For collisional electrons, the heat flux vector is usually assumed proportional to the temperature gradient as [Bit04]

$$\mathbf{Q}_e = -\frac{5}{2} e D_e n_e \nabla T_e \,. \tag{5.30}$$

This closure approximation is derived from the perturbation solution of the Boltzmann equation around a local Maxwellian distribution function f_0 assuming constant kinetic pressure $n_e T_e$; for magnetized electrons the diffusion coefficient D_e is to be replaced by the diffusion tensor $\mathbf{D}_e$. The electron energy equation is then approximated as follows : substitute (5.30), assume an isotropic diagonal pressure tensor, and neglect directed energy such that $\varepsilon_e = (3/2)T_e$:

$$\frac{\partial n_e \varepsilon_e}{\partial t} + \frac{5}{3}\nabla \cdot \left(n_e \mathbf{w}_e \varepsilon_e - n_e D_e \nabla \varepsilon_e \right) = -n_e \mathbf{w}_e \cdot \mathbf{E} + \frac{1}{e}\Pi_e \,, \tag{5.31}$$

and by substitution of the drift-diffusion equation (5.15) :

$$\frac{\partial n_e \varepsilon_e}{\partial t} + \frac{5}{3}\nabla \cdot \left(-\mu_e \mathbf{E} n_e \varepsilon_e - \nabla (D_e n_e \varepsilon_e) \right) = -n_e \mathbf{w}_e \cdot \mathbf{E} + \frac{1}{e}\Pi_e \;; \tag{5.32}$$

for magnetized electrons replace again μ_e by $\boldsymbol{\mu}_e$ and D_e by $\mathbf{D}_e$. However, this electron energy equation is not in general fully consistent with the two-term Boltzmann equation. Evaluation of the energy flux $(m_e/2e)\iiint v^2 \mathbf{v}(\mathbf{v}/v)\cdot\mathbf{f}_1 d^3\mathbf{v}$ from equation (4.5) suggests the following reformulation :

$$\frac{\partial n_e \varepsilon_e}{\partial t} + \nabla \cdot \left(-\mu_\varepsilon \mathbf{E} n_e \varepsilon_e - \nabla (D_\varepsilon n_e \varepsilon_e) \right) = -n_e \mathbf{w}_e \cdot \mathbf{E} + \frac{1}{e}\Pi_e \,, \tag{5.33}$$

where

$$\mu_\varepsilon = -\frac{2\pi}{3 n_e \varepsilon_e} \int_0^\infty \frac{v^5}{\nu_m} \frac{\partial f_0}{\partial v} dv \qquad\qquad D_\varepsilon = \frac{2\pi m_e}{3 e n_e \varepsilon_e} \int_0^\infty \frac{v^6}{\nu_m} f_0 dv \tag{5.34}$$

are the energy mobility and the energy diffusion coefficient[23]. Equation (5.33) is equivalent to equation (5.32) for Maxwellian electrons and for constant momentum frequency : then $\mu_\varepsilon/\mu_e = D_\varepsilon/D_e = 5/3$. The collisional power term is generally negative and can be expressed in terms of rate coefficients as

$$\Pi_e = -e n_e \sum_i U_i n_i k_i - e n_e \sum_j n_j K_j \;\equiv -e n_e \Theta \tag{5.35}$$

$$K_j = \frac{2m_e}{m_j}\frac{m_e}{2e}\left\langle \sigma_{m,j} v^3 \right\rangle \approx \frac{2m_e}{m_j} k_{m,j} \varepsilon_e \,. \tag{5.36}$$

The first term is inelastic energy loss summed over all excitation and ionisation collisions i, where U_i is the threshold energy, n_i is the target particle density, and k_i the rate coefficient. The second term is elastic energy loss summed over all elastic collisions j, where n_j is the target density and K_j is an elastic energy loss coefficient, proportional to the momentum transfer coefficient $k_{m,j}$ in case of constant collision frequency $\sigma_{m,j} v$; cf. equation (3.29). The parameter Θ is commonly defined to represent the mean power loss per electron (in eV/s).[24]

[23] These coefficients are provided by my freeware solver BOLSIG+ as a function of ε_e.

[24] The coefficients K_j and Θ are calculated by BOLSIG+ as a function of ε_e.

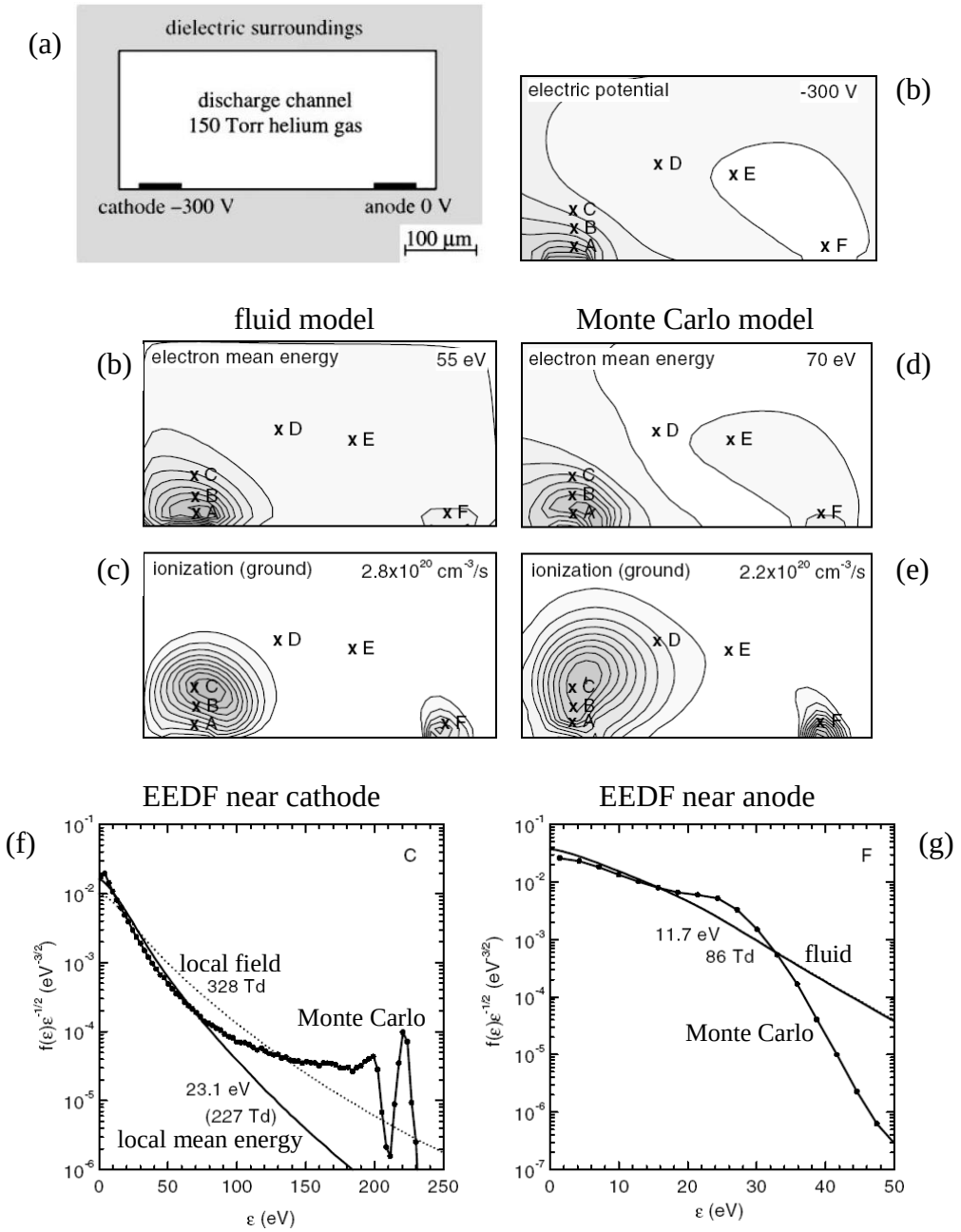

Figure 5.2. Comparison of a fluid model and a Monte-Carlo (MC) particle model of the electrons in a direct-current microdischarge for PALC displays (figure a). The fluid model consists of continuity equations (5.6) and drift-diffusion equations (5.15) for electrons and ions and the energy equation (5.32) for electrons, self-consistently coupled with Poisson's equation. Figures b-d show the spatial profiles of the electric potential, electron mean energy, and ionisation source term from this model. Due to plasma screening most of the applied potential drop occurs in a narrow sheath region in front of the cathode. Secondary electrons, emitted from the cathode by positive ion impact, are accelerated by the cathode sheath field and multiply in ionisation. To get insight in the errors of the fluid ionisation profile, comparison is made with a MC model, simulating the trajectories of individual electrons emitted from the cathode as well as all electrons subsequently created in ionisation, moving in the potential of figure b ; ionisation in fluid model seems too localised near the cathode. Figures f and g compare the electron energy distribution function (EEDF) at different locations near the cathode and anode. The EEDF from the MC model shows non-equilibrium phenomena such as peaks of fast electrons that have undergone none or only few collisions (figure f) and the absence of a high-energy tail (figure g) ; the EEDF assumed by the fluid model (through the ionisation rate coefficient as a function of mean energy) does not include these features but gives a better description than the EEDF of local field equilibrium. From [7].

Mean energy approximation vs. local field approximation

The main purpose of solving the electron energy equation in plasma models is to obtain the electron transport coefficients μ_e and D_e and the rate coefficients k of electron-impact ionisation and excitation in conditions where the local field approximation is not justified because the electric field varies considerably over the energy relaxation length (which is much longer than the mean free path due to the small electron mass and poor elastic energy transfer). The transport and rate coefficients are then treated as functions of the electron mean energy ε_e or temperature $T_e = (2/3)\varepsilon_e$. Since the electrons are generally not Maxwellian, the functional dependencies $D_e(\varepsilon_e)$ $k(\varepsilon_e)$ etc are generalized from the solutions of the homogeneous Boltzmann equation, without real justification ; it is not clear to what extend this approach can capture deviations from local field equilibrium ; see figure 5.2 for illustration. However, even in highly collisional conditions (where the local field approximation would at first sight seem appropriate) it has advantages to solve the electron energy equation. First, the local field approximation can only describe situations where the electron flux is driven by the electric field, whereas bounded plasmas always contain regions where diffusion dominates, e.g. the electrons diffuse across the ambipolar sheath ; the energy equation yields (an estimate of) the electron temperature and transport coefficients in these regions. Second, the energy equation relaxes the coupling between the electron equations and the electric field equation, which makes the numerical solution less sensitive to instabilities.

Heat equation

For neutral gas particles, the energy equation (5.28) is often approximated by the well-known heat equation, neglecting directed energy. The heat equation for molecules is then usually extended to include internal rotational and vibrational energy, assuming thermal equilibrium of all modes of motion, i.e. the mean energy is not $m\langle v^2\rangle/2$ but cT where c is the heat capacity at constant volume, approximately 1/2 per degree of freedom of translational and rotational motion plus (up to) 1 per degree of freedom of vibrational motion[25]. Summing over all gas species j :

$$\sum_j \left\{ \frac{\partial}{\partial t}\left(c_j n_j eT\right) + \nabla\cdot\left((c_j+1)n_j \mathbf{w}_j eT - e\kappa_j \nabla T\right)\right\} = \sum_j \Pi_j = \Pi \qquad (5.37)$$

where κ_j is the thermal conductivity, approximately related to the momentum coefficients as[26]

$$\kappa_j \approx c_j n_j \frac{eT}{m_j}\left(\sum_i \frac{m_i}{m_j+m_i} n_i k_{m,ij}\right)^{-1}, \qquad (5.38)$$

where the sum i runs over all species including the species j ; κ_j is directly available in the literature for pure gases relatively unaffected by the plasma. The gas temperature in these equations is in eV ; to use Kelvin replace eT by $k_B T$; the factor k_B is then sometimes included in c_j and κ_j. The total collisional power Π is generally positive and corresponds to the power lost by the electrons and ions, transferred to gas either directly as thermal energy or as atomic or chemical internal energy subsequently converted to thermal energy by exothermic processes. Equation (5.38) is (sometimes) solved in plasma models to estimate the gas heating due to Π and the resulting decrease of the gas density (by the ideal gas law at constant pressure) and possible thermal dissociation of gas particles. The assumption of thermal

[25] This is according to classical theory. In reality the contributions from rotation and especially vibration are often smaller due to quantization of the energy, e.g. for light diatomic gases at room temperature $c \approx 5/2$ rather than 7/2 because nearly all molecules are in the vibrational ground state.

[26] This expression is not standard but derived by myself by generalisation of the expressions in [Rei65] and is to be verified.

equilibrium of the different modes of motion is questionable : the plasma tends to heat preferentially the vibrational mode ; sometimes a separate energy equation is used for the vibrational temperature or (even more rigorous) different vibrational states are described as separate species.

Ion energy equation

For ions, directed motion has an important (if not dominant) contribution to the mean energy. Assuming a heat capacity c and heat flux $-\kappa\nabla T$ as in equation (5.37) but including the directed energy $mw^2/2$, the ion energy equation becomes :

$$ec_i \frac{\partial n_i T_i}{\partial t} + \nabla\cdot\left(e(c_i+1)n_i\mathbf{w}_i T_i - e\kappa_i\nabla T_i\right) = \Pi_i + q_i n_i \mathbf{w}_i\cdot\mathbf{E} - \frac{m_i}{2}\frac{\partial n_i w_i^{\,2}}{\partial t} - \frac{m_i}{2}\nabla\cdot\left(n_i\mathbf{w}_i w_i^{\,2}\right). \tag{5.39}$$

The collisional power term Π_i is generally negative, as for electrons. The directed energy terms are closely related to the electric work term $qn\mathbf{w}\cdot\mathbf{E}$ and can be conveniently rewritten by substitution of the scalar product of the momentum equation (5.13) and the mean velocity $\mathbf{w}$:

$$ec_i \frac{\partial n_i T_i}{\partial t} + \nabla\cdot\left(ec_i n_i \mathbf{w}_i T_i - e\kappa_i\nabla T_i\right) - en_i(\nabla\cdot\mathbf{w}_i)T_i = \Pi_i + (2\bar{\nu}_{m,i}n_i - S_i)\frac{m_i}{2}w_i^{\,2} \tag{5.40}$$

which shows that the ion temperature (thermal energy) is created from the directed energy by collisions. In local field equilibrium, the ion temperature is controlled by the balance of the terms on the right-hand side of equation (5.40) ; for isotropic-scattering collisions with neutrals of mass m_n and temperature T_n (see equation (3.29)) this yields :

$$\frac{2m_i}{m_i+m_n}\bar{\nu}_{m,i}n_i\left(\frac{m_i}{2}w_i^{\,2} + \frac{3e}{2}(T_i - T_n)\right) = 2\bar{\nu}_{m,i}n_i\frac{m_i}{2}w_i^{\,2} \quad \text{hence} \quad eT_i = eT_n + \frac{1}{3}m_n w_i^{\,2} \tag{5.41}$$

The ion energy equation (5.39/40) is usually not solved in plasma models because the ion temperature is a rather unimportant parameter, e.g. for positive ions the pressure gradient $\nabla(nT)$ is usually negligible with respect to the electric force. The ion transport coefficients are then evaluated by the local field approximation as a function of the reduced electric field or the relative temperature (5.5) estimated substituting (5.41) : $T_r = T_i = T_n + m_n w_i^2/3e$. [Ell76] Note also that the validity of the ion energy equation (5.39/40) and even the concept of ion temperature as introduced in equations (5.11-12) are questionable because the ion pressure tensor tends to be anisotropic, especially when charge-exchange collisions (with neutrals) are dominant.[27, 28]

[27] The ion pressure is anisotropic even when the ion distribution function is fully controlled by isotropic-scattering collisions : from statistical analysis of equation (3.27), assuming local field equilibrium and a constant collision frequency, it follows that $T_{i//} = T_n + [(4m_i+m_n)/(2m_i+m_n)] \times m_n w_i^2/3e$ parallel to the field and $T_{i\perp} = T_n + [(m_i+m_n)/(2m_i+m_n)] \times m_n w_i^2/3e$ perpendicular to the field, rather than equation (5.41).

[28] My paper [5] presents simple analytical expressions to estimate the ion energy distribution in case charge-transfer collisions are dominant.

Chapter 6

BOUNDARY CONDITIONS FOR FLUID MODELS[29]

The fluid equations are solved within a spatial domain with one or more (often all) closed boundaries corresponding to physical walls. The boundaries conditions at these boundaries describe the physical processes at the wall which play an important role in the plasma dynamics : electrons and ions are lost in recombination, excited neutrals de-excited, secondary electrons are emitted by ion and excited neutral impact, etc. Since the fluid equations are conservation equations for particles, momentum, and energy, appropriate boundary conditions specify the fluxes of particles, momentum, and energy perpendicular to the wall surface. To formulate such wall-flux boundary conditions, it is useful to distinguish between particles coming from the plasma, moving toward the wall, and particles coming from the wall, moving away from it ; write the net particle flux as

$$nw_\perp \equiv n\mathbf{w}\cdot\mathbf{n} = nw_w - \Gamma_w , \tag{6.1}$$

where **n** is a normal vector toward the wall, w_w is the effective wall loss speed of the particles coming from the plasma, and Γ_w is the particle flux coming from the wall due to reflection and surface creation ; w_w and Γ_w are positive by definition. The particle flux coming from the wall can be obtained from the incident fluxes as

$$\Gamma_w = rnw_w + \sum_j \gamma_j n_j w_{w,j} . \tag{6.2}$$

The first term represents reflection with a probability r and the second term represents creation due impact of other particle species j with a probability γ. The second term is particularly important for electrons to account for secondary electron emission by ion impact, in which case γ is the secondary emission coefficient.

The effective loss speed w_w is to be derived from kinetic considerations, e.g. from assumptions on the distribution function in the half of velocity space containing the particles moving to the wall. The simplest approach is to assume a Maxwellian distribution function and integrate the particle flux over velocity half-space :

$$w_w = \frac{1}{\sqrt{\pi}v_T}\int_0^\infty v_\perp \exp(-{v_\perp}^2/{v_T}^2)dv_\perp = \frac{1}{2\sqrt{\pi}}v_T = \frac{1}{4}\sqrt{\frac{8eT}{\pi m}} \tag{6.3}$$

where $v_\perp$ is the velocity component perpendicular to the wall and $v_T = (2eT/m)^{1/2}$ is the nominal thermal speed. This is often used for charged particles especially electrons (e.g. in classical sheath theory) but does not account for the effects of the electric field and particle density gradient and gives a bad description in case of significant directed motion, e.g. for ions accelerated to the wall by the electric field. Therefore, many authors add additional contributions to the effective wall loss speed to represent directed motion. Commonly used for collisional charged particles is the expression [Meu95][Boe95]

$$w_w = \frac{1}{2\sqrt{\pi}}v_T + \max\left(\frac{q}{|q|}\mu E_\perp, 0\right), \tag{6.4}$$

i.e. the perpendicular drift velocity is added in case it is directed to the wall. The two terms are sometimes interpreted as boundary expressions for the diffusion term and the drift term of

[29] One of my first papers [3] dealt with boundary conditions for fluid plasma models and excited many (sometimes disapproving) reactions which made me aware of some (conceptual) mistakes in it, e.g. the mobility term in equation (9) is inappropriate. My current views on the subject are presented here.

the drift-diffusion equation. However, such interpretation is not pertinent : the intrinsic approximations of the fluid equations do not hold at the wall and neither does the fluid-like separation into different flux terms. Drift, diffusion, thermal conductivity, heat flux, etc are not well defined at the wall.

Collisional electrons and neutrals

More consistent boundary conditions can be obtained by making more consistent assumptions on the distribution function. For near-isotropic collisional electrons and neutrals, it is reasonable to assume a shifted Maxwellian distribution around the mean velocity $w_\perp$. Approximate for $|w_\perp| < v_T$ and integrate the particle flux over velocity half-space :

$$w_w = \frac{1}{\sqrt{\pi} v_T} \int_0^\infty v_\perp \exp\left(-(v_\perp - w_\perp)^2 / {v_T}^2\right) dv_\perp$$

$$\approx \frac{1}{\sqrt{\pi} v_T} \int_0^\infty v_\perp \left(1 + 2\frac{v_\perp w_\perp}{{v_T}^2}\right) \exp\left(-{v_\perp}^2 / {v_T}^2\right) dv_\perp = \frac{1}{2\sqrt{\pi}} v_T + \frac{1}{2} w_\perp ; \qquad (6.5)$$

this is consistent with the two-term solution of the Boltzmann equation (4.5) for constant collision frequency ν_m. Substitution into equation (6.1) yields[30]

$$w_w = \max\left(\frac{1}{\sqrt{\pi}} v_T - \frac{\Gamma_w}{n}, 0\right), \qquad (6.6)$$

i.e. without reflection or wall creation Γ_w the effective loss speed is twice as large as (6.3), but it is reduced as Γ_w increases. The max-limiter is added to prevent w_w becoming negative in case of strong wall creation, when the approximation $|w_\perp| << v_T$ is no longer justified ; this happens for electrons at the cathode due to secondary emission by ion impact, and it is then indeed appropriate to set $w_w = 0$ because the secondary emission coefficients γ given in the literature have generally been deduced neglecting thermal electron loss to the cathode. In case Γ_w consists only of reflected particles, equations (6.1-2) and (6.6) can be combined to obtain the wall flux as

$$n w_\perp = \frac{1}{\sqrt{\pi}} \frac{1-r}{1+r} n v_T ; \qquad (6.7)$$

this is a common boundary condition for neutrals [Cha87].

Positive ions

For positive ions, which have a strongly directed motion toward the wall $w_\perp > v_T$ due to acceleration by the ambipolar (sheath) field, equation (6.6) is not appropriate. Without the approximation $w_\perp << v_T$ and without wall creation Γ_w, the assumption of a shifted Maxwellian distribution around $w_\perp$ leads to an infinite effective loss speed w_w, i.e. to zero density at the wall. Although this seems unrealistic and is not commonly used, zero wall density $n = 0$ is not a bad boundary condition for ions. In fact, due to the strongly directed motion, the ion boundary condition does not propagate inside the volume (only over a negligible distance of order $T/E_\perp$) provided that the effective wall loss speed be larger than the mean velocity upstream such as to prevent ion accumulation at the wall. Another possible boundary condition for ions is therefore to simply add a drift term to equation (6.6) :

$$w_w = \max\left(\frac{1}{\sqrt{\pi}} v_T - \frac{\Gamma_w}{n}, 0\right) + \max\left(\frac{q}{|q|} \mu E_\perp, 0\right); \qquad (6.8)$$

[30] This equation and many of the following equations in this chapter are not standard ; however I have not checked the literature carefully enough to claim them original.

this exceeds the ion velocity upstream not only in drift-diffusion models but also if the ion inertia terms are retained. Equation (6.8) has consistent limits for all particle species and is recommended instead of equation (6.4).

Ions in quasineutral models

In quasineutral plasma models (see chapter 8), the sheath in front of the wall is not represented and the boundary corresponds to the sheath edge rather than the wall. Then the ion boundary condition propagates inside the volume through its direct influence on the electric field and zero ion density is not an appropriate boundary condition. If the effective ion loss speed is larger than the mean ion velocity upstream e.g. by equation (6.8) then the plasma density gradient is increased near the boundary ; assuming electron Boltzmann equilibrium this increases the electric field towards the wall, which increases the ion velocity and loss speed, which further increases the plasma density gradient, and so on, until the loss speed attains the Bohm speed[31] :

$$w_w = \sqrt{(q_i T_e + e T_i)/m_i} \approx \sqrt{q_i T_e / m_i} \,, \tag{6.9}$$

which is the maximum speed for inertial ions allowed by the quasineutral approximation. This can be shown by a simple stability analysis of the ion fluid equations coupled with the electron Boltzmann relation in one dimension x :

$$\frac{\partial n}{\partial t} + \frac{\partial n w}{dx} = S \quad ; \quad \frac{\partial w}{\partial t} + w\frac{\partial w}{\partial x} + \bar{\nu}_m w = \frac{q_i}{m_i} E - \frac{e T_i}{m_i n}\frac{\partial n}{\partial x} = -\frac{q_i T_e + e T_i}{m_i n}\frac{\partial n}{\partial x} . \tag{6.10}$$

Consider that the ions move in the positive x-direction towards a wall boundary and that the ion velocity near the boundary is slightly increased as $w + w' \exp(\Omega t + Kx)$ on a short length and time scale such that $Kw >> |\partial w/\partial x|$ and $\Omega >> \bar{\nu}_m$; substitution in equations (6.10) yields

$$\Omega = \left(\pm \sqrt{(q_i T_e + e T_i)/m_i} - w \right) K \,: \tag{6.11}$$

there exists a positive Ω so the perturbation grows at arbitrarily large K for any w smaller than the limit (6.9). So, provided the spatial inertia term $(\mathbf{w}\cdot\nabla)\mathbf{w}$ is included in the ion momentum equation, the Bohm speed (6.9) appears automatically from equation (6.8) or any other boundary condition describing complete ion absorption.[32] However, this is rather sensitive to numerical errors due to spatial discretisation, which tend to bring to a halt the growth of the ion velocity before it actually attains the Bohm speed (6.9) ; it can therefore be preferable to impose (6.9) directly as a boundary condition. Equation (6.9) is an appropriate boundary condition also for quasineutral drift-diffusion models neglecting ion inertia. If there are more than one positive ion species then (6.9) is not generally justified for each species separately but rather

$$\sum_i \frac{n_i q_i}{m_i w_{w,i}^{\ 2}} = \frac{n_e}{T_e} \,; \tag{6.12}$$

however, the steady-state loss speed of each species remains close to (6.9) as long as the mean free paths and the spatial ionisation profiles are similar. [Fra00]

[31] It is a common misconception that the description of the Bohm speed requires the description of the sheath ; it is a natural limit also for quasineutral models. In my opinion this is more relevant to the origin of the Bohm criterion than the arguments about space charge inversion advanced in most text books. Note also that the existence of a sheath is implicit in the electron Boltzmann relation : without sheath the electrons would not be in Boltzmann equilibrium.

[32] This holds also for quasineutral PIC or hybrid models based on ion particle description with full ion absorption at the boundary, e.g. my hybrid model of the Hall effect thruster, although important errors can arise from discretisation.

Boundary conditions for the momentum equation are needed only if the inertia or viscosity terms are retained, i.e. for inertial ions or neutrals (Navier-Stokes equation). Usually simple boundary conditions are sufficient : for inertial ions $\nabla_\perp \mathbf{w} = 0$; for collisional neutrals zero parallel velocity $\mathbf{w}_{//} = \mathbf{w} - w_\perp \mathbf{n} = 0$ and $w_\perp$ as above from equations (6.1) and (6.6).

Electron energy

For the electron energy equation it is appropriate to use energy flux boundary conditions in analogy with the particle flux boundary conditions discussed above. Since electrons only transfer kinetic energy to the wall when they are lost, write the energy flux as

$$Q_\perp = n_e w_w \varepsilon_w - \Gamma_w \varepsilon_\Gamma \,, \tag{6.13}$$

where ε_w is the mean energy lost per electron and ε_Γ is the mean energy of the secondary electrons emitted from the surface. The energy loss per electron can be straightforwardly obtained by averaging over a half-Maxwellian distribution :

$$\varepsilon_w = \frac{1}{\sqrt{\pi} v_T w_w} \int_0^\infty \frac{m_e}{2e} (v_T{}^2 + v_\perp{}^2) v_\perp \exp(-v_\perp{}^2 / v_T{}^2) dv_\perp = \frac{m_e}{e} v_T{}^2 = 2T_e \tag{6.14}$$

where w_w from equation (6.3) ; the term $v_T{}^2$ in the particle energy accounts for the velocity components parallel to the surface. The energy loss of $2T_e$ per electron is commonly used in plasma physics. However, for collisional electrons it seems more reasonable to assume a shifted Maxwellian distribution around the mean velocity, as above :

$$\begin{aligned} \varepsilon_w &= \frac{1}{\sqrt{\pi} v_T w_w} \int_0^\infty \frac{m_e}{2e} (v_T{}^2 + v_\perp{}^2) v_\perp \exp\left(-(v_\perp - w_\perp)^2 / v_T{}^2\right) dv_\perp \\ &\approx \frac{m_e}{e} v_T{}^2 \left(1 + \frac{\sqrt{\pi} w_\perp}{4 v_T}\right) = \left(\frac{5}{2} - \frac{\sqrt{\pi}\Gamma_w}{n_e v_T}\right) T_e \,, \end{aligned} \tag{6.15}$$

where w_w from equation (6.6). Without secondary emission this is a factor 5/4 higher than (6.14) but decreases as secondary emission increases.

In quasineutral models, where the boundary corresponds to the sheath edge rather than the wall, the sheath potential must be added to the energy loss per electron to account for the electron energy transferred to the ions by the sheath field :

$$\varepsilon_w = 2T_e + \Phi_s \tag{6.16}$$

where the sheath potential Φ_s is to be deduced from a sheath model. For a non-collisional sheath (mean free path >> sheath thickness), assuming zero current to the wall, Maxwell-Boltzmann electrons, the electron loss speed (6.3) at the wall, zero secondary electron emission, and the ion Bohm speed (6.9) at the sheath edge :

$$\Phi_s = \frac{1}{2} T_e \ln\left(\frac{eT_e}{2\pi m_e w_{\perp i}{}^2}\right) = \frac{1}{2} T_e \ln\left(\frac{m_i}{2\pi m_e}\right); \tag{6.17}$$

the last member is reasonable only for steady state.

It is interesting to observe that the first term $2T_e$ in equation (6.16) holds for both a Maxwellian and a shifted Maxwellian electron distribution. For a shifted Maxwellian, consider that the quasi-totality of electrons is reflected at the sheath edge, substitute $\Gamma_w = rnw_w = (v_T/\pi^{1/2})r/(1+r)$ into equation (6.15) and take the limit for r approaching 1 : this yields $2T_e$ as for a centered Maxwellian. From comparison of equations (6.15) and (6.16) it then follows that in a collisional sheath (mean free path << sheath thickness), neglecting secondary emission and collisional energy loss inside the sheath, the electron temperature drops by a factor 4/5 from the sheath edge to the wall.

Chapter 7

NUMERICAL METHODS FOR FLUID MODELS

Although there exist many sophisticated numerical methods for the solution of fluid equations in general, plasma models are usually based on more basic methods, which provide the flexibility and simplicity that is needed to successfully deal with the coupling between the different fluid equations and with the Maxwell equations (see chapter 8). This chapter describes some basic numerical methods that are well adapted and commonly used for fluid equations in plasma models.

Time integration

Consider the general form of a conservation equation with a drift-diffusion flux :

$$\frac{\partial n}{\partial t} + \nabla \cdot \left(\mathbf{W} n - D \nabla n \right) = S \,, \tag{7.1}$$

where the density n, drift velocity $\mathbf{W}$, diffusion coefficient D, source term S are generic, i.e. can have different physical meanings. This equation corresponds directly to the substitution of the drift-diffusion equation (5.15) into the continuity equation (5.6) ($\mathbf{W} = \pm\mu\mathbf{E}$), to the energy equation (5.32) ($n = n_e\varepsilon_e$; $S = -n_e\mathbf{w}_e\cdot\mathbf{E} - n_e\Theta$ etc), and with some minor modification of the time derivative also to the energy equation (5.31) ($n = \varepsilon_e$; $\mathbf{W} = -(5/3)n_e\mathbf{w}_e$; $D = (5/3)n_eD_e$ etc) and the heat equation (5.37).

Consider that equation (7.1) is part of a self-consistent plasma model where it is coupled with similar equations for other particle species and with the Maxwell equations. The couplings with the other equations act upon $\mathbf{W}$, D and S and are generally resolved by explicit time integration : the model equations are integrated sequentially (one by one) over small time steps Δt, where any coupled quantity is evaluated explicitly from the previous time step. In fact, since fully explicit evaluation requires Δt to be smaller than the characteristic time scale of the coupling, various semi-implicit methods are used to avoid time step constraints (as discussed further on), but the equations are generally kept separated and in the form (7.1). Note that time integration is not only used to describe transient behaviour but is also a common and recommended method to obtain steady state model solutions, because it automatically respects the ordering of the different coupling time scales so that the physical stability properties are preserved ; some initial spatial solution is then advanced in time until it has relaxed to steady state.

Hence, a spatial profile $n(\mathbf{x})$ given at time t^k is to be advanced to time $t^{k+1} = t^k + \Delta t$ from equation (7.1) for given $\mathbf{W}$, D and S. The time derivative is approximated by a finite difference. Simplest is to evaluate n in the transport term explicitly at time t^k :

$$n^{k+1} = n^k + \Delta t S - \Delta t \nabla \cdot \left(\mathbf{W} n^k - D \nabla n^k \right), \tag{7.2}$$

but this requires a severe Courant-Friedrichs-Lewy (CFL) constraint on the time step of the type

$$\Delta t < \left(W_x / \Delta x + W_y / \Delta y + 2D / \Delta x^2 + 2D / \Delta y^2 \right)^{-1} \tag{7.3}$$

where Δx and Δy are spatial discretisation steps in two dimensions. Equation (7.2) is sometimes used in combination with a high-order spatial discretisation scheme to obtain the transport term with high accuracy, but often the accuracy of simple spatial discretisation schemes (see below) is sufficient and it is possible and recommended to evaluate the transport term implicitly at the new time step :

$$\frac{1}{\Delta t} n^{k+1} + \nabla \cdot \left(\mathbf{W} n^{k+1} - D \nabla n^{k+1} \right) = \frac{1}{\Delta t} n^{k} + S \ ; \qquad (7.4)$$

this is stable without time step constraints so Δt can be much larger than (7.3). The accuracy of the time integration is only first order but this is sufficient : Δt tends to be limited more by the (stability of the) coupling with other equations than by accuracy.

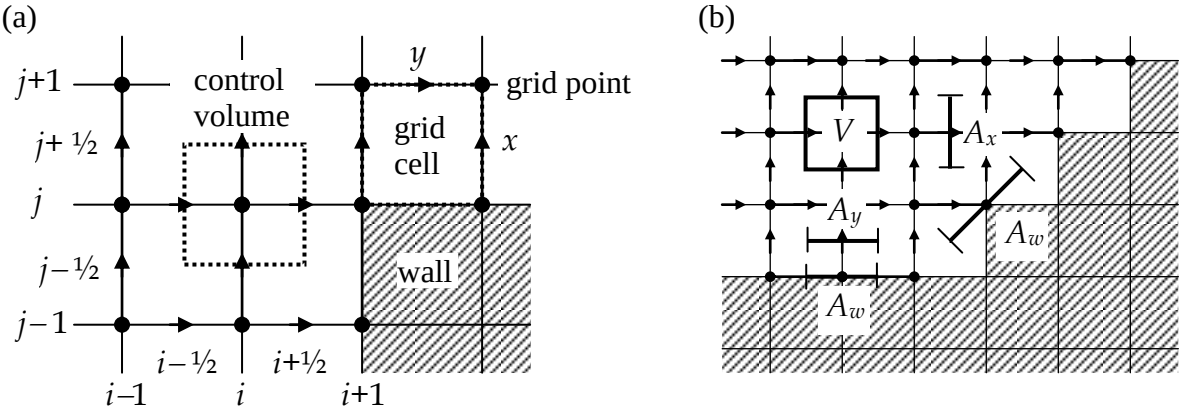

Figure 7.1. Two-dimensional grid for fluid models. Scalar quantities are defined at the dots, *x* and *y* components of vector quantities at the horizontal and vertical arrowheads ; hatched areas represent blocked cells outside the computational domain. Figure a shows the indexing of the different points, figure b some volume and surface elements including an effective wall surface element to represent an oblique domain boundary.

Spatial discretisation

To solve equation (7.4), the space derivatives are discretised as follows. Consider a domain in two spatial dimensions *x* and *y*. The domain is divided in rectangular cells as shown in figure 7.1, usually a hundred or so in each dimension. All scalar quantities are defined at the grid points, corresponding to the cell corners, referred to by indexes (*i,j*). The *x* and *y* components of vector quantities are defined at locations halfway between the grid points, indicated by arrowheads in figure 7.1, referred to by half-indexes (*i*+1/2,*j*) and (*i*,*j*+1/2).

The divergence operator is discretised by the control volume method, according to which so-called control volumes are defined around the grid points with edges passing halfway between the grid points as shown in figure 7.1. Now integrate the conservation equation (7.4) over a control volume, apply the Gauss theorem, and approximate the volume and surface integrals by simple quadratures :

$$\frac{V_{i,j}}{\Delta t} n_{i,j} + A_{x,i+1/2,j} \left(W_x n - D \frac{\partial n}{\partial x} \right)_{i+1/2,j} - A_{x,i-1/2,j} \left(W_x n - D \frac{\partial n}{\partial x} \right)_{i-1/2,j}$$

$$+ A_{y,i,j+1/2} \left(W_y n - D \frac{\partial n}{\partial y} \right)_{i,j+1/2} - A_{y,i,j-1/2} \left(W_y n - D \frac{\partial n}{\partial y} \right)_{i,j-1/2} = V_{i,j} \left(\frac{1}{\Delta t} n^{k}_{i,j} + S_{i,j} \right), \qquad (7.5)$$

where V, A_x, and A_y are the geometrical volume and surface areas of the control volume, depending on the coordinate system (Cartesian, cylindrical etc). This discretisation method imposes conservation of the flux within any ensemble of control volumes so also within the entire domain.

The drift-diffusion flux is discretised by the exponential scheme [Sch69]

$$\left(W_x n - D\frac{\partial n}{\partial x}\right)_{i+1/2} = \frac{W_{x,i+1/2}}{1-\exp(-z_{x,i+1/2})} n_i + \frac{W_{x,i+1/2}}{1-\exp(z_{x,i+1/2})} n_{i+1}$$

$$= \min(W_{x,i+1/2},0) n_{i+1} + \max(W_{x,i+1/2},0) n_i - \left[\frac{|z_{x,i+1/2}|}{\exp(|z_{x,i+1/2}|)-1}\right] D_{i+1/2}\frac{n_{i+1}-n_i}{x_{i+1}-x_i} \qquad (7.6)$$

where

$$z_{x,i+1/2} = W_{x,i+1/2}(x_{i+1}-x_i)/D_{i+1/2}\,. \qquad (7.7)$$

This is scheme is based on the analytical solution for *n* as a function of space assuming a piecewise constant flux, drift velocity, and diffusion coefficient. Since these assumptions are often reasonable, especially for electrons, the exponential scheme leads to accurate density profiles even with only few grid points, especially for the electron density in the sheath.[33] When diffusion is negligible ($|z| >> 1$), the exponential scheme turns into the classical upwind scheme, and when diffusion is dominant ($|z| << 1$), into the central difference scheme. The third member of equation (7.6) shows that the exponential scheme can be directly written as a combination of the upwind scheme for drift (first two terms) and the central difference scheme for diffusion (last term) with a decreased diffusion coefficient ; the factor in square brackets decreases from unity to zero as |z| increases.

Linear system

By substitution of (7.6) in (7.5), the spatial differential equation (7.4) is approximated by a system of linear five-point equations

$$a^{\mathrm{C}}_{i,j} n_{i,j} + a^{\mathrm{E}}_{i,j} n_{i+1,j} + a^{\mathrm{W}}_{i,j} n_{i-1,j} + a^{\mathrm{N}}_{i,j} n_{i,j+1} + a^{\mathrm{S}}_{i,j} n_{i,j-1} = a^{\mathrm{R}}_{i,j} \qquad (7.8)$$

relating the *n*-value at each grid point to those at the four neighbour points, where a^{C}, a^{E}, a^{W}, a^{N}, a^{S}, and a^{R} are (central, east, west, north, south, result) coefficients depending on **W**, *D* and *S* as follows :

$$a^E_{i,j} = a^W_{i+1,j} + \left[A_x W_x\right]_{i+1/2,j} = -\left[A_x W_x/\left(\exp(z_x)-1\right)\right]_{i+1/2,j}$$

$$a^N_{i,j} = a^S_{i,j+1} + \left[A_y W_y\right]_{i,j+1/2} = -\left[A_y W_y/\left(\exp(z_y)-1\right)\right]_{i,j+1/2}$$

$$a^C_{i,j} = V_{i,j}/\Delta t - a^E_{i-1,j} - a^W_{i+1,j} - a^N_{i,j-1} - a^S_{i,j+1}$$

$$a^R_{i,j} = V_{i,j}\left(n^k_{i,j}/\Delta t + S_{i,j}\right). \qquad (7.9)$$

The central coefficient is dominant : $|a^{\mathrm{C}}| > |a^{\mathrm{E}} + a^{\mathrm{W}} + a^{\mathrm{N}} + a^{\mathrm{S}}|$ which ensures the existence of the solution of the linear system. Arbitrarily shaped plasma domains can be described by blocking grid cells as shown in figure 7.1b, such that the plasma boundaries pass through grid points. Boundary conditions for the wall flux of form (6.1) can then be directly implemented into the linear system by adding contributions $A_w w_w$ and $A_w \Gamma_w$ to the coefficients a^{C} and a^{R}, respectively, where A_w is the surface area element at the wall. The boundary points have no links to points outside the plasma domain ; the corresponding coefficients $a^{\mathrm{E\text{-}S}}$ are zero. The system of linear five-point equations is solved most efficiently by iterative methods since a good estimate of the solution is available from the previous time step ; a recommended solution method that is well adapted for plasma models is the so-called modified-strongly-implicit procedure [Sch81]. In one-dimensional models, the discretised equations have a three-point form are solved directly by tridiagonal Gaussian elimination.

[33] The exponential scheme is also very appropriate to discretise the two-term Boltzmann equation (4.10) and is used by my freeware solver BOLSIG+.

Full momentum equation

In case inertia or viscosity is included in the momentum equation (for ions or neutrals), the above methods are still applicable but they require some extensions. The following scheme is effective even if the inertia and viscosity terms completely dominate the momentum equation.[34] First, calculate $\mathbf{W} \approx \mathbf{w}^{k+1}$ as the new mean velocity from the momentum equation using the old density n^k for the pressure gradient. To avoid CFL time step constraints, treat the space derivatives implicitly and solve a linear system of five-point equations for each velocity component, e.g. for the ion momentum equation (5.13) :

$$\frac{1}{\Delta t}\mathbf{W} + (\mathbf{w}^k \cdot \nabla)\mathbf{W} + \bar{\nu}_m \mathbf{W} = \frac{1}{\Delta t}\mathbf{w}^k + \frac{q}{m}\mathbf{E} - \frac{e}{mn^k}\nabla(Tn^k)\,. \tag{7.10}$$

Subsequently, solve the new density n^{k+1} from the continuity equation including an implicit diffusion-correction of the mean velocity to account for changes in the pressure gradient :

$$\frac{1}{\Delta t}n^{k+1} + \nabla\cdot\left(\mathbf{W}n^{k+1} - D\nabla n^{k+1}\right) = \frac{1}{\Delta t}n^k + S - \nabla\cdot\left(D\nabla n^k\right) \tag{7.11}$$

The diffusion-correction terms appear on either side of the equation and cancel in steady state, but they are necessary to ensure numerical stability at larger time steps. The diffusion coefficient D is essentially a numerical parameter which does not require precise evaluation ; it is sufficient to estimate D approximately, e. g. for ions

$$D \simeq \frac{e(T+T_e)}{m(\bar{\nu}_m + \nu^*)} \qquad\qquad \nu^* \simeq \frac{1}{R}\sqrt{e\langle T_e\rangle/m} \tag{7.12}$$

where ν^* is an effective frequency characterising the global ion transport, R is some average plasma radius, and the triangular brackets represent some volume average. The electron temperature is included in D to correct for changes in the electric field due to changes in the electron pressure (assuming quasi-neutrality and Maxwell-Boltzmann electrons) ; this facilitates the coupling with Poisson's equation in self-consistent plasma models (see chapter 8). For neutrals described by the Navier-Stokes equation (5.26) the diffusion coefficient is estimated as $D \approx eT/m\nu^*$ with $\nu^* \approx 8\langle\eta\rangle/R^2$. Finally, update the new mean velocity with the new pressure gradient:

$$\mathbf{w}^{k+1} = \mathbf{W} + \frac{D}{n^{k+1}}\nabla(n^{k+1} - n^k)\,. \tag{7.13}$$

The continuity equation (7.11) can be discretised and solved as above, but care must be taken that both diffusion terms are discretised likewise (so that they really cancel in steady state) e.g. by using the last member of equation (7.6) without the exponential-factor in square brackets. The space derivative in (7.10) can be discretised by the upwind scheme :

$$\begin{aligned}\left((\mathbf{w}\cdot\nabla)w_x\right)_{i+1/2,j} = {} & \frac{\min(w_{x,i+3/2,j} + w_{x,i+1/2,j}, 0)}{2(x_{i+3/2} - x_{i+1/2})}(w_{x,i+3/2,j} - w_{x,i+1/2,j}) \\ & + \frac{\max(w_{x,i+1/2,j} + w_{x,i-1/2,j}, 0)}{2(x_{i+1/2} - x_{i-1/2})}(w_{x,i+1/2,j} - w_{x,i-1/2,j}) \\ & + \frac{\min(w_{y,i+1/2,j+1} + w_{y,i+1/2,j}, 0)}{2(y_{j+1} - y_j)}(w_{x,i+1/2,j+1} - w_{x,i+1/2,j}) \\ & + \frac{\max(w_{y,i+1/2,j} + w_{y,i+1/2,j-1}, 0)}{2(y_j - y_{j-1})}(w_{x,i+1/2,j} - w_{x,i+1/2,j-1})\,.\end{aligned} \tag{7.14}$$

[34] This scheme is used in my low-pressure plasma model for the ICP source for ITER.

Implicit source term prediction

The source term S in equation (7.4) often depends on n. Explicit evaluation can then require time step constraints. To see this, consider a perturbation $\tilde{n}$ around the stationary solution of n and assume the transport term proportional to n :

$$\frac{\tilde{n}^{k+1}-\tilde{n}^k}{\Delta t}+\left(\frac{S}{n}\right)\tilde{n}^{k+1}=\left(\frac{\partial S}{\partial n}\right)\tilde{n}^k \qquad \text{i.e.} \qquad \frac{\tilde{n}^{k+1}}{\tilde{n}^k}=\frac{1+\Delta t\,\partial S/\partial n}{1+\Delta t\,S/n}. \tag{7.15}$$

The perturbation grows so the stationary solution is unstable if $\partial S/\partial n > S/n$, e.g. for electrons with an ionisation source term $S = kn_e^2$; the solution is then stabilised externally by coupling with some other equation, e.g. the ionisation rate coefficient k depends indirectly on n_e through the electron energy equation. If $\partial S/\partial n < S/n$ then the solution is intrinsically stable provided that $\tilde{n}^{k+1}/\tilde{n}^k > -1$, i.e.

$$\Delta t\left(\partial S/\partial n+S/n\right)>-2\,. \tag{7.16}$$

This time step constraint can be prohibitive if the transport term is small with respect to different positive and negative contributions of the source term but can be avoided by the following implicit linear prediction of the new source term :

$$S=S^k+\min\left(\partial S/\partial n, S/n, 0\right)(n^{k+1}-n^k)\,, \tag{7.17}$$

as can be readily verified from the above analysis. The term S/n in the min-delimiter is included to prevent n becoming negative during transient stages of the time evolution. Implicit source term prediction is of particular interest for the electron energy equation (5.31/32). The energy source term is

$$S=-n_e\mathbf{w}_e\cdot\mathbf{E}-n_e\Theta=n_e\mu_eE^2+\nabla(D_en_e)\cdot\mathbf{E}-n_e\Theta\,. \tag{7.18}$$

Neglecting energy transport, the electron mean energy is controlled by equilibrium of the positive heating term and the negative terms for diffusion cooling and collisional energy loss. Explicit evaluation tends to cause instabilities because D_e and especially Θ are strongly rising functions of the electron mean energy so that $\partial S/\partial\varepsilon_e >> |S/\varepsilon_e|$ and the time step constraint (7.16) can be very severe. Using the Einstein relation $D_e = (2/3)\mu_e\varepsilon_e$ and neglecting the energy-dependence of μ_e, the implicitly predicted energy source term (7.17) becomes[35]

$$S=-n_e\mathbf{w}_e\cdot\mathbf{E}-n_e\Theta^k+\left(\frac{2}{3}\mu_e\nabla n_e\cdot\mathbf{E}-n_e\left[\frac{\partial\Theta}{\partial\varepsilon_e}\right]^k\right)(\varepsilon_e^{\,k+1}-\varepsilon_e^{\,k})\,. \tag{7.19}$$

Sometimes the energy equation (5.32) is solved for the energy density $(n_e\varepsilon_e)^{k+1}$ rather than $\varepsilon_e^{\,k+1}$ and the appropriate implicit expression is

$$S=-n_e\mathbf{w}_e\cdot\mathbf{E}-n_e\Theta^k+\left(\frac{2\mu_e}{3n_e}\nabla n_e\cdot\mathbf{E}-\left[\frac{\partial\Theta}{\partial\varepsilon_e}\right]^k\right)\left((n_e\varepsilon_e)^{k+1}-n_e^{\,k+1}\varepsilon_e^{\,k}\right), \tag{7.20}$$

where the electron conservation equation must be solved before the electron energy equation so that $n_e^{\,k+1}$ is known ; the mean energy is then obtained afterwards by dividing $(n_e\varepsilon_e)^{k+1}/n_e^{\,k+1}$. The min-delimiter has been omitted in equations (7.19-20) because it is generally superfluous. The prediction term adds positive contributions to the coefficients a^C and a^R of the five-point system. Note that when applied to particle source terms, equation (7.17) can affect the conservation of mass and charge of the plasma model because the source terms for different species are no longer entirely consistent.

[35] My paper [2] presents a more precise version of this energy source term prediction method, based on the linearisation of the exponential scheme (7.6-7) and accounting for the energy-dependence of the mobility. Unfortunately this paper contains sign errors throughout which have persisted even in the corresponding chapter of my thesis.

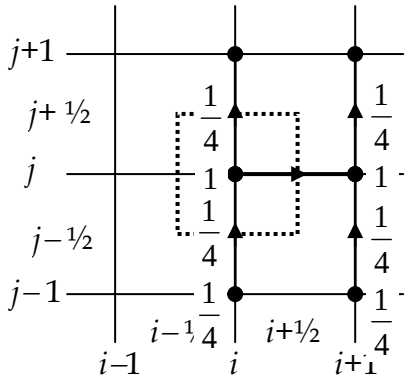

Figure 7.2. Numerical grid points involved in the discretisation of a (horizontal) magnetised flux component at position (i+1/2, j).

Magnetized fluid equations

The above methods can be extended to account for the drift-diffusion flux and energy flux of magnetised electrons as follows. The magnetised fluid equations do not have the form (7.1) but rather

$$\frac{\partial n}{\partial t} + \nabla \cdot \mathbf{\Gamma} = S$$

$$\mathbf{\Gamma} \equiv n\mathbf{w} = \frac{1}{1+\Omega^2}\left(\mathbf{G} - \mathbf{\Omega}\times\mathbf{G} + (\mathbf{\Omega}\cdot\mathbf{G})\mathbf{\Omega}\right) \qquad \mathbf{G} \equiv \mathbf{W}n - D\nabla n\,. \tag{7.21}$$

Consider an axisymmetric configuration with $\mathbf{\Omega} = q\mathbf{B}/m\nu$ in the axial and radial directions ; this corresponds to most magnetised discharges. The transport in the axial-radial plane is then characterized by anisotropy of the transport coefficients $D_{/\!/}/D_\perp = 1 + \Omega^2$ up to 6 orders of magnitude. The control volume method can be applied as before :

$$(Vn/\Delta t)_{i,j}^{k+1} + (A_x\Gamma_x)_{i+1/2,j}^{k+1} - (A_x\Gamma_x)_{i-1/2,j}^{k+1} + (A_r\Gamma_r)_{i,j+1/2}^{k+1} - (A_r\Gamma_r)_{i,j-1/2}^{k+1} = (Vn/\Delta t + VS)_{i,j}^{k}\,,$$

but the discretisation of the flux $\mathbf{\Gamma}$ is delicate. Expressing the flux components in cylindrical coordinates yields

$$\Gamma_x = \frac{1+\Omega_x{}^2}{1+\Omega^2}\left(W_x n - D\frac{\partial n}{\partial x}\right) + \frac{\Omega_x\Omega_r}{1+\Omega^2}\left(W_r n - D\frac{\partial n}{\partial r}\right) \tag{7.22}$$

and an analogous expression for Γ_r. Clearly, if the magnetic field is not exactly aligned with the grid ($\Omega_x\Omega_r \neq 0$) the flux components contain a cross term proportional to the gradient of n in the transverse direction. The two terms of (7.22) can be discretised separately by the exponential scheme (7.6-7) but the cross term requires interpolation from 4 locations involving 6 grid points as indicated in figure 7.2 :

$$\Gamma_{x,i+1/2,j}^{k+1} = \left[\left(1-\hat{\Omega}_r{}^2\right)\left(\tilde{W}_x n - \tilde{D}\frac{\partial n}{\partial x}\right)\right]_{i+1/2,j}^{k+1} + \left[\hat{\Omega}_r\right]_{i+1/2,j}\left[\hat{\Omega}_x\left(\tilde{W}_r n - \tilde{D}\frac{\partial n}{\partial r}\right)\right]_{\frac{1}{4}\left|\begin{matrix} i,j-1/2 \\ i,j+1/2 \\ i+1,j-1/2 \\ i+1,j+1/2 \end{matrix}\right.}^{k} \tag{7.23}$$

$$\hat{\mathbf{\Omega}} = \mathbf{\Omega}\Big/\sqrt{1/\alpha + \Omega^2}$$

$$\tilde{\mathbf{W}} = \mathbf{W}(1+\alpha\Omega^2)\big/(1+\Omega^2)$$

$$\tilde{D} = D(1+\alpha\Omega^2)\big/(1+\Omega^2)$$

where

$$\alpha = \min(\Omega_{\max}^2\big/\Omega^2, 1) \tag{7.24}$$

is a numerical parameter introduced to facilitate the solution and limit discretisation errors for large Hall parameters (large anisotropy) as discussed below. In order to keep the discretised linear system in five-point form (7.8) as before, the cross term is evaluated explicitly from the previous time step, i.e. it is included in the result coefficient a^R. This explicit treatment of the cross term converges regardless of the time step ; e.g. consider a stationary solution and perturb $\mathbf{\Gamma}$ and $\mathbf{G}$ with a form $\exp(i\mathbf{k}\cdot\mathbf{x})$ assuming $\mathbf{k}\cdot\mathbf{\Gamma} = 0$ (continuity) and $\mathbf{k}\times\mathbf{G} = 0$ ($\mathbf{G}$ is the gradient of a scalar quantity) ; then equation (7.23) yields

$$\frac{G^{k+1}}{G^k} = \frac{|\,2\alpha\Omega_x\Omega_r k_x k_r\,|}{(1+\alpha\Omega_x^2)k_x^2 + (1+\alpha\Omega_r^2)k_r^2} \le \frac{1}{1+2/\min(\Omega^2,\Omega_{\max}^2)}, \qquad (7.25)$$

i.e. the perturbation is dissipated. However, as shown in the last member of (7.25), the convergence is slower as the Hall parameter Ω is larger so that more iterations (time steps) are required to obtain the correct solution ; this seems to be a general problem which also occurs if the cross term is treated implicitly by a nine-point iterative solution procedure [Sch81].

A second and more serious problem is that the magnetised flux is very sensitive to discretisation errors : both terms in equation (7.23) are of the order of the non-magnetised flux G and tend to be opposite in sign and very much larger than the net flux Γ ; since the terms are discretised independently (from different grid points) the relative discretisation error in $\mathbf{\Gamma}$ can be enormous. This is illustrated in figure 7.3. In fact, beyond a certain Hall parameter $\Omega >$ 5-10, the flux across the magnetic field tends to be determined by numerical errors rather than by the physical coefficients $\mu_\perp$ and $D_\perp$; hence equation (7.23) is not appropriate for models of $\mathbf{E}\times\mathbf{B}$ discharges (Hall effect thruster, Penning trap, magnetron). To limit these numerical errors, the factor α in equation (7.23) reduces the transport coefficients parallel to the magnetic field for large $\Omega > \Omega_{\max}$ while keeping the perpendicular coefficients intact.[36]

A more proper way to limit numerical errors across the magnetic field is to modify the flux discretisation scheme by elimination of the cross term using the expression for the transverse flux component :[37]

$$\Gamma_{x,i+1/2,j}^{k+1} = \left[\frac{1}{1+\tilde\Omega_r^{\,2}}\left(\tilde W_x n - \tilde D\frac{\partial n}{\partial x}\right)\right]_{i+1/2,j}^{k+1} + \left[\frac{\tilde\Omega_r}{1+\tilde\Omega_r^{\,2}}\right]_{i+1/2,j}\left[\tilde\Omega_x\Gamma_r\right]_{\frac{1}{4}\left|\begin{smallmatrix} i,j-1/2 \\ i,j+1/2 \\ i+1,j-1/2 \\ i+1,j+1/2 \end{smallmatrix}\right.}^{k} \qquad (7.26)$$

$$\tilde{\mathbf{\Omega}} = \sqrt{\alpha}\,\mathbf{\Omega},$$

where the first term is discretised by the exponential scheme (7.6) like before and the second term is evaluated explicitly from the magnetised flux at the previous time step ; this converges as equation (7.25) but then for Γ^{k+1}/Γ^k. Both terms of equation (7.26) are of the order of the flux across the magnetic field so their (relative) discretisation errors are not amplified in $\mathbf{\Gamma}$. However, with (7.26) the parallel transport involves iterative, mutual reinforcement of the two flux terms and tends to be slowed down, which can impede the establishment of the Boltzmann relation along the magnetic field lines and can even affect the stability of the ambipolar field. Depending on the discharge configuration one of the discretisation schemes

[36] Strong electron magnetisation usually occurs at very low gas pressure when the electrons are nearly collisionless as they move (oscillate) along the magnetic field lines. The drift-diffusion equation parallel to the magnetic field is then justified only insofar it yields the Boltzmann relation (5.19) and the parallel transport coefficients are not physically relevant ; all that counts is that they are much larger than the perpendicular coefficients.

[37] I originally developed this scheme for two-stage Hall effect thrusters with a complex magnetic field, for which it works very well even without the factor α. When I recently applied the scheme to a magnetron discharge it turned out to work less well and lead to unphysical artefacts and convergence problems for $\Omega_{\max} > 10$. The scheme is briefly described in my paper [27].

is preferable : equation (7.26) for **E**×**B** discharges and equation (7.23) for discharges with free transport along the magnetic field lines ; neither scheme is appropriate for all configurations.

For simple magnetic field topologies, numerical errors can be rigorously limited by the use of an orthogonal curvilinear grid following the magnetic field lines, so that the cross term vanishes from the flux expressions.[38]

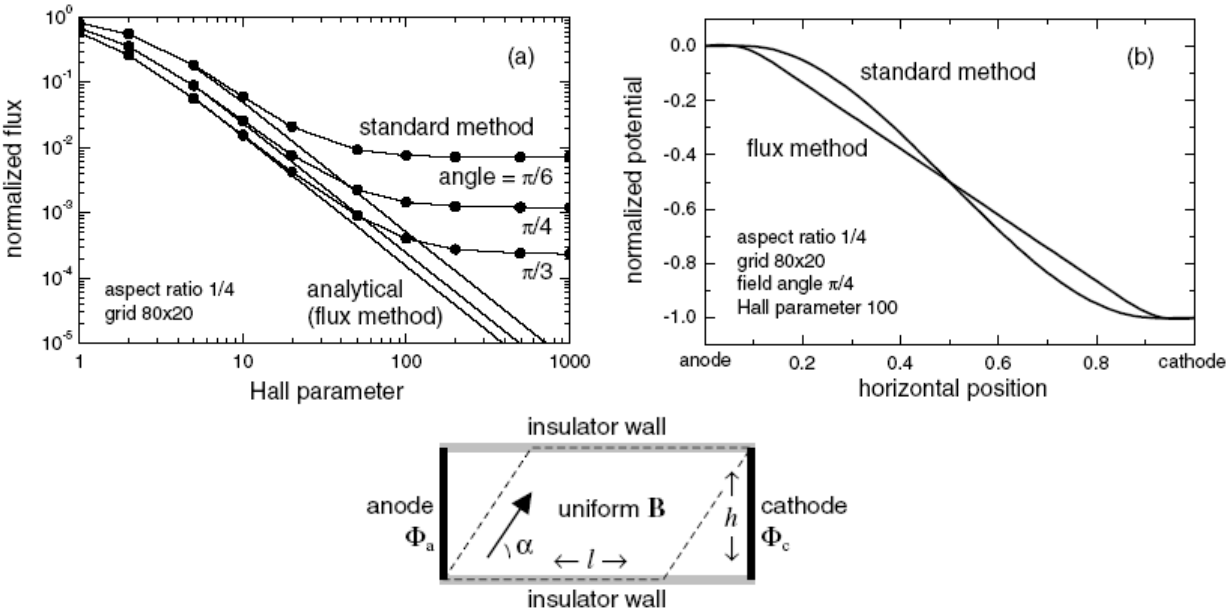

Figure 7.3. Numerical test results for a simple **E**×**B** discharge where a horizontal electron flux is forced through a uniform plasma in a rectangular channel across an oblique magnetic field. The plasma potential and electron flux are solved from the electron continuity equation and magnetized drift-diffusion equation (7.21), assuming fixed ion density, quasineutrality, fixed potentials Φ_a and Φ_c at the vertical boundaries, and zero current at the horizontal boundaries. Figure a shows the electron flux in the centre of the channel obtained from different numerical methods for different magnetic field angles α and different Hall parameters. The standard method based on discretisation of transverse gradients as shown in equation (7.23) tends to overestimate the electron flux with respect to the transverse flux method of equation (7.26) ; the latter is in agreement with the analytical solution. Figure b shows the horizontal potential profile in the centre of the channel ; the analytical potential is linear (uniform electric field) within the triangular region where the magnetic field lines intercept the horizontal walls, but the standard method (7.23) yields a spurious curved potential profile. From [27].

[38] Recently I have come across a publication [Gün05] proposing a simple scheme to calculate heat transport in strongly magnetised plasmas using a non-aligned grid, where numerical errors are strongly reduced by "symmetric" discretisation of the longitudinal and transverse gradients around the points (i+1/2, j+1/2). I have done some preliminary test calculations using this scheme in combination with an iterative 9-point solver ; the results are very promising ; it should be possible to adapt the scheme to the magnetised drift-diffusion equation coupled with Poisson's equation in arbitrary geometry. To be continued.

Chapter 8

AMBIPOLAR AND ELECTROSTATIC APPLIED FIELDS

The ambipolar field generated by plasma charges is described by Poisson's equation

$$\nabla\cdot(\varepsilon_0\mathbf{E}) = -\nabla\cdot(\varepsilon_0\nabla\Phi) = \sum_j q_j n_j \,, \tag{8.1}$$

where the right-hand side is the plasma space charge density. Applied electrostatic fields can be taken into account by applying potential differences in the boundary conditions. To account for dielectric materials surrounding the plasma, Poisson's equation must be solved also inside these materials, including the relative dielectric permittivity ($1+\chi$) in the left-hand side, up to a distance far enough to suppress the influence of any artificial boundary conditions at the domain edge (usually $\nabla_{//}\Phi = 0$) ; plasma charges accumulated on the dielectric surface can be included in the right-hand side of equation (8.1) ; an example is shown in figure 8.1. Poisson's equation can be solved numerically by the same implicit method described in chapter 7 for the fluid equations, involving finite volumes for the divergence, central differences for the gradient, and some (iterative) solution procedure for the discretised system :

$$a^{\mathrm{C}}_{i,j}\Phi_{i,j} + a^{\mathrm{E}}_{i,j}\Phi_{i+1,j} + a^{\mathrm{W}}_{i,j}\Phi_{i-1,j} + a^{\mathrm{N}}_{i,j}\Phi_{i,j+1} + a^{\mathrm{S}}_{i,j}\Phi_{i,j-1} = a^{\mathrm{R}}_{i,j}$$

where

$$\begin{aligned}
a^E_{i,j} = a^W_{i+1,j} &= -[A_x(1+\chi)\varepsilon_0]_{i+1/2,j}/(x_{i+1}-x_i) \\
a^N_{i,j} = a^S_{i,j+1} &= -[A_y(1+\chi)\varepsilon_0]_{i,j+1/2}/(y_{j+1}-y_j) \\
a^C_{i,j} &= -a^E_{i,j} - a^W_{i,j} - a^N_{i,j} - a^S_{i,j} \\
a^R_{i,j} &= \left[V\sum_l q_l n_l + A_w \int^t \sum_l q_l n_l w_{\perp l} dt \right]_{i,j} .
\end{aligned} \tag{8.2}$$

The last term in the result coefficient a^R represents surface charges.

When coupling Poisson's equation self-consistently with the description of the charged particle motion, it is important to observe the characteristic length and time scales of the coupling. From substitution of the electron Boltzmann relation (5.19) in Poisson's equation $\varepsilon_0\nabla^2\Phi \approx en_e\Phi/T_e$ it follows that the characteristic length is the Debye length

$$\lambda_{\mathrm{D}} = \sqrt{\varepsilon_0 T_e / e n_e} \,, \tag{8.3}$$

corresponding to the distance over which electron pressure variations can resist to the space charge field ; this also characterises the thickness of the ambipolar sheath at the wall. To find the characteristic time of the ambipolar coupling, differentiate Poisson's equation with respect to time and substitute the electron and ion continuity and momentum equations such as to obtain a differential equation for $\nabla^2\Phi$ as function of time. In the absence of collisions, the characteristic time is $1/\omega_p$ the inverse of the plasma frequency

$$\omega_{\mathrm{p}} = \sqrt{\sum_j q_j^{\,2} n_j / \varepsilon_0 m_j} \cong \sqrt{e^2 n_e / \varepsilon_0 m_e} \,. \tag{8.4}$$

Plasma oscillations can easily be excited at this angular frequency but are dissipated by collisions. Therefore, in collisional plasmas ($\nu_m >> \omega_p$) the ambipolar coupling is rather determined by the dielectric relaxation time

$$\tau_{\mathrm{d}} = \frac{\varepsilon_0}{\sum_j |q_j|\mu_j n_j} \cong \frac{\varepsilon_0}{e\mu_e n_e} \; (> 1/\omega_{\mathrm{p}}) \; . \tag{8.5}$$

To fully resolve the ambipolar coupling, the numerical discretisation must respect the following constraints : spatial step $\Delta x < \lambda_{\mathrm{D}}$, time step $\Delta t < 0.2/\omega_{\mathrm{p}}$ for non-collisional and PIC models, and $\Delta t < \tau_{\mathrm{d}}$ for collisional drift-diffusion models.

Semi-implicit method

Often, however, one is not interested in describing ambipolar plasma oscillations or dielectric relaxation, but rather in plasma evolution on a much longer scale, and the above time step constraints can be very prohibitive. Then a semi-implicit time integration method can be used to achieve numerical stability at larger time steps. [Ven93] Consider a self-consistent plasma model consisting of continuity equations and drift-diffusion equations for electrons and ions coupled with Poisson's equation. All quantities are known at a time t^k and are to be advanced to time $t^{k+1} = t^k + \Delta t$. The particle densities are advanced implicitly as discussed in chapter 7 :

$$\frac{1}{\Delta t} n^{k+1} + \nabla \cdot \left(\frac{q}{|q|} \mu n^{k+1} \nabla \Phi^{k+1} - D \nabla n^{k+1} \right) = \frac{1}{\Delta t} n^k + S \tag{8.6}$$

To avoid the time step constraints due to the ambipolar coupling, it is necessary to use the new potential Φ^{k+1} accounting for the new space charge density through Poisson's equation (8.1). Fortunately, however, it is not necessary to account for the *exact* new space charge density (which would imply solving all equations simultaneously) ; it is sufficient to estimate the new space charge in Poisson's equation by replacing n^{k+1} by n^k in the transport terms of the electron and ion equations (8.6), i.e. to use equation (7.2). Poisson's equation then becomes

$$-\nabla \cdot (\varepsilon_0 \nabla \Phi^{k+1}) = \sum_j \left[q_j n_j^{\,k} - \Delta t \nabla \cdot \left(|q_j| \mu_j n_j^{\,k} \nabla \Phi^{k+1} - q_j D \nabla n^k \right) \right] . \tag{8.7}$$

Substituting (8.6) for the previous time step (from k–1 to k), this can be written as[39]

$$-\nabla \cdot \left(\varepsilon_0 (1 + \chi_e) \nabla \Phi^{k+1} \right) = \sum_j q_j (2 n_j^{\,k} - n_j^{\,k-1}) - \nabla \cdot \left(\varepsilon_0 \chi_e \nabla \Phi^k \right) \tag{8.8}$$

$$\chi_e = \frac{\Delta t}{\varepsilon_0} \sum_j |q_j| \mu_j n_j^{\,k} = \frac{\Delta t}{\tau_{\mathrm{d}}} . \tag{8.9}$$

So the modified Poisson's equation (8.8) includes a semi-implicit prediction of the future space charge density and is solved separately before the time advancement of the densities by equation (8.6). This scheme remains stable even if $\Delta t >> \tau_{\mathrm{d}}$. Similar semi-implicit methods have been developed for non-collisional fluid models [Cri07] in which case $\chi_e \approx \Delta t^2 e^2 n_e / m_e \varepsilon_0$ and even for PIC models [Lan83].

Electron Maxwell-Boltzmann models

A related problem occurs in models based on the Boltzmann relation (5.19) for electrons, i.e. $n_e = n_0 \exp(\Phi / T_e)$. Since electron inertia and collisions are neglected, the electron density responds instantaneously to the potential and requires implicit treatment in Poisson's equation ; however, it also has to satisfy the global (space integrated) electron conservation equation (through the reference density n_0)

$$\frac{\partial}{\partial t} \iiint n_e d^3V + \iint n_e w_{e\perp} d^2A = \iiint S_e d^3V \; , \tag{8.10}$$

[39] My paper [2] presents a more precise version of the semi-implicit method based on linearisation of the exponential scheme of equation (7.6-7) ; for most purposes however the simpler equations shown here work just as well.

which makes fully implicit treatment into a global problem. To avoid solving an implicit integro-differential equation, the following semi-implicit scheme can be used for the time advancement.[40] First, the new reference density n_0 is calculated from global electron conservation as

$$a^k {n_0}^{k+1} = \left(a^{k-1} + (a^k - a^{k-1})\sqrt{b^k / a^k} \right) {n_0}^k - b^k + \Delta t \iiint S_e d^3V \tag{8.11}$$

$$a^k = \iiint \exp(\Phi^k / T_e) d^3V$$

$$b^k = \Delta t \iint w_{e\perp} \exp(\Phi^k / T_e) d^2A ,$$

where the square-root term under-relaxes n_0 such as to critically damp oscillations. Then, the new potential is solved from Poisson's equation with implicit linearised Boltzmann factor :

$$-\nabla \cdot (\varepsilon_0 \nabla \Phi^{k+1}) = \sum_i q_i n_i - e {n_0}^{k+1} \exp(\Phi^k / T_e) \left(1 + (\Phi^{k+1} - \Phi^k) / T_e \right), \tag{8.12}$$

where summation only includes the ion species. This scheme is stable without electron-related time step constraints. The critical damping term in (8.11) has been derived from analytical considerations on the behaviour of the ambipolar field, explained in detail in [29].

Quasi-neutral models

Sometimes the Debye length is so small with respect to the plasma size that resolving it is prohibitive and of limited interest. It is then customary to eliminate Poisson's equation from the model by the assumption of quasineutrality, i.e. the electron density is calculated from

$$n_e = \frac{1}{e} \sum_i q_i n_i , \tag{8.13}$$

after which the electron equations are solved for the potential Φ rather than n_e. In case there is only one ion species (of charge $+e$) then quasi-neutral drift-diffusion models can be elegantly reformulated by splitting the electric field into the driving field $-\nabla\Phi_\mathrm{d}$ (applied field) and the ambipolar field $-\nabla\Phi_\mathrm{a}$ defined by the zero-current condition

$$-e(\mu_e + \mu_i) n_e \nabla \Phi_\mathrm{a} + e(D_e - D_i) \nabla n_e = 0 . \tag{8.14}$$

The ambipolar field is eliminated to obtain two separate equations for the plasma density and the driving potential :

$$\frac{\partial n_e}{\partial t} - \nabla \cdot \left(\frac{\mu_i D_e + \mu_e D_i}{\mu_e + \mu_i} \nabla n_e \right) \equiv \frac{\partial n_e}{\partial t} - \nabla \cdot \left(D_\mathrm{a} \nabla n_e \right) = S_e \tag{8.15}$$

$$\nabla \cdot \left(e(\mu_e + \mu_i) n_e \nabla \Phi_\mathrm{d} \right) \equiv \nabla \cdot \left(\sigma \nabla \Phi_\mathrm{d} \right) = 0 , \tag{8.16}$$

where the effective transport coefficients are the ambipolar diffusion coefficient D_a and the electric plasma conductivity σ. This is approach is frequently used in text books on plasma physics but is awkward and not recommended in case of multiple ion species.[41] An additional complication of quasi-neutral models is that the sheath potential must be estimated analytically and included explicitly in the boundary conditions for the potential and the electron energy flux as shown in equation (6.17). In fact, the semi-implicit method presented above offers a good alternative to the explicit use of the quasi-neutrality condition (8.13) : this method remains stable even if the Debye length is not resolved, in which case it automatically

[40] I originally developed this method for a hybrid model of a vacuum circuit breaker ; it was then also used by Albert Meige to study electro-negative double layers and briefly described in his thesis ; it was finally the subject of a publication in J. Comp. Phys. : [29].

[41] I applied the quasineutral approach with multiple ion species in the first version of my model of the micro-hollow-cathode-sustained discharge, used by E. Muñoz-Serrano [25] ; due to persistent numerical problems I later replaced the quasineutral approximation by the semi-implicit Poisson equation, in the version used by K. Makasheva [31][37] ; this turned out to work much better.

yields a plasma sheath with a thickness of one spatial discretisation step and a sheath potential reasonably close to the analytical value. Note that for larger time steps $\chi_e >> 1$, the modified Poisson equation (8.8) becomes equivalent to the quasi-neutral current conservation equation (8.16).

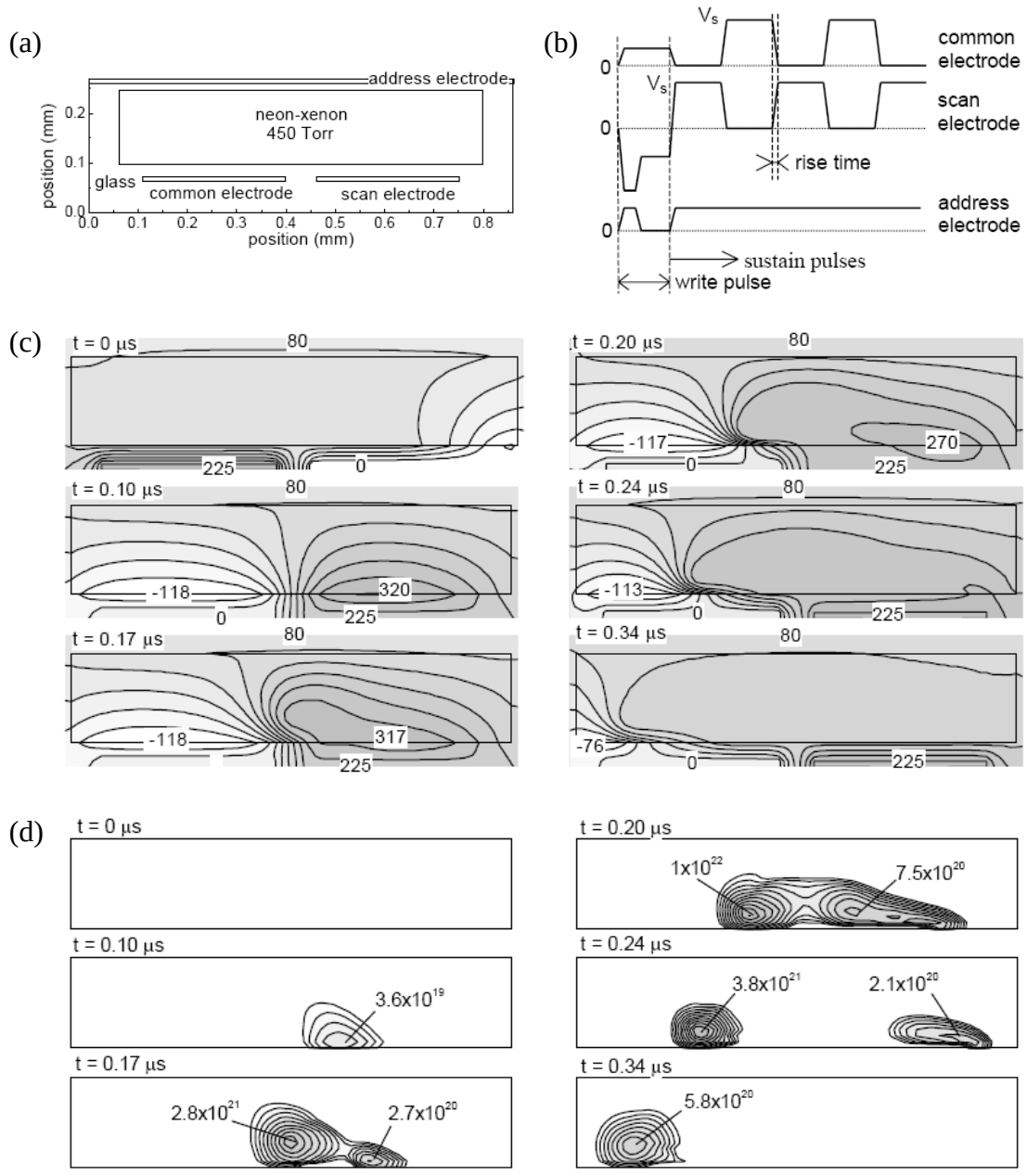

Figure 8.1. Simulation of a microdischarge in one cell of plasma display panel (PDP) by a self-consistent fluid model consisting of continuity equations (5.6) and drift-diffusion equations (5.15) for about 10 different plasma species, the electron energy equation (5.33), and Poisson's equation (8.1). The plasma is sustained by coplanar electrodes (called common and scan in figure a) covered with a dielectric layer and driven with a 50 kHz alternating square voltage (figure b). When the PDP cell is on, a transient discharge occurs each time the sustain voltage changes polarity and is quenched by accumulation of surface charges on the dielectric, which screen the plasma from the voltage but reinforce the voltage at the next polarity switch. Figure c shows the time evolution of the electrostatic potential during the discharge ; the voltage is switched at t = 0 µs with a rise time of 0.1 µs and is almost fully screened by surface charges at t = 0.34 ; the extreme potential values are indicated in volts. Figure d shows the corresponding time evolution of the excitation rate of the resonant $Xe^*(^3P_1)$ state in logarithmic scale from 10^{18} to 10^{22} $cm^{-3}\,s^{-1}$; these states emit ultraviolet photons that excite the phosphors of the display. From [9].

Chapter 9

MICROWAVE FIELDS

To describe the interaction between a plasma and applied microwave fields, recognise that the microwave period is orders of magnitude shorter than the time scale of the evolution of the plasma density and chemistry, and hence decompose the electromagnetic field and particle quantities into separate components for plasma evolution and microwave oscillations, respectively denoted without and with tilde. The microwave fields are described by the Maxwell equations

$$\varepsilon_0 \nabla \cdot \tilde{\mathbf{E}} = -e\tilde{n}_e \qquad \text{(Gauss)} \qquad (9.1)$$

$$\nabla \cdot \tilde{\mathbf{B}} = 0 \qquad (9.2)$$

$$\nabla \times \tilde{\mathbf{E}} = -\frac{\partial \tilde{\mathbf{B}}}{\partial t} \qquad \text{(Faraday)} \qquad (9.3)$$

$$\frac{1}{\mu_0} \nabla \times \tilde{\mathbf{B}} = \mathbf{J}_\mathrm{d} - e n_e \tilde{\mathbf{w}}_e + \varepsilon_0 \frac{\partial \tilde{\mathbf{E}}}{\partial t}, \qquad \text{(Ampere)} \qquad (9.4)$$

where $\mathbf{J}_\mathrm{d}$ is the driving current density exciting the microwaves somewhere outside the plasma. The first two Maxwell equations prescribe the initial conditions for the last two and are superfluous for periodic wave solutions. The plasma current is approximated as follows. First, ion motion on the microwave time scale is neglected with respect to electron motion due to the much larger ion mass. Second, since the Debye length is usually much smaller than the length scale of the microwave interaction (skin depth), the electron density $n_e \approx n_i >> \tilde{n}_e$ is assumed constant on the microwave time scale. The electron mean velocity is given by the local momentum equation (5.23) :

$$\frac{\partial \tilde{\mathbf{w}}_e}{\partial t} + \bar{\nu}_{m,e} \tilde{\mathbf{w}}_e = -\frac{e}{m_e} \tilde{\mathbf{E}}, \qquad (9.5)$$

neglecting the magnetic force (with respect to the electric force) and the distances travelled by the electrons during a microwave period (with respects to any gradient length).

With the above approximations, the plasma-microwave interaction is completely linear and the periodic solution has simple harmonic time dependence at the (angular) wave frequency ω. Substituting the electron momentum equation in the Maxwell-Ampere equation, the plasma current can be represented by a combination of conductivity and permittivity :

$$\frac{1}{\mu_0} \nabla \times \tilde{\mathbf{B}} = \left(\frac{\varepsilon_0 \omega_p{}^2 \bar{\nu}_{m,e}}{\omega^2 + \bar{\nu}_{m,e}{}^2} \right) \tilde{\mathbf{E}} + \left(1 - \frac{\omega_p{}^2}{\omega^2 + \bar{\nu}_{m,e}{}^2} \right) \varepsilon_0 \frac{\partial \tilde{\mathbf{E}}}{\partial t}, \qquad (9.6)$$

or rather, using the complex notation $\exp(i\omega t)$, by a complex permittivity alone :

$$\frac{1}{\mu_0} \nabla \times \tilde{\mathbf{B}} = \left(1 - \frac{\omega_p{}^2}{\omega(\omega - i\bar{\nu}_{m,e})} \right) \varepsilon_0 (i\omega \tilde{\mathbf{E}}). \qquad (9.7)$$

The interaction depends on the ratios of the plasma frequency, collision frequency, and wave frequency ; its characteristic length scales can be found from the complex wave number of the plane wave solution (assume $\mathbf{E} \perp \mathbf{B} \perp \nabla$ and ω_p constant), which has the limits

$$k \approx \frac{\omega}{c} + i \frac{\omega_p{}^2 \bar{\nu}_{m,e}}{2c(\omega^2 + \bar{\nu}_{m,e}{}^2)} \qquad \omega_p{}^2 << \omega^2 + \bar{\nu}_{m,e}{}^2 \qquad (9.8)$$

$$k \approx \frac{\omega_p}{c}\sqrt{\frac{\omega}{2\bar{\nu}_{m,e}}}(1+i) \qquad \omega_p{}^2 >> \bar{\nu}_{m,e}{}^2 >> \omega^2 \tag{9.9}$$

$$k \approx \frac{\omega_p}{c}\left(\frac{\bar{\nu}_{m,e}}{2\omega}+i\right) \qquad \omega_p{}^2 >> \omega^2 >> \bar{\nu}_{m,e}{}^2 . \tag{9.10}$$

The real part is the inverse wave length and the imaginary part is the inverse skin depth, corresponding to exponential decay of the wave amplitudes.

From the microwave solution, the time average power absorption per electron is

$$P = -\frac{e\omega}{2\pi}\int_0^{2\pi/\omega} \tilde{\mathbf{E}}\cdot\tilde{\mathbf{w}}dt . \tag{9.11}$$

This can be injected in the source term of an electron energy equation that is part of a plasma model describing the plasma evolution time scale. A self-consistent description of a microwave-sustained plasma can thus be obtained by iteration : the microwave solution yields the time-average power absorption, which is injected in a plasma model to simulate the evolution of the plasma density over a certain time, which is injected back into the microwave equations to update the power absorption, etc, until a steady state is reached. During such iteration procedure, it is appropriate to continuously renormalise the power absorption such as to keep the total (space-integrated) absorbed power constant : this minimizes the coupling between the microwave and plasma-evolution parts of the model.

Boundary conditions

The microwave fields are solved not only inside the plasma but also in the surroundings. Boundary conditions for the microwave fields on metal surfaces are :

$$\tilde{E}_{//} = 0 \qquad \tilde{B}_{\perp} = 0 \tag{9.12}$$

i.e. zero parallel electric field and zero perpendicular magnetic field. For open domain boundaries there exist simple approximate absorption boundary conditions [Mur81, Kun93], e.g. for right axial (+), left axial (–), and radial boundaries :

$$\frac{\partial W}{\partial t} \pm c\frac{\partial W}{\partial x} = 0$$

$$\frac{\partial W}{\partial t} + \frac{c}{\sqrt{r}}\frac{\partial}{\partial r}\left(\sqrt{r}W\right) = 0 , \tag{9.13}$$

where W is any electric or magnetic field component.

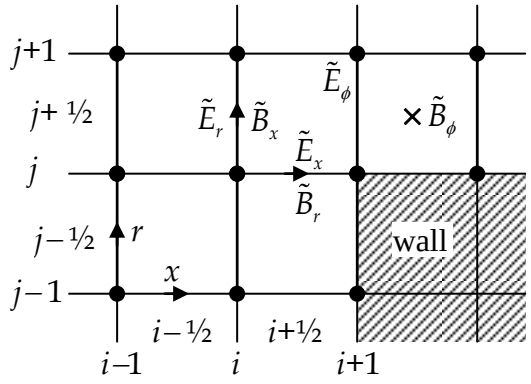

Figure 9.1. Two-dimensional (axial-radial) grid arrangement of the different electromagnetic field components for the FDTD method.

FDTD method

A common and convenient method to solve the Maxwell equations for microwave fields is the so-called Finite Difference Time Domain (FDTD) method [Kun93], according to which the equations are explicitly integrated in time. Space is divided in a grid of rectangular (usually uniform) cells, and the different components of $\tilde{\mathbf{E}}$ and $\tilde{\mathbf{B}}$ are defined at different grid positions (shifted by half cells) and different times (shifted by half time steps), such as to enable central difference discretisation of all derivatives. An appropriate grid arrangement for a two-dimensional axisymmetric domain is shown in figure 9.1, where $\tilde{\mathbf{E}}$ is defined at times t^k and $\tilde{\mathbf{B}}$ at $t^{k+1/2}$. The fields are then advanced in time from the Faraday and Ampere equations as follows :

$$\tilde{B}^{k+1/2}_{x,i,j+1/2} = \tilde{B}^{k-1/2}_{x,i,j+1/2} - \Delta t \frac{r_{j+1}\tilde{E}^{k}_{\varphi,i,j+1} - r_j \tilde{E}^{k}_{\varphi,i,j}}{r_{j+1/2}\Delta r} \tag{9.14}$$

$$\tilde{E}^{k+1}_{x,i+1/2,j} = \tilde{E}^{k}_{x,i+1/2,j} + \frac{\Delta t}{\mu_0 \varepsilon_0} \frac{r_{j+1/2}\tilde{B}^{k+1/2}_{\varphi,i+1/2,j+1/2} - r_{j-1/2}\tilde{B}^{k+1/2}_{\varphi,i+1/2,j-1/2}}{r_j \Delta r} + \frac{e\Delta t}{\varepsilon_0}[n_e \tilde{w}_{e,x}]^{k+1/2}_{i+1/2,j} \tag{9.15}$$

and similar for the other components. Rather than representing the plasma current by a conductivity and permittivity as shown in equation (9.6), it is preferable to integrate the electron momentum equation (9.5) explicitly in time, so that also possible non-harmonic behaviour can be captured :

$$\tilde{\mathbf{w}}^{k+1/2}_e = \frac{2}{1+\bar{\nu}_{m,e}\Delta t/2}\left(\tilde{\mathbf{w}}^{k-1/2}_e - \frac{e\Delta t}{2m_e}\tilde{\mathbf{E}}^k\right) - \tilde{\mathbf{w}}^{k-1/2}_e, \tag{9.16}$$

where $\tilde{\mathbf{w}}_e$ is most conveniently defined at the same positions as $\tilde{\mathbf{E}}$ and the same times as $\tilde{\mathbf{B}}$. Due to the explicit time advancement, FDTD requires a CFL time step constraint, e.g.

$$\Delta t < \frac{\Delta x \Delta r}{c(\Delta x + \Delta r)} \tag{9.17}$$

for cylindrical axisymmetric coordinates. This condition, combined with the requirement that the spatial step Δx be smaller than the skin depth $1/k$ (9.8-10), also ensures the stability of the explicit evaluation of the current (9.16) ($\Delta t < 1/\omega_p$). The time integration is continued over a number of microwave periods, until the solution becomes periodic, after which the power absorption per electron (and other quantities of interest) are averaged over one period.

The FDTD method is particularly well adapted to account for arbitrarily-shaped dielectric or conducting materials surrounding the plasma and capture abrupt transitions between these materials. Material properties can be defined per grid cell as shown in figure 9.1. Inside dielectrics the relative permittivity is added in Ampere's equation (9.4). Inside conductors all field components are set to zero ; the grid definition is such that the boundary conditions (9.12) are automatically satisfied on the metal boundary points. The microwaves are excited by a sheet of current somewhere outside the plasma, usually inside some conductor-bounded area, e.g. TEM waves are excited in a coaxial wave-guide by adding a contribution $J_0 \sin(\omega t)(r_0/r)\Delta t/\varepsilon_0$ each time step to the radial electric field at a given axial position, where J_0 is an arbitrary excitation current amplitude. The fields, currents, and power absorption are renormalized afterwards to impose a fixed total power.

FDTD with magnetized electrons

The FDTD method can also be adapted to account for magnetization of the electrons by a steady magnetic field, such as used in electron-cyclotron-resonance discharges to obtain electron heating at low gas density. The electron momentum equation is then

$$\frac{\partial \tilde{\mathbf{w}}_e}{\partial t} + \bar{\nu}_{m,e}\tilde{\mathbf{w}}_e - \frac{e}{m_e}\mathbf{B}\times\tilde{\mathbf{w}}_e = -\frac{e}{m_e}\tilde{\mathbf{E}}\,, \tag{9.18}$$

where the last term on the left is the force of the steady magnetic field **B**, which reduces the electron transport perpendicular to **B** and creates drift in the direction of $\tilde{\mathbf{E}}\times\mathbf{B}$, often the azimuthal direction of an axisymmetric configuration, thereby changing the polarisation state of the waves. Resonant plasma-wave interaction occurs wherever the cyclotron frequency eB/m_e equals ω. Several authors [Hun92, Lee99] translate the magnetized momentum equation (9.18) into a plasma conductivity and permittivity, which then take the form of tensors in analogy with the magnetized mobility and diffusion tensors in equation (5.22). For FDTD calculations, however, it is much more convenient to integrate the magnetized momentum equation explicitly in time, as above. For this, rewrite the central difference discretisation of equation (9.18) as follows :

$$\tilde{\mathbf{w}}_e^{k+1/2} = \frac{2}{z^2+b^2}\left(z^2\mathbf{w}_1 + z\mathbf{w}_1\times\mathbf{b} + (\mathbf{w}_1\cdot\mathbf{b})\mathbf{b}\right) - \tilde{\mathbf{w}}_e^{k-1/2} \tag{9.19}$$

where

$$z = 1 + \nu_{m,e}\Delta t/2$$

$$\mathbf{w}_1 = \frac{1}{z}\left(\tilde{\mathbf{w}}_e^{k-1/2} - \frac{e\Delta t}{2m_e}\tilde{\mathbf{E}}\right)$$

$$\mathbf{b} = -\frac{e\Delta t}{2m_e}\mathbf{B}$$

in analogy with the leap-frog scheme for particle models shown in equation (3.3). The time step must be much smaller than the inverse cyclotron frequency : $\Delta t << m_e/eB$ but this is usually satisfied by condition (9.17). To achieve the vector multiplications in equation (9.19) without interpolation errors, to which the magnetized electron velocity is very sensitive, it is necessary to define all velocity components at the same points in space, e.g. the grid points (i,j) in figure 9.1. As a result, the electric field components must be interpolated in equation (9.19) and the electron current in equation (9.15), e.g. for the radial components

$$\tilde{E}_{r,i,j} = \frac{1}{2r_j}\left(r_{j-1/2}\tilde{E}_{r,i,j-1/2} + r_{j+1/2}\tilde{E}_{r,i,j+1/2}\right) \tag{9.20}$$

$$[n_e\tilde{w}_{e,r}]_{i,j+1/2} = \frac{1}{2r_{j+1/2}}\left([rn_e\tilde{w}_{e,r}]_{i,j} + [rn_e\tilde{w}_{e,r}]_{i,j+1}\right), \tag{9.21}$$

where the weighting by r preserves the divergence of the electric field and electron flux. Special care must be taken of grid points at the plasma edge : due to a space charge layer the electric field is discontinuous at the plasma edge and instead of the latter interpolation the field on the edge points must be extrapolated from inside the plasma.

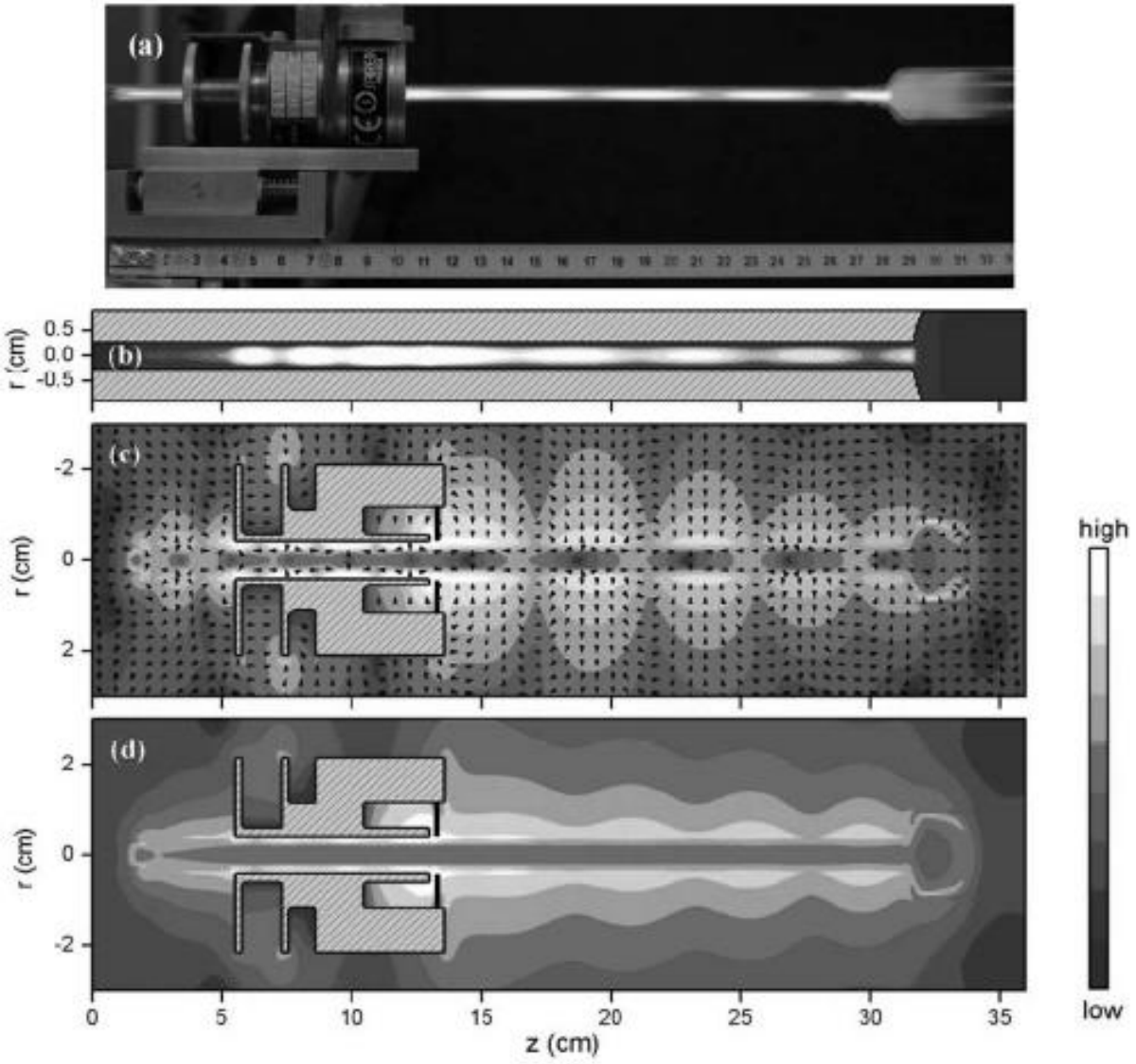

Figure 9.2. Self-consistent simulation of a surface wave discharge for the production of reactive species (e.g. for sterilization of medical equipment) in a gas flowing through a glass tube (here argon). The plasma is sustained by 2.45 GHz microwave fields applied by a so-called surfatron, which propagate as surface waves along the plasma-glass interface and are gradually absorbed by the plasma ; the length of the plasma column depends on the injected microwave power. Figure a shows that a transition in the tube diameter induces periodic spatial variations in the discharge intensity. This phenomena is simulated in figures b-d respectively showing : Ar^{**} decay rate (~ visual light intensity), instantaneous electric field, and time-average field strength ; clearly part of the surface waves is reflected against the diameter transition thus creating standing wave patterns. These results are obtained by iteration between a FDTD microwave calculation and a fluid plasma model accounting for 5 argon species and simplified argon excitation kinetics. The length of the simulated plasma column is very sensitive to the (assumed) effective life-time of resonant argon states which has here been adjusted to obtain agreement with experiments. From [20].

Chapter 10

ELECTRODYNAMIC POTENTIALS AND INDUCTIVE COUPLING

Potential formulation of the Maxwell equations

An alternative to solving the Maxwell equations directly for the fields by FDTD as described in the previous chapter, is to solve them by the electrodynamic potentials, i.e. by substitution of $\tilde{\mathbf{E}} = -\nabla\tilde{\Phi} - \partial\mathbf{A}/\partial t$ and $\tilde{\mathbf{B}} = \nabla\times\mathbf{A}$. Imposing the Lorenz condition

$$\nabla\cdot\mathbf{A} = -\frac{1}{c^2}\frac{\partial\tilde{\Phi}}{\partial t}, \tag{10.1}$$

the Maxwell equations (9.1-4) become

$$\varepsilon_0\frac{\partial^2\tilde{\Phi}}{\partial t^2} - \varepsilon_0 c^2\nabla^2\tilde{\Phi} = -c^2 e\tilde{n}_e \tag{10.2}$$

$$\varepsilon_0\frac{\partial^2\mathbf{A}}{\partial t^2} - \varepsilon_0 c^2\nabla^2\mathbf{A} = \mathbf{J}_\mathrm{d} - en_e\tilde{\mathbf{w}}_e \tag{10.3}$$

where

$$\frac{\partial\tilde{n}_e}{\partial t} = -\nabla\cdot(n_e\tilde{\mathbf{w}}_e). \tag{10.4}$$

The advantage of this approach is that it connects naturally to the usual description of the ambipolar and electrostatic fields by Poisson's equation as described in chapter 8, so that the same semi-implicit numerical methods can be used to avoid time step constraints, and the electrodynamic interaction can be described at arbitrarily low frequency. If desired the equations (10.2-3) can be extended to include the ion charge and current, the wave potential $\tilde{\Phi}$ can be merged with the ambipolar potential Φ, and the simplified continuity equation (10.4) can be replaced by a full fluid model.

Generalization of the semi-implicit method for Poisson's equation yields

$$\frac{\varepsilon_0}{\Delta t^2}\tilde{\Phi}^{k+1} - \varepsilon_0 c^2\nabla\cdot\left((1+\chi_e)\nabla\tilde{\Phi}^{k+1}\right) = \frac{\varepsilon_0}{\Delta t^2}\left(2\tilde{\Phi}^k - \tilde{\Phi}^{k-1}\right) + c^2\tilde{\rho}^k \tag{10.5}$$

$$\frac{\varepsilon_0}{\Delta t^2}(1+\chi_e)\mathbf{A}^{k+1} - \varepsilon_0 c^2\nabla^2\mathbf{A}^{k+1} = \frac{\varepsilon_0}{\Delta t^2}\left((2+\chi_e)\mathbf{A}^k - \mathbf{A}^{k-1}\right) + \mathbf{J}_\mathrm{d}{}^{k+1} - en_e\tilde{\mathbf{w}}_e{}^k \tag{10.6}$$

where the terms containing

$$\chi_e = \frac{e^2 n_e\Delta t^2}{m_e\varepsilon_0} \tag{10.7}$$

predict the future electron current and charge density from the following approximation of the momentum equation :

$$\tilde{\mathbf{w}}_e{}^{k+1} \approx \tilde{\mathbf{w}}_e{}^k + (e/m_e)(\mathbf{A}^{k+1} - \mathbf{A}^k + \Delta t\nabla\tilde{\Phi}^{k+1});$$

this is not as precise as the semi-implicit prediction of equation (8.8) for drift-diffusion models (e.g. the collision term has been neglected) but prevents instabilities at larger time steps without significant consequences for the accuracy, even for magnetized electrons. The actual mean velocity is calculated from a more complete momentum equation, e.g. equation (9.5) or (9.18). Each of the Maxwell equations (10.5-6) can be solved by the control volume method described in chapter 7.

Note that it is not appropriate to calculate the scalar potential $\tilde{\Phi}$ from the Lorenz condition (10.1) because this is very sensitive to numerical errors and instabilities. In a near-electrostatic case (wave length >> domain size), the second time derivatives in the Maxwell

equations are negligible and the difference between Lorenz gauge and Coulomb gauge $\nabla\cdot\mathbf{A} = 0$ vanishes. It is therefore necessary to solve $\tilde{\Phi}$ from the Maxwell-Gauss equation with the space charge density from the current conservation equation (10.4) :

$$\tilde{n}_e^{\,k+1} = \tilde{n}_e^{\,k} - e\Delta t\nabla\cdot(n_e\tilde{\mathbf{w}}_e^{\,k+1}) \,. \tag{10.8}$$

Boundary conditions

The boundary conditions for the potentials depend on the choice of gauge. In fact, the potential components can be transformed using a gauge function $\psi(\mathbf{x},t)$ as $\mathbf{A} = \mathbf{A}' + \nabla\psi$ and $\Phi = \Phi' - \partial\psi/\partial t$ without this changing the fields. Imposing the Lorenz condition (10.1), the gauge freedom is restricted to gauge functions that are solutions of the homogeneous wave equation

$$\frac{\partial^2\psi}{\partial t^2} - c^2\nabla^2\psi = 0 \,. \tag{10.9}$$

Since these solutions are uniquely determined by the boundary values, $\psi(\mathbf{x},t)$ can be freely chosen (only) at the boundaries ; hence the scalar potential Φ can be fixed to zero at the boundaries and separate boundary conditions for the different components of $\mathbf{A}$ can be derived from a physical model. For metal walls this yields : $\nabla_\perp A_\perp = 0$ and $\nabla_{/\!/} A_{/\!/} = 0$. [Jel70] However, important complications arise if the metal parts have corners ; the boundary conditions are then ill-defined at the corner points. In fact, the above electrodynamic potential method fails to account for wave scattering from any kind of metallic corner or angular surface (something that is well captured by FDTD). For similar reasons, the description of dielectric materials is complicated, involving the explicit description of magnetisation currents along the dielectric interfaces. This seriously limits the use of the electrodynamic potentials.[42]

Inductive coupling

The potential method, however, is well adapted to describe inductive coupling in radio-frequency range $\omega/2\pi$ = 1-100 MHz. Inductive discharges usually have a cylindrical axisymmetric configuration where the fields are excited by an azimuthal driving current in a coil outside the plasma. For symmetry reasons, and neglecting the magnetic force on the electrons, the fields are described by the azimuthal component of the vector potential A_ϕ alone, so only the azimuthal component of equation (10.3/6) needs to be solved.

The main difficulty in describing inductive coupling is that often the gas density is so low that the simple electron momentum equation (9.5) is not appropriate. Due to thermal motion, in the near absence of collisions, the electrons tend to travel important distances during the field periods which destroys the local relation between field and current and causes the anomalous skin effect : the skin becomes non-monotonic and much larger than expected from equation (9.10) and the electrons are heated stochastically by resonance effects. To describe this effect in detail requires electron particle-simulation, but an approximate description can be obtained by including an effective viscosity term V in the electron momentum equation :[43]

$$\frac{\partial\tilde{w}_{e,\phi}}{\partial t} + \bar{\nu}_{m,e}\tilde{w}_{e,\phi} + V = -\frac{e}{m_e}\tilde{E}_\phi = \frac{e}{m_e}\frac{\partial A_\phi}{\partial t} \tag{10.10}$$

[42] These are provisional conclusions of my personal attempts to use electrodynamic potentials to describe microwave plasmas.

[43] I developed this effective viscosity approach for an inductive negative-ion source for neutral beam injection for ITER ; the approach has been presented and analysed in two publications : [33] and [34].

$$V + \tau \frac{\partial V}{\partial t} = -\eta \left(\frac{1}{n_e} \nabla \cdot (n_e \nabla \tilde{w}_{e,\phi}) - \frac{\tilde{w}_{e,\phi}}{r^2} \right) \tag{10.11}$$

where η and τ are effective viscosity coefficients :

$$\eta = \frac{{v_T}^2}{\sqrt{\pi} k_0 v_T + (\pi - 2)\bar{\nu}_{m,e}} = \frac{{v_T}^2}{\pi - 2} \tau \tag{10.12}$$

depending on the electron thermal speed $v_T = (2eT_e/m_e)^{1/2}$ and the inverse anomalous skin depth

$$k_0 = \left(\frac{\sqrt{\pi} \omega \omega_p}{c^2 v_T} \right)^{1/3} . \tag{10.13}$$

Equations (10.10-13) have been derived from a perturbation solution of the Boltzmann equation coupled with the Maxwell-Ampere equation for a 1D semi-infinite plasma [33][34] ; it is not entirely clear to what extend the equations can capture the anomalous skin effect in multidimensional configurations.

The viscosity term V in equation (10.10) represents diffusion of the electron current due to thermal motion. Since the characteristic time of this diffusion is shorter than the wave period (in cases where the anomalous skin effect is important), it is appropriate to treat the viscosity implicitly in the momentum equation in order to avoid CFL time step constraints of the type $\eta \Delta t < \Delta x^2$. A simple way to achieve this is by semi-implicit prediction, in analogy with the method for the Maxwell equations :

$$\left(1 + \frac{\tau}{\Delta t} + \frac{\eta \Delta t}{r^2} \right) V^{k+1} - \frac{\eta \Delta t}{n_e} \nabla \cdot (n_e \nabla V^{k+1}) = \frac{\tau}{\Delta t} V^k - \eta \left(\frac{1}{n_e} \nabla \cdot (n_e \nabla \tilde{w}_{e,\phi}) - \frac{\tilde{w}_{e,\phi}}{r^2} \right)^k . \tag{10.14}$$

The prediction terms on the left-hand side (terms in $\eta \Delta t$) are obtained from simplifying the momentum equation as $\tilde{w}_{e,\phi}^{k+1} = \tilde{w}_{e,\phi}^{k} - V \Delta t$. The viscosity V^{k+1} is solved from (10.14) and then substituted explicitly in the momentum equation (10.10).

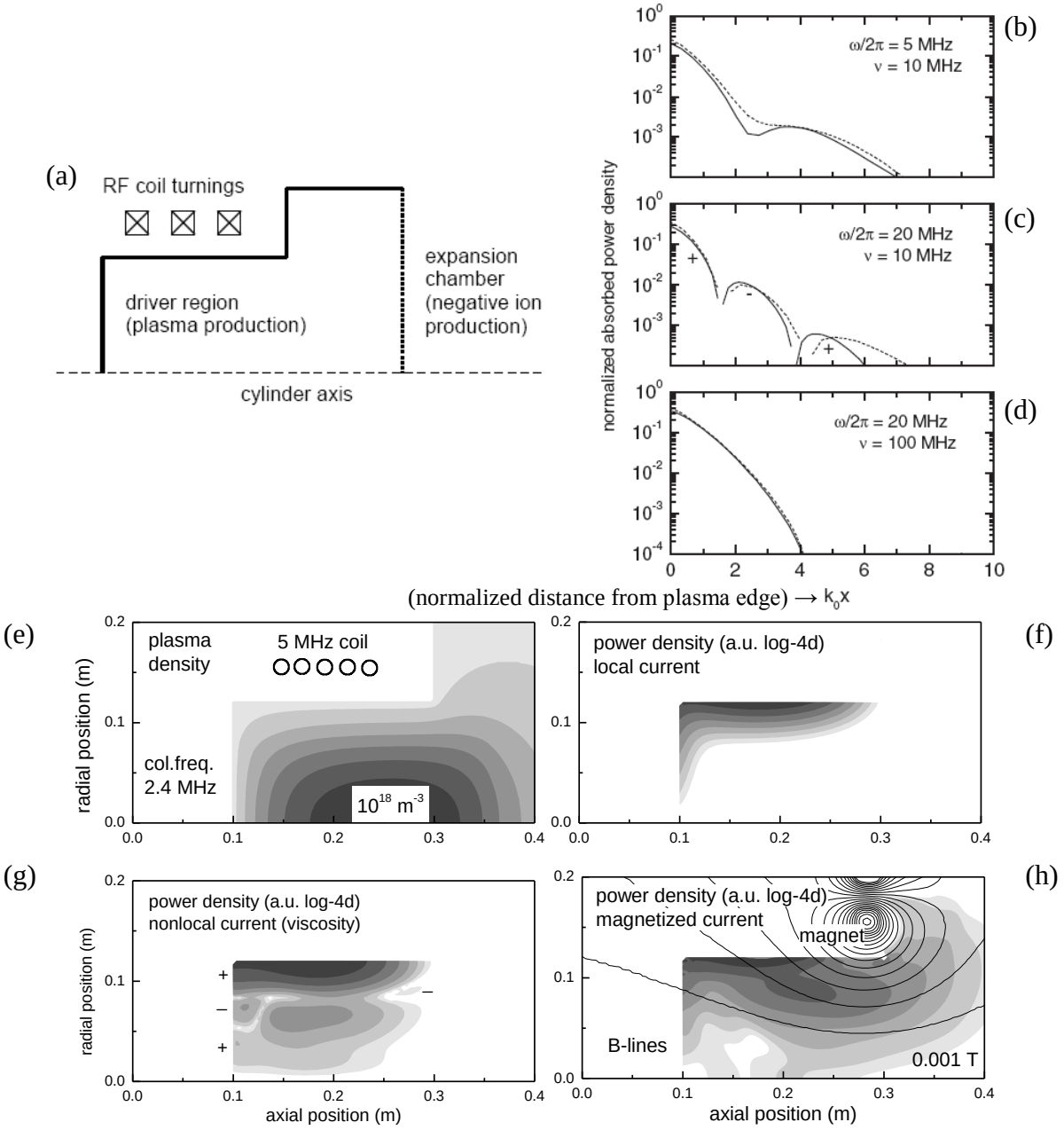

Figure 10.1. Modelling study of the energy coupling in an inductive ion source for a neutral beam injection system to heat fusion plasmas [Spe06]. The plasma is sustained in a cylindrical chamber (driver) by a radio-frequency (RF) current in a coil wound around it (figure a), which generates an RF magnetic field, which induces a azimuthal RF electric field in the plasma, which heats the electrons. Due to the low gas density (2×10^{19} m^{-3}) and driving frequency (5 MHz) the electron kinetics is strongly non-local which leads to the anomalous skin effect. In some recent publications [33][34] I have proposed to represent the non-local kinetics by an effective electron viscosity as shown in equations (10.10-13). Figure b compares the spatial power absorption profiles obtained from this equation (solid lines) with those from a more detailed particle-in-cell model (dashed lines) for a simplified semi-infinite plasma ; the effective viscosity approach seems to capture the qualitative features of the anomalous skin, including regions of negative power absorption appearing at intermediate frequency. The viscosity approach can be generalized to the more realistic two-dimensional configuration of figure c ; the plasma density, electron temperature, and collision frequency are assumed fixed. Figures e-g show the power absorption profiles from the local momentum equation (9.5), the momentum equation (10.10) with the effective viscosity term, and the magnetised momentum equation (9.18) to account for the effect of permanent magnets in the vicinity of the driver chamber ; in the latter case non-local effects seem of little importance but the magnetised electron current excites all components of the electromagnetic field which requires the solution of the full Maxwell equations (10.2-3). These results are preliminary and do not account for the effect of surrounding materials.

Chapter 11

RESEARCH PROJECT

Brief overview and scientific context of my work

During the past 12 years I have developed low-temperature plasma models for different applications on the basis of the methods presented in the previous chapters. Much of my work has been concentrated on self-consistent fluid models, in particular the coupling of electron fluid equations with the Maxwell equations in different two-dimensional configurations. I have done some work on the Boltzmann equation, mainly for the purpose of complementing the electron fluid equations, e.g. to obtain fluid coefficients (BOLSIG+ [22]) or a fluid-like representation of non-local electron heating (effective viscosity [33]). I have also developed particle models, mainly to test the validity of fluid equations or combined with fluid equations in hybrid models. I have implemented my models as numerical computer codes (FORTRAN and C) and made several contributions to the numerical methods to solve the plasma equations.

This fluid or hybrid approach corresponds to the state-of-the-art in low-temperature plasma modelling for technological applications and presents in this context significant advantages over the more fundamental PIC approach : it yields small-scale computer codes that run on a standard desktop computer within a few hours and often only a few minutes ; results are readily obtained and relatively easy to interpret in terms of elementary plasma physics. On the other hand, fluid and hybrid plasma models require physical approximations that can affect their accuracy and need to be adapted to each specific plasma configuration and to the purpose of the modelling ; it takes substantial expertise and understanding of plasma physics to achieve this.

The self-consistent fluid approach has been very successful for the microdischarge models that I developed during my Ph.D. research for Philips, providing near-quantitative agreement with experiments and being of real help for the optimisation of the discharge configuration ; similar models were intensively used in the late 1990s by the television industry worldwide for the development of flat television [Boe03].

For many low-temperature plasmas, however, modelling is subject to two kinds of complications. First, in molecular gases or gas mixtures, especially at higher pressure, the plasma chemistry and excitation kinetics are very complex, involving hundreds of species and processes for which hardly any data are available ; this is the main challenge in the modelling of atmospheric discharges or chemical processing plasmas. Second, at low pressure the validity of the fluid approach breaks down because the mean free path is not negligible with respect to the macroscopic length scales, e.g. the energy distribution is distorted by non-local effects, the pressure tensor is not diagonal, etc ; in addition the fluid equations tend to be more difficult to solve numerically due to inertia terms, anisotropy, etc. In principle low-pressure plasmas can be properly simulated by PIC models, but this is practically feasible only for the simplest configurations and often not very effective for technological purposes.

This second complication has been (and will continue to be) a major focus in much of my work at the LAPLACE. The fluid and hybrid models I developed for the low-pressure (magnetized) plasmas of Hall-effect thrusters, electron-cyclotron-resonance sources, and

inductive ion sources, provide an approximate description of the plasma ; they are extremely useful to get insight in some of the main principles of the discharge operation but it is not clear to what extend their results are quantitatively accurate ; e.g. the hybrid Hall-effect thruster model has limited predictive capabilities because it fails to describe anomalous electron transport across the magnetic field due to microscopic field fluctuations. One of the main goals I have identified for my future research is to improve the modelling of low-pressure (magnetized) low-temperature plasmas.

Organisational context

Most of the work that I did after my Ph.D. has been part of the research of the group GREPHE[44] at the LAPLACE. This research group, founded and directed by Jean-Pierre Boeuf and Leanne Pitchford and currently comprising 14 permanent staff members (7 on plasma research), is one of the leading groups worldwide in modelling of low-temperature plasmas for technological applications. Over the years I have gradually taken up more and more responsibilities in the group ; I have developed many of the models currently used by the group and implemented the corresponding FORTRAN codes ; I am responsible for the physical and numerical pertinence of these models and work intensively with the Ph.D. students and researchers who use them (see the end of the introductory chapter). I expect to continue along these lines in the next few years.

My current research activities are concentrated around two projects of the group GREPHE, concerning inductive negative-ion sources for neutral-beam injection and multi-dipolar electron-cyclotron-resonance sources. These two projects form the basis of my personal research project for the near future and are described more in detail in the next few sections.

Project part 1 : Negative-ion sources for neutral beam injection

The group GREPHE has been involved in the modelling of these sources since end 2006 through several contracts with the CEA/EURATOM Cadarache and has recently become associated with the Fédération de Recherche Fusion Magétique ITER[45] ; in addition the group takes part in the ANR project ITER-NIS[46] that will start in November 2008. Negative-ion sources are necessary for the generation of fast neutral beams (> 200 keV) that are used to heat fusion plasmas and drive the plasma current that ensures their magnetic confinement. The eventual aim of the modelling work of GREPHE is to obtain a complete self-consistent model of a source proposed by the IPP Garching [Spe06] to produce negative hydrogen and deuterium ions at low gas pressure (< 0.3 Pa) and high current density (> 200 A/m^2) and which is currently under development for the ITER fusion project. The plasma is generated by an inductive discharge at radio-frequency and then diffuses into the source body where permanent magnetic fields filter out the fast electrons. The negative ions are created in the plasma volume by electron attachment to high vibrational hydrogen states and by plasma-wall interactions involving caesium ; they are extracted from the plasma by a system of extraction grids and magnetic fields, accelerated to high velocities, neutralised, and finally injected into

[44] Groupe de Recherche Energétique, Plasma, Hors-Equilibre
[45] The Fédération Nationale de Recherche Fusion par Confinement Magnétique - ITER is a French organisation created in April 2008 on the initiative of the CNRS, CEA, INRIA, universities of Aix-Marseilles, Nice, Nancy, and Ecole Polytechnique, in order to coordinate the French research related to the ITER project.
[46] ITER Negative Ion Source research project ; project number : BLAN08-2_310122

the fusion plasma. The modelling of this source is extremely challenging and will require several years of research and development.

During the first year (2007), the ion-source modelling project was fully managed by myself ; I developed a 2D fluid model of the inductive discharge which I am currently extending to describe the magnetized plasma in the source body ; preliminary results from this model show the depletion of neutrals in the discharge volume and compression of the plasma by the driving field (ponderomotive force). By the end of 2007, post-doctoral researcher Stanimir Kolev joined the project ; he is developing a 1D PIC model of plasma transport through the magnetic filter in order to check and complement the 2D fluid model. Early 2008, the CNRS recruited the associate researcher Gweneal Fubiani on the project ; he is currently studying the volume and surface chemistry of the source and collecting the necessary data from different international groups. October 2008, Ph. D. student Nicolas Kohen will join the project ; he will start by using the 2D fluid model in realistic source conditions and making systematic comparisons with all available experimental data from the IPP Garching.

For the moment the 2D fluid model will be at the heart of our modelling activities and serve as a framework for the description of the source as a whole. I will be in charge of this model and the integration of the more detailed works of S. Kolev and G. Fubiani ; I will also strongly participate in the supervision of N. Kohen.

Project part 2 : Multidipolar plasmas

Since November 2006, the group GREPHE is involved in the ANR project PLASMODIE[47] aiming at the development of a new generation of microwave-plasma reactors operating in a wide pressure and frequency range, piloted by the experimental group CRPMN[48] of Jacques Pelletier in Grenoble. The role of GREPHE in this project is to develop models to accompany the experimental development and guide performance optimisation. The modelling work is mainly focused on the description of so-called dipolar sources (antennas) which can be used in a network to generate the plasma at the reactor wall. A single dipolar source consists of a permanent magnet, trapping fast electrons in an axisymmetric dipole field, and a microwave applicator, heating the trapped electrons by cyclotron resonance (ECR).

Until recently, I managed this project by myself ; I have developed a self-consistent 2D model describing the resonant microwave coupling and the plasma transport and chemistry of a single dipolar source. Further development and exploitation of this model and confrontation with experimental results will be done together with the post-doctoral researcher Kremena Makasheva.

Project part 3 : Model unification

The above plasmas (of the negative-ion source and multi-dipolar source) present many similarities with the plasma of Hall-effect thrusters studied by GREPHE for over 10 years : the electrons are trapped in steady magnetic fields, the ions are not magnetised and nearly collisionless, etc. Hence also the models that I developed for these different applications are in part similar, e.g. they are all based on anisotropic drift-diffusion equations for magnetised

[47] PLASmas Micro-Onde DIstribués à conditions opératoires Etendues ; project number ANR-06-BLAN-0177.
[48] Centre de Recherche Plasmas-Matériaux-Nanostructures

electrons in 2D cylindrical space. In the near future I intend to combine these different models into one general model for magnetised low-temperature plasmas, which can then be used to study also other types of magnetised plasma sources, e.g. magnetrons and so-called Kaufmann sources used in the industry. Applying such a general model to many different sources and systematically comparing the results with the experimental data available for each of them will be of great interest to asses the validity and limitations of the fluid approach for magnetised electrons.

In parallel to the unification of the existing models based on electron fluid equations, it is important to explore other more detailed modelling methods such as PIC in order to check, complement, and if necessary replace the electron fluid equations. Among the questions that need to be investigated are the description of the magnetic mirror force and its effect on the magnetised plasma transport, the tail of the electron energy distribution function and its effect on the plasma chemistry, etc. In this context a new Ph. D. student has been recruited as from October 2008, Nourredine Oudini, whom I will supervise and who will help me with the general improvement of our magnetised low-temperature plasma models.

In addition to my activities on the modelling of magnetized plasmas for the negative-ion source and the multi-dipolar source, I will continue to participate in several other research projects of the group GREPHE such as the RTRA[49] project PLASMAX[50] on microwave plasmas for aerospace applications and the ANR project on micro-hollow cathode discharges (see introduction).

[49] Réseau Thématique de Recherche Avancée = French national research program
[50] Full project title : Modélisation des interactions microondes/plasma pour des applications aérospatiales

LITERATURE

[Bir94] G. A. Bird, Molecular gas dynamics and the direct simulation of gas flows (Clarendon Press, Oxford, 1994).

[Bir91] C. K. Birdsall and A. B. Langdon, Plasma physics via computer simulation (Taylor & Francis, New York, 1991).

[Bit04] J. A. Bittencourt, Fundamentals of plasma physics, third edition, (Springer, New York, 2004).

[Bla08] A. Blanc, J. Phys. **7**, 825 (1908).

[Boe03] J. P. Boeuf, *Plasma display panels: physics, recent developments and key issues*, J. Phys. D: Appl. Phys. **36**, R53-R79 (2003).

[Boe95] J.-P. Boeuf and L. C. Pitchford, *Two-dimensional model of a capacitively coupled rf discharge and comparison with experiments in the Gaseous Electronics Conference reference cell*, Phys. Rev. E **51**, 1376-1390 (1995).

[Bro66] S. C. Brown, Basic data of plasma physics (MIT Press, Cambridge MA, 1966).

[Cha87] P. J. Chantry, *A simple formula for diffusion calculations involving wall reflection and low density*, J. Appl. Phys. **62** (4), 1141-1148 (1987).

[Che84] F. C. Chen, Introduction to plasma physics and controlled fusion, second edition (Plenum Press, New York, 1984).

[Cri07] P. Crispel, P. Degond, M.-H. Vignal, *An asymptotic preserving scheme for the two-fluid Euler-Poisson model in the quasineutral limit*, J. Comp. Phys. **223** (1), 208-234 (2007).

[Ell76] H. W. Ellis, R. Y. Pai, E. W. McDaniel, A. Mason, and L. A. Viehland, *Transport properties of gaseous ions over a wide energy range*, Atomic Data and Nuclear Data Tables **17**, 177-210 (1976); and updates in the same journal: **22**, 179 (1978); **31**, 113 (1984); **60**, 37 (1995).

[Fra00] R. N. Franklin, *Plasmas with more than one species of positive ion and the Bohm criterion*, J. Phys. D: Appl. Phys. **33**, 3189-3189 (2000).

[Gün05] S. Günter, Q. Yu, J. Krüger, K. Lackner, *Modelling of heat transport in magnetised plasmas using non-aligned coordinates*, J. Comp. Phys. **209**, 354-370 (2005).

[Hay81] M. Hayashi, *Recommended values of the transport cross sections for elastic collision and total collision cross section for electrons in atomic and molecular gases*, report IPPJ-AM-19, Institute of Plasma Physics, Nagoya University Japan (1981).

[Hun92] F. Hunsberger, R. Luebbers, and K. Kunz, *Finite-difference time-domain analysis of gyrotropic media – I: magnetized plasma*, IEEE Trans. Antennas and Propagation **40** (12), 1489-1495 (1992).

[Jel70] L. F. Jelsma, E. D. Tweed, R. L. Phillips, and R. W. Taylor, *Boundary conditions for the four vector potential*, IEEE Trans. Microwave Theory and Techniques, September 1970, 648-649 (1970).

[Kor96] U. Kortshagen, C. Busch, and L. D. Tsendin, *On simplifying approaches to the solution of the Boltzmann equation in spatially inhomogeneous plasmas*, Plasma Sources Sci. Technol. **5**, 1-17 (1996).

[Kun93] K. S. Kunz and R. J. Luebbers, The finite difference time domain method for electromagnetics (CRC, Boca Raton, Florida USA 1993).

[Lan83] A. B. Langdon, B. I. Cohen, and A. Friedman, *Direct implicit large time-step particle simulation of plasmas*, J. Comp. Phys. **51**, 107-138 (1983).

[Lee99] J. H. Lee and D. K. Kalluri, *Three-dimensional FDTD simulation of electromagnetic wave transformation in a dynamic inhomogeneous magnetized plasma*, IEEE Trans. Antennas and Propagation **47** (7), 1146-1151 (1999).
[Lie05] M. A. Lieberman and A. Lichtenberg, Principles of plasma discharges and materials processing, second edition (John Wiley & Sons Inc. USA, 2005).
[Meu95] J. Meunier, Ph. Belenguer, and J.-P. Boeuf, *Numerical model of an ac plasma display panel cell in neon-xenon mixtures*, J. Appl. Phys. **78**, 731 (1995).
[Mur81] G. Mur, *Absorbing boundary conditions for the finite-difference approximation of the time domain electromagnetic field equations*, IEEE Trans. Electromagnetic Compatibility EMC **23**(4), 377-382 (1981).
[Nan97] K. Nanbu, *Theory of cumulative small-angle collisions in plasmas*, Phys. Rev. E **55** (4), 4642-4652 (1997).
[Nan00] K. Nanbu, *Probability theory of electron-molecule, ion-molecule, molecule-molecule, and Coulomb collisions for particle modelling of materials processing plasmas and gases*, IEEE Trans. Plasma Sci. 28 (3), 971-990 (2000).
[Phe94] A. V. Phelps, *The application of scattering cross sections to ion flux models in discharge sheaths*, J. Appl. Phys. 76 (2), 747-753 (1994).
[Pis03] D. Piscitelli, A. V. Phelps, J. de Urqujio, E. Basurto, and L. C. Pitchford, *Ion mobilities in Xe/Ne and other rare gas mixtures*, Phys. Rev. E **68**, 046408 (2003).
[Rai91] Y. P. Raizer, Gas discharge physics (Springer-Verlag Berlin, 1991).
[Rax05] J.-M. Rax, Physique des plasmas (Dunod, Paris, 2005).
[Rei65] F. Reif, Fundamentals of statistical and thermal physics (McGraw-Hill Kogakusha, Ltd, Tokyo, 1965).
[Roc73] S. D. Rockwood, *Elastic and inelastic cross sections for electron-Hg scattering from Hg transport data*, Phys. Rev. A 8 (5), 2348-2358 (1973).
[Sch69] D. L. Scharfetter and H. K. Gummel, *Large-signal analysis of a silicon Read diode oscillator*, IEEE Trans. Electron. Devices ED **16**, 64 (1969).
[Sch81] G. E. Schneider and M. Zedan, *A modified strongly implicit procedure for the numerical solution of field problems*, Numerical Heat Transfer **4**, 1-19 (1981).
[Sku68] H. R. Skullerud, *The stochastic computer simulation of ions in a gas subjected to a constant electric field*, J. Phys. D2 **1**, 1567-1568 (1968).
[Spe06] E. Speth, H. D. Falter, F. Franzen, U. Fantz, M. Bandyopadhyay, S. Christ, A. Encheva, M. Fröschle, D. Holtum, B. Heinemann, W. Kraus, A. Lorenz, Ch. Martens, P. McNeely, S. Obermayer, R. Reidl, R. Süss, A. Tanga, R. Wilhelm, and D. Wünderlich, *Overview of the RF source development programme at IPP Garching*, Nucl. Fusion **46**, S220-S228 (2006).
[Tur06] M. M. Turner, *Kinetic properties of particle-in-cell simulations compromised by Monte Carlo collisions*, Phys. Plasmas **13**, 033506 (2006).
[Vah95] V. Vahedi and M. Surendra, *A Monte Carlo collision model for the particle-in-cell method: applications to argon and oxygen discharges*, Computer Physics Communications 87, 179-198 (1995).
[Ven93] P. L. G. Ventzek, T. J. Sommerer, R. J. Hoekstra, and M. J. Kushner, *Two-dimensional hybrid model of inductively coupled plasmasources for etching*, Appl. Phys. Lett. **63**, 605-607(1993).
[Ver05] J. P. Verboncoeur, *Particle simulation of plasmas: review and advances*, Plasma Phys. Control. Fusion **47**, A231-A260 (2005).

INTERNATIONAL REFEREED JOURNAL PUBLICATIONS

my name simply underlined
names of students whom I have supervised doubly underlined

[1] G. J. M. Hagelaar and G. M. W. Kroesen, *Implementing arbitrarily shaped boundaries in two-dimensional discharge modeling*, IEEE Trans. Plasma Sci. **27** (6), 1606-1609 (1999).

[2] G. J. M. Hagelaar and G. M. W. Kroesen, *Speeding up fluid models for gas discharges by implicit treatment of the electron energy source term*, J. Comput. Phys. **159**, 1-12 (2000).

[3] G. J. M. Hagelaar, F. J. de Hoog, and G. M. W. Kroesen, *Boundary conditions in fluid models of gas discharges*, Phys. Rev. E **62** (1), 1452-1454 (2000).

[4] G. J. M. Hagelaar, G. M. W. Kroesen, U. van Slooten, and H. Schreuders, *Modeling of the microdischarges in plasma addressed liquid crystal displays*, J. Appl. Phys. **88** (5), 2252-2262 (20070).

[5] G. J. M. Hagelaar, G. M. W. Kroesen, and M. H. Klein, *Energy distribution of ions and fast neutrals in microdischarges for display technology*, J. Appl. Phys. **88** (5), 2240-2245 (2000).

[6] M. H. Klein, R. J. M. M. Snijkers, and G. J. M. Hagelaar, *Energy loss mechanisms in AC-PDP discharges*, IEICE Transactions **E83-C** (10), 1602-1607 (2000).

[7] G. J. M. Hagelaar and G. M. W. Kroesen, *A Monte Carlo modeling study of the electrons in the microdischarges in plasma addressed liquid crystal displays*, Plasma Sources Sci. Techn.. **9** (4), 605-614 (2000).

[8] G. J. M. Hagelaar, M. H. Klein, R. J. M. M. Snijkers, and G. M. W. Kroesen, *Resonance radiation transport in plasma display panels*, J. Appl. Phys. **88** (10), 5538-5542 (2000).

[9] G. J. M. Hagelaar, M. H. Klein, R. J. M. M. Snijkers, and G. M. W. Kroesen, *Energy loss mechanisms in the microdischarges in plasma display panels*, J. Appl. Phys. **89** (4), 2033-2039 (2001).

[10] G. J. M. Hagelaar, J. Bareilles, L. Garrigues, and J.-P. Boeuf, *Two-dimensional model of a stationary plasma thruster*, J. Appl. Phys. **91** (9), 5592-5598 (2002).

[11] G. J. M. Hagelaar and L. C. Pitchford, *Estimated mass loss due to evaporation for zinc cathodes in analytical glow discharges*, J. Anal. Atom. Spectroscopy **17** (10), 1408-1410 (2002).

[12] G. J. M. Hagelaar, J. Bareilles, L. Garrigues, and J.-P. Boeuf, *Role of anomalous electron transport in a stationary plasma thruster simulation*, J. Appl. Phys. **93** (1) , 67-75 (2003).

[13] L. Garrigues, G. J. M. Hagelaar, J. Bareilles, C. Boniface, and J.-P. Boeuf, *Model study of the influence of the magnetic field configuration on the performance and lifetime of a Hall thruster*, Phys. Plasmas **10** (12), 1-7 (2003).

[14] G. J. M. Hagelaar, J. Bareilles, L. Garrigues, and J.-P. Boeuf, *Modelling of stationary plasma thrusters*, Contrib. Plasma Phys. **44** (5-6), 529-535 (2003).

[15] D. Hayashi, G. Heusler, G. Hagelaar, and G. Kroesen, *Discharge efficiency in high-Xe-content plasma display panels*, J. Appl. Phys. **93** (4), 1656-1661 (2004).

[16] J. Bareilles, G. J. M. Hagelaar, L. Garrigues, C. Boniface, and J.-P. Boeuf, *Critical assessment of a two-dimensional hybrid Hall thruster model: Comparisons with experiments*, Phys. Plasmas **11** (6), 3035-3046 (2004).

[17] G. J. M. Hagelaar, K. Hassouni, and A. Gicquel, *Interaction between the electromagnetic fields and the plasma in a microwave plasma reactor*, J. Appl. Phys. **96** (4), 1819-1828 (2004).

[18] L. Garrigues, G. J. M. Hagelaar, C. Boniface, and J.-P. Boeuf, *Optimized atom injection in a Hall effect thruster*, Appl. Phys. Lett., 85 (22), 5460-5462 (2004).
[19] A. Meige, R. Boswell, C. Charles, G. J. M. Hagelaar, J.-P. Boeuf, and M. M. Turner, *One-dimensional simulation of an ion beam generated by a current-free double-layer*, IEEE Trans. Plasma Sci. **33** (2), 334-335 (2005).
[20] G. J. M. Hagelaar and S. Villeger, *Simulation of geometrical effects on surface wave discharges*, IEEE Trans. Plasma Sci. **33** (2), 496-497 (2005).
[21] C. Boniface, G. J. M. Hagelaar, L. Garrigues, and J.-P. Boeuf, *Modeling of Double Stage Hall Effect Thrusters*, IEEE Trans. Plasma Sci. **33** (2), 522-523 (2005).
[22] G. J. M. Hagelaar and L. C. Pitchford, *Solving the Boltzmann equation to obtain electron transport coefficients and rate coefficients for fluid models*, Plasma Sources Sci. Technol. **14**, 722-733 (2005).
[23] K. Hassouni, G. Lombardi, X. Duten, G. Hagelaar (misspelled: Haagelar), F. Silva, A. Gicquel, T. A. Grotjohn, M. Capitelli, and J. Röpcke, *Overview of the different aspects in modeling moderate pressure H_2 and H_2/CH_4 microwave discharges*, Plasma Sources Sci. Technol. **15**, 117-125 (2006).
[24] C. Boniface, L. Garrigues, G. J. M. Hagelaar, J.-P. Boeuf, D. Gawron, and S. Mazouffre, *Anomalous cross field electron transport in a Hall effect thruster*, Appl. Phys. Lett. **89**, 161503 (2006).
[25] E. Muñoz-Serrano, G. Hagelaar, Th. Callegari, J. P. Boeuf and L. C. Pitchford, *Properties of plasmas generated in microdischarges*, Plasma Physics and Controlled Fusion (2006).
[26] L. Garrigues, G. J. M. Hagelaar, C. Boniface, and J.-P. Boeuf, *Anomalous conductivity and secondary emission in Hall effect thrusters*, J. Appl. Phys. **100** 132301 (2006).
[27] G. J. M. Hagelaar, *Modelling electron transport in magnetized discharge plasmas*, Plasma Sources Sci. Technol. **16**, S57-S66 (2007).
[28] A. Meige, N. Plihon, G. Hagelaar, J.-P. Boeuf, P. Chabert and R. W. Boswell, *Propagating double-layer in electronegative plasmas*, Phys. Plasmas **14**, 053508 (2007).
[29] G. J. M. Hagelaar, *How to normalize Maxwell-Boltzmann electrons in transient plasma models*, J. Comp. Phys. **227**, 871-876 (2007).
[30] J. Perez-Luna, G. J. M. Hagelaar, L. Garrigues, and J.-P. Boeuf, *Model analysis of a double-stage Hall effect thrusters with double-peaked magnetic field and intermediate electrode*, Phys. Plasmas **14**, 113502 (2007).
[31] K. Makasheva, E. Muñoz-Serrano, G. Hagelaar, J.-P. Boeuf, and L. C. Pitchford, *A better understanding of microcathode sustained discharges*, Plasma Phys. Control. Fusion **49**, B233-B238 (2007).
[32] P. Sarrailh, L. Garrigues, G. J. M. Hagelaar, G. Sandolache, S. Rowe, B. Jusselin, and J.-P. Boeuf, *Expanding sheath in a bounded plasma in the context of the post-arc phase of a vacuum arc*, J. Phys. D: Appl. Phys. **41**, 015203 (2008).
[33] G. J. M. Hagelaar, *Effective viscosity approach for non-local electron kinetics in inductively coupled plasmas*, Phys. Rev. Lett. **100**, 025001 (2008).
[34] G. J. M. Hagelaar, *Fluid description of non-local electron kinetics in inductively coupled plasmas*, Plasma Sources Sci. Technol. **17**, 025017 (2008).
[35] N. Balcon, G. J. M. Hagelaar, and J. P. Boeuf, *Numerical model of an argon atmospheric pressure RF discharge*, IEEE Trans. Plasma Sci. 36 (5) 2782-2787 (2008).
[36] J. Pérez-Luna, N. Dubuit, L. Garrigues, G. Hagelaar, J. P. Boeuf, *Electron trajectories in a Hall effect thruster*, IEEE Trans. Plasma Sci. **36** (4) 1212-1213 (2008).
[37] K. Makasheva, G. Hagelaar, J.-P. Boeuf and L. C. Pitchford, *Ignition of microcathode sustained discharge*, IEEE Trans. Plasma Sci. **36** (4) 1236-1237 (2008).

[38] P. Sarrailh, L. Garrigues, G. J. M. Hagelaar, J.-P. Boeuf, G. Sandolache, S. Rowe, and B. Jusselin, *Two dimensional simulation of the post-arc phase of a vacuum arc circuit breaker*, IEEE Trans. Plasma Sci. **36** (4) 1046-1047 (2008).
[39] J. C. Adam, J. P. Boeuf, N. Dubuit, M. Dudeck, L. Garrigues, D. Gresillon, A. Heron, G. Hagelaar, V. Kulaev, N. Lemoine, S. Mazouffre, J. Perez-Luna, V. Pisarev, S. Tsikata, *Physics, simulation, and diagnostics of Hall effect thrusters*, Plasma Phys. Control. Fusion **50** 124041 (2008).
[40] J. Pérez-Luna, G. J. M. Hagelaar, L. Garrigues, and J. P. Boeuf, *Method to obtain the electric field and the ionisation frequency from laser induced fluorescence measurements*, Plasma Sources Sci. Technol. (accepted).
[41] L. Garrigues, C. Boniface, G. J. M. Hagelaar, and J. P. Boeuf, *Performance modelling of a thrust vectoring device for Hall effect thrusters*, (submitted).
[42] L. Garrigues, G.J.M. Hagelaar, J.P. Boeuf, Y. Raitses, A. Smirnov, and N.J. Fisch, *Simulations of a Miniaturized Cylindrical Hall Thruster***,** IEEE Trans. Plasma Sci. **36** 2034 (2008).
[43] D. Mihailova, M. Grozeva, G. J. M. Hagelaar, J. van Dijk, W. J. M. Brok, and J. J. A. M. van der Mullen, *A flexible platform for simulations of sputtering hollow cathode discharges for laser applications*, accepted J. Phys. D: Appl. Phys. (2008).
[44] L. Garrigues, C. Boniface, G. J. M. Hagelaar, and J.-P. Boeuf, *Modeling of an advanced concept of double stage Hall effect thruster*, Phys. Plasmas **15** 113502 (2008).

Annexe A

CURRICULUM VITAE

Pour la description du contenu scientifique de mes activités voir la fin du chapitre 1.

Candidat
Nom : HAGELAAR
Prénom : Gerardus Johannes Maria (Gerjan)
Née le : 8 avril 1973
Nationalité : néerlandaise
Fonctions : ingénieur de recherche CNRS, laboratoire LAPLACE, Toulouse
Doctorat obtenu le 13 novembre 2000 (Pays-Bas)
Autre diplôme : ingénieur (≈ M. Sc., Université Eindhoven, Pays-Bas)

I – Parcours universitaire
09/1991 – 12/1996 : technische natuurkunde, Technische Universiteit Eindhoven, Pays-Bas
09/1994 – 09/1996 : propaedeuse psychologie, Katholieke Univ. Brabant, Tilburg, Pays-Bas
02/1997 – 11/2000 : doctorat, Technische Universiteit Eindhoven, Pays-Bas

II – Parcours professionnel
02/2001 – 12/2002 : post-doctorant, Centre de Physique des Plasmas et Applications de Toulouse (CPAT), UMR 5002, Université Paul Sabatier, Toulouse.
01/2003 – 12/2003 : ingénieur de recherche CNRS contractuel, Laboratoire d'Ingénierie des Matériaux et des Hautes Pressions (LIMHP), UPR 1311, Université Paris 13, Villetaneuse.
01/2004 – 11/2004 : ingénieur de recherche contractuel, CPAT, UMR 5002, Université Paul Sabatier, Toulouse.
12/2004 – présent : ingénieur de recherche CNRS, CPAT puis Laboratoire Plasma et Conversion d'Energie (LAPLACE), UMR 5213, Université Paul Sabatier, Toulouse.

III – Activités d'enseignement
Intervenant du cours "Sources de plasma et applications" du DEA "Ingénierie des plasmas de décharge" en 2004, 2005, et 2006 (quelques heures seulement)

IV – Activités de recherche
Publications internationales : 44 (42 paru, 19 premier auteur, 4 seul auteur)
Publications nationales : 1
Proceedings à des congrès internationaux : 73
Chapitres d'ouvrage : 0
Conférences invitées à des congrès internationaux (en orateur) : 5
Autres présentations orales à des congrès internationaux : 5
Séminaires : 16

V – Activités d'encadrement
(les publications communes sont citées de la liste exhaustive dans la section précédente)
1. **Jérôme Bareilles**, doctorant 02/2001 – 12/2002, co-encadrement 1/3 + jury de thèse + 5 publications internationales [10] [12] [13] [14] [16] et 6 conférences communes p. ex. J. Bareilles, G. J. M. Hagelaar, L. Garrigues, C. Boniface, and J.-P. Boeuf, *Critical*

assessment of a two-dimensional hybrid Hall thruster model: Comparisons with experiments, Phys. Plasmas **11** (6), 3035-3046 (2004).

2. **Claude Boniface**, doctorant 09/2002 – 02/2006, co-encadrement 1/3 + jury de thèse + 7 publications internationales [13] [16] [18] [21] [24] [26] [41] et 8 conférences communes p. ex. C. Boniface, G. J. M. Hagelaar, L. Garrigues, and J.-P. Boeuf, *Modeling of Double Stage Hall Effect Thrusters*, IEEE Trans. Plasma Sci. **33 (**2), 522-523 (2005).
3. **Albert Meige**, doctorant 01/2003 – 09/2006, co-encadrement 1/3 + jury de thèse + 2 publications internationales [19] [28] et 9 conférences communes p. ex. A. Meige, N. Plihon, G. Hagelaar, J.-P. Boeuf, P. Chabert and R. W. Boswell, *Propagating double-layer in electronegative plasmas*, Phys. Plasmas **14**, 053508 (2007).
4. **Nicolas Balcon**, doctorant 2004 – 11/2007, co-encadrement 1/3 + jury de thèse + 1 publication internationale [35] et 1 conférence communes : N. Balcon, G. J. M. Hagelaar, and J. P. Boeuf, *Numerical model of an argon atmospheric pressure RF discharge*, IEEE Trans. Plasma Sci. (submitted).
5. **Jaime Pérez-Luna**, doctorant 09/2005 – présent, co-encadrement 1/3 + 4 publications internationales [30] [36] [39] [40] et 7 conférences communes p. ex. J. Perez-Luna, G. J. M. Hagelaar, L. Garrigues, and J.-P. Boeuf, *Model analysis of a double-stage Hall effect thrusters with double-peaked magnetic field and intermediate electrode*, Phys. Plasmas **14**, 113502 (2007).
6. **Boris Legradic**, stagiaire master-2 03/2005 – 06/2005, encadrement 100%

VI – Autres

- Séjour à l'Australian National University (ANU) à Canberra, Australie, en février-mars 2005, dans le cadre de l'encadrement de A. Meige et N. Balcon, doctorants en co-tutelle
- Arbitrage pour des revues internationales: J. Appl. Phys., J. Comp. Phys., IEEE Trans. Plasma Sci., J. Phys. D, Phys. Plasmas, Plasma Source Sci. Technol., etc.

Annexe B

AUTRES PUBLICATIONS ET COMMUNICATIONS

mon nom sous-ligné
noms des étudiants encadrés doublement sous-lignés

Publications dans des revues internationales avec comité de lecture sont données dans la section INTERNATIONAL REFEREED JOURNAL PUBLICATIONS

Publications dans des revues nationales

1. L. Garrigues, J. Perez-Luna, G. J. M. Hagelaar, N. Dubuit, J. P. Boeuf, *Propulsion à plasma : vers de nouveaux concepts pour les missions du futur*, Revue de l'Electricité et de l'Electronique **4**, 53 (2008).

Conférences invitées à des congrès internationaux (en orateur)

1. G. J. M. Hagelaar, *Modeling stationary plasma thrusters*, 26th International Conference on Phenomena of Ionized Gases (ICPIG), 15-20 juillet 2003, Greifswald, Allemagne.
2. G. J. M. Hagelaar, *Modelling electron transport in magnetized discharge plasmas*, 18th Europhysics Conference on Atomic & Molecular Physics of Ionized Gases (ESCAMPIG), 12-16 juillet 2006, Lecce, Italie.
3. G. J. M. Hagelaar, *Hybrid models of magnetized discharge plasmas: fluid electrons + particle ions*, Conference on Computational Physics (CCP), 29 août -1 septembre 2006, Gyeongju, République de Corée.
4. G. J. M. Hagelaar, J. P. Boeuf, A. Simonin, *Modelling of a high power icp source for negative ion production*, 18th International Symposium on Plasma Chemistry (ISPC), 26-31 août 2007, Kyoto, Japon.
5. G. J. M. Hagelaar, J. P. Boeuf, A. Simonin, *Inductive plasma sources for H- for ITER*, International Conference on Research and Applications of Plasmas (PLASMA2007), 16-19 octobre 2007, Greifswald, Allemagne.

Autres présentations orales à des congrès internationaux

1. G. Hagelaar and G. Kroesen, *Modeling of micro-discharges in plasma addressed liquid crystal (PALC) displays*, 2nd Workshop on the Exploration of Low Temperature Plasma Physics, décembre 1999, Rolduc, Kerkrade, Pays-Bas.
2. G. Hagelaar and G. Kroesen, *Modeling of micro-discharges in plasma addressed liquid crystal (PALC) displays*, 52nd Gaseous Electronics Conference, 5-8 octobre 1999, Norfolk, Virginia, USA.
3. G. Hagelaar, J. Bareilles, L. Garrigues, and J.-P. Boeuf, *Parametric study of a stationary plasma thruster using a two-dimensional hybrid model*, 27th International Electronic Propulsion Conference, papier IEPC-01-28, 15-19 octobre 2001, Pasadena, California, USA.
4. G. J. M. Hagelaar, K. Hassouni, and A. Gicquel, *Interaction between the electromagnetic field and the plasma in a microwave plasma reactor*, 15th International Conference on Gas Discharges and their Applications, 5-10 septembre 2004, Toulouse, France.
5. G. J. M. Hagelaar, *Modeling energy coupling in nonequilibrium plasmas: Limits of the fluid description*, 15th International Conference on Gas Discharges and their Applications, 5-10 septembre 2004, Toulouse, France.

Seminaires (en orateur)

1. *Modeling of microdicharges in plasma-addressed-liquid-crystal displays*, novembre 1999, Philips Nat. Lab., Eindhoven, Pays-Bas.
2. *Two-dimensional model of a stationary plasma thruster*, 23 septembre 2002, Ecole Polytechnique Fédérale de Lausanne (EPFL), Suisse.
3. *Model of a stationary plasma thruster*, 8 novembre 2002, Dublin City University, Irlande.
4. *Modelling of a stationary plasma thrusters*, 28 aout 2003, Technische Universiteit Eindhoven, Pays-Bas.
5. *Modélisation auto-cohérente des plasmas micro-onde*, 5 janvier 2004, Laboratoire d'Ingénierie des Matériaux et des Hautes Pressions (LIMHP), Université Paris 13, Villetaneuse, France.
6. *Modélisation auto-cohérente des plasmas micro-onde*, 9 janvier 2004, ONERA Toulouse, France.
7. *Modélisation des plasmas hors équilibre*, Journée plasma - écoulement, mars 2004, Toulouse, France.
8. *Description fluide dans des conditions de forte anisotropie du transport électronique*, Séminaire du GDR Propulsion Plasma, 22 septembre 2005, Paris, France.
9. *Collisionless plasmas with magnetized electrons: some modeling problems*, 19 décembre 2005, Centrum voor Wiskunde en Informatica (CWI), Amsterdam, Pays-Bas.
10. *Modelling electron transport in magnetized discharge plasmas*, séminaire GDR propulsion plasma, 20 septembre 2006, Cadarache, France.
11. *Hybrid models of magnetized discharge plasmas: fluid electrons + particle ions*, 18 décembre 2006, Institut de Mathématiques de Toulouse (IMT), France.
12. *Chauffage électronique dans un champ alternatif*, 15 mars 2007, séminaire 3EP, Toulouse, France.
13. *Modélisation source HF*, 23 octobre 2007, réunion CEA-CNRS-Université injecteurs de neutres à base d'ions négatifs pour ITER, CEA Cadarache, France.
14. *Modelling of a high power icp source for negative ion production*, 5 novembre 2008, Laboratoire Physique et Technologie des Plasmas (LPTP), Ecole Polytechnique, Paris, France.
15. *Two-dimensional model of a high-power inductive plasma source for negative ion production*, 8 avril 2008, meeting on simulations of the ITER ions source, Max-Planck-Institut für Plasmaphysik, Garching, Allemagne.
16. *Examples of microwave plasma models*, 22 mai 2008, séminaire intéraction plasma micro-onde (Plasmax), LAPLACE, Toulouse, France.

Contributions à des congrès internationaux

1. 10th NNV/CPS Symposium on Plasma Physics and Radiation Technology, mars 1997, Lunteren, Pays-Bas.
2. NATO Advanced Research Workshop on Electron Kinetics, mai 1997, Saint-Pétersbourg, Russie.
3. 50th Gaseous Electronics Conference, 5-9 octobre 1997, Madison WI, USA.
4. 11th NNV/CPS Symposium on Plasma Physics and Radiation Technology, mars 1998, Lunteren, Pays-Bas.
5. Gordon Research Conference on Plasma Processing Science, 9-14 août 1998, Tilton School, Tilton, New Hampshire, USA.
6. 25th Europhysics Conference on Atomic & Molecular Physics of Ionized Gases, septembre 1998, Malahide, Dublin, Irlande.
7. 1st Workshop on the Exploration of Low Temperature Plasma Physics, novembre 1998, Rolduc, Kerkrade, Pays-Bas.

8. 12th NNV/CPS Symposium on Plasma Physics and Radiation Technology, mars 1999, Lunteren, Pays-Bas.
9. International workshop on experimental data for gas discharge modeling, mai 1999, Greifswald, Allemagne.
10. Eurodisplay, septembre 1999, Berlin, Allemagne.
11. 6th International Display Workshop, 1-3 décembre 1999, Sendai, Japon.
12. G. Hagelaar and G. Kroesen, *Modeling of micro-discharges in plasma addressed liquid crystal (PALC) displays*, 52nd Gaseous Electronics Conference, 5-8 octobre 1999, Norfolk, Virginia, USA (oral).
13. G. Hagelaar and G. Kroesen, *Modeling of micro-discharges in plasma addressed liquid crystal (PALC) displays*, 2nd Workshop on the Exploration of Low Temperature Plasma Physics, décembre 1999, Rolduc, Kerkrade, Pays-Bas (oral).
14. 15th Europhysics Conference on Atomic & Molecular Physics of Ionized Gases, 26-30 août 2000, Lillafüred, Miskolc, Hongrie.
15. G. Hagelaar, J. Bareilles, L. Garrigues, and J.-P. Boeuf, *Parametric study of a stationary plasma thruster using a two-dimensional hybrid model*, 27th International Electronic Propulsion Conference, papier IEPC-01-28, 15-19 octobre 2001, Pasadena, California, USA (oral).
16. L. Garrigues, J. Bareilles, G. J. M. Hagelaar, and J. P. Boeuf, *Influence of the Magnetic Field Magnitude in a Stationary Plasma Thruster using a Hybrid Two-Dimensional Model*, 16th Europhysics Conference on Atomic and Molecular Physics of Ionized Gases, Grenoble, France, 14-18 July 2002 (poster).
17. G. J. M. Hagelaar, J. Bareilles, L. Garrigues, and J. P. Boeuf, *Two-Dimensional Hybrid Model of a Stationary Plasma Thruster*, 16th Europhysics Conference on Atomic and Molecular Physics of Ionized Gases, Grenoble, France, 14-18 July 2002 (poster).
18. L. Garrigues, C. Boniface, J. Bareilles, G. J. M. Hagelaar, and J.P. Boeuf, *Parametric Study of Hall Thruster Operation Based on a 2D Hybrid Model – Influence of the Magnetic Field on the Thruster Performance and Lifetime*, 27th International Electric Propulsion Conference, Toulouse, France, March 2003, paper IEPC-03-183 (oral).
19. 28th International Electronic Propulsion Conference, 17-21 mars 2003, Toulouse, France.
20. L. Garrigues, J. Bareilles, G. J. M. Hagelaar, C. Boniface, J. P. Boeuf, S. Roche, J. Bretagne, M. Touzeau, and D. Pagnon, *Influence of the Stepwise Ionization in a Hall Thruster*, 16th International Symposium on Plasma Chemistry, Taormina, Italy, June 2003 (poster).
21. L. Garrigues, J. Bareilles, G. J. M. Hagelaar, C. Boniface, and J. P. Boeuf, *Calculations of Hall Thruster Lifetime using a Hybrid Two-Dimensional Model*, 16th International Symposium on Plasma Chemistry, Taormina, Italy, June 2003 (poster).
22. K. Hassouni, T. Grotjohn, A. Giquel, and G. Hagelaar, *2D self-consistent modelling of moderate pressure hydrogen microwave plasma's*, 5th International Workshop on Microwave Discharges: Fundamentals and Applications, 8-12 juillet 2003, Greifswald, Allemagne.
23. G. J. M. Hagelaar, *Modeling of stationary plasma thrusters*, 26th International Conference on Phenomena of Ionized Gases, 15-20 juillet 2003, Greifswald, Allemagne.
24. L. Garrigues, G. J. M. Hagelaar, C. Boniface, and J. P. Boeuf, *Effect of a Localized Neutral Atom Mass Flow Injection in Hall Effect Thrusters*, 4th International Spacecraft Propulsion Conference, Chia-Laguna, Sardinia, Italy, June 2004.
25. G. J. M. Hagelaar, K. Hassouni, and A. Gicquel, *Interaction between the electromagnetic field and the plasma in a microwave plasma reactor*, 15th International Conference on Gas Discharges and their Applications, 5-10 septembre 2004, Toulouse, France (oral).

26. G. J. M. Hagelaar, *Modeling energy coupling in nonequilibrium plasmas: Limits of the fluid description,* 15th International Conference on Gas Discharges and their Applications, 5-10 septembre 2004, Toulouse, France (oral).
27. L. Garrigues, G. J. M. Hagelaar, C. Boniface, and J. P. Boeuf, "Influence of a Modified Injection of Neutrals in a Hall Thruster using a Two-Dimensional Hybrid Model", *15th International Conference on Gas Discharges and their Applications,* Toulouse, France, September 2004 (oral).
28. G. J. M. Hagelaar, Two-dimensional simulation of surface wave discharges, 57th Gaseous Electronics Conference, 25-29 septembre 2004, Bunratty, Co. Clare, Irlande.
29. Workshop on the Multiscale Nature of Spark Precursors and High-Altitude Lightning, 9-13 mai 2005, Leiden, Pays-Bas.
30. C. Boniface, G. J. M. Hagelaar, L. Garrigues, J. P. Boeuf, and M. Prioul, *A Monte Carlo Study of Ionization Processes in Double Stage Hall Effect Thrusters*, 27th International Conference on Phenomena in Ionized Gases, Eindhoven, The Netherlands, July 2005 (poster).
31. A. Meige, G. J. M. Hagelaar, R.W. Boswell, C. Charles, J.-P. Boeuf., *Numerical modeling of electronegative electric double-layers*, 27th International Conference on Phenomena in Ionized Gases, Eindhoven, The Netherlands, July 2005.
32. K. Hassouni, A. Gicquel, X. Duten, G. Hagelaar, G. Lombardi, F. Benedic, F. Silva, *Modeling of moderate pressure H_2/CH_4 and $Ar/H_2/CH_4$ microwave plasmas used for diamond deposition*, 27th International Conference on Phenomena in Ionized Gases, Eindhoven, The Netherlands, July 2005.
33. 58th Gaseous Electronics Conference, 16-20 octobre 2005, San Jose, California, USA.
34. A. Meige and G. Hagelaar, *Stochastic heating in non-uniform transverse ac electric field*, 8th Asia-Pacific Conference on Plasma Science and Technology, 2-5 juillet 2006, Cairns, Queensland, Australia.
35. G. J. M. Hagelaar, *Modelling electron transport in magnetized discharge plasmas*, 18th Europhysics Conference on Atomic & Molecular Physics of Ionized Gases (ESCAMPIG), 12-16 juillet 2006, Lecce, Italie.
36. C. Boniface, L. Garrigues, G. J. M. Hagelaar, J. P. Boeuf, S. Mazouffre, and D. Gawron, *Parametric study of anomalous electron transport in high power hall effect thrusters: comparisons between experiments and model*, 18th Europhysics Conference on Atomic & Molecular Physics of Ionized Gases (ESCAMPIG), 12-16 juillet 2006, Lecce, Italie.
37. P. Sarrailh, L. Garrigues, G. J. M. Hagelaar, J. P. Boeuf, G. Sandolache, and S. Rowe, *Simulation of the vacuum circuit breaker post-arc phase*, 18th Europhysics Conference on Atomic & Molecular Physics of Ionized Gases (ESCAMPIG), 12-16 juillet 2006, Lecce, Italie (poster).
38. E. Muñoz-Serrano, G. J. M. Hagelaar, L. C. Pitchford, and J. P. Boeuf, *Numerical simulation of microhollow cathode sustained discharges in Ar and O_2*, 18th Europhysics Conference on Atomic & Molecular Physics of Ionized Gases (ESCAMPIG), 12-16 juillet 2006, Lecce, Italie (poster).
39. G. J. M. Hagelaar, *Hybrid models of magnetized discharge plasmas: fluid electrons + particle ions*, Computational Physics Conference (CCP), 29 août – 1 septembre 2006, Gyeongju, République de Corée (conférence invitée).
40. E. Munoz-Serrano, G. Hagelaar, J. P. Boeuf, L. C. Pitchford, *Model calculations of O2(1D) production in microcathode sustained discharges in argon / oxygen mixtures*, 59th Gaseous Electronics Conference, 9-13 octobre 2006, Columbus, Ohio, USA.
41. A. Meige, N. Plihon, G. J. M. Hagelaar, J.-P. Boeuf, P. Chabert and R. W. Boswell. *Propagating double layers in electronegative plasmas*, 16th International Colloquium on Plasma Processes, Toulouse, France, June 2007.

42. A. Meige, N. Plihon, G. J. M. Hagelaar, J.-P. Boeuf, P. Chabert and R. W. Boswell, *Propagating double layers in electronegative plasmas*, 1st InternationalWorkshop on Radio Frequency Discharges, Dublin, Ireland, June 2007 (poster).
43. P. Sarrailh, L. Garrigues, G. J. M. Hagelaar, J.-P. Boeuf, G. Sandolache, S. Rowe, and B. Jusselin, *Plasma erosion kinetic model of vacuum circuit breaker post-arc phase*, 16th International Colloquium on Plasma Processes, Toulouse, France, 4-8 June 2007.
44. X. Aubert, G. Hagelaar, J. F. Lagrange, E. Munoz-Serrano, L. C. Pitchford, N. Sadeghi, A. Rousseau, *Diagnostics and modelling in microdischarges in argon*, 16th International Colloquium on Plasma Processes, Toulouse, France, 4-8 June 2007.
45. G. Bauville, B. Lacour, L. Magne, V. Puech, J. Santos Sousa, J. P. Boeuf, G. Hagelaar, E. Munoz-Serrano, L. C. Pitchford, N. Sadeghi, and M. Touzeau, *Experimental and theoretical studies of singlet delta oxygen production in microcathode sustained discharges,* 38th AIAA Plasmadynamics and Lasers Conference, 25-28 juin 2007, Miami, FL, USA.
46. A. Meige, N. Plihon, G. J. M. Hagelaar, J.-P. Boeuf, P. Chabert and R. W. Boswell, *Propagating double layers in electronegative plasmas*, 28th International Conference on Phenomena in Ionized Gases, Prague, Czech Republic, 15-20 July 2007 (poster).
47. J. Perez-Luna, G. J. M. Hagelaar, L. Garrigues, N. Dubuit, J.-P. Boeuf, *Impact of azimuthal instabilities on electron behaviour in a Hall Effect thruster*, 28th International Conference on Phenomena in Ionized Gases, Prague, Czech Republic, 15-20 July 2007.
48. P. Sarrailh, L. Garrigues, G. J. M. Hagelaar, J.-P. Boeuf, G. Sandolache, S. Rowe, and B. Jusselin, *One dimensional hybrid Maxwell-Boltzmann modelof sheath evolution comparison with PIC simulation*, 28th International Conference on Phenomena in Ionized Gases, Prague, Czech Republic, 15-20 July 2007.
49. N. Balcon, A. Aanesland, G. J. M. Hagelaar, R. Boswell, and J.-P. Boeuf, *Atmospheric pressure RF discharge in argon: optical diagnostic, fluid model and applications*, 28th International Conference on Phenomena in Ionized Gases, Prague, Czech Republic, 15-20 July 2007.
50. N. Plihon, C. S. Corr, P. Chabert, J.-L. Raimbault, A. Meige, G. J. M. Hagelaar, J.-P. Boeuf, R. W. Boswell, M. A. Lieberman and A.J. Lichtenberg, *Double Layers in Inductively coupled discharges in electronegative gases*, 1st International Workshop on Radio Frequency Discharges, Dublin, Ireland, June 2007.
51. G. J. M. Hagelaar, J. P. Boeuf, and A. Simonin, *Modelling of a high power icp source for negative ion production,* 18th International Symposium on Plasma Chemistry (ISPC), 26-31 août 2007, Kyoto, Japon.
52. J. Pérez-Luna, G. J. M. Hagelaar, L. Garrigues, N. Dubuit, and J. P. Boeuf, *Influence of azimuthal instabilites on electron motion in a Hall effect thruster*, IEPC-2007-124, proc 30th International Electric Propulsion Conference, Florence, Italy, 17-20 September 2007.
53. J. Pèrez-Luna, G. J. M. Hagelaar, L. Garrigues, and J. P. Bœuf, *Model analysis of a double stage Hall effect thruster with double-peaked magnetic field and intermediate electrode*, IEPC-2007-124, proc. 30th International Electric Propulsion Conference, Florence, Italy, 17-20 September 2007.
54. L. Garrigues, G. J. M. Hagelaar, J. P. Boeuf, Y. Raitses, A. Smirnov, and N. J. Fisch, *Two Dimensional Hybrid Model of a Miniaturized Cylindrical Thruster***,** 29th International Electric Propulsion Conference, Florence, Italy, September 2007, paper IEPC-2007-157.
55. G. J. M. Hagelaar, J.-P. Boeuf, and A. Simonin, *Inductive plasmas for H- for ITER*, International Conference on Research and Applications of Plasmas (PLASMA2007), 16-19 octobre 2007, Greifswald, Allemagne.

56. J.-P. Boeuf, J. Pérez-Luna, L. Garrigues, G. J. M. Hagelaar, N. Dubuit, *Plasma sources for space propulsion,* International Conference on Research and Applications of Plasmas (PLASMA2007), 16-19 octobre 2007, Greifswald, Allemagne.
57. A. Meige, N. Plihon, G. J. M. Hagelaar, J.-P. Boeuf, P. Chabert and R. W. Boswell, *Propagating double layers in electronegative plasmas,* 60th Annual Gaseous Electronics Conference, Washington DC, USA, October 2007 (poster).
58. A. Meige, N. Plihon, P. Chabert, G. J. M. Hagelaar, J.-P. Boeuf, R. W. Boswell, M. A. Lieberman, and A. J. Lichtenberg, Double layers in electronegative plasmas. 49th Annual Meeting of the Division of Plasma Physics, Orlando, USA, November 2007.
59. A. Zahri, G. Hagelaar, L. Therese, Ph. Guillot, T. Nelis, Ph. Belenguer, *Two dimensional particle in cell monte carlo model of the glow discharge cell for mass-spectrometry or optical emission spectroscopy*, Winter Conference on Plasma Spectrochemistry, Temecula, USA, January 2008.
60. J. Pérez-Luna, N. Dubuit, L. Garrigues, G. J. M. Hagelaar, J.-P. Boeuf, *Challenges in Hall effect thrusters*, 5th International Spacecraft Propulsion Conference, Heraklion, Crete, Greece, 5-9 May 2008 (oral).
61. L. Garrigues, G. J. M. Hagelaar, C. Boniface, and J. P. Boeuf, *Hall Effect Thruster Study using Ambiant Atmospheric Gas as Propellant*, 5th International Spacecraft Propulsion Conference, Heraklion, Crete, Greece, 5-9 May 2008 (oral).
62. A. Meige, G. J. M. Hagelaar, and P. Chabert, *Formation of ion-ion plasmas by electron magnetic filtering: 2D fluid simulation,* 24th International Symposium on the Physics of Ionized Gases, Novi Sad, Serbia, 25-29 August 2008.
63. S. Pancheshnyi, B. Eismann, G. Hagelaar, and L. Pitchford, ZDPLASKIN: *a new tool for plasmachemical simulations,* HAKONE XI Oleron Island, France, 7-12 September 2008.
64. G. J. M. Hagelaar, L. Garrigues, K. Makasheva, and J.-P. Boeuf, *Model of a multi-dipolar microwave plasma*, 19th Europhysics Conference on Atomic & Molecular Physics of Ionized Gases (ESCAMPIG), 15-19 juillet 2008, Granada, Espagne (poster).
65. G. J. M. Hagelaar, S. Kolev, G. Fubiani, and J.-P. Boeuf, *Modeling of an inductive ion source for neutral beam injection,* 19th Europhysics Conference on Atomic & Molecular Physics of Ionized Gases (ESCAMPIG), 15-19 juillet 2008, Granada, Espagne (poster).
66. L. Garrigues, N. Dubuit, J. Pérez-Luna, G. J. M. Hagelaar, J.-P. Boeuf, J.-C. Adam, and A. Héron, *Kinetic effects on the electron transport in a Hall effect thruster*, 19th Europhysics Conference on Atomic & Molecular Physics of Ionized Gases (ESCAMPIG), 15-19 juillet 2008, Granada, Espagne (poster).
67. K. Makasheva, G. J. M. Hagelaar, J.-P. Boeuf, Th. Callegari, and L. C. Pitchford, *Transition to a microcathode sustained discharge*, 19th Europhysics Conference on Atomic & Molecular Physics of Ionized Gases (ESCAMPIG), 15-19 juillet 2008, Granada, Espagne (poster).
68. K. Makasheva, E. Muñoz-Serrano, G. J. M. Hagelaar, J.-P. Boeuf, Th. Callegari, and L. C. Pitchford, *Spatial profiles of plasma densities in microcathode sustained discharges*, 19th Europhysics Conference on Atomic & Molecular Physics of Ionized Gases (ESCAMPIG), 15-19 juillet 2008, Granada, Espagne (poster).
69. E. Muñoz-Serrano, K. Makasheva, G. J. M. Hagelaar, L. C. Pitchford, and J.-P. Boeuf, *Microhollow cathode sustained discharge: plasma properties and parametric study*, 19th Europhysics Conference on Atomic & Molecular Physics of Ionized Gases (ESCAMPIG), 15-19 juillet 2008, Granada, Espagne (poster).
70. B. Eismann, S. Pancheshnyi, G. J. M. Hagelaar, K. Makasheva, and L. C. Pitchford, *Zero-dimensional chemical analysis of positive columns in Ar and Ar-O2 plasmas*, 19th Europhysics Conference on Atomic & Molecular Physics of Ionized Gases (ESCAMPIG), 15-19 juillet 2008, Granada, Espagne (poster).

71. P. Sarrailh, L. Garrigues, G. J. M. Hagelaar, J.-P. Boeuf, G. Sandolache, S. Rowe, and B. Jusselin, *Collisional model of the plasma decay during the post-arc phase of a vacuum circuit breaker*, 19th Europhysics Conference on Atomic & Molecular Physics of Ionized Gases (ESCAMPIG), 15-19 juillet 2008, Granada, Espagne (poster).
72. J. Pérez-Luna, G. J. M. Hagelaar, L. Garrigues, and J.-P. Boeuf, *Means of investigation of laser induced fluorescence measurements in low-temperature plasmas*, 19th Europhysics Conference on Atomic & Molecular Physics of Ionized Gases (ESCAMPIG), 15-19 juillet 2008, Granada, Espagne (présentation orale invitée).
73. D.Mihailova, J. van Dijk, G. J. M. Hagelaar, W. J. M. Brok, M. Grozeva, and J. J. A. M.van der Mullen, *Plasimo simulations of a sputtering hollow cathode discharge for laser applications,* 11th Euroregional WELT PP Workshop on the Exploration of Low Temperature Plasma Physics, 13-14 novembre 2008, Rolduc, Kerkrade, Pays-Bas (poster).

Contributions à des congrès nationaux

1. L. Garrigues, C. Boniface, G. J. M. Hagelaar, J. P. Boeuf, D. Gawron et S. Mazouffre, *Propulsion à Effet Hall : Physique, Modélisation et Expériences*, 9ème Congrès de la Société Française de Physique Division Plasmas, Pont-à-Mousson, France, Mai 2006 (conférence invitée).
2. L. Garrigues, J. Perez-Luna, G. J. M. Hagelaar, N. Dubuit, et J. P. Boeuf, *Propulsion à Plasma : vers de Nouveaux Concepts pour les Missions du Futur*, Journées Electrotechnique du Futur, Toulouse, France, Septembre 2007 (conférence invitée).
3. P. Sarrailh, L. Garrigues, G. J. M. Hagelaar, J. P. Boeuf, G. Sandolache, S. Rowe, et B. Jusselin *Modèle d'Erosion Plasma lors de la Phase Post-Arc d'un Disjoncteur à Arc Sous-Vide*, Journées Electrotechnique du Futur, Toulouse, France, Septembre 2007.
4. A. Meige, G. Hagelaar, and P. Chabert, *Electron magnetic filtering for ion-ion plasmas: Preliminary results of a fluid simulation*, 10ème Congrès de la Société Française de Physique Division Plasmas, Paris, France, 19-21 Mai 2008 (conférence invitée).

Annexe C

PRINCIPALES PUBLICATIONS

1. G. J. M. Hagelaar, M. H. Klein, R. J. M. M. Snijkers, and G. M. W. Kroesen, *Energy loss mechanisms in the microdischarges in plasma display panels*, J. Appl. Phys. **89** (4), 2033-2039 (2001).

2. G. J. M. Hagelaar, J. Bareilles, L. Garrigues, and J.-P. Boeuf, *Two-dimensional model of a stationary plasma thruster*, J. Appl. Phys. **91** (9), 5592-5598 (2002).

3. G. J. M. Hagelaar and L. C. Pitchford, *Solving the Boltzmann equation to obtain electron transport coefficients and rate coefficients for fluid models*, Plasma Sources Sci. Technol. **14**, 722-733 (2005).

4. G. J. M. Hagelaar, *Modelling electron transport in magnetized discharge plasmas*, Plasma Sources Sci. Technol. **16**, S57-S66 (2007).

5. G. J. M. Hagelaar, *Effective viscosity approach for non-local electron kinetics in inductively coupled plasmas*, Phys. Rev. Lett. **100**, 025001 (2008).

Energy loss mechanisms in the microdischarges in plasma display panels

G. J. M. Hagelaar[a)]
Department of Physics, Eindhoven University of Technology, P.O. Box 513, 5600 MB Eindhoven, The Netherlands

M. H. Klein and R. J. M. M. Snijkers
Philips Research Laboratories Aachen, Weisshausstrasse 2, 52066 Aachen, Germany

G. M. W. Kroesen
Department of Physics, Eindhoven University of Technology, P.O. Box 513, 5600 MB Eindhoven, The Netherlands

(Received 23 August 2000; accepted for publication 8 November 2000)

Low luminous efficacy is one of the major drawbacks of plasma display panels (PDPs), where the main limiting factor is the efficiency of the microdischarges in generating UV radiation. In this work we use a two-dimensional self-consistent fluid model to analyze the energy loss mechanisms in neon–xenon discharges in coplanar-electrode color PDPs and interpret experimental data on the luminous efficacy of these PDPs. The modeling results are in good agreement with the measured UV emission spectrum and measured trends in the efficacy. Most of the electrical input energy is transferred to ions and subsequently to the gas and the surface. The electrical energy transferred to electrons is mostly used for ionization and excitation, where the part used for xenon excitation largely ends up in UV radiation. The amplitude, frequency, and rise time of the driving voltage mainly affect the energy losses due to ion heating. The xenon content also affects the conversion of electron energy into UV energy. © *2001 American Institute of Physics.*
[DOI: 10.1063/1.1337084]

I. INTRODUCTION

Plasma display panel (PDP) technology is a promising technology for large, lightweight, flat displays.[1,2] In PDPs, the light of each picture element (pixel) is emitted from a tiny high-pressure glow discharge, typically called a microdischarge. Color PDPs use microdischarges in xenon mixtures to generate UV radiation, and convert this into red, blue, and green light by phosphors. One of the major drawbacks of PDPs is their low luminous efficacy: about 1 lm/W, compared to 4 lm/W for the conventional cathode ray tube (CRT) displays.

In color PDPs, energy loss occurs in various ways: Only about 40% of the UV photons emitted by the discharges is captured by the phosphors, where an additional 80% of photon energy is lost in the conversion to visible light, mainly due to the difference in wavelength of the visible light (~600 nm) and the UV radiation (~150 nm). Next, only about half of the visible light emitted by the phosphors leaves the display on the front side, the other half is absorbed somewhere in the display. However, the largest energy loss occurs in the microdischarges themselves: only about 10% of the electrical input energy is used for the emission of UV photons. In this article, we use a two-dimensional self-consistent fluid model[3] to analyze the energy loss mechanisms in the microdischarges and interpret experimental data on the luminous efficacy. We extend, improve, and discuss more elaborately the analysis briefly presented in Refs. 4 and 5.

We consider the most common type of color PDP: the coplanar-electrode ac PDP.[6] Figure 1 schematically depicts a PDP of this type. The panel consists of two glass plates, separated by a gap of about 150 μm that is filled with a mixture of neon and a small percentage of xenon at 450 Torr. Each plate is equipped with a large number of parallel electrodes, covered by dielectric material. A discharge cell (corresponding to a pixel) is formed by the intersection of a pair of sustain electrodes on the front plate, and an address electrode on the back plate. In operation, a square wave voltage with a frequency of 50–250 kHz is constantly applied between each pair of sustain electrodes. The amplitude of this sustain voltage is below the breakdown voltage. To switch a certain discharge cell on, a write voltage pulse is applied between the address electrode and one of the sustain electrodes of the cell. This initiates a microdischarge, which is quickly quenched due to the accumulation of surface charge on the dielectric material that covers the electrodes. On its next half cycle, the sustain voltage changes polarity. The stored surface charge now reinforces the sustain voltage, causing the ignition of a new microdischarge, despite the fact that the sustain voltage itself is below the breakdown voltage. A new surface charge distribution develops, quenches the discharge again, and so on. In this way, a transient microdischarge occurs in the cell every time the sustain voltage changes polarity, due to the presence of surface charge.

The article is organized as follows: Secs. II and III outline the fluid model and the simulation of the transient microdischarges in a PDP cell. In Sec. IV we analyze how the electrical energy is dissipated in the discharge. In Sec. V we study how the energy dissipation and the resulting discharge

a)Electronic mail: hagelaar@discharge.phys.tue.ni

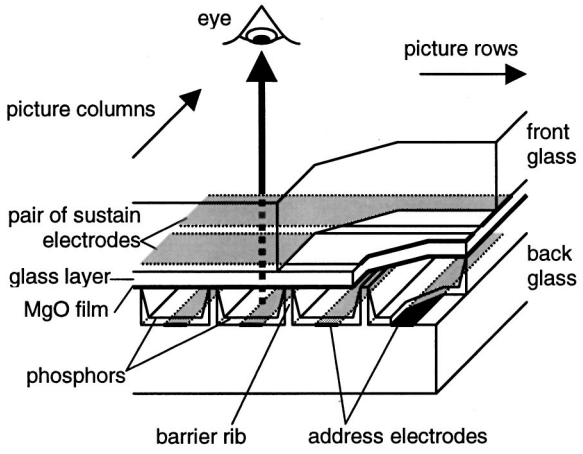

FIG. 1. Schematic drawing of a coplanar-electrode ac PDP.

efficiency are influenced by several discharge parameters, thus interpreting measured trends in the luminous efficacy.

II. DESCRIPTION OF THE MODEL

To simulate the PDP discharges we use the two-dimensional model presented in Ref. 3. Following the well-known fluid approach, this model describes the behavior of plasma particle species (electrons, ions, and excited neutrals) by the first few moments of the Boltzmann equation: the continuity equation, the momentum transport equation, and the energy transport equation. For each plasma particle species p the evolution of the number density n_p is calculated from a continuity equation

$$\frac{\partial n_p}{\partial t}+\nabla\cdot\Gamma_p=\sum_r c_{p,r}R_r, \tag{1}$$

where Γ_p is the particle flux, and the right hand side represents the total particle production or loss in reactions. The summation is over all possible reactions r, where R_r is the reaction rate and $c_{p,r}$ is the net number (positive or negative) of particles of species p created in one reaction of type r. The flux is given by the momentum transport equation, which we approximate by the drift-diffusion equation

$$\Gamma_p=\mathrm{sgn}(q_p)\mu_p\mathbf{E}n_p-D_p\nabla n_p. \tag{2}$$

Here $\mathbf{E}$ is the electric field, q_p is the particle charge, μ_p is the mobility and D_p is the diffusion coefficient. The first term represents the flux due to the electric field (drift), the second term the flux due to concentration gradients (diffusion). Particle inertia is neglected. The electric field is self-consistently calculated from Poisson's equation

$$\nabla\cdot(\varepsilon\mathbf{E})=\sum_p q_p n_p, \tag{3}$$

where ε is the dielectric permittivity.

Equations (1) and (2) require the input of mobilities, diffusion coefficients, and reaction rate coefficients. In general these quantities depend on the energy distribution of the considered particles. For ions we use the local field approximation, which assumes a direct relation between the particle energy distribution and the local electric field: the ion diffusion coefficients and mobilities are regarded as functions of the electric field. For the electrons however, the local field approximation seems unrealistic, in view of the combination of the poor energy transfer in electron-neutral collisions and the strong spatial variations of the electric field in PDP discharges. Unlike most PDP models,[7–11] our model does not adopt the local field approximation for electrons, but assumes the electron mobility, electron diffusion coefficient, and the rate coefficients of electron impact reactions to be functions of the electron mean energy. The electron mean energy $\overline{\varepsilon}$ is calculated from the energy balance equation

$$\frac{\partial(n_e\overline{\varepsilon})}{\partial t}+\nabla\cdot\left(-\frac{5}{3}\mu_e\mathbf{E}(n_e\overline{\varepsilon})-\frac{5}{3}D_e\nabla(n_e\overline{\varepsilon})\right)$$
$$=-e\Gamma_e\cdot\mathbf{E}-\sum_r\overline{\varepsilon_r}R_r, \tag{4}$$

where n_e is the electron density, μ_e is the electron mobility, D_e is the electron diffusion coefficient, and Γ_e is the electron flux. The two terms on the right-hand side represent heating by the electric field and energy loss in collisions, respectively. The summation in the loss term is only over the electron impact reactions, with $\overline{\varepsilon_r}$ the threshold energy. Energy loss due to elastic collisions is included in this term by using an imaginary threshold energy of 1 eV in combination with an effective collision rate. Contrary to Ref. 12, we found that

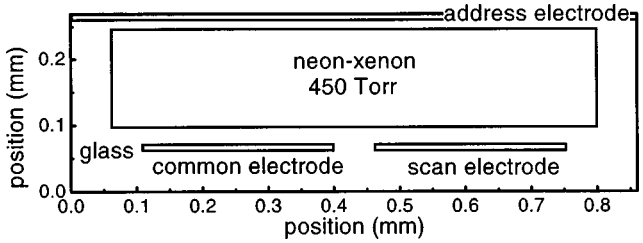

FIG. 2. Model geometry used in the calculations. This geometry represents a discharge cell of a coplanar-electrode PDP. The top of the geometry corresponds to the back plate of the display, the bottom to the front plate. The sustain electrodes are indicated as the common and scan electrodes. The dielectric constant of the glass is 11.0.

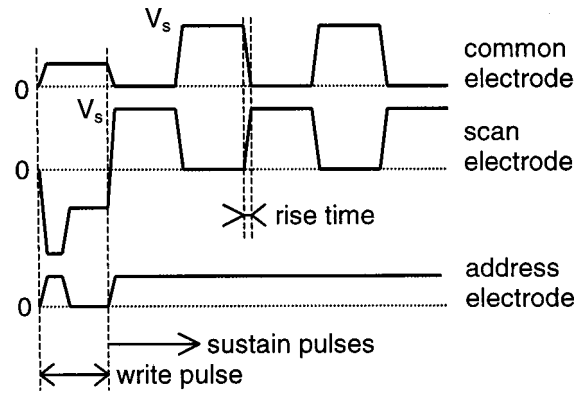

FIG. 3. Electrode potentials as a function of time in the model driving scheme. This figure relates to the model geometry shown in Fig. 2, where the common and scan electrodes are the sustain electrodes. Typically the amplitude of the sustain voltage is $V_s=180-300$ V, its frequency 50–250 kHz.

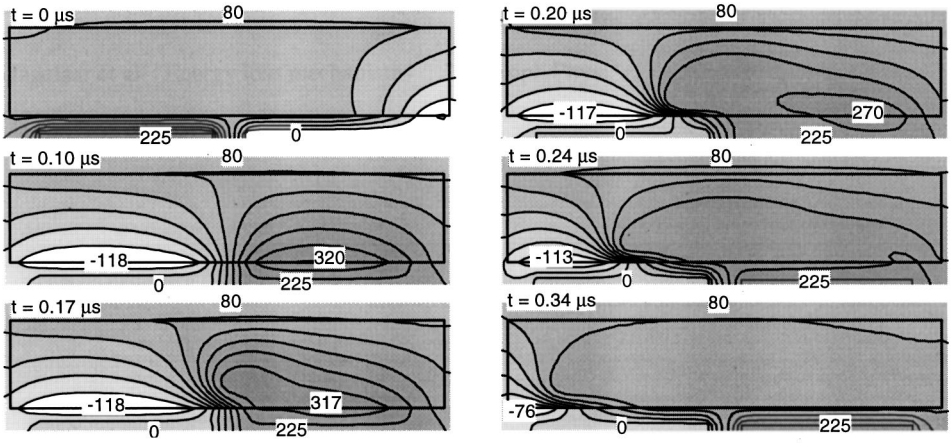

FIG. 4. Time evolution of the electric potential profile during a PDP discharge. The geometry is shown in Fig. 2. The sustain voltage is 225 V, the sustain frequency is 50 kHz, the pressure is 450 Torr, and the xenon percentage is 5%. The moment $t=0$ corresponds to the end of the previous sustain pulse; the sustain voltage is switched between $t=0$ μs and $t=0.10$ μs, with a rise time of 0.10 μs. The increment of the contours is 1/10 times the difference of the maximum and minimum values, which are indicated in each plot. The unit of the indicated potentials is V.

the electron energy equation considerably improves the reliability of the PDP model; for the calculated discharge efficiency the difference with the local field approximation may be as large as a factor of two.

The transport Eqs. (1) and (2) for heavy species are solved for the boundary condition of zero particle reflection and influx. The boundary conditions for the electron equations are similar, but include an influx by secondary electron emission. Poisson's equation is solved not only in the discharge, but also in surrounding dielectric materials, taking into account possible surface charge. For details on the basic equations and the boundary conditions we refer to Ref. 3.

The considered model geometry, shown in Fig. 2, represents a discharge cell, or actually an entire row, of the display. Due to its two dimensionality, the model geometry is only an approximation of the real PDP geometry, which has important three-dimensional features. The barrier ribs that separate the columns of the display are not represented in the model; instead, the model cell has side walls along the sustain electrodes. (Compare Fig. 2 with Fig. 1.) The model electrode driving scheme is shown in Fig. 3. Although each simulation is started with a write pulse to initiate the discharges and switch the cell on, we will not consider the writing itself in this article. An external circuit, involving backcoupling from the current to the electrode voltage, is not included in the model. We do however take into account a realistic rise time ($\sim$100 ns) for all voltage changes. We remark that in the model the required sustain voltages are generally slightly higher (20%) than in reality. This difference can easily be removed by adjusting the model input data (e.g., the secondary emission coefficients) within their experimental inaccuracies, but in our opinion such adjustments are unnecessary and might even be deceiving. The electrical behavior of the discharge and the mechanisms of UV photon generation are described by an extensive reaction scheme, similar to the scheme used in Ref. 7, consisting of 80 reactions, involving 15 different plasma species. The full simulation of a single PDP discharge takes 15–20 min on a modern personal computer.

III. SIMULATION OF A PDP DISCHARGE

Figures 4 and 5 show the electric potential and the xenon excitation rate in the model geometry, during the simulation of a typical PDP discharge. By the end of the discharge that precedes the one considered in these figures, stored surface charge screens the discharge gas almost entirely from the applied voltage. After the sustain voltage has been switched, the same surface charge reinforces the applied voltage rather than canceling it. The total voltage across the discharge gas is now so high that the ignition of a new discharge takes place. It appears from Figs. 4 and 5 that the discharge starts in the center of the geometry, where the electrodes are close together. As soon as a new surface charge distribution is established in the center of the geometry, the discharge spreads outward. Eventually, all the electrodes are screened by the new surface charge distribution, and the discharge stops. Note that the current through the electrodes is a displacement current resulting from the changes in the electric fields in the dielectric layer that covers them. During the discharge extremely strong electric fields are present in the

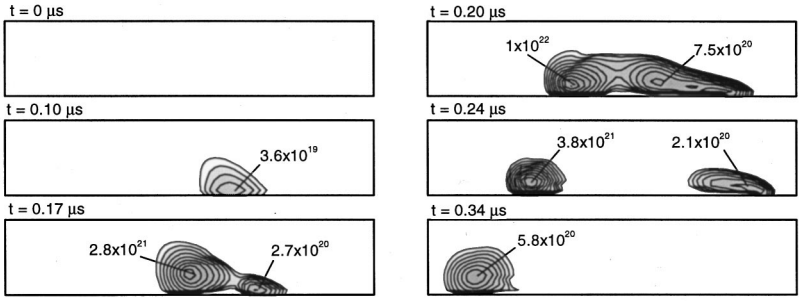

FIG. 5. Time evolution of the excitation rate of the resonant $Xe^*(^3P_1)$ state during a PDP discharge. This figure shows results of the same simulation as Fig. 4; the discharge conditions are indicated in the caption of that figure. For all plots the contours correspond to a logarithmic scale covering the range from 10^{18} to 10^{22} cm^{-3} s^{-1}; the increment of the contours is a factor of 2.51. The unit of the values indicated in the plots is cm^{-3} s^{-1}.

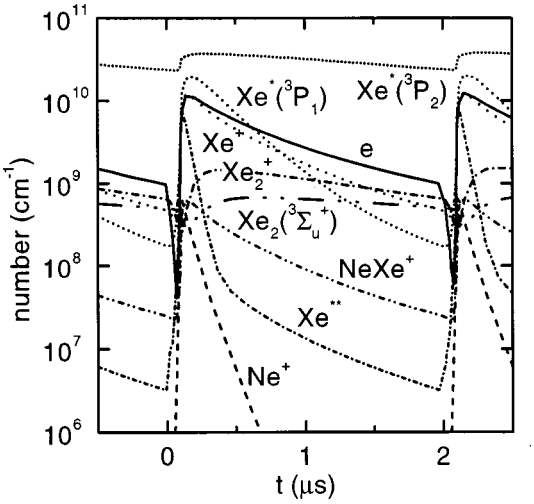

FIG. 6. Time evolution of the numbers of particles of the most important species. This figure shows results of the same simulation as Fig. 4; the discharge conditions are indicated in the caption of that figure.

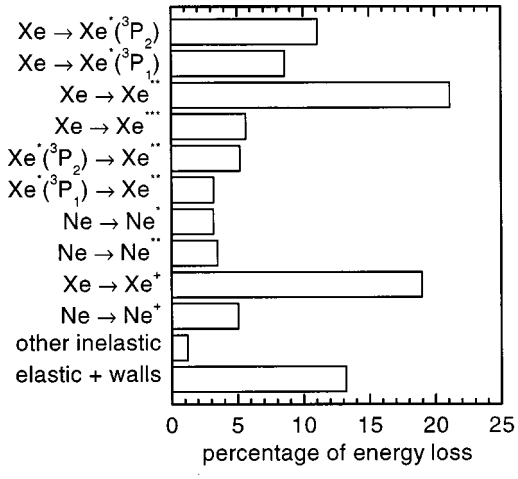

FIG. 8. Breakdown of the loss of electron energy into the different electron impact excitation and ionization processes. The discharge conditions are indicated in the caption of Fig. 7.

plasma sheath front of the cathode, which has the character of a cathode fall. Ionization and excitation mainly take place in the vicinity of this cathode sheath.

Figure 6 shows the calculated time evolution of the (space integrated) densities of the most important species during the discharge. The densities rapidly increase at the beginning of the sustain pulse and then gradually decay. Neon ions are only present during the very first part of the discharge; during the plasma decay Xe_2^+ becomes the most important ion species.

IV. ANALYSIS OF THE ENERGY DISSIPATION

During the discharge electrical energy is transferred to the plasma through the acceleration of the charged particles. The energy that is thus consumed by the particle species p is

$$W_p = \int_{\text{time}} \int\int\int_{\substack{\text{discharge}\\ \text{volume}}} q_p \Gamma_p \cdot \mathbf{E} d^3V dt. \tag{5}$$

Note that the sum of these energies must be equal to the total electrical energy input:

$$\sum_p W_p = \int_{\text{time}} I \times V dt, \tag{6}$$

where I is the (displacement) current through a sustain electrode and V is the sustain voltage. We confirmed that this relation is reproduced by the fluid model within 0.01%, which illustrates its numerical consistency. The main energy consumption takes place in the plasma sheaths, mostly on the cathode side of the discharge, where the sheath contains an extremely strong electric field, as can be seen in Fig. 4.

Figure 7 shows the calculated energy consumption of the various charged particle species in a typical PDP discharge. The larger part of the energy turns out to be consumed by ions. This energy is forever lost for the production of UV photons: under PDP discharge conditions ionization or excitation by ion impact seem negligible, which implies that all the ion energy is eventually transferred to the gas and the surface. We remark that ion impact ionization or excitation is not included in the model; even if they would occur, we

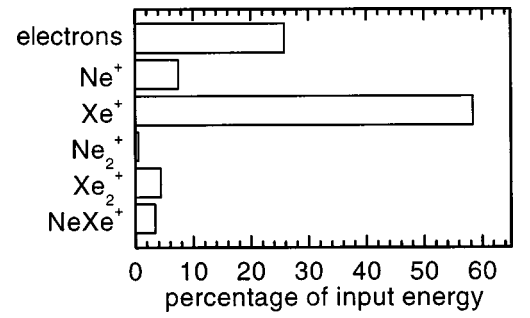

FIG. 7. Breakdown of the electrical input energy into the heating of the different charged particle species. The total energy consumption is 3.4 $\times 10^{-7}$ J per discharge (pulse) per cm^{-1} of row length. The sustain voltage is 225 V, the sustain frequency is 250 kHz, the gas pressure is 450 Torr, and the xenon percentage is 5%.

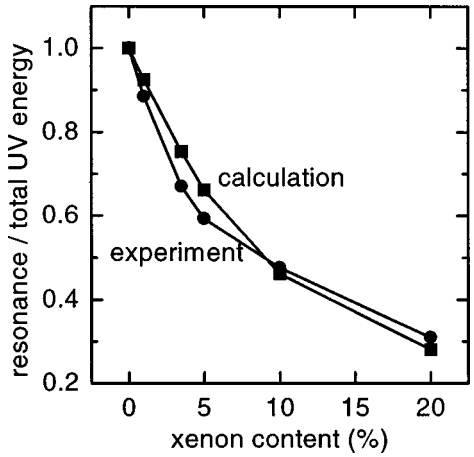

FIG. 9. Ratio of the energy carried by 147 nm resonance photons and the total energy carried by UV photons. This plot compares the result of fluid simulations to the experimental data of Ref. 13. The discharge conditions, for both simulation and experiment, are the same as with Fig. 7. The experimental discharge geometry is very similar to the model geometry of Fig. 2.

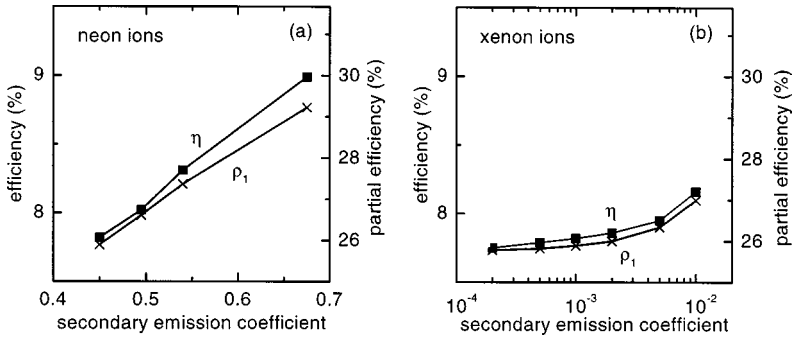

FIG. 10. Calculated efficiency as a function of the secondary emission coefficient, for (a) neon ions and (b) xenon ions. The sustain voltage is 225 V, the sustain frequency is 250 kHz, the xenon percentage is 5%.

would not see them in the simulations. The electron energy, on the other hand, is largely used for the excitation and ionization. The energy that is used for a reaction r is

$$W_r = \int_{\text{time}} \int_{\substack{\text{discharge} \\ \text{volume}}} \overline{\varepsilon_r} R_r d^3V dt. \tag{7}$$

Figure 8 shows how the electron energy is used in the different reactions. Note that the electron energy Eq. (4) ensures that the sum of all the energy losses in Fig. 8 is equal to the total energy transferred to electrons by the field as given by Eq. (5).

Of all the processes in Fig. 8 it is mainly the excitation of xenon atoms that eventually leads to the generation of UV photons. There are several possible mechanisms: First, the resonant state $Xe^*(^3P_1)$ decays directly to the ground state, emitting UV photons at a wavelength of 147 nm. Second, both the resonant $Xe^*(^3P_1)$ and metastable $Xe^*(^3P_2)$ states may attach to xenon gas atoms and form excited dimers Xe_2^*; these dimers decay radiatively into ground state atoms. The photons thus emitted by the higher vibrational levels $Xe_2^*(O_u^+)$ are distributed around 150 nm, those emitted by the lower vibrational levels $Xe_2^*(^3\Sigma_u^+, ^1\Sigma_u^+)$ around 173 nm. The higher atomic states Xe** and Xe*** do not directly lead to UV photons, but cascade down to the $Xe(^3P_1, ^3P_2)$ levels. In this case some amount of energy is lost in the form of infrared radiation or gas heating.

The energy that is emitted from the discharge in the form of UV photons with a wavelength λ is

$$W_\lambda = \int_{\text{time}} \int_{\substack{\text{discharge} \\ \text{volume}}} (hc/\lambda) R_\lambda d^3V dt, \tag{8}$$

where h is Planck's constant, c is the velocity of light, and R_λ is the rate of the decay process leading to the emission. The relative importance of the different UV wavelengths (147, 150, and 173 nm) depends heavily on partial xenon pressure. Figure 9 shows the fraction of the UV energy emitted at 147 nm, $W_{147\,\text{nm}}/(W_{147\,\text{nm}}+W_{150\,\text{nm}}+W_{172\,\text{nm}})$, as a function of the xenon content. The simulation results are in excellent agreement with the experimental values of Ref. 13, determined by integrating the measured emission spectrum.

V. PARAMETRIC STUDIES

The efficiency of the discharge in generating UV photons is defined as

$$\eta = \sum_\lambda W_\lambda \Big/ \sum_p W_p. \tag{9}$$

In view of the analysis given in the previous section, it is interesting to split the discharge efficiency into two partial efficiencies

$$\rho_1 = W_e \Big/ \sum_p W_p, \tag{10}$$

$$\rho_2 = \sum_\lambda W_\lambda \Big/ W_e, \tag{11}$$

where W_e is the electrical energy transferred to the electrons, as given by Eq. (5) and $\eta = \rho_1 \rho_2$. The partial efficiency ρ_1 is the efficiency of the discharge in heating the electrons, ρ_2 is the efficiency of the electrons in generating UV radiation.

We will now investigate how the η, ρ_1, and ρ_2 are influenced by various discharge parameters. Wherever possible, we will compare the simulation results with experi-

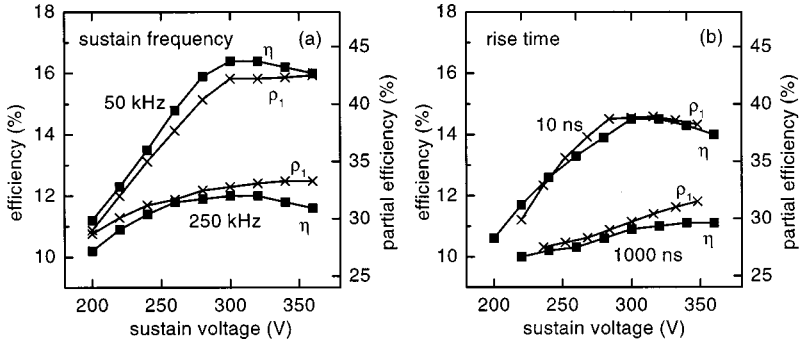

FIG. 11. Calculated efficiency as a function of the sustain voltage, for (a) two different frequencies and a rise time of 100 ns, and (b) two different rise times and a frequency of 250 kHz. The xenon percentage is 5%.

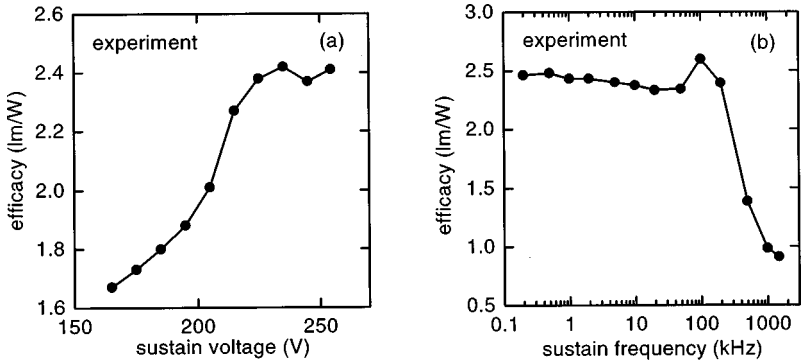

FIG. 12. Measured efficacy as a function of (a) the sustain voltage, where the frequency is 250 kHz, and (b) the sustain frequency, where the voltage is 225 V (Ref. 12). The xenon percentage is 10%.

mental data on the PDP efficacy of 4 in. test panels, taken from Ref. 14. The efficacy is a measure for the light output of the display—weighted according to the sensitivity of the human vision—per unit of electrical input energy; it is thus not only determined by the discharge efficiency, but also by other factors, such as the efficiency of the phosphors in converting the UV radiation into visible light. Here we assume that these other factors stay constant. The experimental electrode size and distance, thickness of the covering dielectric layer, and cell height are well reflected by the model geometry of Fig. 2.

We start with the influence of the secondary emission coefficient. In present day PDPs, where the surface is coated with magnesium oxide, this coefficient has been estimated to be around 0.45 for neon ions and below 0.001 for xenon ions.[15] Figure 10 shows that both η and ρ_1 increase with increasing secondary emission coefficient; ρ_2 is nearly unaffected. This result is not very surprising: The secondary emission coefficient directly determines the relative contributions of the electrons and the ions to the current density in the cathode fall, where the main particle heating occurs. The relative contribution of the electrons—and consequently ρ_1—increases monotonically with increasing secondary emission coefficient. Of main importance is the secondary emission coefficient of the neon ions. For xenon ions, the secondary emission coefficient is so low that its exact value does not really matter: xenon hardly contributes to the secondary emission anyway.

The effect of the sustain voltage is shown in Fig. 11. For not too high sustain voltages, both η and ρ_1 increase with increasing voltage. This trend is also seen in the efficacy measurements shown in Fig. 12(a). The model reveals the mechanism behind this trend: As the voltage increases, the electric fields and the electron energies in the discharge go up. Since neon has a higher ionization energy than xenon, this leads to an increase of the relative contribution of neon to the total ion flux, which implies an increase of the average secondary emission coefficient. As we have seen before, this is favorable for the electron heating efficiency ρ_1.

Figure 11(a) also shows that the sustain frequency has a strong effect on the calculated efficiency. This fact is known from experiments; see Fig. 12(b): Beyond a certain sustain frequency, the discharge efficiency drops dramatically. In Refs. 4 and 5 it is suggested that this effect is caused by the role played by metastable xenon atoms. However, when looking at the modeling results more carefully, we find an entirely different underlying mechanism: At low frequencies (50 kHz) there is a short time between the switching of the sustain voltage and the breakdown. At high frequencies (250 kHz), the plasma does not completely decay in between the discharges, which facilitates their ignition: breakdown now already occurs during the switching of the voltage. This is illustrated by Fig. 13. Due to the premature breakdown, the surface charge on the dielectric layer is already changed before the sustain voltage reaches its full value, so that the final voltage across the gas is lower. As we have seen before, this results in a lower ρ_1. This observation suggests that for high frequencies (250 kHz) the rise time of the sustain voltage might influence the efficiency. According to the simulation results shown in Fig. 11(b) this is indeed the case. For 50 kHz no influence of the rise time is found: rise times of 10, 100, and 1000 μs yield exactly the same efficiency [not shown in Fig. 11(b)]. We remark that these results are only of qualitative value. In general, the exact time between the switching of the voltage and the breakdown is not very accurately predicted by fluid models.[8]

As we have seen, the amplitude, frequency, and rise time of the sustain voltage mainly affect η via ρ_1, leaving ρ_2 nearly unchanged. A parameter that can be expected to directly affect ρ_2 is the xenon content of the gas mixture. Fig-

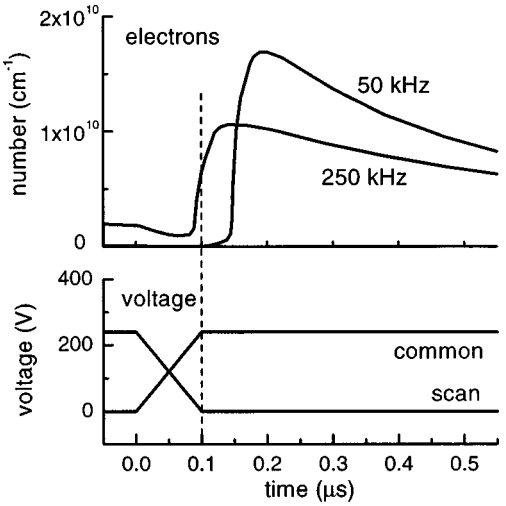

FIG. 13. Comparison between of the time evolution of the electron density for two different sustain frequencies. The xenon percentage is 5%.

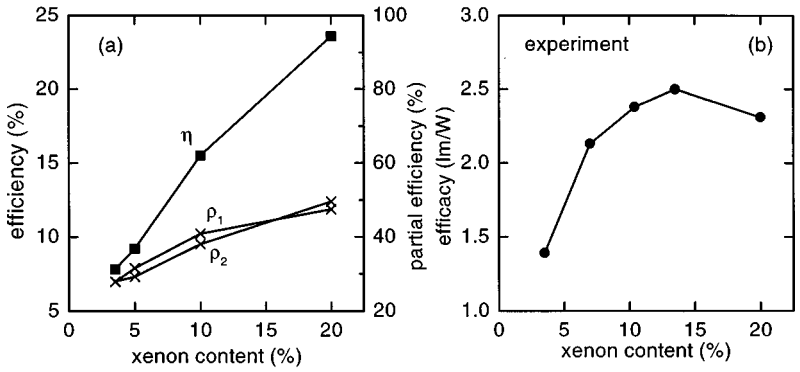

FIG. 14. Influence of the percentage of xenon on (a) the calculated efficiency and (b) the measured efficacy (Ref. 12). In both the simulation and the experiment the sustain frequency is 250 kHz. The sustain voltage is 260 V in the simulation and 225 V in the experiment.

ure 14(a) shows that the calculated efficiency increases with increasing percentage of xenon. This trend has been reported in the literature, e.g., in Ref. 7, but is not fully reflected by the efficacy measurements shown in Fig. 14(b). We remark that it is known that the phosphor performance strongly depends on the UV wavelength, which is influenced as well by the xenon percentage (see Fig. 9). It appears from Fig. 14(a) that not only ρ_2, but also ρ_1 is responsible for the increase of η with increasing xenon content.

VI. CONCLUSIONS

The fluid model presented in Ref. 3 is capable of simulating the microdischarges in a coplanar-electrode PDP. We have reproduced a write pulse and a series of sustain pulses in one cell of the display.

From the simulation results, we have analyzed how the electrical input energy is dissipated in the cell. The largest part of the electrical energy is transferred to ions and subsequently to the gas and the surface. The electrical energy transferred to electrons is mostly used for ionization and excitation. The part used for xenon excitation largely ends up in UV radiation. The calculated fraction of the UV energy that is carried by resonance photons is in excellent agreement with experimental results.

We have studied how the energy loss mechanisms are influenced by several discharge parameters. The amplitude, frequency, and rise time of the sustain voltage mainly affect the losses due to ion heating. The xenon content also affects the conversion of electron energy into UV energy. The trends in the calculated discharge efficiency are in good agreement with measured trends in the luminous efficacy.

ACKNOWLEDGMENTS

This work was supported by the Philips Research Laboratories in Eindhoven, The Netherlands. The authors thank G. Oversluizen and S. de Swart of these laboratories for the experimental data on the luminous efficacy.

[1] L. Weber, in *Flat-Panel Displays and CRTs*, edited by L. Tannas (Van Nostrand Reinhold, New York, 1985), pp. 332–407.
[2] A. Sobel, IEEE Trans. Plasma Sci. **19**, 1032 (1991).
[3] G. J. M. Hagelaar, G. M. W. Kroesen, U. van Slooten, and H. Schreuders, J. Appl. Phys. **88**, 2252 (2000).
[4] M. Klein, R. Snijkers, and G. Hagelaar, *Proceedings of the 6th International Display Workshop* (Society for Information Display, Japan, 1999), pp. 695–698.
[5] M. H. Klein, R. J. M. M. Snijkers, and G. J. M. Hagelaar, IEICE Transactions *E83-C*, 1602 (Institute of Electronic, Information and Commincation Engineers, 2000).
[6] H. Hirakawa *et al.*, SID Digest 279 (Society for information Display, 1998).
[7] J. Meunier, Ph. Belenguer, and J. P. Boeuf, J. Appl. Phys. **78**, 731 (1995).
[8] C. Punset, J.-P. Boeuf, and L. C. Pitchford, J. Appl. Phys. **83**, 1884 (1998).
[9] R. Veerasingam, R. B. Campbell, and R. T. McGrath, IEEE Trans. Plasma Sci. **23**, 688 (1995).
[10] R. Veerasingam, R. B. Campbell, and R. T. McGrath, IEEE Trans. Plasma Sci. **24**, 1411 (1996).
[11] S. Rauf and M. J. Kushner, J. Appl. Phys. **85**, 3470 (1999).
[12] S. Rauf and M. J. Kushner, J. Appl. Phys. **85**, 3460 (1999).
[13] R. Snijkers and M. Klein, *52nd Gaseous Electronics Conference*, Norfolk, Virginia, 5–8 October 1999.
[14] G. Oversluizen and S. de Zwart (private communication).
[15] C. Punset, Th. Callegari, and J.-P. Boeuf, *Proceedings of the International Symposium on Future Emissive Displays*, Tottori University, Tottori, Japan, 10–11 December 1998, pp. 87–93.

Two-dimensional model of a stationary plasma thruster

G. J. M. Hagelaar,[a] J. Bareilles, L. Garrigues, and J. -P. Boeuf
Centre de Physique des Plasmas et Applications de Toulouse, Bâtiment 3R2, Université Paul Sabatier, 118 Route de Narbonne, 31062 Toulouse Cedex, France

(Received 4 December 2001; accepted for publication 5 February 2002)

Stationary plasma thrusters (SPTs) are advanced propulsion devices that use a gas discharge to ionize and accelerate the propellant. We present in detail a two-dimensional model of an SPT discharge. The model combines a particle simulation of neutral atoms and ions with a fluid description of electrons, where the electric field is obtained from imposing quasineutrality. The electron mobility and energy loss are treated in an empirical way and characterized by ad hoc parameters. Typical simulation results are shown. © *2002 American Institute of Physics.*
[DOI: 10.1063/1.1465125]

I. INTRODUCTION

Stationary plasma thrusters (SPTs), also known as Hall thrusters, are advanced electrostatic propulsion devices.[1] In an SPT, a propellant (typically xenon) is ionized by an electrical discharge. The electric field of the discharge subsequently accelerates the produced ions to a high exhaust velocity (~20 km/s). Because of this high exhaust velocity, SPTs consume, when providing a certain thrust, much less propellant than conventional chemical propulsion devices. SPTs have been developed for almost four decades now, mainly in Russia; many Russian satellites use them for station keeping and orbit correction. Since the late eighties, important SPT research and development efforts have been undertaken also in the US, Europe, and Japan.

Figure 1 shows a schematic picture of an SPT. The discharge takes place in an annularly shaped discharge channel (central radius ~4 cm, width ~1.5 cm, and length ~3 cm). External electromagnets generate a radial magnetic field in the channel, with a maximum strength (~0.02 T) near the channel exhaust. The discharge voltage (~300 V) is applied axially, between an anode at the closed end of the channel and an external hollow cathode, situated beyond the exhaust. The propellant is introduced in the channel via holes in the anode. The gas density ($\sim 10^{18}$–$10^{20}\,\mathrm{m}^{-3}$) is so low that the mean free paths of both electrons and ions are much larger than the channel dimensions. However, having a small Larmor radius (~1 mm), the electrons are confined by the magnetic field: they cycle around the magnetic field lines and at the same time drift in the azimuthal direction ($E\times B$ drift). Net electron transport in the axial direction (along the electric field) can take place only when collisions occur. The ion Larmor radius is relatively large (~1 m) so that the ion motion is nearly unaffected by the magnetic field and collisionless.

Up until now, the SPT discharge operation is far from fully understood. Within the past few years, several discharge models have been developed to better understand and predict the SPT discharge behavior. Most of these models are based on the ideas of the Russian SPT specialist Morozov,[2] combining a particle description of neutral atoms and ions with a fluid description of electrons. Among the first were the one-dimensional model of Boeuf and Garrigues,[3] which explained observed low-frequency discharge oscillations, and the two-dimensional model of Fife.[4]

In this article, we present a two-dimensional model of the SPT discharge, similar to Fife's model. We point out that, due to a lack of understanding of some of the involved physical phenomena, the model has some important empirical aspects. Our aim here is to document the principles of the model; some typical simulation results are presented for demonstration, but detailed results and parametric studies are saved for future publication.

II. DESCRIPTION OF THE MODEL

This section describes in detail the physical and numerical basis of our model.

A. Geometry

Only the axial and radial dimensions of the SPT geometry and discharge are represented in the model; azimuthal symmetry is assumed. The main computational grid is rectangular in cylinder coordinates. The two-dimensional calculation domain, which comprises both the discharge channel and the near exterior of the thruster, is shown in Fig. 2. The discharge is simulated only within a certain region that is confined by physical walls and magnetic field lines. Note that the magnetic field is curved and not perfectly radial, especially outside the channel.

B. Magnetic field

The magnetic field is assumed to be entirely determined by the electromagnets and to be unaffected by the discharge. This assumption is realistic and makes it possible to calculate the magnetic field *a priori* from

$$\nabla\cdot\mathbf{B}=\nabla\cdot\nabla\sigma=0, \tag{1}$$

where $\mathbf{B}$ is the magnetic field and σ is a magnetic potential. Rather than being calculated directly from the configuration

[a]Electronic mail: hagelaar@cpat.ups-tlse.fr

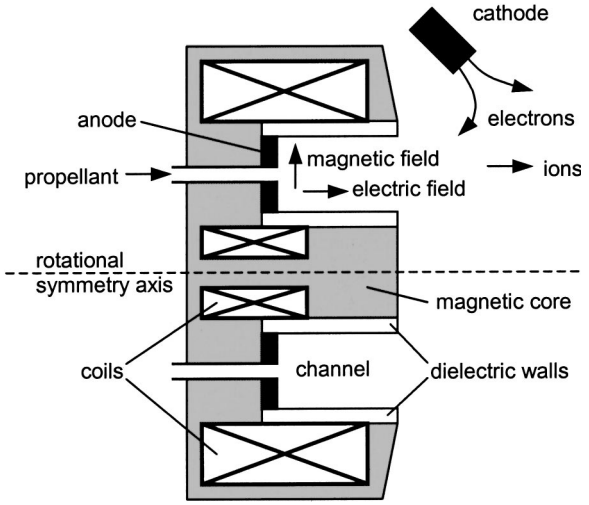

FIG. 1. Schematic picture of an SPT.

of electromagnets, the magnetic field in the discharge channel is obtained from a set of boundary values that are specified on the domain boundaries. This allows the direct implementation of experimental magnetic field data and the deliberate adjustment of the magnetic field, which is useful for studying its influence. However, Eq. (1) implies that the perpendicular magnetic field integrated over any closed surface must be zero. The specified boundary values are corrected in order to ensure this.

To facilitate the solution of the electron transport equations, a magnetic stream function λ is calculated from

$$\frac{\partial \lambda}{\partial x} = rB_r \quad \text{and} \quad \frac{\partial \lambda}{\partial r} = -rB_x, \tag{2}$$

where x and r are the axial and radial position coordinates and B_x and B_r are the axial and radial components of the magnetic field. The λ defined by these equations is constant along magnetic field lines ($\mathbf{B}\cdot\nabla\lambda=0$) and usually increases monotonically from anode to cathode. The cross field gradient of any quantity Q can be expressed in terms of λ as

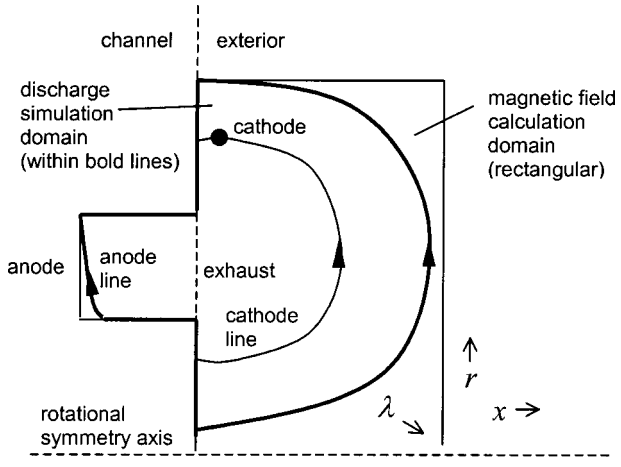

FIG. 2. SPT simulation domain.

$$\nabla_\perp Q = rB\frac{\partial Q}{\partial \lambda}, \tag{3}$$

which we will use in the following.

C. Neutral gas particles

We consider xenon as a propellant gas. The density of neutral xenon atoms in the thruster, essential to find the ionization rate and the electrical conductivity of the plasma, is obtained from a Monte Carlo simulation. That is, the individual paths of a large number of neutrals are calculated, where collisions are treated with random numbers. This approach is realistic but takes much computation time and introduces statistical errors.

The neutrals are introduced in the simulation at a certain injection region at the anode and are followed until they reach the right boundary of the geometry. Their initial velocity distribution is taken to be isotropic and Maxwellian with a temperature of typically about 500 K. Only collisions with walls are considered, in which the neutrals may be either specularly reflected or isotropically scattered. Neutral loss by ionization is implemented as follows: to each simulated neutral a certain weight w is attributed, which gradually decreases in time as

$$w = w_0 \exp(-nk_i t), \tag{4}$$

where w_0 is the initial weight, n is the local plasma density, k_i is the ionization rate coefficient dependent on the local electron mean energy, and t is the time. This technique leads to better statistics than simply eliminating neutrals from the simulation according to their ionization probability, especially beyond the exhaust where the neutral density may be quite low.

D. Ions

Only singly charged xenon ions are included in the model. Like the neutrals, the ions are described by a Monte Carlo simulation. They are introduced in the simulation at positions that are randomly chosen according to the ionization rate profile. The initial ion velocity distribution is isotropic and Maxwellian at the neutral gas temperature. The ions are assumed to be accelerated by the electric field only, i.e., to be insensitive to the magnetic field. Ion collisions are not considered. The ions are followed until they reach any of the boundaries of the simulation domain; ions striking the walls are thus assumed to recombine at the surface. Besides the ion density, the ion Monte Carlo simulation yields the ion flux and the ion energy distribution.

E. Electrons and electric field

The electrons are described by a fluid model, i.e., the behavior of the electron density, flux, and mean energy is described by the first few moments of the Boltzmann equation (transport equations). This approach incorporates many assumptions and is not entirely realistic. In view of the high plasma density in SPTs, it is assumed that the electron density is everywhere equal to the ion density. With this assumption, it becomes impossible to obtain the electric field from

Poisson's equation. Instead, knowing the electron density, we use the electron transport equations to calculate the electric field. Note that there is indeed a space charge; in reality Poisson's equation is valid.

The electron transport equations are: the continuity equation

$$\nabla \cdot \Gamma_e = Nnk_i - \frac{\partial n}{\partial t} = \nabla \cdot \Gamma_i, \tag{5}$$

the momentum equation, which we approximate by the drift–diffusion equation

$$\Gamma_e = -\mu \mathbf{E} n - \frac{2}{3e}\mu \nabla(n\epsilon), \tag{6}$$

and the energy equation

$$\frac{\partial(n\epsilon)}{\partial t} + \frac{5}{3}\nabla\cdot(\Gamma_e \epsilon) - \frac{10}{9e}\nabla\cdot(\mu n \epsilon \nabla \epsilon) = -e\mathbf{E}\cdot\Gamma_e - Nn\kappa - nW. \tag{7}$$

In these equations, n is the plasma density, Γ_e is the electron flux, ϵ is the electron mean energy, N is the gas density, Γ_i is the ion flux, $\mathbf{E}$ is the electric field, μ is the electron mobility, and e is the elementary charge. The last two terms in the energy equation represent energy loss by collisions with gas particles and with the walls, respectively, where κ and W are effective energy loss coefficients dependent on ϵ. The wall-loss coefficient W is further discussed in Sec. III B. Equations (6) and (7) assume the electron distribution to be Maxwellian and predominantly isotropic; the same assumption is used to obtain the collision coefficients k_i and κ from cross section data.

Due to the magnetic field, the mobility μ is not a simple scalar: its value is much larger for electron transport along magnetic field lines than for transport across them. From current conservation, however, it is clear that the electron flux can not be much larger along magnetic field lines than across them. This implies that along the field lines, the two terms of Eq. (6) should virtually cancel each other. Taking into account similar considerations for the electron energy flux, one can derive that the electron mean energy must be constant along magnetic field lines and that the electric potential V behaves as

$$V(x,r) = V^*(\lambda) + \frac{2}{3e}\epsilon(\lambda)\ln\frac{n(x,r)}{n_0}, \tag{8}$$

where V^* is a function and n_0 is a reference density. While V and n vary over all space, V^* and ϵ depend only on the stream function λ. Note that by using Eq. (8), we lose the possibility to calculate the electron flux along magnetic field lines from the drift-diffusion equation. For the cross field electron flux on the other hand, we find

$$\Gamma_{e,\perp} = rB\mu_\perp n\frac{\partial V}{\partial \lambda} - \frac{2}{3e}rB\mu_\perp \frac{\partial(n\epsilon)}{\partial\lambda} = rB\mu_\perp n\frac{\partial V^*}{\partial\lambda} + \frac{2}{3e}rB\mu_\perp n\left(\ln\frac{n}{n_0} - 1\right)\frac{\partial\epsilon}{\partial\lambda}, \tag{9}$$

where $\mu_\perp$ is now the cross field mobility, which is further discussed in Sec. III A.

Let us now define the following (surface!) integrals along magnetic field lines

$$c_1 = \iint \Gamma_{i,\perp}\, \mathrm{d}s, \tag{10}$$

$$c_2 = \iint rB\mu_\perp n\, \mathrm{d}s, \tag{11}$$

$$c_3 = \iint rB\mu_\perp n\left(\ln\frac{n}{n_0} - 1\right)\mathrm{d}s, \tag{12}$$

and (volume) integrals between consecutive field lines

$$c_4 = \iiint n\, \mathrm{d}v, \tag{13}$$

$$c_5 = \iiint Nn\, \mathrm{d}v, \tag{14}$$

$$c_6 = \iiint -eE_\perp \Gamma_{e,\perp}\, \mathrm{d}v, \tag{15}$$

where $\mathrm{d}s$ and $\mathrm{d}v$ are surface and volume elements.

Using these integrals, the continuity and momentum equations can be replaced by the following one-dimensional equation for current conservation:

$$\iint \Gamma_{e,\perp}\, \mathrm{ds} = c_2\frac{\partial V^*}{\partial\lambda} + \frac{2}{3e}c_3\frac{\partial\epsilon}{\partial\lambda} = c_1 - \frac{\beta}{e}I, \tag{16}$$

where I is the discharge current and β is a multiplicity factor representing the number of times the current crosses the field line, i.e., $\beta=1$ for the field lines between the anode and the cathode and 0 for field lines beyond the cathode. It is assumed that no current escapes to the walls.

In a similar way, the energy equation can be written as

$$\frac{\partial(c_{4,k}\epsilon_k)}{\partial t} + \frac{5}{3}\left(c_{1,k+1/2} - \frac{1}{e}\beta_{k+1/2}I\right)\epsilon_{k+1/2} - \frac{5}{3}\left(c_{1,k-1/2} - \frac{1}{e}\beta_{k-1/2}I\right)\epsilon_{k-1/2} - \frac{10}{9e}c_{2,k+1/2}\epsilon_{k+1/2}\left.\frac{\partial\epsilon}{\partial\lambda}\right|_{k+1/2} + \frac{10}{9e}c_{2,k-1/2}\epsilon_{k-1/2}\left.\frac{\partial\epsilon}{\partial\lambda}\right|_{k-1/2} = c_{6,k} - c_{5,k}\kappa_k - c_{4,k}W_k, \tag{17}$$

where $k+1/2$ and $k-1/2$ refer to two field lines, and k to the interval between them. This equation neglects electron transport to the surface and does not hold for the interval containing the cathode because of the strong electron inflow there.

From Eqs. (16) and (17), we calculate ϵ and V^* as a function of λ, fixing ϵ to a few eVs at the boundaries and at the cathode. Subsequently, the spatial profile of the electric potential is found from Eq. (8). The current in Eqs. (16) and (17) is chosen such that a specified voltage drop results between anode and cathode:

$$V_a - V_c = -\int_a^c \frac{\partial V^*}{\partial\lambda}d\lambda + \frac{2}{3e}\epsilon_a\ln\frac{n_a}{n_0} - \frac{2}{3e}\epsilon_c\ln\frac{n_c}{n_0}, \tag{18}$$

where the labels a and c refer to anode and cathode, and the $n_{a,c}$ are spatially averaged over the electrode lines. How exactly this is done is described in Sec. II F.

F. Numerical solution technique

The solution of the system of electron transport equations constitutes a delicate numerical problem and deserves some further description. The electron mean energy and the electric field are strongly coupled and can therefore not be calculated separately. Furthermore, the energy equation is nonlinear and its source term tends to produce numerical oscillations. Suppose that all quantities are known at a certain time t^l. We found the following numerical scheme to be most appropriate to calculate their values a moment Δt later, at time $t^{l+1}=t^l+\Delta t$:

(1) The ions and atoms in the Monte Carlo model are moved. This yields N^{l+1}, n^{l+1} and Γ_i^{l+1}.
(2) The integrals c^{l+1} are calculated; the electron heating integral is evaluated as

$$c_6^{l+1}=e\iiint r^2B^2\mu_\perp n^{l+1}\frac{\partial V^l}{\partial\lambda}\left(\frac{\partial V^{*l}}{\partial\lambda}+\frac{2}{3}\left(\ln\frac{n^{l+1}}{n_0}-1\right)\frac{\partial\epsilon^l}{\partial\lambda}\right)\mathrm{d}v. \tag{19}$$

(3) The discharge current is estimated from Eqs. (8), (16), and (18), as

$$I^{l+1}=e\left(V_a-V_c-\frac{2}{3e}\epsilon_a^l\ln\frac{n_a^{l+1}}{n_0}+\frac{2}{3e}\epsilon_c^l\ln\frac{n_c^{l+1}}{n_0}+\int_a^c\frac{c_1^{l+1}}{c_2^{l+1}}\mathrm{d}\lambda-\frac{2}{3e}\int_a^c\frac{c_3^{l+1}}{c_2^{l+1}}\frac{\partial\epsilon^l}{\partial\lambda}\mathrm{d}\lambda\right)\Bigg/\int_a^c\frac{\beta}{c_2^{l+1}}\mathrm{d}\lambda. \tag{20}$$

(4) The electron mean energy is calculated from the energy equation

$$\begin{aligned}&\frac{1}{\Delta t}(c_{4,k}^{l+1}\epsilon_k^{l+1}-c_{4,k}^l\epsilon_k^l)+\frac{5}{3}\left(c_{1,k+1/2}^{l+1}-\frac{1}{e}\beta_{k+1/2}I^{l+1}\right)\epsilon_{k+1/2}^{l+1}\\&-\frac{5}{3}\left(c_{1,k-1/2}^{l+1}-\frac{1}{e}\beta_{k-1/2}I^{l+1}\right)\epsilon_{k-1/2}^{l+1}\\&-\frac{10}{9e}c_{2,k+1/2}^{l+1}\epsilon_{k+1/2}^l\left.\frac{\partial\epsilon^{l+1}}{\partial\lambda}\right|_{k+1/2}\\&+\frac{10}{9e}c_{2,k-1/2}^{l+1}\epsilon_{k-1/2}^l\left.\frac{\partial\epsilon^{l+1}}{\partial\lambda}\right|_{k-1/2}\\&=c_{6,k}^{l+1}-c_{5,k}^{l+1}\kappa_k^l-c_{5,k}^{l+1}\left.\frac{\partial\kappa^l}{\partial\epsilon}\right|_k(\epsilon_k^{l+1}-\epsilon_k^l)\\&-c_{4,k}^{l+1}W_k^l-c_{4,k}^{l+1}\left.\frac{\partial W^l}{\partial\epsilon}\right|_k(\epsilon_k^{l+1}-\epsilon_k^l),\end{aligned} \tag{21}$$

in which the energy loss terms are linearly corrected for changes in the electron energy; this avoids strong time-step restrictions; for more details see Ref. 5. Note that the nonlinear terms on the left-hand side are linearized by partially evaluating them explicitly. We use an exponential scheme[6] to further discretize Eq. (21) in space, where the argument of the exponential functions is given by

$$3(\lambda_{k+1}-\lambda_k)(ec_{1,k+1/2}-\beta_{k+1/2}I)/c_{2,k+1/2}(\epsilon_{k+1}+\epsilon_k).$$

(5) The electric potential is calculated from current conservation

$$\frac{\partial V^{*l+1}}{\partial\lambda}=\frac{c_1^{l+1}}{c_2^{l+1}}-\frac{\beta}{ec_2^{l+1}}I^{l+1}-\frac{2c_3^{l+1}}{3ec_2^{l+1}}\frac{\partial\epsilon^{l+1}}{\partial\lambda}, \tag{22}$$

followed by

$$V^{l+1}=V^{*l+1}+\frac{2}{3e}\epsilon^{l+1}\ln\frac{n^{l+1}}{n_0}. \tag{23}$$

This scheme is very robust. Note that we use the same numerical time step for both the electron equations and the heavy particle Monte Carlo simulation. The simulation of 1 ms of SPT discharge operation, sufficient to see most of its temporal features, takes typically a few tens of minutes of CPU time on a 1 GHz personal computer (PC).

III. EMPIRICAL ASPECTS OF THE MODEL

The model described in Sec. II is incomplete without the formulation of the cross field electron mobility $\mu_\perp$ and the energy loss to the walls W. Unfortunately, a lack of understanding forces us to treat these quantities in a rather empirical, phenomenological way. We discuss this next.

A. Cross field electron mobility

Cross field electron mobility is a crucial parameter that has strong influence on the simulation results.[7] The classical expression for $\mu_\perp$ is given by

$$\mu_{\perp,c}=\frac{e\nu_m/m_e}{\nu_m^2+(eB/m_e)^2}\approx\frac{m_e\nu_m}{eB^2}, \tag{24}$$

where m_e is the electron mass and ν_m is the momentum–transfer frequency of electron–particle collisions. It is clear however that the classical mobility is too small to be realistic for the electron transport in SPTs, especially near and beyond the exhaust where the gas density is very low.

Apparently, there are additional mechanisms of electron transport. As a first additional mechanism, it is generally assumed that electron collisions with the channel walls cause momentum transfer, thus enabling cross field electron transport. This effect is sometimes referred to as near-wall conductivity or near-wall current.[8–10] In our model, it can be taken into account by including the momentum–transfer frequency of the wall collisions in the cross field mobility of Eq. (24). However, being dependent on the plasma sheath voltage and very sensitive to the electron energy distribution function, the wall–collision frequency is difficult to quantify.[10] Rough estimates yield 10^6–10^7 s^1. Therefore, we use, as in Ref. 3,

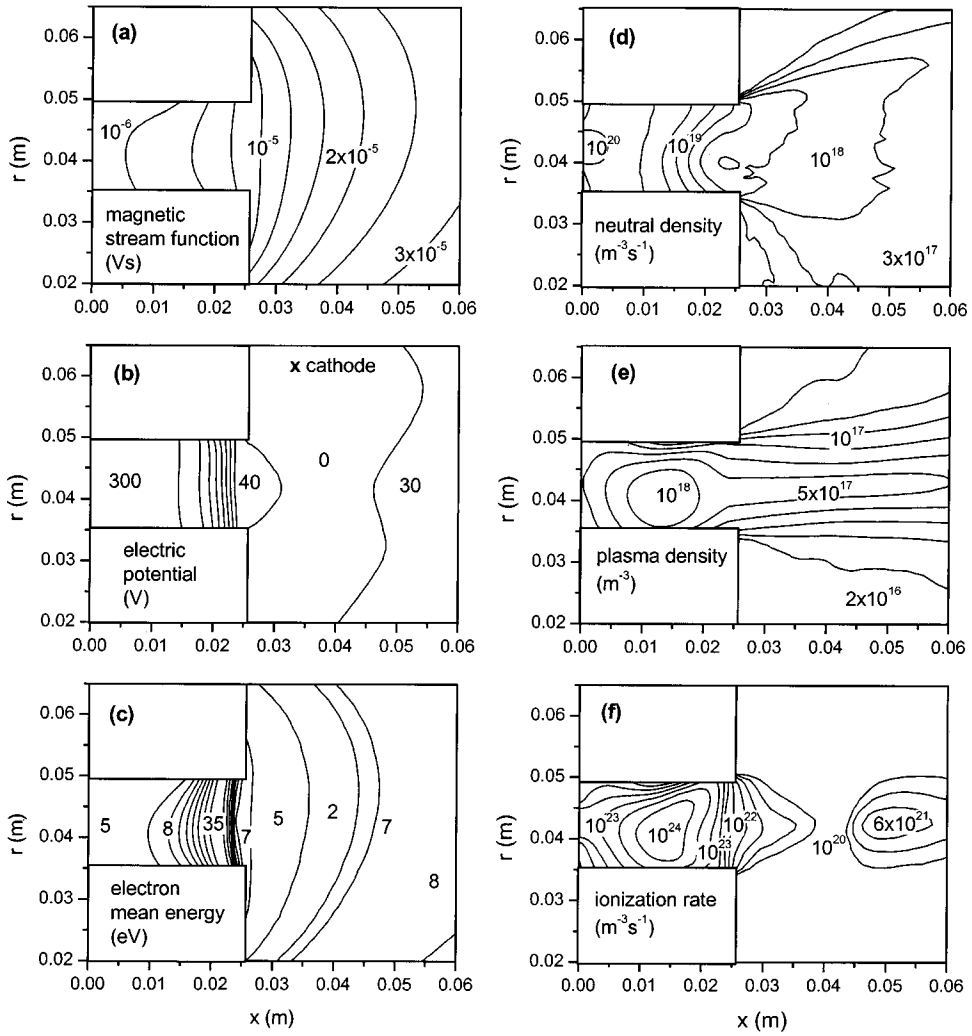

FIG. 3. Time-averaged profiles of various quantities in the typical simulation of an SPT discharge. Each plot shows ten equidistant contours, on the right-hand side in linear scale and on the left-hand side in a log scale covering three decades. Note that the plots show only a part of the simulation domain. The channel exhaust is at $x=0.025$ m; its inner and outer radii are 0.035 m and 0.05 m, respectively.

$$\nu_m = \nu_{m,\text{particles}} + \nu_{m,\text{walls}} = \nu_{m,\text{particles}} + \alpha \times 10^7 \quad (\text{s}^{-1}), \tag{25}$$

where α is a constant fitting parameter. We find that for α in the range 0.1–0.5, the discharge is reasonably simulated inside the channel (i.e., there is a qualitative agreement with experimental data).

Outside the channel wall collisions are not expected to be of much importance. Here most authors attribute the electron transport to the Bohm effect:[1,4] plasma fluctuations alow the electrons to cross the magnetic field. The resulting anomalous Bohm mobility is proportional to $1/B$; for some magnetized plasmas a proportionality constant of 1/16 has been found empirically. Outside the channel, we use therefore

$$\mu_\perp = \frac{K}{16B}, \tag{26}$$

where K is a fitting parameter. It turns out that in order to yield acceptable results, our simulation requires K to be on the order of 1.

Note that we do not use Bohm mobility inside the channel; mainly because we can not find reasonable simulation results if we do. Also, it has been suggested that the plasma is more stable where the magnetic field strength increases in the direction of the ion flow, i.e., inside the channel.[1] Note furthermore, that the Bohm mobility is orders of magnitude larger than the classical mobility; much larger also than the assumed mobility inside the channel, including the wall collisions.

Finally, we remark that exactly what kind of fluctuations would cause the Bohm effect in SPTs is unclear. Several mechanisms have been proposed. For instance, azimuthal plasma waves, not described by our model, can be shown to lead to an increased cross field electron transport behaving as $1/B$.[4] Full particle in cell (PIC) simulations reveal turbulence increasing the cross field transport.[11,12]

B. Electron energy loss

Electron energy loss due to collisions with neutrals is insufficient to explain observed electron mean energies.[4,13] It is believed that important additional energy loss is due to

electron-impact secondary-electron emission from the channel walls: when a high-energy electron strikes the wall, it is likely to cause the emission of a low-energy secondary electron. How this process takes place exactly and how much net energy loss it causes is unclear. In addition, as stated in the Sec. III A, it is difficult to calculate the frequency of the wall collisions. Some authors[4,10] argue that beyond a certain breakpoint energy, strong secondary-electron emission causes the plasma sheath to collapse, which results in an enormous wall-collision frequency and an enormous energy loss preventing the mean energy from increasing further. More detailed treatments[10,14,15] however show that the wall collisions depopulate the tail of the electron energy distribution, thus strongly reducing the effective secondary-emission coefficient and the energy loss at the wall.

In view of the this, we choose to use the phenomenological expression of Ref. 3,

$$W=\alpha_\epsilon\times 10^7 \epsilon \exp\left(-\frac{U}{\epsilon}\right) \quad (\mathrm{s}^{-1}), \tag{27}$$

where α and U are once again fitting parameters. This does not result from physical derivation, but is simply a convenient expression stating that the energy loss increases monotonically with increasing mean energy, becoming important beyond an energy U. We find reasonable simulation results using $U=20\,\mathrm{eV}$ and α_ϵ in the range 0.1–0.5.

IV. TYPICAL SIMULATION RESULTS

In this section we show simulation results for the typical conditions that the applied voltage is 300 V, the xenon debit is 5 mg/s, the wall parameters $\alpha=\alpha_\epsilon=0.1$, and the Bohm parameter $K=1$. The position of the cathode is marked in Fig. 3(b). The results presented here are in good qualitative agreement with experimental data from, for instance, Refs. 13, 16, and 17.

The two-dimensional plots of Fig. 3 demonstrate the main features of the discharge. The magnetic field is slightly curved so as to form a convex magnetic lense. Its strength, maximum at the exhaust, decreases only slowly outside the channel. The electric potential lines deviate significantly from the magnetic field lines due to the second term of Eq. (8). Most of the electric field is concentrated in a so-called acceleration region which is located near the exhaust, where the neutral density is so low that the electron mobility is determined by the wall collisions alone. Outside the channel the much larger Bohm mobility prevents a strong electric field; the potential drop outside is only about 50 V. Note that the abruptness of the transition from the high field inside to the low field outside reflects the discontinuity in the assumed electron mobility; a smooth transition would obviously be more realistic. The simulation suggests that beyond the cathode line the potential rises again to ensure an electron flux along with the ion flux. This rise has been reported previously in Ref. 18. It depends heavily on the assumed electron mobility outside the channel.

The plasma density is highest in the center of the channel and decreases in the acceleration region due to the increasing ion velocity. Ionization takes place in a region slightly shifted inward with respect to the acceleration region. This implies that most of the created ions will eventually leave the thruster with an energy approximately corresponding to the applied voltage. Deep into the channel the electric field is small and many produced ions are lost to the channel walls, where they recombine into neutrals.

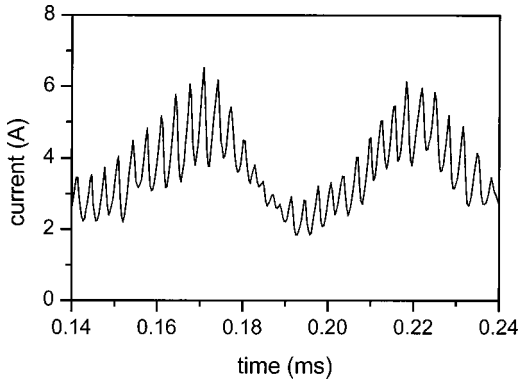

FIG. 4. Discharge current in a typical SPT simulation.

The results in Fig. 3 are time averaged; the simulation however shows oscillating discharge behavior. This is illustrated by Fig. 4, which presents the discharge current as a function of time. We find that the calculated oscillations depend strongly on the electron mobility parameters. In addition to the low frequency (15–20 kHz) oscillations previously reported in Ref. 3 and related to the depletion of neutrals, the simulation may develop high frequency (150–200 kHz) oscillations, related to local plasma density maxima traveling outward with the ion velocity. For the case shown here, both oscillations are present. We intend to elaborate further on the results of our model in a future article.

V. CONCLUSION

We have developed a two-dimensional hybrid model of an SPT discharge. The model provides a complete simulation of the temporal and spatial behavior of the discharge, both inside and outside the SPT channel. The numerical code is robust and efficient; a typical simulation takes a few tens of CPU minutes on a 1 GHz PC.

The model uses ad hoc empirical parameters to characterize the cross field electron mobility and the electron energy loss. By appropriately choosing these parameters, we can obtain simulation results that seem to be quite realistic and lead to useful insight in the operation of the SPT discharges. To perform quantitative predictions however we need more understanding and experimental evidence on the electron mobility and energy loss.

ACKNOWLEDGMENTS

The SPT model has been developed in the framework of the Groupement De Recherche CNRS/CNES/SNECMA/ONERA 2232 ''Propulsion Plasma pour Systèmes Spatiaux''. One of the authors (G.H.) would like to acknowledge support from the European Office of Aerospace Research and

Development, Air Force Office of Scientific Research, Air Force Research Laboratory, under Contract No. F61775-01-WE015.

[1] V. V. Zhurin, H. R. Kaufmann, and R. S. Robinson, Plasma Sources Sci. Technol. **8**, R1 (1999).
[2] A. I. Morozov, Y. V Esinchuk, G. N. Tilinin, A. V. Trofimov, Y. A. Sharov, and G. Y. Shchepkin, Sov. Phys. Tech. Phys. **17**, 38 (1972).
[3] J.-P. Boeuf and L. Garrigues, J. Appl. Phys. **84**, 3541 (2001).
[4] J. M. Fife, Ph.D. thesis, Massachusettes Institute of Technology, 1998.
[5] G. J. M. Hagelaar and G. M. W. Kroesen, J. Comput. Phys. **159**, 1 (2000).
[6] D. L. Scharfetter and H. K. Gummel, IEEE Trans. Electron Devices **16**, 64 (1969).
[7] G. J. M. Hagelaar, J. Bareilles, L. Garrigues, and J.-P. Boeuf, *Proceedings of the 27th International Electronic Propulsion Conference*, Pasadena, California, 15–19 October 2001, paper IEPC-01-28.
[8] A. I. Morozov, Sov. Phys. Tech. Phys. **32**, 901 (1987).
[9] A. I. Bugrova, A. I. Morozov, and V. K. Kharchevnikov, Sov. J. Plasma Phys. **16**, 849 (1991).
[10] A. I. Morozov, Sov. J. Plasma Phys. **17**, 393 (1991).
[11] M. Hirakawa and Y. Arakawa, *Proceedings of the 24th International Electronic Propulsion Conference*, Moscow, Russia, September 19–23 1995, paper IEPC-95-164.
[12] J. C. Adam and A. Héron, research reports of the Groupement De Recherche CNRS/CNES/SNECMA/ONERA 2232 (Ecole Polytechnique, Palaiseau, France, 2000–2001).
[13] A. M. Bishaev and V. Kim, Sov. Phys. Tech. Phys. **23**, 1055 (1978).
[14] N. B. Meezan and M. Cappelli, *Proceedings of the 27th International Electronic Propulsion Conference*, Pasadena, California, October 15–19 2001, paper IEPC-01-51.
[15] L. Jolivet and J. F. Roussel, IEEE Trans. Plasma Sci. (to be published).
[16] M. Touzeau *et al.*, Plasma Phys. Controlled Fusion **42**, B323 (2000).
[17] A. Bouchoule *et al.*, Plasma Sources Sci. Technol. **10**, 364 (2001).
[18] M. Keidar and I. D. Boyd, J. Appl. Phys. **86**, 4786 (1999).

INSTITUTE OF PHYSICS PUBLISHING PLASMA SOURCES SCIENCE AND TECHNOLOGY
Plasma Sources Sci. Technol. **14** (2005) 722–733 doi:10.1088/0963-0252/14/4/011

Solving the Boltzmann equation to obtain electron transport coefficients and rate coefficients for fluid models

G J M Hagelaar and L C Pitchford

Centre de Physique des Plasmas et de leurs Applications de Toulouse,
Université Paul Sabatier, 118 route de Narbonne, 31062 Toulouse Cedex 9, France

Received 13 June 2005
Published 5 October 2005
Online at stacks.iop.org/PSST/14/722

Abstract
Fluid models of gas discharges require the input of transport coefficients and rate coefficients that depend on the electron energy distribution function. Such coefficients are usually calculated from collision cross-section data by solving the electron Boltzmann equation (BE). In this paper we present a new user-friendly BE solver developed especially for this purpose, freely available under the name BOLSIG+, which is more general and easier to use than most other BE solvers available. The solver provides steady-state solutions of the BE for electrons in a uniform electric field, using the classical two-term expansion, and is able to account for different growth models, quasi-stationary and oscillating fields, electron–neutral collisions and electron–electron collisions. We show that for the approximations we use, the BE takes the form of a convection-diffusion continuity-equation with a non-local source term in energy space. To solve this equation we use an exponential scheme commonly used for convection-diffusion problems. The calculated electron transport coefficients and rate coefficients are defined so as to ensure maximum consistency with the fluid equations. We discuss how these coefficients are best used in fluid models and illustrate the influence of some essential parameters and approximations.

1. Introduction

Fluid models of gas discharges describe the transport of electrons, ions and possibly other reactive particle species by the first few moments of the Boltzmann equation (BE): (1) the continuity equation, (2) the momentum equation, usually approximated by the drift-diffusion equation and (3) the energy equation, usually only for electrons. Each of these equations contains transport coefficients or rate coefficients which represent the effect of collisions and which are input data for the fluid model [1–4] (see also references therein).

Transport coefficients and rate coefficients may be rather specific for the discharge conditions. In particular, coefficients concerning electrons depend on the electron energy distribution function (EEDF), which in general is not Maxwellian but varies considerably depending on the conditions. For simple conditions (swarm experiments) and common gases, the electron transport coefficients and rate coefficients have been measured and tabulated as functions of the reduced electric field E/N (ratio of the electric field strength to the gas particle number density) [5].

In general, the EEDF and the electron coefficients for the given discharge conditions can be calculated from the fundamental collision cross-section data by solving the electron BE [6]. A common approach is to solve some approximation of the BE for a series of reduced electric-field values and to put the resulting coefficients in tables versus the reduced field or versus the mean electron energy (disregarding the field values), which are then used in the fluid model to find the transport coefficients and rate coefficients by interpolation. Fluid models without electron energy equation treat the electron coefficients as functions of the local reduced field; models with an electron energy equation treat them as functions of the local mean electron energy.

The BE solvers used to generate the electron-related input data for fluid models are usually based on techniques developed during the 1970s and 1980s, when much work was done on the solution of the BE for the purpose of checking the consistency

between cross-section data and transport coefficients or rate coefficients measured in different experiments [7–16]. These solution techniques originally aimed at simulating specific experiments and calculating the exact physical quantities measured in these experiments with high numerical precision. For fluid discharge modelling, however, one has somewhat different objectives:

(1) the BE solver should work over a large range of discharge conditions (reduced electric field, ionization degree, gas composition, field frequency) rather than simulate a specific experiment;
(2) the calculated transport coefficients and rate coefficients should correspond formally to the same coefficients appearing in the fluid equations (moments of the BE) rather than to quantities measured in experiments; note that the literature gives different definitions of the transport coefficients, some of which are not completely consistent with the fluid equations;
(3) the errors in the calculated transport coefficients and rate coefficients should not limit the accuracy of the fluid model; this is a less strict requirement than the extreme precision (e.g. 0.1% in the drift velocity) needed for the cross-section testing of the 1970s and 1980s;
(4) the BE solver should be fast and reliable without ad hoc calculation parameters to adjust.

There exist several user-friendly BE solvers that are often used and cited by authors in the field of fluid discharge modelling; we mention in particular the commercial ELENDIF [13] and the freeware BOLSIG [17], but there are many others. These solvers however were not designed with the above objectives in mind: they can be applied only for a limited range of discharge conditions, are inconvenient to generate the tables of coefficients or are ill-documented (especially the popular BOLSIG), making it difficult to evaluate the appropriateness of their results for fluid modelling. For years we have felt the need for a new BE solver, able to deal with a larger range of discharge conditions, faster, easier to use and paying more attention to a consistent definition of the calculated coefficients. This is the reason why we have recently developed a new user-friendly BE solver and made it freely available to the discharge modelling community under the name BOLSIG+ [18].

In this paper we document BOLSIG+ in detail. We discuss its physical approximations, numerical techniques, calculated transport coefficients and rate coefficients, and how to use these coefficients in fluid models. In doing so, we provide an extensive discussion on the topic of solving the BE to obtain input data for fluid models. We believe that this is extremely useful: although the techniques used by BOLSIG+ and described in this paper may be well known to BE specialists, developers and users of fluid models are often not aware of them and have little feeling for the precision of the calculated coefficients. The existing literature on BE calculations is so specialized, focusing on specific details, that it is hard to see the consequences for fluid models. This paper looks at the BE from the point of view of a fluid modeller.

2. Boltzmann equation solver

In the following sections we document the physical assumptions and numerical techniques used by our BE solver. We indicate the relation with previous work without trying to be exhaustive; the literature on the electron BE in this context is vast.

The BE for an ensemble of electrons in an ionized gas is

$$\frac{\partial f}{\partial t} + \boldsymbol{v} \cdot \nabla f - \frac{e}{m}\boldsymbol{E} \cdot \nabla_{\mathbf{v}} f = C[f], \tag{1}$$

where f is the electron distribution in six-dimensional phase space, $\boldsymbol{v}$ are the velocity coordinates, e is the elementary charge, m is the electron mass, $\boldsymbol{E}$ is the electric field, $\nabla_{\mathbf{v}}$ is the velocity-gradient operator and C represents the rate of change in f due to collisions.

To be able to solve the BE, we need to make drastic simplifications. To start with, we limit ourselves to the case where the electric field and the collision probabilities are all spatially uniform, at least on the scale of the collisional mean free path. The electron distribution f is then symmetric in velocity space around the electric field direction. In position space f may vary only along the field direction. Using spherical coordinates in velocity space, we obtain

$$\frac{\partial f}{\partial t} + v\cos\theta\frac{\partial f}{\partial z} - \frac{e}{m}E\left(\cos\theta\frac{\partial f}{\partial v} + \frac{\sin^2\theta}{v}\frac{\partial f}{\partial\cos\theta}\right) = C[f], \tag{2}$$

where v is the magnitude of the velocity, θ is the angle between the velocity and the field direction and z is the position along this direction.

The electron distribution f in equation (2) depends on four coordinates: v, θ, t and z. The next few sections describe how we deal with this. We simplify the θ-dependence by the classical two-term approximation (section 2.1). To simplify the time dependence, we only consider steady-state cases where the electric field and the electron distribution are either stationary or oscillate at high frequency (section 2.3). Additional exponential dependence of f on t or on z is assumed to account for electron production or loss due to ionization and attachment (section 2.2). We then describe the collision term (section 2.4), put all pieces together into one equation for the EEDF (section 2.5), and discuss the numerical techniques we use to solve this equation (section 2.6).

2.1. Two-term approximation

A common approach to solve equation (2) is to expand f in terms of Legendre polynomials of $\cos\theta$ (spherical harmonics expansion) and then construct from equation (2) a set of equations for the expansion coefficients. For high precision results six or more expansion terms are needed [15], but for many cases a two-term approximation already gives useful results. This two-term approximation is often used (e.g. by the BE solvers BOLSIG and ELENDIF) and has been extensively discussed in the literature [19, 20]. Although the approximation is known to fail for high values of E/N when most collisions are inelastic and f becomes strongly anisotropic [21], the errors in the calculated transport coefficients and rate coefficients are acceptable for fluid discharge modelling in the usual range of discharge conditions. Note that when the two-term approximation fails, some other, intrinsic approximations of fluid models also fail.

Using the two-term approximation we expand f as

$$f(v, \cos\theta, z, t) = f_0(v, z, t) + f_1(v, z, t)\cos\theta, \quad (3)$$

where f_0 is the isotropic part of f and f_1 is an anisotropic perturbation. Note that θ is defined with respect to the field direction, so f_1 is negative; this differs from some other texts where θ is defined with respect to the electron drift velocity and f_1 is positive. Also note that f is normalized as

$$\iiint f \,\mathrm{d}^3v = 4\pi \int_0^\infty f_0 v^2 \,\mathrm{d}v = n, \quad (4)$$

where n is the electron number density.

Equations for f_0 and f_1 are found from equation (2) by substituting equation (3), multiplying by the respective Legendre polynomials (1 and $\cos\theta$) and integrating over $\cos\theta$:

$$\frac{\partial f_0}{\partial t} + \frac{\gamma}{3}\varepsilon^{1/2}\frac{\partial f_1}{\partial z} - \frac{\gamma}{3}\varepsilon^{-1/2}\frac{\partial}{\partial \varepsilon}(\varepsilon E f_1) = C_0, \quad (5)$$

$$\frac{\partial f_1}{\partial t} + \gamma\varepsilon^{1/2}\frac{\partial f_0}{\partial z} - E\gamma\varepsilon^{1/2}\frac{\partial f_0}{\partial \varepsilon} = -N\sigma_\mathrm{m}\gamma\varepsilon^{1/2} f_1, \quad (6)$$

where $\gamma = (2e/m)^{1/2}$ is a constant and $\varepsilon = (v/\gamma)^2$ is the electron energy in electronvolts. The right-hand side of equation (5) represents the change in f_0 due to collisions and will be discussed in detail in section 2.4. The right-hand side of equation (6) contains the total momentum-transfer cross-section σ_m consisting of contributions from all possible collision processes k with gas particles:

$$\sigma_\mathrm{m} = \sum_k x_k \sigma_k, \quad (7)$$

where x_k is the mole fraction of the target species of the collision process; realize that the gas can be a mixture of different species, including excited states[1]. For elastic collisions, σ_k is the effective momentum-transfer cross-section, as clearly discussed in [22], accounting for possible anisotropy of the elastic scattering. For inelastic collisions, σ_k is the total cross section, assuming that all momentum is lost in the collision, i.e. that the remaining electron velocity after the collision is scattered isotropically. One needs to be careful about the definition of σ_m: omitting, for example, the contribution from inelastic collisions completely changes the calculation results; some data for σ_m in the literature are unclear on this point.

2.2. Growth of the electron density

We further simplify equations (5) and (6) by making assumptions about the temporal and spatial dependence of f_0 and f_1. In general f cannot be constant in both time and space because some collision processes (ionization, attachment) do not conserve the total number of electrons. Previous work [19, 22–24] proposed a simple technique to approximately describe the effects of net electron production in swarm type experiments. Following this technique, we separate the energy-dependence of f from its dependence on time and space by assuming that

$$f_{0,1}(\varepsilon, z, t) = \frac{1}{2\pi\gamma^3} F_{0,1}(\varepsilon) n(z, t), \quad (8)$$

where the energy distribution $F_{0,1}$ is constant in time and space and normalized by

$$\int_0^\infty \varepsilon^{1/2} F_0 \,\mathrm{d}\varepsilon = 1. \quad (9)$$

The time or space dependence of the electron density n is now related to the net electron production rate. For this, we consider two simple cases corresponding to specific swarm experiments. Most discharges resemble at least one of these cases.

Exponential temporal growth without space dependence. This case corresponds to Pulsed Townsend experiments [11]. The temporal growth rate of the electron number density equals the net production frequency $\bar{\nu}_i$:

$$\frac{1}{n_\mathrm{e}}\frac{\partial n_\mathrm{e}}{\partial t} = \bar{\nu}_i \equiv N\gamma \int_0^\infty \left(\sum_{k=\text{ionization}} x_k\sigma_k - \sum_{k=\text{attachment}} x_k\sigma_k \right) \times \varepsilon F_0 \,\mathrm{d}\varepsilon, \quad (10)$$

where the sum is over the ionization and attachment processes; we remind that x_k is the mole fraction of the target species of collision process k.

Equation (6) becomes

$$F_1 = \frac{E}{N}\frac{1}{\tilde{\sigma}_\mathrm{m}}\frac{\partial F_0}{\partial \varepsilon}, \quad (11)$$

where

$$\tilde{\sigma}_\mathrm{m} = \sigma_\mathrm{m} + \frac{\bar{\nu}_i}{N\gamma\varepsilon^{1/2}}. \quad (12)$$

Substituting this in equation (5), we find

$$-\frac{\gamma}{3}\frac{\partial}{\partial\varepsilon}\left(\left(\frac{E}{N}\right)^2 \frac{\varepsilon}{\tilde{\sigma}_\mathrm{m}}\frac{\partial F_0}{\partial\varepsilon}\right) = \tilde{C}_0 + \tilde{R}, \quad (13)$$

where the collision term

$$\tilde{C}_0 = 2\pi\gamma^3\varepsilon^{1/2}\frac{C_0}{Nn} \quad (14)$$

has been divided by the gas density N and the electron density n with respect to the collision term C_0 in equation (5), which makes it largely independent of these densities[2]. The term

$$\tilde{R} = -\frac{\bar{\nu}_i}{N}\varepsilon^{1/2} F_0 \quad (15)$$

ensures that F_0 remains normalized to unity in the case of net electron production. Previous work [23] interpreted this term as the energy needed to heat the secondary electrons up to the mean electron energy.

[1] The momentum-transfer cross-section σ_m appearing in equation (5) is equivalent to the diffusion cross section discussed in [22]. It can also be identified with the effective momentum-transfer cross-section derived from analysis of swarm experiments, at least at low E/N where ionization can be treated as an excitation process.

[2] Note that $\tilde{C}_0$ and C_0 are physical quantities and not collision operators as used in some other texts.

Exponential spatial growth without time dependence. This case corresponds to Steady State Townsend experiments [11]. While the electrons drift against the electric field their flux and density grow exponentially with a constant spatial growth rate α (Townsend coefficient), which is related to the net electron production by

$$\alpha \equiv -\frac{1}{n}\frac{\partial n}{\partial z} = -\frac{\bar{\nu}_i}{w}, \tag{16}$$

where the mean velocity w is determined by F_1, constant in space and negative.

Using the definition of α, equation (6) becomes

$$F_1 = \frac{1}{\sigma_m}\left(\frac{E}{N}\frac{\partial F_0}{\partial \varepsilon} + \frac{\alpha}{N}F_0\right) \tag{17}$$

and equation (5) can again be written in the form

$$-\frac{\gamma}{3}\frac{\partial}{\partial \varepsilon}\left(\left(\frac{E}{N}\right)^2 \frac{\varepsilon}{\tilde{\sigma}_m}\frac{\partial F_0}{\partial \varepsilon}\right) = \tilde{C}_0 + \tilde{R}, \tag{18}$$

where this time $\tilde{\sigma}_m = \sigma_m$ and the growth-renormalization term is

$$\tilde{R} = \frac{\alpha}{N}\frac{\gamma}{3}\left[\frac{\varepsilon}{\sigma_m}\left(2\frac{E}{N}\frac{\partial F_0}{\partial \varepsilon} + \frac{\alpha}{N}F_0\right) + \frac{E}{N}F_0\frac{\partial}{\partial \varepsilon}\left(\frac{\varepsilon}{\sigma_m}\right)\right]. \tag{19}$$

The value of α is found from combining equations (16) and (17):

$$w = \frac{1}{3}\gamma\int_0^\infty F_1 \varepsilon \,\mathrm{d}\varepsilon \equiv -\mu E + \alpha D = -\frac{\bar{\nu}_i}{\alpha}, \tag{20}$$

which yields

$$\alpha = \frac{1}{2D}(\mu E - \sqrt{(\mu E)^2 - 4D\bar{\nu}_i}), \tag{21}$$

where μ and D are written out and identified with the mobility and the diffusion coefficient, respectively, in section 3.1.

2.3. High frequency fields

The quasi-stationary approach of the previous sections assumes that the electric field remains constant on the time scale of the collisions. With some slight modifications, however, the same approach can also be used for high-frequency oscillating fields [19]. Using the complex notation, we express the oscillating electric field as

$$E(t) = E_0\,\mathrm{e}^{\mathrm{i}\omega t}. \tag{22}$$

Rather than equation (3), we use the following two-term approximation:

$$f(v, \cos\theta, z, t) = f_0(v, z, t) + f_1(v, z, t)\cos\theta\,\mathrm{e}^{\mathrm{i}\omega t}, \tag{23}$$

where the time-variation of f_0 and f_1 is slow with respect to the oscillation; f_1 may be complex to account for phase shifts with respect to the electric field.

Equation (23) is appropriate if the field frequency is so high that the electron energy lost over one field cycle is small. For elastic collisions this implies that the field frequency should be much greater than the collision frequency times the ratio of the electron mass to the gas particle mass: $\omega/N \gg (2m/M)\sigma_m\gamma\varepsilon^{1/2}$. A frequency limit related to inelastic collisions is more difficult to estimate. In practice equation (23) is reasonable for field frequencies in the gigahertz range (microwave discharges) and beyond (optical breakdown). For intermediate field frequencies, where the energy transfer per cycle is neither full nor negligible, a more complete solution of the time-dependent BE is necessary [25].

Using equation (23), we proceed exactly as before. Only the temporal growth model makes sense, because the high frequency field does not lead to time-averaged transport, and we find

$$F_1 = \frac{E_0}{N}\frac{\tilde{\sigma}_m - \mathrm{i}q}{\tilde{\sigma}_m^2 + q^2}\frac{\partial F_0}{\partial \varepsilon}, \tag{24}$$

where $\tilde{\sigma}_m = \sigma_m + \bar{\nu}_i/N\gamma\varepsilon^{1/2}$ and $q = \omega/N\gamma\varepsilon^{1/2}$. Substituting this in the equation for F_0 and averaging the energy absorption over the field cycle, we finally obtain

$$-\frac{\gamma}{3}\frac{\partial}{\partial \varepsilon}\left(\left(\frac{E_0}{N}\right)^2 \frac{\tilde{\sigma}_m \varepsilon}{2(\tilde{\sigma}_m^2 + q^2)}\frac{\partial F_0}{\partial \varepsilon}\right) = \tilde{C}_0 + \tilde{R}, \tag{25}$$

where the growth-renormalization term $\tilde{R}$ is given by equation (15).

We remark that in the case of a constant momentum-transfer frequency $\nu = \tilde{\sigma}_m N\gamma\varepsilon^{1/2}$ (σ_m is inversely proportional to $\varepsilon^{1/2}$), equation (25) can be written exactly as equation (13) for a stationary electric field, where the field E is replaced by an effective field $E_{\mathrm{eff}} = 2^{-1/2}(1 + \omega^2/\nu^2)^{-1/2}E_0$. This concept of effective field is used by some authors [26] to relate the EEDF and the electron properties in oscillating fields to those in dc fields.

2.4. Collision terms

The right-hand sides of equations (13), (18) and (25) contain the collision term consisting of contributions from all different collision processes k with neutral gas particles and from electron–electron collisions:

$$\tilde{C}_0 = \sum_k \tilde{C}_{0,k} + \tilde{C}_{0,e}. \tag{26}$$

Here we describe these contributions in detail.

Elastic collisions. The effect of elastic collisions can be described by [20]

$$\tilde{C}_{0,k=\mathrm{elastic}} = \gamma x_k \frac{2m}{M_k}\frac{\partial}{\partial \varepsilon}\left[\varepsilon^2\sigma_k\left(F_0 + \frac{k_B T}{e}\frac{\partial F_0}{\partial \varepsilon}\right)\right], \tag{27}$$

where M_k is the mass of the target particles and T is their temperature. The first term represents the kinetic energy lost to the target particles and the second term is the energy gained from the target particles assuming that these are Maxwellian; this term is important only at very low E/N.

Excitation/de-excitation. Excitation and de-excitation collisions cause a discrete energy loss or gain, continuously removing electrons from the energy distribution and reinserting them somewhere else [19]:

$$\tilde{C}_{0,k=\text{inelastic}} = -\gamma x_k[\varepsilon\sigma_k(\varepsilon)F_0(\varepsilon) - (\varepsilon+u_k)\sigma_k(\varepsilon+u_k)\,F_0(\varepsilon+u_k)], \tag{28}$$

where u_k is the threshold energy of the collision and is negative for de-excitation. The two terms are known, respectively, as the scattering-out and scattering-in terms; the scattering-in term clearly vanishes for $\varepsilon < -u_k$ in the case of de-excitation.

Ionization. The effect of ionization depends on how the remaining energy is shared by the two electrons after ionization. For some gases differential cross sections can be found for the energy sharing, which usually show that the energy is shared less equally as the remaining energy is large [27]. Here we consider only the two limiting cases of equal and zero energy sharing. In the case of equal energy sharing:

$$\tilde{C}_{0,k=\text{ionization}} = -\gamma x_k[\varepsilon\sigma_k(\varepsilon)F_0(\varepsilon) - 2(2\varepsilon+u_k)\sigma_k(2\varepsilon+u_k)F_0(2\varepsilon+u_k)], \tag{29}$$

where the factor 2 in the scattering-in term represents the secondary electrons being inserted at the same energy as the primary electrons. In case the primary electron takes all remaining energy (zero sharing)

$$\tilde{C}_{0,k=\text{ionization}} = -\gamma x_k[\varepsilon\sigma_k(\varepsilon)F_0(\varepsilon) - (\varepsilon+u_k)\sigma_k(\varepsilon+u_k)F_0(\varepsilon+u_k)] + \delta(\varepsilon)\gamma x_k\int_0^\infty u\sigma_k(u)F_0(u)\,\mathrm{d}u, \tag{30}$$

where δ is the Dirac delta-function. The last term denotes the secondary electrons, which are all inserted at zero energy.

Attachment. Attachment simply removes electrons from the energy distribution:

$$\tilde{C}_{0,k=\text{attachment}} = -\gamma x_k\varepsilon\sigma_k(\varepsilon)F_0(\varepsilon). \tag{31}$$

Electron–electron collisions. Previous work [9] gives the following expression for the collision term due to electron–electron collisions, assuming the electron distribution to be isotropic:

$$\tilde{C}_{0,e} = a\frac{n}{N}\left[3\varepsilon^{1/2}F_0^2 + 2\varepsilon^{3/2}\frac{\partial\psi}{\partial\varepsilon}\frac{\partial}{\partial\varepsilon}\left(\varepsilon^{1/2}\frac{\partial F_0}{\partial\varepsilon}\right) + \psi\frac{\partial F_0}{\partial\varepsilon}\right], \tag{32}$$

where

$$\psi = 3A_1 - \frac{A_2}{\varepsilon} + 2\varepsilon^{1/2}A_3, \tag{33}$$

$$A_1 = \int_0^\varepsilon u^{1/2}F_0(u)\,\mathrm{d}u, \tag{34}$$

$$A_2 = \int_0^\varepsilon u^{3/2}F_0(u)\,\mathrm{d}u, \tag{35}$$

$$A_3 = \int_\varepsilon^\infty F_0(u)\,\mathrm{d}u, \tag{36}$$

$$a = \frac{e^2\gamma}{24\pi\varepsilon_0^2}\ln\Lambda, \qquad \Lambda = \frac{12\pi(\varepsilon_0 k_\mathrm{B}T_\mathrm{e})^{3/2}}{e^3 n^{1/2}}, \qquad k_\mathrm{B}T_\mathrm{e} = \frac{2}{3}eA_2(\infty). \tag{37}$$

After some manipulation this becomes:

$$\tilde{C}_{0,e} = a\frac{n}{N}\frac{\partial}{\partial\varepsilon}\left[3A_1F_0 + 2(A_2+\varepsilon^{3/2}A_3)\frac{\partial F_0}{\partial\varepsilon}\right], \tag{38}$$

which expresses the electron–electron collision term as the divergence of the electron flux in energy space. The first term of the flux represents cooling by collisions with colder electrons (A_1 is the fraction of electrons below ε) and the second term is usually heating (diffusion to higher energies). For a Maxwellian distribution function the two terms cancel out, as can be readily seen by substituting $F_0 \propto \exp(-\varepsilon/\tau)$ for arbitrary τ.

2.5. Equation for the EEDF

When combining the previous equations, we find an equation for F_0 that looks like a convection-diffusion continuity-equation in energy space:

$$\frac{\partial}{\partial\varepsilon}\left(\tilde{W}F_0 - \tilde{D}\frac{\partial F_0}{\partial\varepsilon}\right) = \tilde{S}, \tag{39}$$

where

$$\tilde{W} = -\gamma\varepsilon^2\sigma_\varepsilon - 3a\frac{n}{N}A_1, \tag{40}$$

$$\tilde{D} = \frac{\gamma}{3}\left(\frac{E}{N}\right)^2\frac{\varepsilon}{\tilde{\sigma}_\mathrm{m}} + \frac{\gamma k_\mathrm{B}T}{e}\varepsilon^2\sigma_\varepsilon + 2a\frac{n}{N}(A_2+\varepsilon^{3/2}A_3), \tag{41}$$

$$\sigma_\varepsilon = \sum_{k=\text{elastic}}\frac{2m}{M_k}x_k\sigma_k, \tag{42}$$

$$\tilde{S} = \sum_{k=\text{inelastic}}\tilde{C}_{0,k} + G. \tag{43}$$

It is instructive to interpret the left-hand side of equation (39) as the divergence of the electron flux in energy space. This flux then has a convection part with a negative flow velocity $\tilde{W}$, representing cooling by elastic collisions with less energetic particles (neutrals or electrons), and a diffusive part with diffusion coefficient $\tilde{D}$, representing heating by the field and by elastic collisions with more energetic particles. Note that in the case of HF fields the heating term is modified as discussed in section 2.3. Note also that the source term $\tilde{S}$ on the right-hand side of equation (39) has the special property that it is non-local: due to the scattering-in terms it depends on energies elsewhere in energy space. This means that the equation is no ordinary differential equation and solving it requires some special care.

2.6. Numerical solution of the equation

Equation (39) is discretized on a grid in energy space, consisting of a series of subsequent energy intervals, here called grid cells, numbered $i = 1, 2, \ldots$. The subscript i refers to the centre of the grid cell i and the subscript $i+\frac{1}{2}$ to the boundary between the cells i and $i+1$. The energy distribution function F_0 is defined in the cell centres. For each cell i we obtain a linear equation relating the local value $F_{0,i}$ to the values $F_{0,j}$ in the other cells, by integrating the differential equation over the cell:

$$\left[\tilde{W}F_0 - \tilde{D}\frac{\partial F_0}{\partial\varepsilon}\right]_{i+1/2} - \left[\tilde{W}F_0 - \tilde{D}\frac{\partial F_0}{\partial\varepsilon}\right]_{i-1/2} = \int_{\varepsilon_{i-1/2}}^{\varepsilon_{i+1/2}}\tilde{S}\,\mathrm{d}\varepsilon \tag{44}$$

and then discretizing the various terms.

The left-hand side of the equation is discretized by the exponential scheme of Scharfetter and Gummel [28] commonly used for convection-diffusion problems:

$$\left[\tilde{W}F_0 - \tilde{D}\frac{\partial F_0}{\partial \varepsilon}\right]_{i+1/2} = \frac{\tilde{W}_{i+1/2}F_{0,i}}{1-\exp[-z_{i+1/2}]} + \frac{\tilde{W}_{i+1/2}F_{0,i+1}}{1-\exp[z_{i+1/2}]}, \tag{45}$$

where $z_{i+1/2} = \tilde{W}_{i+1/2}(\varepsilon_{i+1}-\varepsilon_i)/\tilde{D}_{i+1/2}$ (Peclet number). This scheme is very accurate when the convection and diffusion terms are about equal, i.e. when inelastic collisions play no important role, and becomes equivalent to a second-order accurate central-difference scheme when the diffusion term is dominant. The electron–electron collision terms in $\tilde{W}$ and $\tilde{D}$ depend on F_0 and require iteration. To speed up convergence these terms are implicitly corrected. In addition, we start the iteration procedure from a Maxwellian distribution function at a temperature deduced from the global energy balance of the electrons.

The inelastic collision terms on the right-hand side are non-local in energy but linear in F_0 and are evaluated fully implicitly, which involves direct inversion of a matrix that is more or less sparse, depending on the different threshold energies of the collisions. We discretize as follows:

$$\int_{\varepsilon_{i-1/2}}^{\varepsilon_{i+1/2}} \tilde{S}\,\mathrm{d}\varepsilon \equiv -P_i F_{0,i} + \sum_j Q_{i,j}F_{0,j}, \tag{46}$$

where the two terms represent scattering-out and scattering-in:

$$P_i = \sum_{\text{inelastic}} \gamma x_k \int_{\varepsilon_{i-1/2}}^{\varepsilon_{i+1/2}} \varepsilon\sigma_k \exp[(\varepsilon_i-\varepsilon)g_i]\,\mathrm{d}\varepsilon, \tag{47}$$

$$Q_{i,j} = \sum_{\text{inelastic}} \gamma x_k \int_{\varepsilon_1}^{\varepsilon_2} \varepsilon\sigma_k \exp[(\varepsilon_j-\varepsilon)g_j]\,\mathrm{d}\varepsilon, \tag{48}$$

where the interval $[\varepsilon_1, \varepsilon_2]$ is the overlap of cell j, and cell i shifted by the threshold energy u_k:

$$\varepsilon_1 = \min(\max(\varepsilon_{i-1/2}+u_k, \varepsilon_{j-1/2}), \varepsilon_{j+1/2}), \tag{49}$$

$$\varepsilon_2 = \min(\max(\varepsilon_{i+1/2}+u_k, \varepsilon_{j-1/2}), \varepsilon_{j+1/2}). \tag{50}$$

The exponential factors in the P- and Q-integrals assume the distribution F_0 to be piecewise exponential, with a (local) logarithmic slope estimated as

$$g_i = \frac{1}{\varepsilon_{i+1}-\varepsilon_{i-1}} \ln\left(\frac{F_{0,i+1}}{F_{0,i-1}}\right). \tag{51}$$

This technique requires iteration but converges extremely rapidly. The P- and Q-integrals are calculated exactly, assuming the cross sections to be linear in between the points specified by the user in a table of cross section versus energy.

For simplicity we have not written out the effects of ionization or attachment in the above equations. In the case of ionization the scattering-in term accounts for the secondary electrons, as discussed before, and in the case of attachment there is no scattering-in. In either case an additional growth-renormalization term is included accounting for temporal or spatial growth, as discussed before. The growth-renormalization term is non-linear in F_0 and also requires iteration. To ensure convergence, however, this term must be linearized and partly evaluated implicitly. We use different ways of linearizing this term depending on the growth type (temporal growth or spatial growth) and on the sign of the net electron production (production or loss). We impose that the term integrated over all energies equals exactly the net production.

We impose the boundary condition that there is no flux in energy space at zero energy. In addition we impose the normalization condition.

3. Coefficients for fluid equations

Although more flexible than BOLSIG and most other solvers, our BE solver only describes the simplest discharge conditions: uniform electric field, uniform or exponentially growing electron density, etc. We now want to use the results from the BE solver to obtain transport coefficients and rate coefficient for fluid models which describe much more general conditions: arbitrarily varying electric fields, electron densities, etc. This implies a generalization of the coefficients as a function of E/N or mean electron energy, which is difficult to justify and should be seen as just an assumption made out of technical necessity. However, if we are careful about the definition of the coefficients, we can ensure that whenever the fluid model is used for the simple conditions assumed by the BE solver, it yields exactly the same mean velocity and mean energy as the solver. We thus obtain maximum consistency between the fluid model and the BE.

In order to find out how best to calculate the transport coefficients and rate coefficients from the energy distribution function F_0, we need to make the link between the two-term formulation of the BE equation, represented by equations (5) and (6), and the fluid equations. In the next few sections we discuss this for common fluid equations and their coefficients.

3.1. Electron transport

The continuity equation for electrons can be obtained from equation (5) by multiplying by $\varepsilon^{1/2}$ and integrating over all energies:

$$\frac{\partial n}{\partial t} + \frac{\partial \Gamma}{\partial z} = S, \tag{52}$$

where S is the net electron source term and the electron flux is

$$\Gamma = nw = n\frac{\gamma}{3}\int_0^\infty \varepsilon F_1\,\mathrm{d}\varepsilon. \tag{53}$$

Combining this with equation (6), we find the well-known drift-diffusion equation

$$\Gamma = -\mu E n - \frac{\partial(Dn)}{\partial z}, \tag{54}$$

where the mobility and diffusion coefficient are given by

$$\mu N = -\frac{\gamma}{3}\int_0^\infty \frac{\varepsilon}{\tilde{\sigma}_\mathrm{m}}\frac{\partial F_0}{\partial \varepsilon}\mathrm{d}\varepsilon, \tag{55}$$

$$DN = \frac{\gamma}{3}\int_0^\infty \frac{\varepsilon}{\tilde{\sigma}_\mathrm{m}} F_0\,\mathrm{d}\varepsilon. \tag{56}$$

The effective momentum-transfer cross-section $\tilde{\sigma}_\mathrm{m}$ in these equations includes the effect of possible temporal growth as

given by equation (12). Although the normalized energy distribution F_0 is assumed to be independent of space when solving the BE, the above fluid equations and coefficient definitions are also valid in case the energy distribution is space dependent. The diffusion coefficient in equation (54) then clearly appears inside the divergence and can generally not be put in front of it, as is done in Fick's law.

3.2. Energy transport

Similar to the derivation of the continuity equation in the previous section, the energy equation is obtained from equation (5) by multiplying by $\varepsilon^{3/2}$ and integrating:

$$\frac{\partial n_\varepsilon}{\partial t} + \frac{\partial \Gamma_\varepsilon}{\partial z} + E\Gamma = S_\varepsilon, \tag{57}$$

where the energy density and the energy flux are given by

$$n_\varepsilon = n\int_0^\infty \varepsilon^{3/2} F_0 \,\mathrm{d}\varepsilon \equiv n\bar{\varepsilon}, \tag{58}$$

$$\Gamma_\varepsilon = n\frac{\gamma}{3}\int_0^\infty \varepsilon^2 F_1 \,\mathrm{d}\varepsilon, \tag{59}$$

where $\bar{\varepsilon}$ is the mean electron energy in electronvolts. The last term on the left-hand side of equation (57) represents heating by the electric field; the term S_ε on the right-hand side is the total energy transfer (usually loss) due to collisions. Using equation (6), we can write the energy flux as well in a drift-diffusion form:

$$\Gamma_\varepsilon = -\mu_\varepsilon E n_\varepsilon - \frac{\partial(D_\varepsilon n_\varepsilon)}{\partial z}, \tag{60}$$

where the energy mobility and the energy diffusion coefficient are defined by

$$\mu_\varepsilon N = -\frac{\gamma}{3\bar{\varepsilon}}\int_0^\infty \frac{\varepsilon^2}{\tilde{\sigma}_\mathrm{m}}\frac{\partial F_0}{\partial \varepsilon}\,\mathrm{d}\varepsilon, \tag{61}$$

$$D_\varepsilon N = \frac{\gamma}{3\bar{\varepsilon}}\int_0^\infty \frac{\varepsilon^2}{\tilde{\sigma}_\mathrm{m}} F_0 \,\mathrm{d}\varepsilon. \tag{62}$$

The above formulation of the energy equation is somewhat unusual but we recommend it because of its consistency with the two-term BE. The formulation is basically equivalent to that of Allis [29]; our energy mobility and diffusion coefficient are straightforwardly related to Allis' thermoelectricity β and heat diffusion G as $\mu_\varepsilon = \beta/\bar{\varepsilon}$ and $D_\varepsilon = G/\bar{\varepsilon}$; some other authors using this approach are Ingold [30] and Alves *et al* [31].

Other formulations of the energy equation found in the literature [32] show a separation of the electron energy flux into a convective part proportional to the electron flux and a thermal conduction part proportional to the gradient of the mean electron energy; this however involves additional assumptions and may lead to ambiguity in the definition of the energy transport coefficients (e.g. the thermal conductivity appearing in such energy equations); some further discussion on this issue is given in section 4.5.

Note also that the above formulation of the energy equation is technically convenient because it has exactly the same form as the particle continuity equation and can be solved for n_ε by the same numerical routine. The mean energy is subsequently obtained by dividing, $\bar{\varepsilon} = n_\varepsilon/n$. A semi-implicit technique to avoid numerical instabilities due to the possible energy-dependence of the source term S_ε has previously been developed [33] and proved to work very well.

3.3. Source terms

Various coefficients can be defined for the purpose of calculating the reaction rates appearing in the source terms of fluid equations. Most straightforward is to define rate coefficients (in units of volume per time) as

$$k_k = \gamma\int_0^\infty \varepsilon\sigma_k F_0 \,\mathrm{d}\varepsilon, \tag{63}$$

from which the reaction rate for the collision processes k is obtained by multiplication by the density of the electrons and the target species:

$$R_k = k_k x_k N n. \tag{64}$$

In an alternative approach one can define Townsend coefficients α_k (in units of inverse length) such that

$$R_k = \alpha_k x_k |\Gamma|. \tag{65}$$

For the cases of temporal and spatial growth discussed in section 2.2, these Townsend coefficients are then given by

$$\frac{\alpha_k}{N} = \frac{k_k \alpha}{\bar{\nu}_i} \tag{66}$$

and

$$\frac{\alpha_k}{N} = \frac{k_k}{\mu E}. \tag{67}$$

Using Townsend coefficients, the reaction rates are calculated from the electron flux rather than from the electron density. Clearly this makes no difference for the cases of pure spatial or temporal growth, but in general equations (66) and (67) yield different results. It is recommended to use rate coefficients in situations where the electrons diffuse against the electric force (plasma bulk) and Townsend coefficients in situations where the flux is field driven. The use of Townsend coefficients is especially recommended for modelling the cathode region in dc discharges, where the poor physical reality of the drift-diffusion equation leads to large errors in the electron density but hardly affects the electron flux; models without energy equation may not even have a solution when rate coefficients are used in the cathode fall.

3.4. High frequency momentum equation

Some models of HF discharges use an electron momentum equation of the form

$$\frac{\partial w}{\partial t} + \bar{\nu}_\mathrm{eff} w = -\phi\frac{e}{m}E, \tag{68}$$

where w is the electron drift velocity and $\bar{\nu}_\mathrm{eff}$ is an effective collision frequency. The factor ϕ is usually omitted, but we show here that this factor is needed to be consistent with the BE. According to the two-term approach of section 2.3, and using the complex notation, the electron drift velocity in HF fields is equal to

$$\begin{aligned} w &= \gamma \mathrm{e}^{\mathrm{i}\omega t}\int_0^\infty \varepsilon F_1 \,\mathrm{d}\varepsilon = -\frac{\gamma E}{3N}\int_0^\infty \varepsilon\frac{\tilde{\sigma}_\mathrm{m} - \mathrm{i}q}{\tilde{\sigma}_\mathrm{m}^2 + q^2}\frac{\partial F_0}{\partial \varepsilon}\mathrm{d}\varepsilon \\ &\equiv -(\mu_r + \mathrm{i}\mu_i)E, \end{aligned} \tag{69}$$

which defines a complex electron mobility $\mu = \mu_r + \mathrm{i}\mu_i$. Substituting this in the momentum equation, we find that the coefficients must be calculated as

$$\bar{\nu}_{\mathrm{eff}} = -\frac{\mu_r}{\mu_i}\omega, \tag{70}$$

$$\phi = -\frac{\mu_r^2 + \mu_i^2}{\mu_i}\frac{m_e\omega}{e}. \tag{71}$$

The factor ϕ equals unity for a constant momentum-transfer frequency (σ_m inversely proportional to $\varepsilon^{1/2}$) but may be quite different from unity in case the momentum-transfer frequency depends on energy. This has been pointed out previously [34] but is frequently overlooked.

We remark that, strictly speaking, the momentum equation (68) is not very useful to describe the electron motion in a pure harmonic HF field, since the electron drift velocity w can be obtained directly from the complex mobility by equation (69). However, the momentum equation is useful to describe more general cases where the electric field is not purely harmonic, but resembles a harmonic oscillation at a certain frequency.

4. Examples of results

We have extensively tested our BE solver for the gases argon and nitrogen. These are model gases used in many BE calculations described in the literature; we use the cross sections recommended by Phelps [35]. As default options for our calculations we consider the assumptions done by BOLSIG and most other BE solvers available: exponential temporal growth, quasi-stationary electric field, only collisions with ground state gas particles. For these assumptions our calculation results are identical to those obtained with BOLSIG. We consider that this exact agreement obtained using two very different solution techniques validates each. The typical calculation time for one EEDF is on the order of a few tens of milliseconds on a standard 2 GHz PC.

Calculation results for the default options are so well known from previous work that there is no use showing them again in this paper. Instead, we show results for options different from default, not included in BOLSIG and most other solvers. The next few sections illustrate the influence of the growth model (section 4.1), electron–electron collisions (section 4.2), electron collisions with excited neutrals (section 4.3), high frequency field oscillations (section 4.4), and some commonly used assumptions concerning the transport coefficients (section 4.5). Similar results have been presented previously and are known to BE specialists, but often overlooked by developers and users of fluid models. Our aim here is to provide a feeling of how and when the new options of our BE solver should be used and how they might affect the fluid model coefficients. We do not intend to be exhaustive; the presented results are just illustrative examples and more systematic investigation is saved for future work.

4.1. Influence of growth model

When solving the BE one needs to make assumptions on what happens if collision processes (ionization, attachment) do not conserve the total number of electrons. In section 2.2 we discussed two model cases included in our BE solver, where the net production (loss) of electrons leads to exponential temporal growth (decay) and exponential spatial growth (decay) of the electron density. Clearly these are only ideal cases that do not always exactly fit real discharges. Some discharges, such as a fully developed dc glow discharge between parallel plates, closely resemble the case of exponential spatial growth. Other discharge situations, such as the ignition of a dielectric barrier discharge, have features of both spatial and temporal growth. Yet other discharge situations cannot be described by either of the exponential growth models; in a dc positive column, for example, net production is balanced by transverse diffusion loss. There is no growth model that works for all discharges, but we estimate that for many cases the exponential spatial growth model is probably the most realistic. Note however that BOLSIG and most other solvers assume exponential temporal growth.

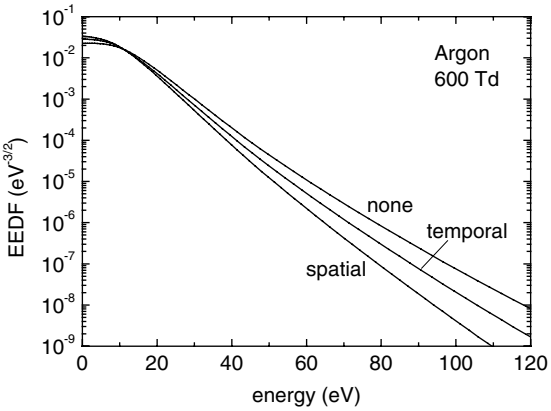

Figure 1. EEDF for 600 Td in argon calculated using the exponential temporal growth model, exponential spatial growth model, and neglecting growth (treating ionization as excitation).

In general the growth effects reduce the mean electron energy (for a given E/N) but have only a minor influence on the shape of the EEDF (for a given mean energy). This is illustrated for argon by figure 1, which compares the EEDFs for the different exponential growth models with the EEDF when growth is neglected, i.e. when ionization is treated as an excitation process and no secondary electrons are inserted. Note that the difference between the two exponential growth models is on the same order as the difference between the temporal growth model and no growth model at all. Figure 2 then shows the influence of the growth effects on the ionization rate coefficient in argon. Although the differences between the curves for the different growth models in figure 2 seem relatively small, our experience is that they can have serious consequences for the fluid simulation results. More systematic investigation on this point is definitely needed but beyond the scope of this paper.

4.2. Influence of electron–electron collisions

Electron–electron collisions cause the EEDF to tend towards a Maxwellian distribution function. The influence of these collisions depends essentially on the ionization degree n/N and is known to become significant for $n/N > 10^{-6}$ in some gases. Note from equation (32) that there is also a

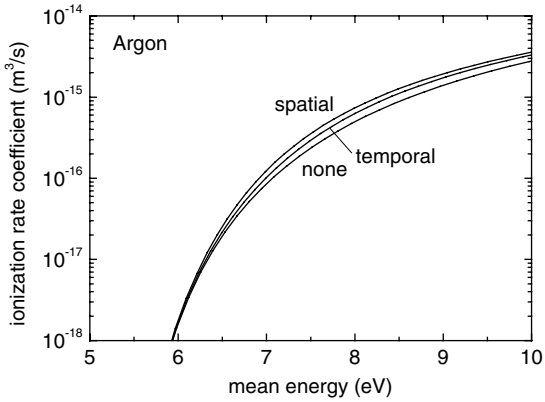

Figure 2. Ionization rate coefficient in argon for different exponential growth models.

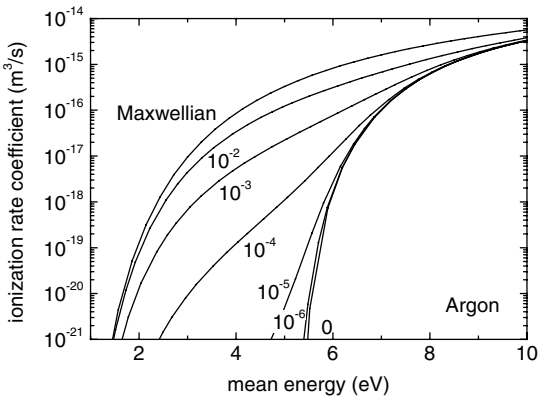

Figure 4. Ionization rate coefficient in argon, taking into account electron-electron collisions, for different ionization degrees and for a Maxwellian EEDF.

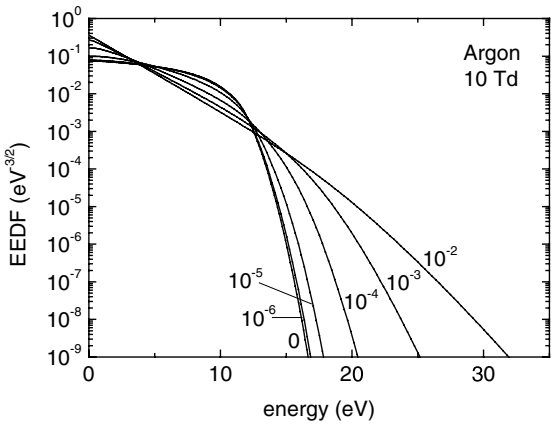

Figure 3. EEDF for 10 Td in argon, taking into account electron–electron collisions, for different ionization degrees.

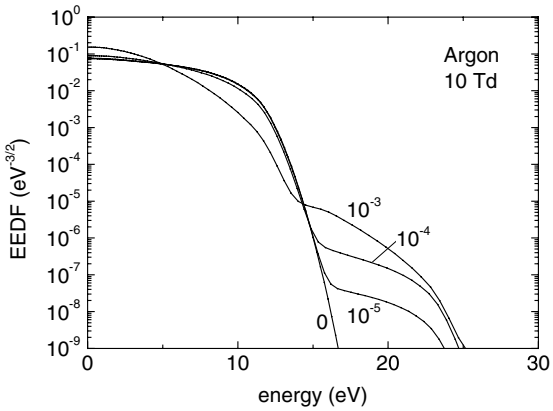

Figure 5. EEDF for 10 Td in argon, taking into account collisions with excited neutrals, for different excitation degrees.

weak dependence on the plasma density which appears in the Coulomb logarithm accounting for the screening of the Coulomb potential by space charge effects. Figure 3 shows the EEDF in argon for different ionization degrees, a plasma density of 10^{18} m^{-3} and a weak reduced electric field of 10 Td. For increasing ionization degree the EEDF resembles more and more a Maxwellian distribution function, i.e. a straight line in the logarithmic plot of figure 3.

These effects are usually neglected in fluid models, but is this justified? The most important consequence of electron–electron collisions for fluid models is that they increase the rate coefficients of inelastic collisions (ionization, excitation) by repopulating the tail of the EEDF. This is illustrated by figure 4 which shows the ionization rate coefficient of ground state argon for different ionization degrees. The inelastic rate coefficients may be strongly increased for ionization degrees of 10^{-5} and higher, but only at low mean electron energy, because the cross-section for electron–electron collisions drops off rapidly with increasing electron energy.

The eventual consequences of this for fluid simulations clearly depend on the discharge conditions. Many discharges have such low ionization degree or such high mean electron energy that it is perfectly justified to neglect the influence of electron–electron collisions. Some discharges, however, operate at precisely those conditions where electron–electron collisions are important; microwave discharges, for example, can have a high ionization degree beyond 10^{-5} and a low electron mean energy of only a few electronvolts. These conditions occur typically in discharges sustained by stepwise ionization and where the EEDF is also influenced by electron collisions with excited neutrals; see section 4.3.

We remark that it may be technically cumbersome to account for the influence of electron–electron collisions in a fluid model: due to these collisions the rate coefficients are functions not only of E/N or the mean energy, but also of the ionization degree n/N; this implies using two-dimensional interpolation tables.

4.3. Influence of collisions with excited neutrals

Collisions with excited neutrals may be super-elastic and accelerate electrons immediately into the tail of the EEDF. The influence of this on the EEDF is shown by figure 5 for argon for different excitation degrees (fractional densities of excited neutrals). The results in this figure have been obtained by regrouping all excited argon states in one compound state, for which we estimated an overall super-elastic cross-section by detailed balancing, taking into account only transitions to the ground state.

As with electron–electron collisions, the most important consequence for fluid simulations is an increase of the rate

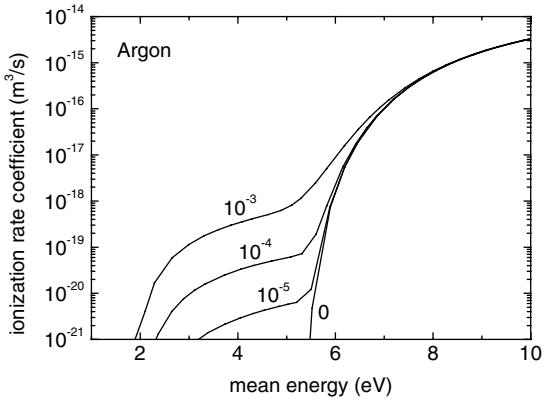

Figure 6. Ionization rate coefficient in argon, taking into account collisions with excited neutrals, for different excitation degrees.

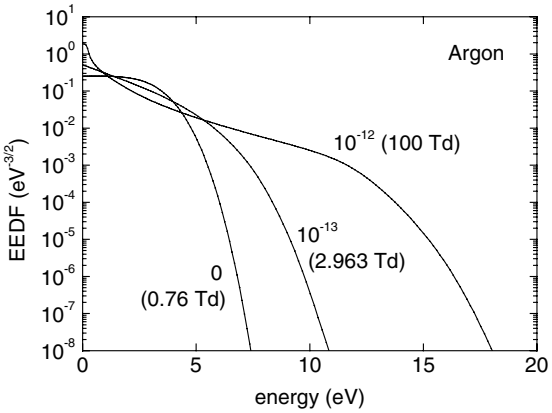

Figure 7. EEDF in argon for oscillating electric fields with different amplitudes and different reduced frequencies ω/N (in units of $\mathrm{m^3\,s^{-1}}$), each having the same mean electron energy of 2.150 eV.

coefficients of inelastic collisions at low mean electron energy. Figure 6 shows the ionization rate coefficient of ground state argon. See further our discussion on electron–electron collisions.

4.4. Influence of high-frequency oscillations

In HF oscillating fields with a frequency comparable with or greater than the collision frequency, the electron heating is less efficient than in dc fields. As a result, a stronger reduced field is required to achieve the same mean electron energy. In addition the shape of the EEDF may be different (for the same mean energy), because the electron heating depends differently on collisional momentum transfer: in dc fields collisions impede the heating whereas in HF fields they enhance it; compare the electron heating terms in equations (13) and (25). In gases where the momentum-transfer frequency depends strongly on the electron energy, this leads to large differences in the shape of EEDF. This is illustrated by figure 7, which shows the EEDF in argon for the same mean energy and for different reduced field-frequencies ω/N.

Rate coefficients for fluid models of HF discharges (e.g. microwave discharges) need to account for the field-oscillation effects on the shape of the EEDF. Figure 8 shows the ionization rate coefficient of ground state argon as a function of the

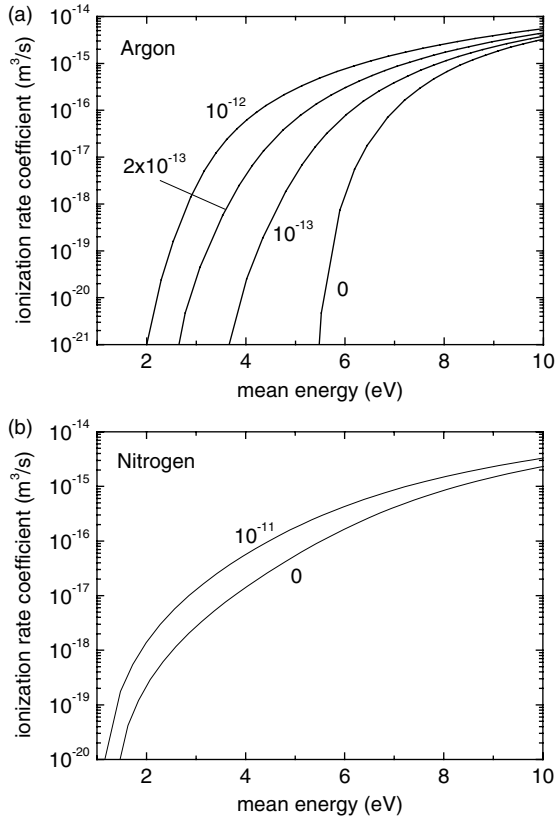

Figure 8. Ionization coefficient in (*a*) argon and (*b*) nitrogen for oscillating electric fields with different reduced frequencies ω/N (in units of $\mathrm{m^3\,s^{-1}}$).

mean energy for different reduced frequencies. The effects are important mainly at lower mean electron energy (where more electrons see the Ramsauer minimum in the elastic collision cross section) which is exactly where most HF discharges operate. The influence of the oscillations is much less important in gases with a more constant collision frequency, as is illustrated in figure 8 for the case of nitrogen.

When implementing the high-frequency rate coefficients in a fluid model a technical complication can arise when the gas is heated by the discharge such that ω/N is not constant; two-dimensional interpolation tables may then be necessary. We also remark that for some gases and some values of ω/N the mean energy may not be a monotonic function of E/N: there may exist two different EEDFs with the same mean energy, so that it becomes impossible to define rate coefficients or transport coefficients as unique functions of the mean energy. We found this behaviour for argon for a wide range of ω/N (10^{-13}–$10^{-11}\,\mathrm{m^3\,s^{-1}}$) and low mean energies (around 2 eV), but not for nitrogen.

4.5. Accuracy of some common approximations

Fluid models often use approximations concerning the transport coefficients, such as the Einstein relation between the diffusion coefficient and the mobility. In this section we check some of these approximations against the results of our BE solver in order to get an idea of their accuracy.

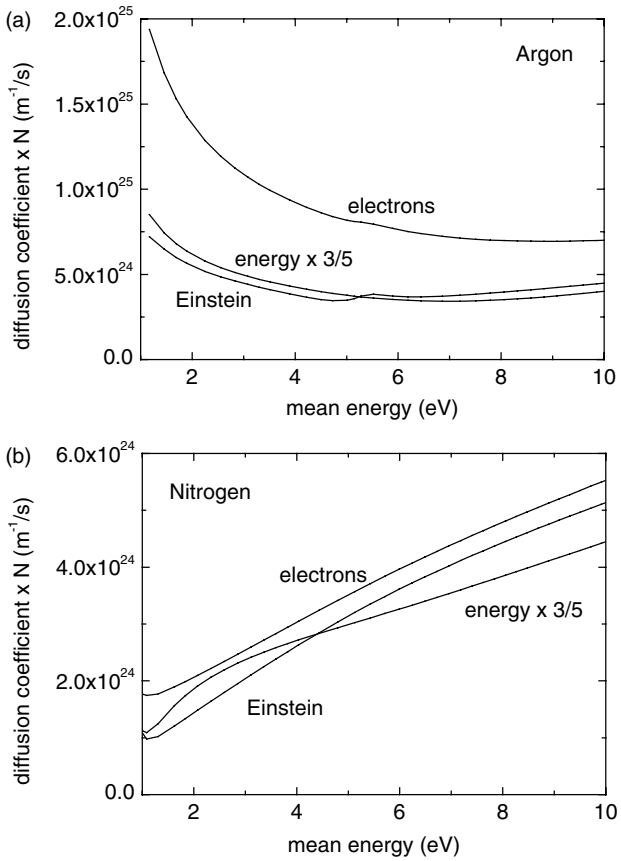

Figure 9. Diffusion coefficients in (*a*) argon and (*b*) nitrogen for electrons and electron energy, calculated precisely and calculated from the Einstein relation.

The commonly used Einstein relation is [36]:

$$D = \tfrac{2}{3}\mu\bar{\varepsilon}, \tag{72}$$

which is exact for a Maxwellian EEDF or a constant momentum-transfer frequency (σ_m inversely proportional to $\varepsilon^{1/2}$) but more or less approximate for real discharge situations. To illustrate the possible errors of the Einstein relation, figure 9 shows the diffusion coefficient in argon and in nitrogen calculated exactly from equation (62) and calculated from the Einstein relation. For argon the Einstein relation is off by a factor 2 due to the strong energy-dependence of the momentum-transfer frequency; for nitrogen the errors are much smaller.

One must realize, however, that the results of our BE solver are approximations as well. For instance, more detailed analysis [37] shows different diffusion coefficients for transport along and perpendicular to the electric field direction, whereas this distinction vanishes with our BE solver based on the two-term expansion. Realize also that for many discharge conditions the drift-diffusion equation itself gives a rather bad description of reality, without this having too serious consequences for the discharge simulation as a whole [38]. In the cathode region of dc discharges the drift-diffusion equation is known to lead to large errors in the electron density without seriously affecting the rest of the discharge; also see our also remarks in section 3.3.

Further common approximations concern the electron energy transport. Many fluid models in the literature use an electron energy equation where (once written as equation (60)) the energy transport coefficients are given by

$$\mu_\varepsilon = \tfrac{5}{3}\mu \qquad \text{and} \qquad D_\varepsilon = \tfrac{5}{3}D. \tag{73}$$

These approximations can be derived by assuming a Maxwellian EEDF, a constant momentum-transfer frequency and constant kinetic pressure [36]. The approximations allow the separation of the energy flux into a part proportional to the electron flux and a part proportional to the gradient of the mean energy, as in classical fluid mechanics:

$$\Gamma_\varepsilon = \tfrac{5}{3}\Gamma\bar{\varepsilon} - \tfrac{5}{3}nD\nabla\bar{\varepsilon}, \tag{74}$$

where the factor in front of the energy gradient is the electron thermal conductivity.

Some authors [29–31] however avoid the approximations given by equation (73) and calculate the energy transport coefficients more precisely as discussed in section 3.2. To illustrate the difference between the approximations and the more precise expressions given by equations (61) and (62), figure 9 also shows the energy diffusion coefficient D_ε calculated from equation (62) and multiplied by 3/5, which (according to equation (73)) is to be compared with the electron diffusion coefficient D. Once again the difference is about a factor 2 for argon and much smaller for nitrogen. For the energy mobility μ_ε the difference is usually much smaller than for D_ε. To our knowledge the consequences of equation (73) for fluid simulations have never been investigated systematically, but one can imagine that for some gases they are quite significant.

5. Conclusions

We have developed a new user-friendly BE solver to calculate the electron transport coefficients and rate coefficients that are input data for fluid models. Our BE solver is called the BOLSIG+ and is available as a freeware [18]. The solver provides steady-state solutions of the BE for electrons in a uniform electric field, using the classical two-term expansion, and is able to account for different growth models, quasi-stationary and oscillating fields, electron–neutral collisions and electron–electron collisions. We show that for the approximations we use, the BE takes the form of a convection-diffusion continuity-equation with a non-local source term. To solve this equation we use an exponential scheme commonly used for convection-diffusion problems. The calculation time for one EEDF is on the order of tens of milliseconds on a standard 2 GHz PC. The calculated electron coefficients are defined so as to ensure maximum consistency with the fluid equations. Special care must be taken of the transport coefficients for electron energy, for which we recommend the formulation proposed previously by Allis [29].

We have illustrated the influence of several non-standard options included in our BE solver, frequently overlooked by users and developers of fluid models. The results from our BE solver show that growth effects significantly reduce the mean electron energy and the ionization rate coefficient; there are also significant differences between the exponential models for temporal and spatial growth. Electron–electron collisions may strongly increase the rate coefficients of

inelastic collisions (excitation, ionization) for low electron mean energies ($\ll$ threshold energy) and ionization degrees of 10^{-5} and higher; these conditions are present in some common gas discharges. A similar increase in the inelastic rate coefficients can be due to super-elastic collisions with excited neutrals for excitation degrees of 10^{-5} and higher. In HF oscillating fields the shape of the EEDF can be strongly modified by oscillation effects, causing large differences in the electron coefficients as a function of mean electron energy with respect to dc fields, especially for gases where the momentum-transfer frequency depends strongly on energy. For such gases also the Einstein relation can be wrong by as much as a factor 2, and special care must be taken about the definition of energy transport coefficients. All results presented here are just illustrative examples; more systematic investigation is necessary to obtain a complete picture of when and how best to use the different options of our BE solver.

References

[1] Ingold J H 1989 *Phys. Rev.* A **40** 3855–63
[2] Graves D B and Jensen K F 1986 *IEEE Trans. Plasma Sci.* **PS-14** 78
[3] Boeuf J-P 1987 *Phys. Rev.* A **36** 2782
[4] Salabas A, Gousset G and Alves L L 2002 *Plasma Sources Sci. Technol.* **11** 448
[5] Dutton J 1975 *J. Phys. Chem. Ref. Data* **4** 577
[6] Frost L S and Phelps A V 1962 *Phys. Rev.* **127** 1621
[7] Wilhelm R and Winkler R 1969 *Ann. Phys.* **23** 28
[8] Winkler R *et al* 1984 *Beitr. Plasmaphys.* **24** 657–74
[9] Rockwood S D 1973 *Phys. Rev.* A **40** 399
[10] Luft P E 1975 *JILA Information Center Report* No. 14 University of Colorado, Boulder
[11] Tagashira H, Sakai Y and Sakamoto S 1977 *J. Phys. D: Appl. Phys.* **10** 1051–63
[12] Morgan W L 1979 *JILA Information Center Report* No. 19 University of Colorado, Boulder
[13] Morgan W L and Penetrante B M 1990 *Comput. Phys. Commun.* **58** 127–52
[14] Lin S L, Robson R E and Mason E A 1979 *J. Chem. Phys.* **71** 3483–98
[15] Pitchford L C, ONeil S V and Rumble J J R 1981 *Phys. Rev.* A **23** 294
[16] Segur P *et al* 1983 *J. Comput. Phys.* **50** 116
[17] BOLSIG 1997 CPAT: http://www.cpat.ups.-tlse.fr/operations/operation_03/POSTERS/BOLSIG/index.html
[18] BOLSIG+ 2005 CPAT: http://www.codiciel.fr/plateforme/plasma/bolsig/bolsig.php
[19] Holstein T 1946 *Phys. Rev.* **70** 367
[20] Allis W P 1956 *Handbuch der Physik* ed S Flugge (Berlin: Springer) p 383
[21] Allis W P 1982 *Phys. Rev.* A **26** 1704–12
[22] Phelps A V and Pitchford L C 1985 *Phys. Rev.* A **31** 2932–49
[23] Thomas W R L 1969 *J. Phys. B: At. Mol. Opt. Phys.* **2** 551
[24] Brunet H and Vincent P 1979 *J. Appl. Phys.* **50** 4700
[25] Wilhelm J and Winkler R 1979 *J. Phys.* **40** C7-251
[26] McDonald A D 1953 *Microwave Breakdown in Gases* (London: Oxford University Press)
[27] Opal C B, Peterson W K and Beaty E C 1971 *J. Chem. Phys.* **55** 4100
[28] Scharfetter D L and Gummel H K 1969 *IEEE Trans. Electron. Devices* **16** 64
[29] Allis W P 1967 *Electrons, Ions, and Waves* (Cambridge: MIT Press)
[30] Ingold J H 1997 *Phys. Rev.* E **56** 5932–44
[31] Alves L L, Gousset G and Ferreira C M 1997 *Phys. Rev.* E **55** 890–906
[32] Boeuf J P and Pitchford L C 1995 *Phys. Rev.* E **51** 1376–90
[33] Hagelaar G J M and Kroesen G M W 2000 *J. Comput. Phys.* **159** 1–12
[34] Whitmer R F and Herrmann G F 1966 *Phys. Fluids* **9** 768–73
[35] Phelps A V ftp://jila.colorado.edu/collision_data/.
[36] Bittencourt J A 1986 *Fundamentals of Plasma Physics* (Oxford: Pergamon)
[37] Parker J H and Lowke J J 1969 *Phys. Rev.* **181** 290–301
[38] Hagelaar G J M and Kroesen G M W 2000 *Plasma Sources Sci. Technol.* **9** 605–14

INSTITUTE OF PHYSICS PUBLISHING PLASMA SOURCES SCIENCE AND TECHNOLOGY
Plasma Sources Sci. Technol. **16** (2007) S57–S66 doi:10.1088/0963-0252/16/1/S06

Modelling electron transport in magnetized low-temperature discharge plasmas

G J M Hagelaar

Centre de Physique des Plasmas et Applications de Toulouse, Université Paul Sabatier, 118 Route de Narbonne, 31062 Toulouse Cedex, France

Received 24 July 2006, in final form 25 October 2006
Published 31 January 2007
Online at stacks.iop.org/PSST/16/S57

Abstract
Magnetic fields are sometimes used to confine the plasma in low-pressure low-temperature gas discharges, for example in magnetron discharges, Hall-effect-thruster discharges, electron-cyclotron-resonance discharges and helicon discharges. We discuss how these magnetized discharges can be modelled by two-dimensional self-consistent models based on electron fluid equations. The magnetized electron flux is described by an anisotropic drift–diffusion equation, where the electron mobility is much smaller perpendicular to the magnetic field than parallel to it. The electric potential is calculated either from Poisson's equation or from the electron equations, assuming quasineutrality. Although these models involve many assumptions, they are appropriate to study the main effects of the magnetic field on the charged particle transport and space charge electric fields in realistic two-dimensional discharge configurations. We demonstrate by new results that these models reproduce known phenomena such as the establishment of the Boltzmann relation along magnetic field lines, the penetration of perpendicular applied electric fields into the plasma bulk and the decrease in magnetic confinement by short-circuit wall currents. We also present an original method to prevent numerical errors arising from the extreme anisotropy of the electron mobility, which tend to invalidate model results from standard numerical methods.

1. Introduction

The use of steady, external magnetic fields makes it possible to create high-density low-temperature plasmas in gas discharges at very low gas pressure. There are different types of such magnetized discharges, where the magnetic field plays different roles. In general, the magnetic field confines the plasma and limits charge particle loss to the walls, which allows magnetron discharges to operate at relatively low dc or rf voltage. More specifically, in Hall-effect thrusters (HETs), the magnetic field allows perpendicular applied electric fields to penetrate inside the plasma bulk, heat the bulk electrons and accelerate the ions. In electron-cyclotron-resonance (ECR) discharges and helicon discharges, the electrons are heated by magnetized wave modes. Throughout the present paper we will simply refer to these discharges as magnetized discharges; this is not to be confused with fusion-related discharges.

The magnetic field complicates the physics and hence the numerical modelling of magnetized discharges. Standard discharge modelling techniques, such as particle-in-cell (PIC), are often cumbersome for these discharges, and low-order physical approximations are necessary to avoid technical complications and limit computation times. On the other hand, even the lowest order approximations show rich and interesting physics. There is great interest in developing relatively simple numerical models, not to be (mis)used as predictive simulation tools, but simply to help identify and understand the physical principles of magnetized discharges. In fact, the most basic principles of magnetized discharges are known from early analytical work for idealized configurations and can be found in classical texts, but numerical models are necessary to investigate the role of these basic principles in realistic multi-dimensional discharge configurations.

In this context, the present paper provides a general description and discussion of self-consistent models based on simple fluid equations for magnetized electrons. We discuss the principles, use and limits of these models, both from a physical and a numerical point of view. We demonstrate, by new calculation results, that these models are appropriate to study the main effects of the magnetic field on the particle transport and space charge electric fields in two-dimensional discharge configurations and in much greater detail than analytical treatments. We focus on charged particle transport and do not describe electron heating or energy, which we consider beyond the scope of this paper. The relation to previous work and work by others is indicated, but not exhaustively; this is not a review paper.

2. Elementary physics

We shall briefly recall the principal effects of the magnetic field on charged particle transport on a microscopic level. Due to the Lorentz force

$$\boldsymbol{F} = q\boldsymbol{v} \times \boldsymbol{B}, \tag{1}$$

where q and $\boldsymbol{v}$ are the particle charge and velocity, charged particles gyrate around the direction of the magnetic field $\boldsymbol{B}$, so as to generate a diamagnetic current. The angular frequency and the radius of the gyration, called the cyclotron frequency and the Larmor radius, are

$$\omega_c = \frac{|q|}{m}B, \qquad \rho_L = \frac{v_\perp}{\omega_c}, \tag{2}$$

where m is the particle mass and $v_\perp$ is the velocity component perpendicular to the magnetic field. This means that charged particles are unable to travel perpendicular to the magnetic field over distances greater than ρ_L: they are confined. In case there is a perpendicular electric field trying to push the particles across the magnetic field ($E \times B$ configuration), the following happens: the particles drift in the direction perpendicular to both the electric field and the magnetic field. This phenomenon is called the $E \times B$ drift and is illustrated in figure 1. Most magnetized discharges have a cylindrical geometry, where the electric and magnetic fields are in the radial-axial plane, so that the $E \times B$ drift is closed along the azimuthal direction.

The magnetic confinement is destroyed in case the charged particles undergo collisions and exchange momentum, for example with neutral gas particles or with walls. In each collision, the centre of the gyration is allowed to shift over a distance ρ_L (see figure 1) perpendicular to the magnetic field, which gives rise to so-called cross-field diffusion and cross-field mobility. The magnetic confinement can be characterized by the Hall parameter

$$\Omega \equiv \frac{\omega_c}{\nu} = \frac{|q|B}{m\nu}, \tag{3}$$

where ν is the total collision frequency (momentum-transfer frequency); good confinement requires $\Omega \gg 1$.

Table 1 lists typical conditions for magnetized low-temperature discharge plasmas. Only the electrons are really magnetized (confined), having a small Larmor radius and a large Hall parameter, whereas the ion Larmor radius is often comparable to or larger than the plasma dimensions. In spite of the long mean free path, of the order of the plasma dimensions, the magnetic confinement ensures that the electrons undergo many collisions during their lifetime, which makes it possible to sustain a plasma.

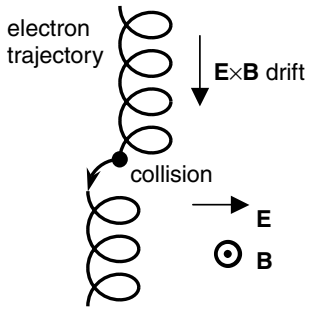

Figure 1. Electron drift in an $E \times B$ configuration.

Table 1. Typical conditions for magnetized discharges.

Plasma parameters	
Pressure	0.1–20 mTorr
Plasma density	10^{15}–10^{19} m^{-3}
Electron temperature	2–20 eV
Magnetic field	0.001–0.1 T
Lengths	
Debye length	10^{-5}–10^{-3} m
Electron Larmor radius	10^{-4}–0.01 m
Ion Larmor radius	0.02–5 m
Mean free path	0.01–1 m
Plasma size	0.01–1 m
Frequencies	
Electron-plasma frequency	2×10^9–2×10^{11} s^{-1}
Electron-cyclotron frequency	2×10^8–2×10^{10} s^{-1}
Electron-collision frequency	3×10^5–10^8 s^{-1}
Electron Hall parameter	10–1000
Ion Hall parameter	0.01–1

3. Modelling

It is customary to describe low-pressure discharges (<1 Torr) by PIC models, calculating the trajectories of large numbers of electrons and ions from Newton's equations, self-consistently coupled with the space charge electric field from Poisson's equation. For magnetized discharges, however, PIC models are particularly cumbersome, because

(1) the plasma density is much higher than in unmagnetized low-pressure discharges, resulting in a higher electron-plasma frequency and a shorter Debye length, requiring smaller numerical time steps and smaller grid cells for the PIC scheme to be stable and
(2) the magnetized discharges are often very sensitive to the magnetic field configuration and other geometrical parameters requiring a multi-dimensional description.

PIC models have been developed for ECR sources [1], dc magnetron discharges [2, 3] and HETs [4] but are of limited practical use because of their long computation times. There is great interest in simpler faster models, even if these are only approximate and fail to describe part of the physics.

Fortunately, the electrons have collisional properties due to the magnetic confinement and can, to some extend, be described by fluid equations. Replacing the electron particle description of PIC models by fluid equations, one obtains much faster hybrid models appropriate to study the overall plasma dynamics in two spatial dimensions. Such hybrid models have been developed and used for ECR plasma reactors [5] and HETs [6,7]. Some magnetized discharge models [8–10] describe also the ions by fluid equations and are pure fluid models, but in general the ions undergo only few collisions and an ion particle description seems both more realistic and practical. Note, however, that (for the most part) these hybrid and fluid models are very similar and that most of the discussion presented here on hybrid models also holds for fluid models. We shall now briefly describe the electron fluid equations and the way they are used in hybrid models; a more physical discussion is given in the next section.

The equation for electron conservation is

$$\frac{\partial n_e}{\partial t} + \nabla \cdot \Gamma_e = S, \tag{4}$$

where n_e is the electron density, Γ_e is the electron flux and S is the ionization source term. Following the standard approach, the electron flux is related to the electron density and to the electric potential Φ by the drift–diffusion equation:

$$\Gamma_e = \mu n_e \nabla\Phi - \mu\nabla(n_e T_e), \tag{5}$$

where the two terms describe transport due to the electric force and due to the kinetic pressure gradient; μ is the electron mobility and T_e is the electron temperature in eV. Due to the magnetic field, the mobility is not a scalar but a tensor: its value depends on the direction with respect to the magnetic field direction. It is shown in classical text books [11, 12] that the mobility components parallel and perpendicular to the magnetic field are

$$\mu_\parallel = \mu_0 \equiv \frac{e}{m_e \nu}, \tag{6}$$

$$\mu_\perp = \frac{1}{1+\Omega^2}\mu_0 = \frac{e\nu/m_e}{\nu^2+\omega_c^2}, \tag{7}$$

where ν is the collision frequency, μ_0 is the mobility without magnetic field and Ω is the Hall parameter. The perpendicular mobility (cross-field mobility) is smaller than the parallel mobility, often by many orders of magnitude, and is approximately proportional to the collision frequency. The standard boundary condition for electron conservation is to set the electron flux at the wall equal to $n_e v_{th}/4$, where $v_{th} = (8eT_e/\pi m_e)^{1/2}$ is the Maxwellian thermal speed; since v_{th} is very large this is almost equivalent to setting the electron density at the wall equal to zero.

The fluid equations for electron conservation and flux can be complemented by an equation for electron energy in order to obtain a self-consistent estimate of the electron temperature (appearing in the diffusion flux) and the ionization source term. We will not discuss this here, but we note that the electron energy transport also shows strong anisotropy. Similar to the mobility, the electron thermal conductivity is much smaller perpendicular to the magnetic field than parallel to it.

A typical hybrid model is now composed as follows:

(1) ion velocity distribution, density and flux from a particle description,
(2) electron density and flux from equations (4) and (5),
(3) electric potential from Poisson's equation:

$$\varepsilon_0\nabla^2\Phi = e(n_e - n_i), \tag{8}$$

all coupled together in a self-consistent manner. The advantage with respect to PIC models is that the time integration of the electron equations can be implicitly coupled with Poisson's equation, which damps away electron-plasma oscillations and makes it possible to use much larger numerical time steps.

The above hybrid scheme can be further simplified by assuming quasineutrality, as follows:

(1) ion velocity distribution, density and flux from a particle description,
(2) electron density set equal to the ion density,
(3) electric potential from the electron equations (4) and (5) or equivalently from current conservation (generalized Ohm's law):

$$\nabla \cdot \Gamma_e = \nabla \cdot (\mu n_i \nabla\Phi - \mu\nabla(n_i T_e)) = \nabla \cdot \Gamma_i. \tag{9}$$

The quasineutral scheme does not resolve the space charge sheaths, which makes it possible to use numerical cells much larger than the electron Debye length. On the other hand, although the magnetized plasma sheaths are often negligibly thin, the sheath potentials can play an important role in the macroscopic plasma dynamics. Some quasineutral models use the sheath potential from analytical sheath models in the boundary conditions for the current conservation equation [5,6]. Lampe *et al* [13] developed an interesting and sophisticated variant of the quasineutral hybrid scheme for magnetized discharges, where the electron pressure, the electron-collision frequency and the ionization source term are calculated from an electron particle description.

4. Limits of the electron fluid equations

When describing the electrons by fluid equations as shown in the previous section, much physical information is lost with respect to PIC models: all details of the electron velocity distribution are averaged out, as well as the microscopic electron-field interactions, the electron-plasma oscillations are damped away, etc and only the macroscopic dynamics is retained. However, for magnetized electrons it is particularly difficult to describe the macroscopic dynamics without considering the microscopic details, and the magnetized fluid equations are only very approximate, involving many assumptions.

An important problem is the fundamental lack of knowledge of the cross-field electron transport. Experimental data show that the electrons are often much less confined than expected from the classical mobility shown in equation (7), due (probably) to microscopic turbulent electron-field interactions [14, 15]. This phenomenon is known as anomalous electron transport and has also been observed in PIC simulations [4]. In spite of much fundamental research, no theory has been able to correctly predict and quantify the anomalous transport

as yet, but an approximate upper limit has been found as $\mu_\perp < 1/16B$ (Bohm diffusion). For the moment, the only way to deal with this problem is to define empirical transport parameters (for example, an effective collision frequency or Hall parameter) and adjust those for a given discharge configuration so as to obtain agreement between the model results and experimental results. We have used this empirical approach in HET simulations [16].

Apart from the anomalous transport problem, it is important to realize that the drift–diffusion equation is derived from a *local* balance between forces and collisional momentum loss and is therefore only valid if the mean free path is small with respect to the plasma dimensions and gradient lengths. For magnetized electrons, the use of the drift–diffusion equation is justified for the direction perpendicular to the magnetic field by the fact that the perpendicular distance travelled between successive collisions is limited to the Larmor radius, but parallel to the magnetic field it is often more difficult to justify. In fact, the parallel electron flux is sensitive to a number of phenomena not described by the drift–diffusion equation, including

(1) inertia: it takes a finite length for the electrons to accelerate to a certain velocity;
(2) diamagnetic force (grad-B force): as the electrons move along a diverging (converging) magnetic field their gyration velocity is gradually converted into parallel velocity (parallel velocity into gyration) so as to conserve their magnetic moment, which appears as a parallel force pushing the electrons against the gradient of magnetic field strength; the diamagnetic force is sometimes used to enhance magnetic confinement, for example, in multi-pole configurations (mirror confinement) [11, 17].

These non-local phenomena can be approximately included in the electron fluid equations, but only at great cost of complexity and loss of numerical stability. For example, describing the diamagnetic force involves the distinction between two different electron temperatures for gyration and parallel motion, solved from two different but strongly coupled energy equations [13].

Note also that the parallel electron flux is often imposed or limited by the boundary conditions. In particular, the electron flux along magnetic field lines that end on insulator walls must be of the order of the ion flux. The drift–diffusion equation then yields

$$\mu_\parallel n_\mathrm{e} \nabla_\parallel \Phi \approx \mu_\parallel \nabla_\parallel (n_\mathrm{e} T_\mathrm{e}) \tag{10}$$

because of the relatively large parallel mobility. Similarly, the large thermal conductivity along the lines results in an almost uniform electron temperature: $\nabla_\parallel T_\mathrm{e} \approx 0$. From these considerations it follows that

$$\Phi(\boldsymbol{r}) = \Phi^*(\lambda) + T_\mathrm{e}(\lambda) \ln(n_\mathrm{e}(\boldsymbol{r})/n_0), \tag{11}$$

where $\boldsymbol{r}$ are the space coordinates and λ refers to a magnetic field line: the magnetic field lines are equipotential except for a diffusion term of the order of the electron temperature. This is nothing other than the Boltzmann relation applied along magnetic field lines and it provides a well-established rule of thumb, in the context of plasma propulsion sometimes connected with the name of Morozov [18]. Contrary to the drift–diffusion equation, the Boltzmann (Morozov) relation does not directly assume a short mean free path and is meaningful even for collisionless electrons. Therefore, along the magnetic field lines the drift–diffusion equation is justified insofar as it reduces to the Boltzmann relation, but it cannot be expected to correctly predict either the parallel electron flux or deviations from Boltzmann.

Although this is somewhat beyond the scope of the present paper, we remark that the electron fluid equations are particularly limited as it comes to describing ionization. Ionization is often ensured by fast electrons in the tail of the electron energy distribution, whose behaviour can be rather different from that of the 'average' electrons described by the fluid equations and is badly captured by fluid properties such as electron temperature. Some models [8, 10] use an additional particle simulation of fast electrons to predict the ionization source term. On the other hand, in magnetized discharges for plasma propulsion (HETs) the ionization source term is determined mainly by the depletion of the neutral gas and seems relatively insensitive to the approximations of the electron equations.

5. Numerical solution

There exist efficient standard techniques for the numerical solution of the electron fluid equations coupled with Poisson's equation, used for example in fluid models of glow discharges [19]. Most of these techniques can be directly applied to hybrid models of magnetized discharges, but in two-dimensional models additional complications arise from the extreme anisotropy of the electron transport. In particular, the electron flux across the magnetic field tends to be determined by numerical errors rather than by the physical cross-field mobility. This is frequently overlooked and merits some further discussion.

In order to couple the electron equations to the ion particle description, it is convenient to solve them on a rectangular (cylindrical or Cartesian) numerical grid, preferably the same grid used to track the ion density, as is done in PIC simulations for Poisson's equation. Expressing the electron flux in rectangular coordinates x and y, we have

$$\Gamma_{\mathrm{e},x} = \frac{1+\Omega_x^2}{1+\Omega^2}\left[\mu_0 n_\mathrm{e}\frac{\partial\Phi}{\partial x} - \mu_0\frac{\partial n_\mathrm{e}T_\mathrm{e}}{\partial x}\right] + \frac{\Omega_x\Omega_y}{1+\Omega^2}\left[\mu_0 n_\mathrm{e}\frac{\partial\Phi}{\partial y} - \mu_0\frac{\partial n_\mathrm{e}T_\mathrm{e}}{\partial y}\right] \tag{12}$$

and an analogous expression for $\Gamma_{\mathrm{e},y}$, where we have generalized the Hall parameter into a vector $\boldsymbol{\Omega} = \Omega\boldsymbol{B}/B$. Unless the magnetic field is exactly aligned with the grid, each flux component has two terms, proportional to gradients in the longitudinal direction and in the transverse direction, respectively. These two terms are generally opposite in sign and very much larger than the flux itself, whereas their numerical errors are independent. As a result, the relative numerical error in the flux can be enormous, even when accurate numerical schemes are used for the separate terms.

This problem is illustrated by the following example. Consider the Cartesian $E \times B$ configuration in figure 2, where a horizontal electron flux is forced through a uniform plasma in a rectangular channel, across an oblique magnetic field. We

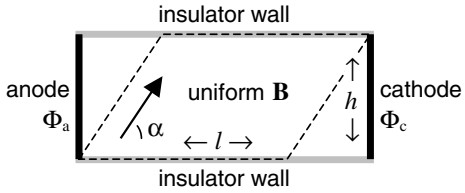

Figure 2. Simple $E \times B$ configuration used for the numerical test. The dashed parallelogram outlines the region where the magnetic field lines intercept only dielectric walls.

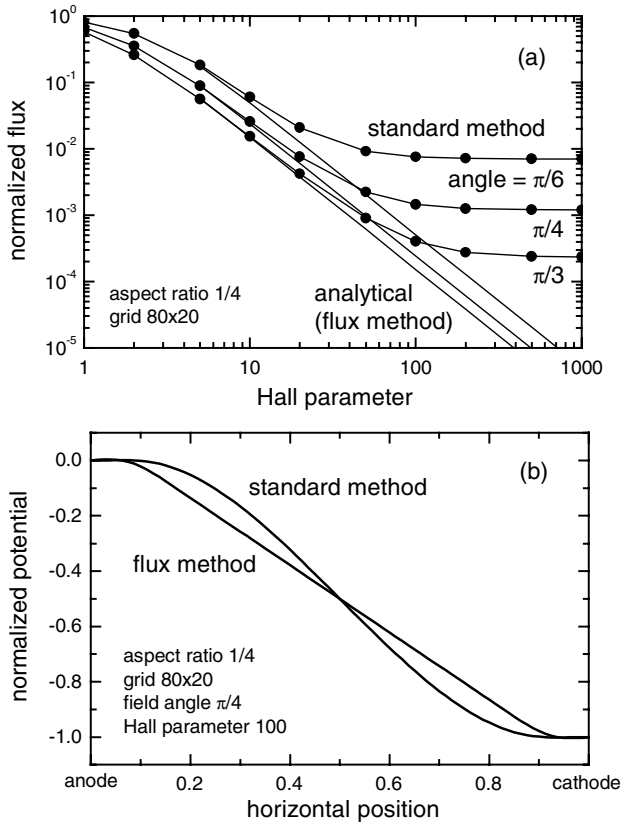

Figure 3. Numerical results for the simple $E \times B$ configuration of figure 2 with an aspect ratio $h/l = 1/4$, compared with the analytical solution shown in equation (13). (*a*) Normalized electron flux $\Gamma_{e,x} l/\mu_0 n_i(\Phi_a - \Phi_c)$ in the centre of the channel for different Hall parameters and different magnetic field angles α. (*b*) Horizontal profile at half the height of the normalized potential $(\Phi - \Phi_a)/(\Phi_a - \Phi_c)$. The grid size is 80 × 20 cells.

describe this configuration by a two-dimensional quasineutral model. Assuming a fixed ion density and neglecting the ion current, the current conservation equation becomes $\nabla \cdot \mathbf{\Gamma}_e = \nabla \cdot (\mu n_i \nabla \Phi) = 0$, which is an anisotropic elliptic equation for Φ. The boundary conditions are fixed potentials $\Phi = \Phi_c$ and $\Phi = \Phi_a$ at the left and right boundaries and zero vertical flux $\Gamma_{e,y} = 0$ at the bottom and top boundaries. Substituting $\Gamma_{e,x}$ and $\Gamma_{e,y}$ from equation (12) and approximating the derivatives by central differences, we obtain a system of linear equations relating the potential in each grid point to that in the surrounding eight neighbour points, which is solved by standard techniques [20]. Figure 3 shows the calculated potential profile and corresponding electron flux in the centre of the channel for different values of the Hall parameter Ω and the magnetic field angle α. Analytically we expect that in the limit $\Omega \to \infty$, the electric field be uniform and perpendicular to the magnetic field over the entire (parallelogram-shaped) region where the magnetic field lines do not intercept the electrodes (see figure 2); the horizontal electron flux in this region is then

$$\Gamma_{e,x} = \frac{-\mu_0 n_i E_x}{1 + \Omega^2 \sin^2 \alpha} = \frac{\mu_0 n_i (\Phi_a - \Phi_c)/l}{(1 + \Omega^2 \sin^2 \alpha)(1 - \cos \alpha h/l)}. \tag{13}$$

The numerical results however show different behaviour: increasing Ω beyond $\Omega \approx 10$, the electric field becomes increasingly non-uniform due to numerical errors, and the electron flux tends asymptotically towards a finite value.

For magnetized discharges Ω is typically >100 and the standard transverse-gradient method seriously overestimates the electron flux and distorts the electric potential profile. This clearly invalidates the hybrid model results, especially for $E \times B$ configurations. Surprisingly, none of the papers we found mentions this problem. Costin *et al* [9] recently presented a solution method for magnetron modelling based on transverse gradients without discussing numerical errors.

We now briefly present a simple numerical method of our own design, which seems appropriate to solve the electron fluid equations in most magnetized discharge models. Rather than calculating each flux component from longitudinal and transverse gradients as shown by equation (12), we calculate it from the longitudinal gradients and the *transverse-flux component*, in an iterative manner:

$$\Gamma_{e,x}^{k+1} = \frac{1}{1 + \Omega_y^2} \left[\mu_0 n_e \frac{\partial \Phi}{\partial x} - \mu_0 \frac{\partial n_e T_e}{\partial x} \right]^{k+1} + \frac{\Omega_x \Omega_y}{1 + \Omega_y^2} \bar{\Gamma}_{e,y}^{k}, \tag{14}$$

where the indexes k and $k+1$ refer to successive iterations. That is, we solve the electron conservation equation several times, each time updating the transverse-flux terms from the previous solution, until convergence. It turns out that the transverse-flux terms can be efficiently updated real-time *during* the solution of the discretized conservation equation, for which we use the modified strongly implicit solver [21]. Note also that, following standard discretization methods, the flux components are defined at different locations midway between the grid points; the bar on $\Gamma_{e,y}$ in the last term of equation (14) symbolizes interpolation from the $\Gamma_{e,y}$ locations to the $\Gamma_{e,x}$ locations.

Our transverse-flux method is appropriate for modelling $E \times B$ configurations, where it yields accurate electron fluxes and correct potential profiles; for the testing of figure 3 the flux agrees with the analytical expression to within a few per cent and the electric potential is linear. We have used the transverse-flux method for the results presented in section 6. However, the method seems less appropriate for configurations where a strong electron flux flows along the magnetic field lines, in which case it tends to underestimate this flux; the transverse-gradient method is then preferable.

Finally, let us say a word about the solution of Poisson's equation in non-quasineutral hybrid models. As mentioned in the previous section, strong numerical time step restrictions (related to electron-plasma oscillations) can be avoided by coupling the solution of Poisson's equation to that of the

electron fluid equations. This is most easily done by the semi-implicit technique described in [19,22], according to which the different equations are still solved separately, but Poisson's equation is modified to include an implicit estimate for the change in the space charge density:

$$\nabla \cdot ((\varepsilon_0 + e\Delta t \mu n_e)\nabla\Phi - e\Delta t \mu \nabla(n_e T_e)) = e(n_e - n_i), \quad (15)$$

where Δt is the time step. This modified Poisson's equation is again an anisotropic elliptic equation for Φ, similar to the current conservation equation (9), and can be solved by the transverse-flux method presented above.

6. Model results

In this section we present examples of steady-state hybrid-model solutions for some typical discharge configurations. Our aim is not to study the operation of these discharges but to demonstrate that relatively simple hybrid models can really help to identify and understand the principles of magnetized electron transport and its interaction with ion transport through space charge electric fields. The different discharge configurations have been chosen to bring out different aspects of the magnetized electron and ion transport.

For the sake of clarity, we consider only the most relevant physics and use a minimal model, consisting of an ion particle simulation, the electron fluid equations (4) and (5) and Poisson's equation (8). Poisson's equation is included to describe the sheath potentials without additional assumptions, and the plasma density is deliberately kept low, much lower than in the real discharges, in order to be able to resolve the sheath regions on a uniform numerical grid. The model includes no equations for electron energy, gas density or ionization: we simply assume a constant uniform electron temperature, a constant two-dimensional Gaussian profile for the ionization source and a constant electron collision frequency (used to calculate the mobility tensor). The ions are assumed to have the argon mass, are created with an isotropic Maxwellian velocity at 300 K and undergo charge-exchange collisions at a constant frequency. Other model input parameters are the magnetic field configuration and the configuration of electrodes and dielectric walls surrounding the plasma. The model results are the electron and ion densities, the electron and ion fluxes and the electric potential. The computation times needed to attain the presented steady-state results are of the order of 15 min on a standard 2 GHz personal computer.

We remark that this minimal hybrid model could be extended to calculate the electron temperature, ionization source, gas density, plasma chemistry, etc, but this would not really change the transport principles we are interested in here. We believe that physical principles are best studied by minimal models where most assumptions are clear and explicit, rather than by complete models where all assumptions are hidden in equations.

6.1. Example I. Magnetized expansion

ECR or helicon discharges typically have a configuration as shown in figure 4. The plasma is created in a cylindrical source chamber with an axial magnetic field, parallel to the side wall, and then expands into a process chamber of much larger diameter. Both chambers are metallic, but the inside of the source chamber is often covered with dielectric, and also the bottom of the source is of dielectric material. In ECR discharges, the magnetic field strength is about 0.1 T in the source chamber (required for microwave ECR) and drops below 0.01 T in the process chamber; in helicon discharges it is somewhat lower. The process that transports the plasma from the source chamber into the process chamber is ambipolar diffusion: the electrons diffuse due to their kinetic pressure, dragging along the ions by space charge fields. However, the electrons mainly diffuse along the diverging magnetic field lines, and almost not across them, which makes the ambipolar diffusion more complicated than in unmagnetized plasmas.

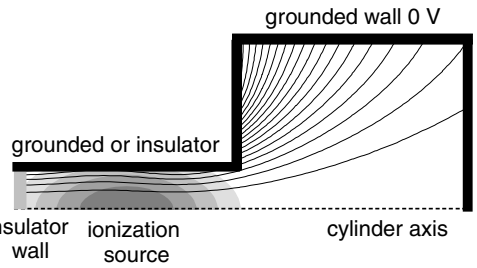

Figure 4. Typical configuration of ECR or helicon discharges. The figure shows the reactor walls (thick line), the magnetic field lines (thin lines) and the ionization source profile (grey scale plot) in the axial-radial plane; the cylinder axis is at the bottom.

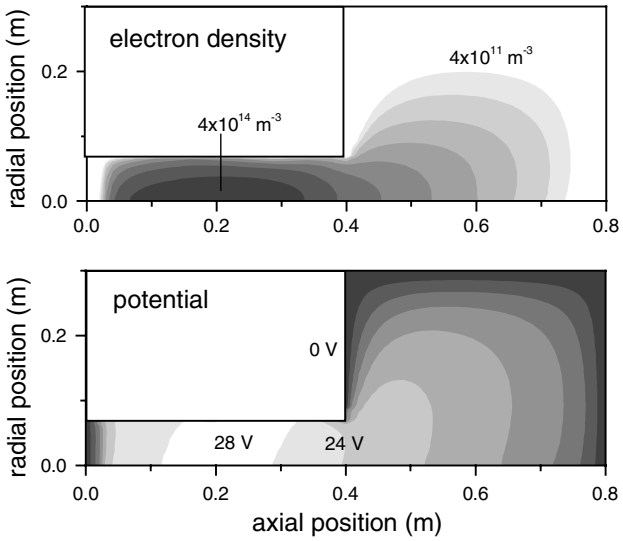

Figure 5. Calculated electron density and potential for the ECR configuration of figure 4 where the side wall of the source chamber is covered with dielectric.

To illustrate that magnetized ambipolar diffusion can involve the chamber walls, we compare the calculated electron density and potential for different source wall materials, shown in figures 5 and 6, and the calculated fractional wall losses shown in table 2. In these calculations the assumed Gaussian ionization source is centred in the source chamber as shown in figure 4, the electron temperature is 3 eV, the electron-collision frequency is $3 \times 10^7\,\mathrm{s}^{-1}$, approximately corresponding to 10 mTorr argon gas, and the ions undergo charge-exchange collisions with a frequency of $10^5\,\mathrm{s}^{-1}$. The numerical grid size is 100×80 cells.

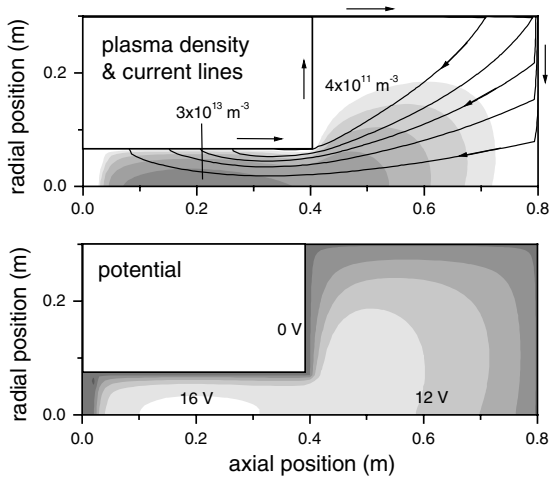

Figure 6. Calculated electron density and potential for the ECR configuration of figure 4 where the side wall of the source chamber is metallic and grounded.

Table 2. Calculated fractions of the electrons and ions that are lost to the different walls of the ECR configuration of figure 4, assuming a dielectric and a metallic source wall, respectively.

	Dielectric		Metallic	
	Electrons	Ions	Electrons	Ions
Source side	0.43	0.43	0.18	0.81
Source bottom	0.28	0.28	0.05	0.05
Process chamber	0.29	0.29	0.78	0.15

In case the source chamber wall is covered with dielectric (figure 5), the electron flux incident on it must be equal to the incident ion flux and therefore $\mathbf{\Gamma}_e \approx \mathbf{\Gamma}_i$ in the source. Since the radial electron flux is impeded by the magnetic field, no sheath or pre-sheath is necessary to attain this, so the radial potential profile in the source becomes almost flat, and the radial plasma loss is relatively small. The dielectric source wall charges up so as to generate an axial electric field that evacuates the ions to the process chamber and to the insulating source bottom.

In case the source chamber wall is grounded (figure 6), the condition $\mathbf{\Gamma}_e \approx \mathbf{\Gamma}_i$ is no longer imposed. The electrons and ions now flow in different directions: the electrons along the magnetic field and the ions mainly to the source wall; see also table 2. This results in a current flowing through the plasma and through the metal chamber walls, short-circuiting the magnetic confinement; some current streamlines are shown in figure 6. The electric potential in the source chamber shows the formation of a (pre)sheath, accelerating the ions to the side wall. The overall wall loss is much greater than with dielectric; the plasma density for a given ionization source term is about one order of magnitude lower; less ions arrive in the process chamber. This reduction in magnetic confinement by short-circuit wall currents has been known since the 1950s and was first described by Simon [23], whose analytical results have later been used and refined, for example in [11, 24, 25].

6.2. *Example II: Hall-effect thruster*

A typical HET configuration is shown in figure 7. The plasma is created in an annular channel between two concentric

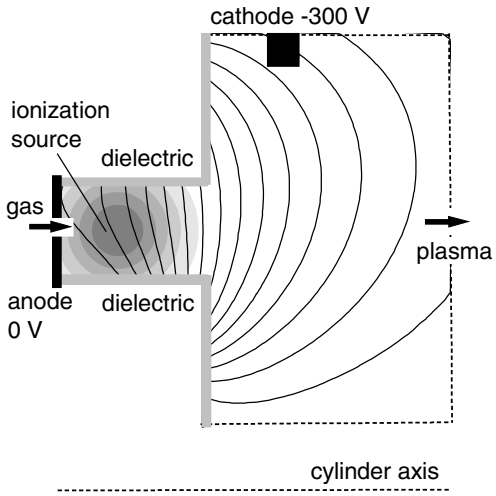

Figure 7. Typical HET configuration.

dielectric walls, containing a radial magnetic field with a maximum strength of about 0.02 T near the channel exit. A constant voltage of about 300 V is applied between the anode at the bottom of the channel and an external hollow cathode. The cathode emits electrons which drift towards the anode across the magnetic field and multiply as they ionize the gas. The gas is injected through holes in the anode at a pressure of a few mTorr and is almost fully ionized. Beyond the channel exit, where the gas density is nearly zero, the electron drift is ensured by anomalous transport mechanisms.

In the calculations presented here, the strongly non-uniform gas density and the anomalous transport are simply represented by an effective electron-collision frequency, linearly decreasing from $\nu = 10^8\,\mathrm{s}^{-1}$ at the anode to $\nu = 10^7\,\mathrm{s}^{-1}$ at the channel exit, and uniform $\nu = 10^7\,\mathrm{s}^{-1}$ outside the channel. The assumed Gaussian ionization source is centred in the channel (figure 7), the electron temperature is 10 eV and the boundary conditions for electron conservation account for the electron current emitted by the hollow cathode. The boundary conditions on the open limits of the computational domain (dashed lines in figure 7) are as follows. In the electron conservation equation, the electron density is set equal to the ion density. In Poisson's equation, these boundaries are described as a dielectric: the potential is locally adjusted so as to ensure zero perpendicular current. The numerical grid has 65×65 cells.

Figure 8 shows the calculated electron density, current streamlines and electric potential. The electron flux along the magnetic field lines is almost completely blocked by the dielectric walls, and the field lines are approximately equipotential, according to the Boltzmann (Morozov) relation shown in equation (11). Because of the small cross-field electron mobility, the electrons are unable to screen the bulk of the plasma from the applied electric field, as they do in unmagnetized plasmas by forming a cathode sheath. The applied electric field penetrates inside the plasma bulk to ensure current conservation and concentrates around the channel exit, where the magnetic field is strongest and the cross-field mobility is smallest. This makes it possible to (1) heat the electrons in the plasma bulk and maintain ionization (not calculated here) and (2) accelerate the created ions in

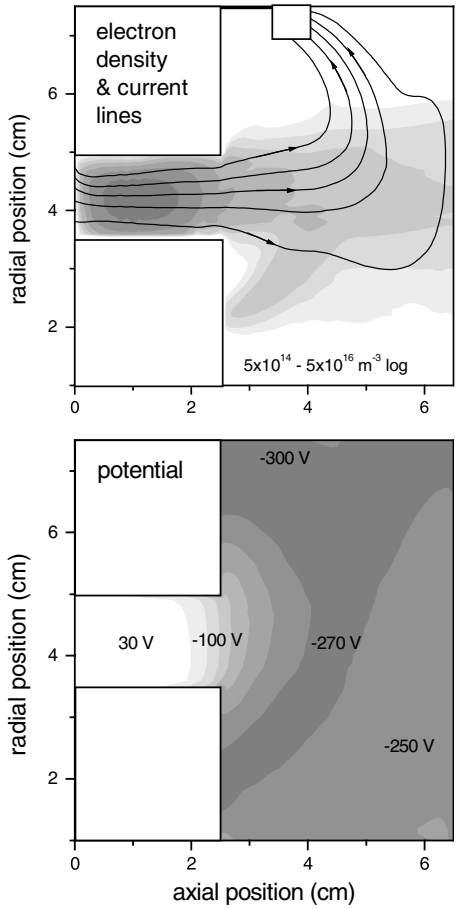

Figure 8. Calculated electron density and potential profile in the HET configuration of figure 7. Also some current streamlines are shown.

a controlled manner towards an open boundary, resulting in an ion beam capable of providing thrust. Previous, more detailed HET modelling studies [6, 7] have shown that the spatial distribution of the electric field and the properties of the ion beam depend strongly on the assumed anomalous transport coefficients. Note also that the density profile in figure 8 shows that some low energy ions are trapped by the electric potential around the magnetic field line intercepting the cathode.

6.3. Example III: Semi-Galathea source

Figure 9 shows the configuration of an ion source for plasma propulsion, based on the Galathea trap developed by Morozov and co-workers [26, 27] and previously modelled in [28]. This source configuration shows some similarity to the Penning discharge configuration developed in the 1930s [29] and used in ion sources in the 1950s [30]. The plasma is created in an annular source chamber containing a complex magnetic field and then flows into an acceleration channel similar to a standard HET channel; we focus on the source chamber. The magnetic field is generated by means of a cylindrical coil in the centre of the chamber, is largely parallel to the chamber walls and has an X-point near the chamber exit. The configuration has several electrodes: (1) the metal wall at the back of the chamber, (2) the central coil, (3) an intermediate electrode near the

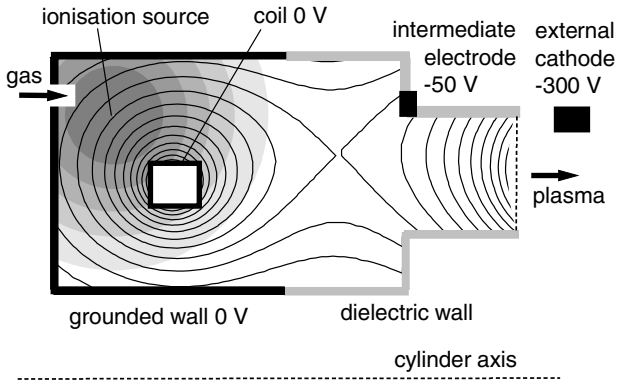

Figure 9. Configuration of a semi-Galathea ion source for plasma propulsion.

chamber exit and (4) an external cathode beyond the chamber exit. A negative voltage of about -50 V is applied to the intermediate electrode with respect to the chamber wall and the central coil. According to the Boltzmann (Morozov) relation, this voltage is felt all along the magnetic field lines intercepting the intermediate electrode, which results in a potential well confining the ions, guiding them to the chamber exit and into the acceleration channel.

In order to correctly describe the chamber exit region, the calculations presented here include the beginning of the acceleration channel. At the calculation boundary inside the acceleration channel we set the electron density equal to the ion density and then fix the potential to -100 V (somewhat arbitrary). We also account for electron emission (0.5 A) from the intermediate electrode in the boundary conditions of the electron equations, for reasons that will be explained below. Other calculation parameters are: Gaussian ionization source centred near the back of the chamber, close to the gas inlet position, uniform electron temperature $T_e = 10$ eV, uniform effective electron-collision frequency $\nu = 3 \times 10^6\ s^{-1}$, no ion collisions and grid size 80×40 cells.

Figure 10 shows the calculation results. As intended, the intermediate electrode lowers the potential in the plasma bulk, resulting in (rather narrow) potential barriers which keep the ions away from the chamber walls and the central coil. Nearly all created ions go into the acceleration channel; only few are lost to the walls. Note however that this potential structure is the opposite of the usual (pre)sheath structure and favours electron wall loss. There is a continuous cross-field electron drift from the intermediate electrode to the chamber wall, illustrated by the current streamlines in figure 10, which requires electron emission from the intermediate electrode.

One might wonder what happens if the intermediate electrode does not emit electrons. Figure 11 shows the answer of the hybrid model: a cathode sheath forms in front of the intermediate electrode and the potential well disappears; most of the ions are lost to the chamber walls. In fact, the need for an emissive intermediate electrode in this plasma source is still a controversial issue. The original concept included an emissive filament-electrode, but recent experiments show that the source performs nearly as well with a normal electrode. When looking into this issue more closely, we note that there is also some electron inflow into the chamber from the acceleration

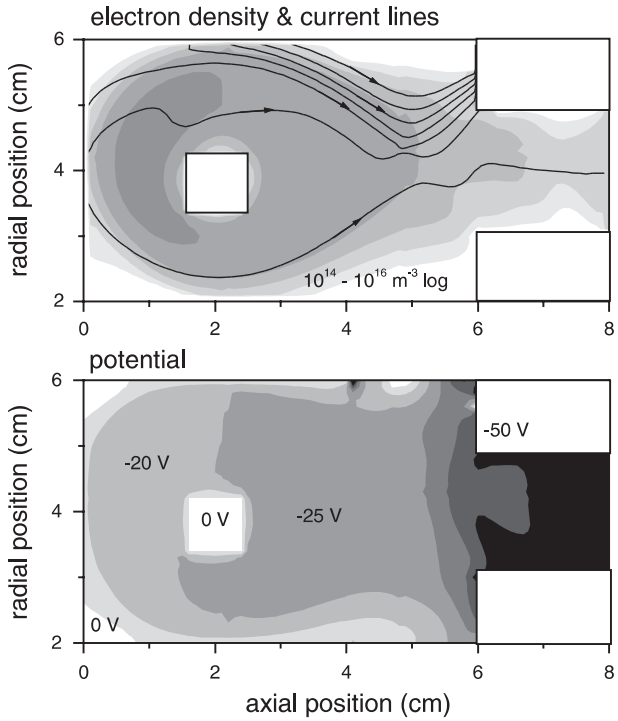

Figure 10. Electron density, current lines and electric potential in the ion source of figure 9, where the intermediate electrode emits electrons.

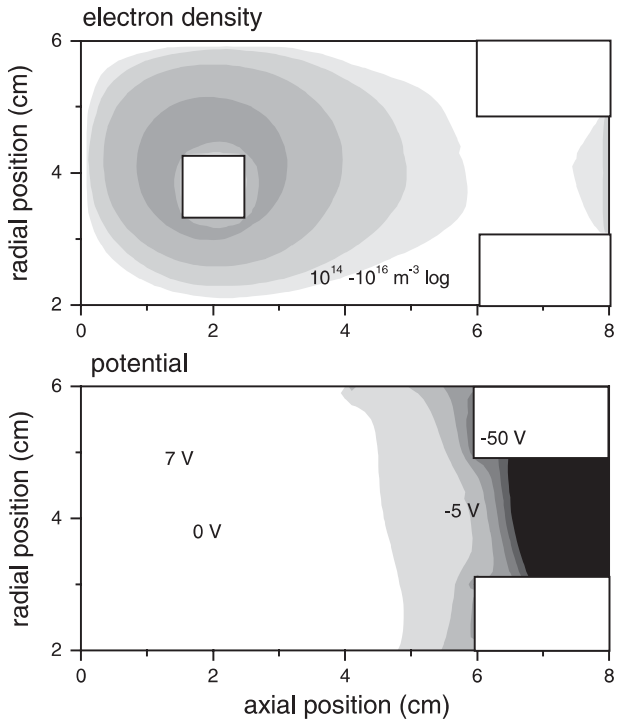

Figure 11. Electron density, current lines and electric potential in the ion source of figure 9, where the intermediate electrode does not emit electrons.

channel; figure 11 suggests that this inflow is not sufficient to compensate for the electron wall loss and maintain the potential well, but this result could depend (for example) on the assumed effective collision frequency (anomalous transport).

7. Conclusions

PIC models are often cumbersome for magnetized discharges and there is an interest in simpler faster models. In this context, we have presented self-consistent hybrid models, combining an ion particle description with electron fluid equations. The magnetized electron flux is described by an anisotropic drift–diffusion equation, where the electron mobility is much smaller in the direction perpendicular to the magnetic field than in the parallel direction. The electric potential is calculated either from Poisson's equation or from the electron equations, assuming quasineutrality.

These hybrid models involve many assumptions: they describe the anomalous electron transport by empirical parameters, they neglect electron inertia and diamagnetic force, etc and can therefore not be expected to yield quantitative results. However, they help to identify and understand the main physical principles of magnetized discharges in realistic two-dimensional configurations. The hybrid models are especially appropriate to study the main effects of the magnetic field on the charged particle transport and space charge electric fields; they demonstrate the important role played by the boundaries and reproduce known phenomena such as the establishment of the Boltzmann relation along magnetic field lines, the penetration of perpendicular applied electric fields into the plasma bulk and the decrease in magnetic confinement by short-circuit wall currents (Simon diffusion); they make the study of these phenomena possible in much greater detail than the analytical treatments found in classical texts, taking into account the two-dimensional magnetic field configuration and other geometrical parameters.

Due to the extreme anisotropy of the electron mobility, the solution of the electron equations is very sensitive to numerical errors. Using standard numerical methods, the numerical errors often dominate the physical behaviour and invalidate the model results, especially for $E \times B$ configurations, where the cross-field electron flux can be strongly overestimated. We have presented an alternative method, based on the interpolation of flux components, which yields accurate electron fluxes and potential profiles in $E \times B$ configurations.

Acknowledgment

The author is indebted to Jean-Pierre Boeuf for inspiring discussions and many useful suggestions.

References

[1] Ashtiani K A, Shohet J L, Hitchon W N G, Kim G-H and Hershkowitz N 1995 A two-dimensional particle-in-cell simulation of an electron-cyclotron-resonance etching tool *J. Appl. Phys.* **78** 2270–8

[2] van der Straaten T A, Cramer N F, Falconer I S and James B W 1998 The cylindrical DC magnetron discharge: I. Particle-in-cell simulation *J. Phys. D: Appl. Phys.* **31** 177–90

[3] Kondo S and Nanbu K 1999 A self-consistent numerical analysis of a planar dc magnetron discharge by the particle-in-cell/Monte Carlo method *J. Phys. D: Appl. Phys.* **32** 1142–52

[4] Adam J C, Heron A and Laval G 2004 Study of stationary plasma thrusters using two-dimensional fully kinetic simulations *Phys. Plasmas* **11** 295–305

[5] Porteous R K, Wu H M and Graves D B 1994 A two-dimensional, axisymmetric model of a magnetized glow discharge plasma *Plasma Sources Sci. Technol.* **3** 25–39
[6] Fife J M 1998 Hybrid-PIC modelling and electrostatic probe survey of Hall thrusters *PhD Thesis* Massachusetts Institute of Technology
[7] Hagelaar G J M, Bareilles J, Garrigues L and Boeuf J-P 2002 Two-dimensional model of a stationary plasma thruster *J. Appl. Phys.* **91** 5592–8
[8] Shidoji E, Ohtake H, Nakano N and Makabe T 1999 Two-dimensional self-consistent simulation of a dc magnetron discharge *Japan. J. Appl. Phys.* **38** 2131–6
[9] Costin C, Marques L, Popa G and Gousset G 2005 Two-dimensional fluid approach to the dc magnetron discharge *Plasma Sources Sci. Technol.* **14** 168–76
[10] Kushner M J 2003 Modeling of magnetically enhanced capacitively coupled plasma sources: Ar discharges *J. Appl. Phys.* **94** 1436–47
[11] Lieberman M A and Lichtenberg A J 1994 *Principles of Plasma Discharges and Materials Processing* (New York: Wiley)
[12] Rax J-M 2005 *Physique des Plasmas* (Paris: Dunod)
[13] Lampe M, Joyce G, Manheimer W M and Slinker S P 1998 Quasi-neutral particle simulation of magnetized plasma discharges: general formalism and application to ECR discharges *IEEE Trans. Plasma Sci.* **26** 1592–609
[14] Yoshikawa S and Rose D J 1962 Anomalous diffusion of a plasma across a magnetic field *Phys. Fluids* **5** 334–40
[15] Janes G S and Lowder R S 1966 Anomalous electron diffusion and ion acceleration in a low-density plasma *Phys. Fluids* **9** 1115–23
[16] Hagelaar G J M, Bareilles J, Garrigues L and Boeuf J-P 2002 Role of anomalous electron transport in a stationary plasma thrusters simulation *J. Appl. Phys.* **93** 67–75
[17] Takekida H and Nanbu K 2004 Particle modelling of plasma confinement by a multipolar magnetic field *J. Phys. D: Appl. Phys.* **37** 1800–8
[18] Morozov A I and Savelyev V V 2000 *Reviews of Plasmas* vol 21, ed B B Kadomtsev and V D Safranov (New York: Consultants Bureau) pp 203–391
[19] Hagelaar G J M 2000 Modeling of microdischarges for display technology *PhD Thesis* Technische Universiteit Eindhoven, The Netherlands
[20] Crumpton P I, Shaw G J and Ware A F 1995 Discretisation and multigrid solution of elliptic equations with mixed derivative terms and strongly discontinuous coefficients *J. Comput. Phys.* **116** 343–58
[21] Schneider G E and Zedan M 1981 A modified strongly implicit procedure for the numerical solution of field problems *Numer. Heat Transfer* **4** 1–19
[22] Ventzek P L G, Hoekstra R J and Kushner M J 1993 Two-dimensional hybrid model of inductively coupled plasma sources for etching *Appl. Phys. Lett.* **63** 605–7
[23] Simon A 1955 Ambipolar diffusion in a magnetic field *Phys. Rev.* **98** 317–8
[24] Vidal F, Johnston T W, Margot J, Chaker M and Pauna O 1999 Diffusion modelling of an hf argon plasma discharge in a magnetic field *IEEE Trans. Plasma Sci.* **27** 727–45
[25] Drentje A G, Wolters U, Nadzeyka A, Meyer D and Weisemann K 2002 Simon short circuit effect in ECRIS *Rev. Sci. Instrum.* **73** 516–20
[26] Morozov A I and Savel'ev V V 1998 On Galateas—magnetic traps with plasma-embedded conductors *Phys.—Usp.* **41** 1049–89
[27] Morozov A I, Bugrova A I, Lipatov A S, Kharchevnikov V K and Kozintseva M V 2000 The barrier operation mode of an electric-discharge Galathea trap *Tech. Phys. Lett.* **16** 686–8
[28] Boniface C, Hagelaar G J M, Garrigues L, Boeuf J P and Prioul M 2005 Modeling of double stage hall effect thrusters *IEEE Trans. Plasma Sci.* **33** 522–3
[29] Penning F M 1936 Glow discharge at low pressure between coaxial cylinders in an axial magnetic field *Physica* **3** 873–94
[30] Meyerand R G and Brown S C 1959 High current ion source *Rev. Sci. Instrum.* **30** 110–1

Effective-Viscosity Approach for Nonlocal Electron Kinetics in Inductively Coupled Plasmas

G. J. M. Hagelaar*

Laboratoire Plasma et Conversion d'Énergie (LAPLACE, CNRS-UPS), Bâtiment 3R2, Université de Toulouse, 118 Route de Narbonne, 31062 Toulouse Cedex 9, France

(Received 18 September 2007; published 15 January 2008)

In inductively coupled plasmas, nonlocal electron kinetics lead to the anomalous skin effect. We show that this can be approximately described through a fluid equation for electron momentum including a viscosity term with an effective-viscosity coefficient. The solution of this momentum equation coupled with the Maxwell equations is in good agreement with results from a particle-in-cell simulation over a wide range of conditions, reproducing the nonmonotonic structure of the anomalous skin with sometimes local negative power absorption.

DOI: 10.1103/PhysRevLett.100.025001 PACS numbers: 52.50.Qt, 52.65.Kj, 52.80.Pi

Inductively coupled plasmas (ICPs), used for material processing in the microelectronics industry [1] and recently proposed as ion sources for thermonuclear fusion [2], are sustained by a rf electric field induced by a rf current in a coil outside the plasma chamber. The description of the inductive field-plasma interaction requires the solution of the Maxwell equations coupled with an equation for the plasma current density in response to the field. For a cylindrical ICP configuration, neglecting the displacement current and the ion contribution to the plasma current, the Maxwell equations reduce to

$$\nabla^2 E - \frac{E}{r^2} = -\mu_0 e n_e \frac{\partial w}{\partial t} \equiv -\frac{m_e \omega_p^2}{e c^2} \frac{\partial w}{\partial t}, \qquad (1)$$

where E is the azimuthal rf electric field, n_e is the electron density, w is the azimuthal mean electron velocity, e is the elementary charge, μ_0 is permeability of vacuum, ω_p is the electron plasma frequency, m_e is the electron mass, and c is the speed of light. According to classical theory [1], the mean electron velocity is related to the local electric field by the local electron momentum equation

$$\frac{\partial w}{\partial t} + \nu w = -\frac{e}{m_e} E, \qquad (2)$$

where ν is the electron-neutral collision frequency (momentum transfer frequency). The self-consistent solution of Eqs. (1) and (2) shows the classical skin effect: exponential decay of the field and current as a function of distance from the plasma edge. From this solution, the time-average power density $\langle -e n_e w E \rangle$ absorbed by the electrons depends on the collision frequency ν with respect to the angular driving frequency ω and vanishes as ν/ω tends to zero (Ohmic heating).

However, these classical results disagree with experimental evidence showing anomalously high power absorption in an anomalously large and sometimes nonmonotonic skin [3–5]. It is well known [6] that the anomalous skin effect in ICPs is due to thermal motion of the electrons: the electrons travel important random distances over the field period which destroys the local relation between field and current as given by Eq. (2). Although a wide variety of theoretical studies [6–9] has demonstrated the principles of this nonlocal electron kinetics, it remains difficult to account for the anomalous skin effect and electron heating in ICP models, especially in multidimensional models used for ICP reactor design and optimization, where the implementation of rigorous nonlocal theory is cumbersome. A common approach to avoid practical complications is to use the local momentum equation (2) but replace the electron-neutral collision frequency by a (higher) effective frequency such as to obtain the correct global power absorption and anomalous skin depth [1]; this however results in incorrect (exponential) spatial profiles of the field and current.

In this Letter we propose an alternative approach: to represent the nonlocal electron kinetics by a viscosity term in the electron momentum equation. To derive this, we consider the electron Boltzmann equation in the case of a one-dimensional plasma in Cartesian coordinates. The plasma extends over a finite length in the x direction and is uniform and infinite in the y and z directions. The rf electric field E is in the y direction. Given this configuration, the Boltzmann equation becomes

$$\frac{\partial f}{\partial t} + v_x \frac{\partial f}{\partial x} + \frac{e}{m_e} \frac{\partial \Phi}{\partial x} \frac{\partial f}{\partial v_x} - \frac{e}{m_e} E \frac{\partial f}{\partial v_y} = \nu (f_0 - f), \qquad (3)$$

where f is the electron distribution function in phase space, v_x and v_y are the velocity coordinates, and Φ is the ambipolar potential. The collision term on the right-hand side of Eq. (3) is an approximation assuming that collisions occur with a constant frequency ν and redistribute the velocity with a given isotropic distribution function f_0. The momentum equation is obtained as the velocity moment of the Boltzmann equation. Multiplying Eq. (3) by $m_e v_y$ and integrating over velocity space we get

$$\frac{\partial m_e n_e w}{\partial t} + \nu m_e n_e w + \frac{\partial S}{\partial x} = -e n_e E, \qquad (4)$$

where n_e is the electron number density, w is the mean velocity (in the y direction), and

$$S = m_e \int v_x v_y f d^3v = m_e \int v_x (v_y - w) f d^3v \quad (5)$$

is the shear pressure. Clearly, any nonlocal effects are represented in Eq. (4) by the shear pressure gradient term, also known as the viscosity term. To evaluate the shear pressure we proceed as follows: we (i) solve the Boltzmann equation by a perturbation approximation, (ii) calculate the mean velocity w and the shear pressure S from the perturbation solution, and (iii) look for a useful relation between S and w. So we substitute $f = f_0(1 + \varphi)$, where $f_0 \sim \exp[(\Phi - m_e v^2/2e)/T_e]$ is the Maxwell-Boltzmann distribution at a given temperature T_e and φ is a small perturbation due to the rf field. The perturbation equation is

$$\frac{\partial \phi}{\partial t} + v_x \frac{\partial \phi}{\partial x} + \frac{e}{m_e} \frac{\partial \Phi}{\partial x} \frac{\partial \phi}{\partial v_x} + \nu \phi = -\frac{E}{T_e} v_y. \quad (6)$$

We consider a uniform plasma density, hence $\Phi = \text{const}$, and apply the usual Fourier-Laplace transformation assuming wave forms $\exp(ikx - i\omega t)$, where k is the wave number (coordinate). The solution of the perturbation equation is then given by

$$\phi_k = -\frac{E_k}{T_e} \frac{v_y}{i(kv_x - \omega) + \nu}, \quad (7)$$

where φ_k and E_k are the transforms of φ and E. The (transform of) the mean velocity is

$$w_k = \frac{1}{n_e} \int v_y \phi_k f_0 d^3\mathbf{v} = -\frac{\sqrt{\pi} e E_k}{m_e v_T} \frac{1}{k} \exp(-z^2) \left(\frac{k}{|k|} + i \operatorname{erfi}(z) \right), \quad (8)$$

where erfi is the imaginary error function, $v_T = (2eT_e/m_e)^{1/2}$ is the nominal thermal speed, and $z = (\omega + i\nu)/kv_T$ is a complex parameter characterizing the "locality" of the electron transport. The shear pressure S_k can be obtained from a similar calculation or more easily from

$$(-i\omega + \nu) m_e n_e w_k + ikS_k = -e n_e E_k. \quad (9)$$

Eliminating E_k from Eqs. (8) and (9), we find the desired relation between S_k and w_k:

$$S_k = \left(\frac{1}{\sqrt{\pi}} \frac{\exp(z^2)}{i(|k|/k) - \operatorname{erfi}(z)} + z \right) v_T m_e n_e w_k. \quad (10)$$

In collisional conditions, the locality parameter $|z| \gg 1$ and Eq. (10) reduces to $S_k = v_T m_e n_e w_k / 2z = -(m_e n_e v_T^2 / 2\nu)(ikw_k)$, which corresponds in real space to the classical expression $S = \mu(\partial w/\partial x)$ with a viscosity coefficient $\mu = m_e n_e v_T^2/2\nu$ as in the Navier-Stokes equations. What we are interested in, however, is the opposite limit $|z| < 1$ describing the case that nonlocal effects are important. Approximating Eq. (10) to first order of z and rearranging the terms, we obtain

$$[\sqrt{\pi}|k| v_T + (\pi - 2)(-i\omega + \nu)] S_k = -m_e n_e v_T^2 (ikw_k). \quad (11)$$

We now wish to transform this result back to real space. The inverse transformation is considerably simplified if we approximate Eq. (10) further to zeroth order of z, i.e., if we neglect the second term on the left:

$$S_k = -\frac{m_e n_e v_T}{\sqrt{\pi}} \frac{1}{|k|} (ikw_k). \quad (12)$$

Realizing that the Fourier transform of $1/x$ is $-(\pi/2)^{1/2} \times (ik/|k|)$ and using the convolution theorem, we find

$$S(x) = -\frac{m_e n_e v_T}{\pi^{3/2}} \int_0^\infty \frac{w(x + x') - w(x - x')}{x'} dx'. \quad (13)$$

This is a nonlocal velocity difference. Equations (12) and (13) were proposed previously by [10] and applied to ICPs by [8]. Although relatively simple, Eq. (13) is still not very satisfactory from a practical point of view, especially since, in order to account for reflection of electrons at the plasma edge, the integral should continue over consecutive mirror images of the plasma repeated until infinity.

We therefore propose another approach. We approximate the absolute wave number $|k|$ on the left-hand side of Eq. (11) by $|k| \approx \langle |k| \rangle$ some kind of average wave number. The inverse transformation is now straightforward:

$$[\sqrt{\pi} \langle |k| \rangle v_T + (\pi - 2)\nu] S + (\pi - 2) \frac{\partial S}{\partial t} = -m_e n_e v_T^2 \frac{\partial w}{\partial x}, \quad (14)$$

but $\langle |k| \rangle$ still needs to be specified. To estimate $\langle |k| \rangle$ we make use of the fact that the wave numbers present in the plasma are not arbitrary but depend on the coupling between w and E via the Maxwell equations. Combining Eq. (14) with the momentum equation (4) and the Maxwell equation (1), neglecting ν and ω with respect to $\langle |k| \rangle v_T$ (as before), we obtain

$$\frac{\partial^4 w}{\partial x^4} = -\frac{\sqrt{\pi} \langle |k| \rangle \omega_p^2}{c^2 v_T} \frac{\partial w}{\partial t}. \quad (15)$$

The general solution of this differential equation is a superposition of four waves each with the same absolute wave number

$$k_0 = \langle |k| \rangle^{1/4} \left(\frac{\sqrt{\pi} \omega \omega_p^2}{c^2 v_T} \right)^{1/4}, \quad (16)$$

which clearly characterizes the length scale of velocity variations in the plasma. We assume now simply that $\langle |k| \rangle = k_0$. Equation (16) becomes

$$\langle |k| \rangle = k_0 = \left(\frac{\sqrt{\pi} \omega \omega_p^2}{c^2 v_T} \right)^{1/3}, \quad (17)$$

which is the inverse of the usual expression for the anomalous skin depth [1]. We then write the momentum equation

(4) and the shear pressure equation (14) in the following convenient form:

$$\frac{\partial w}{\partial t} + \nu w + V = -\frac{e}{m_e} E, \tag{18}$$

$$V + \tau \frac{\partial V}{\partial t} = -\eta \frac{\partial^2 w}{\partial x^2}, \tag{19}$$

where $V = (\partial S/\partial x)/n_e m_e$ and η and τ are effective-viscosity coefficients given by

$$\eta = \frac{v_T^2}{\sqrt{\pi} k_0 v_T + (\pi - 2)\nu} = \frac{v_T^2}{\pi - 2}\tau. \tag{20}$$

The viscosity equation (19) can be generalized to cylindrical coordinates and nonuniform plasma density in analogy with the viscosity term in the cylindrical Navier-Stokes equations:

$$V + \tau \frac{\partial V}{\partial t} = -\eta\left(\frac{1}{n_e}\nabla \cdot (n_e \nabla w) - \frac{w}{r}\right), \tag{21}$$

where w is azimuthal as in Eq. (1).

Finally, we need to specify a boundary condition for Eqs. (18)–(21). Because of the high plasma density in ICPs, the plasma sheaths are negligibly thin, and the plasma is usually described by a quasineutral model (where the sheaths have been analytically removed). It is then appropriate to assume that the quasitotality of the electrons arriving at the plasma edge are specularly reflected. Total reflection destroys the velocity gradient normal to the edge:

$$\nabla_\perp w = 0, \tag{22}$$

which is an appropriate boundary condition.

We propose the fluid equations (18)–(22) as an improvement of the local electron momentum equation (2) to describe nonlocal effects in ICPs. Clearly, the derivation of these equations is not mathematically rigorous and there is no guarantee that they give correct results. To corroborate the equations, we implement and compare two numerical models: a fluid model and a simplified particle-in-cell (PIC) model. Both models provide a self-consistent solution in one spatial dimension of the Maxwell equation (1) coupled with a description of the electrons. We assume a fixed spatial ion-density profile and constant electron temperature. In the fluid model, the electron density is set equal to the ion density and the mean electron velocity is solved from the fluid equations (18)–(22). The PIC model describes the electrons in much greater detail, but is nevertheless designed to reproduce as closely as possible the conditions assumed in the fluid model: nearly Maxwellian electron distribution, total specular electron reflection at the edge, etc.

The principles of the PIC model are as follows. The electrons are represented by a large number of macroparticles, which are conserved throughout the simulation and have a total statistical weight equal to the space-integrated ion density. The macroparticles are simultaneously pushed by integration of Newton's equation over numerical time steps, accounting for (i) the ambipolar electrostatic force along the simulation dimension, (ii) the rf electric force perpendicular to the simulation dimension, and (iii) specular reflection at the plasma edge. Collisions of the macroparticles are simulated by the usual Monte Carlo method, assuming a constant collision probability $\nu\Delta t$ per time step and a random Maxwellian redistribution of the velocity. Each time step, the spatial profiles of the electron density and mean velocity are calculated from the macroparticle positions and velocities. The ambipolar electric potential is solved from Poisson's equation with an increased permittivity to mitigate numerical constraints on the time step and grid spacing. Because of the specular electron reflection at the edge, no plasma sheath forms, but the ambipolar field arises from density gradients in the plasma bulk. To check the numerical convergence of the PIC model, we compare results for different numerical parameters (10^5–10^7 macroparticles, 10^2–10^4 time steps per rf period, 50–500 grid points uniform and nonuniform) and calculate their statistical variance. We estimate that the

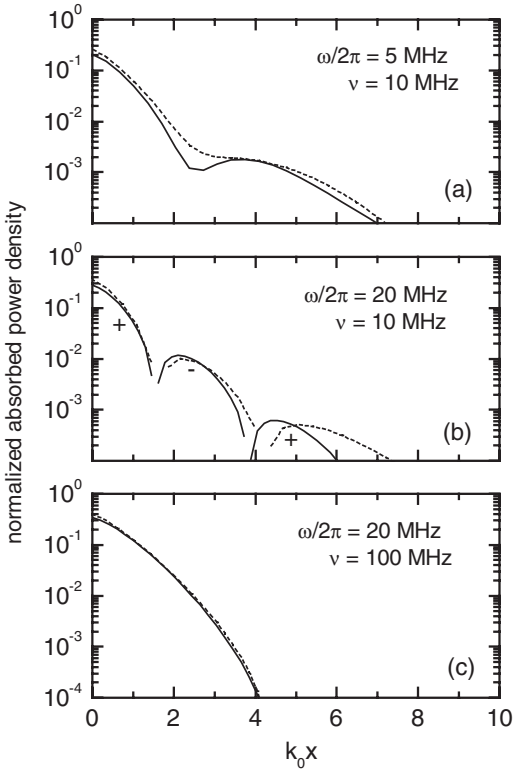

FIG. 1. Comparison of the spatial power absorption profiles from the fluid model (solid line) and the PIC model (dashed line) for a semi-infinite uniform plasma. The different plots correspond to different driving frequencies and collision frequencies (indicated on the plots). The plasma density is 3×10^{17} m^{-3} and the electron temperature is 10 eV. The power absorption density is normalized to $e^2 E_0^2 n_e / 2 m_e \omega$, where E_0 is the field amplitude at the edge.

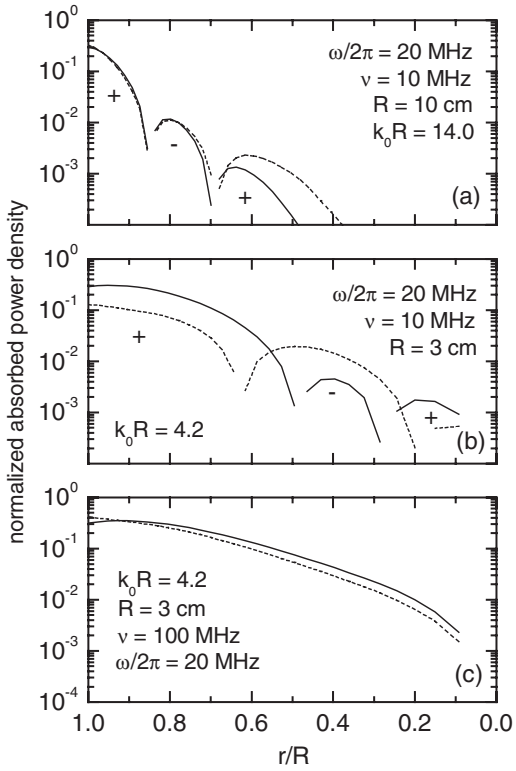

FIG. 2. Comparison of the radial power absorption profiles from the fluid model (solid line) and the PIC model (dashed line) for a finite, diffusive, cylindrical plasma. The different plots correspond to different plasma radii and collision frequencies (indicated on the plots). The plasma density has parabolic radial profile, increasing from 3×10^{17} m^{-3} at the edge ($r/R = 1$) to 10^{18} m^{-3} in the center ($r/R = 0$). The electron temperature is 10 eV. The power absorption density is normalized to $e^2 E_0^2 n_0 / 2 m_e \omega$, where E_0 and n_0 are the field amplitude and the plasma density at the edge. The indicated $k_0 R$ values correspond to n_0.

total error in the presented PIC results does not exceed a few tens of percents over the entire range shown.

First, we compare the results from the fluid and PIC models for the case of a semi-infinite uniform plasma. Using Cartesian coordinates, we define the plasma edge at the left boundary at $x = 0$, impose zero field and current at the right boundary, and make sure that the simulation domain is large enough for the results to be independent of domain size. Figure 1 shows the spatial profiles of the absorbed power (time average rf current $\times$ field) from the two models for different driving frequencies 5–20 MHz, different collision frequencies 10^7–10^8 s^{-1}, plasma density 3×10^{17} m^{-3}, and electron temperature 10 eV. The overall agreement between the models is good. Figure 1(b) shows a negative absorption region, known from experimental measurements [4] and rigorous nonlocal theory [9].

Then, we compare the two models for a more realistic configuration: a diffusive cylindrical plasma of finite radial size (but infinite axial size). We assume a parabolic radial profile for the ion density, decreasing from 10^{18} m^{-3} in the plasma center to 3×10^{17} m^{-3} at the plasma edge. This configuration has an additional degree of freedom with respect to the semi-infinite case: the plasma radius R. Figure 2 shows the power absorption profiles from the two models for different plasma radii 3–5 cm, driving frequency 20 MHz, and different collision frequencies 10^7–10^8 s^{-1}. The agreement between the models is again good for large plasma radii $k_0 R > 5$, but significant differences appear for smaller radii and small collision frequencies [Fig. 2(b)]; at higher collision frequencies the agreement remains good [Fig. 2(c)].

Let us also remark that the results from our fluid model are consistent with those (not shown here) from Eqs. (12) and (13) previously used in [8], except that they are in significantly better agreement with the PIC results at higher driving frequencies and collision frequencies (ω or $\nu > 0.5 k_0 v_T$). Contrary to Eqs. (12) and (13), the viscosity equations (19) and (20) account for oscillation and collision effects on the shear pressure.

In summary, we propose a simple approach to describe the anomalous skin effect and electron heating in ICPs through a fluid equation for electron momentum including a viscosity term with an effective-viscosity coefficient to represent nonlocal kinetics. Specular reflection at the plasma edge is represented as a boundary condition. The numerical solution of the improved momentum equation coupled with the Maxwell equations agrees well with results from a PIC simulation over a wide range of conditions, although for a diffusive cylindrical plasma differences appear as the plasma radius approaches the skin depth at low collision frequency. The proposed equations are straightforwardly generalized and solved for two-dimensional plasma configurations and are of practical use for ICP models.

This work was performed in the framework of a collaboration LAPLACE-CEA Cadarache on the modeling of ICP sources for neutral beam injection for ITER.

*gerjan.hagelaar@laplace.univ-tlse.fr

[1] M. A. Lieberman and A. Lichtenberg, *Principles of Plasma Discharges and Materials Processing* (Wiley, New York, 1994).
[2] E. Speth *et al.*, Nucl. Fusion **46**, S220 (2006).
[3] V. A. Godyak and R. B. Piejak, J. Appl. Phys. **82**, 5944 (1997).
[4] V. A. Godyak and V. I. Kolobov, Phys. Rev. Lett. **79**, 4589 (1997).
[5] V. A. Godyak, R. B. Piejak, B. M. Alexandrovich, and V. I. Kolobov, Phys. Rev. Lett. **80**, 3264 (1998).
[6] E. S. Weibel, Phys. Fluids **10**, 741 (1967).
[7] M. M. Turner, Phys. Rev. Lett. **71**, 1844 (1993).
[8] M. M. Turner, Plasma Sources Sci. Technol. **5**, 159 (1996).
[9] Yu. O. Tyshetskiy, Ph.D. thesis, University of Saskatchewan, 2003.
[10] G. W. Hammett and F. W. Perkins, Phys. Rev. Lett. **64**, 3019 (1990).